

Ministry of Education and Science of the Russian Federation
Saint Petersburg National Research University of Information
Technologies, Mechanics, and Optics

NANOSYSTEMS:
PHYSICS, CHEMISTRY, MATHEMATICS

2021, volume 12(1)

Наносистемы: физика, химия, математика

2021, том 12, № 1



NANOSYSTEMS:

PHYSICS, CHEMISTRY, MATHEMATICS

ADVISORY BOARD MEMBERS

Chairman: V.N. Vasiliev (*St. Petersburg, Russia*),
V.M. Buznik (*Moscow, Russia*); V.M. Ievlev (*Voronezh, Russia*), P.S. Kop'ev (*St. Petersburg, Russia*), N.F. Morozov (*St. Petersburg, Russia*), V.N. Parmon (*Novosibirsk, Russia*),
A.I. Rusanov (*St. Petersburg, Russia*),

EDITORIAL BOARD

Editor-in-Chief: I.Yu. Popov (*St. Petersburg, Russia*)

Section Co-Editors:

Physics – V.M. Uzdin (*St. Petersburg, Russia*),

Chemistry, material science – V.V. Gusarov (*St. Petersburg, Russia*),

Mathematics – I.Yu. Popov (*St. Petersburg, Russia*).

Editorial Board Members:

V.M. Adamyan (*Odessa, Ukraine*); O.V. Al'myasheva (*St. Petersburg, Russia*);
A.P. Alodjants (*Vladimir, Russia*); S. Bechta (*Stockholm, Sweden*); J. Behrndt (*Graz, Austria*);
M.B. Belonenko (*Volgograd, Russia*); A. Chatterjee (*Hyderabad, India*); A.V. Chizhov
(*Dubna, Russia*); A.N. Enyashin (*Ekaterinburg, Russia*), P.P. Fedorov (*Moscow, Russia*);
E.A. Gudilin (*Moscow, Russia*); V.K. Ivanov (*Moscow, Russia*), H. Jónsson (*Reykjavik, Iceland*);
A.A. Kiselev (*Durham, USA*); Yu.S. Kivshar (*Canberra, Australia*); S.A. Kozlov
(*St. Petersburg, Russia*); P.A. Kurasov (*Stockholm, Sweden*); A.V. Lukashin (*Moscow, Russia*);
I.V. Melikhov (*Moscow, Russia*); G.P. Miroshnichenko (*St. Petersburg, Russia*);
I.Ya. Mittova (*Voronezh, Russia*); Nguyen Anh Tien (*Ho Chi Minh, Vietnam*); V.V. Pankov
(*Minsk, Belarus*); K. Pankrashkin (*Orsay, France*); A.V. Ragulya (*Kiev, Ukraine*);
V. Rajendran (*Tamil Nadu, India*); A.A. Rempel (*Ekaterinburg, Russia*); V.Ya. Rudyak
(*Novosibirsk, Russia*); D Shoikhet (*Karmiel, Israel*); P Stovicek (*Prague, Czech Republic*);
V.M. Talanov (*Novocherkassk, Russia*); A.Ya. Vul' (*St. Petersburg, Russia*);
A.V. Yakimansky (*St. Petersburg, Russia*), V.A. Zagrebnov (*Marseille, France*).

Editors:

I.V. Blinova; A.I. Popov; A.I. Trifanov; E.S. Trifanova (*St. Petersburg, Russia*),
R. Simoneaux (*Philadelphia, Pennsylvania, USA*).

Address: University ITMO, Kronverkskiy pr., 49, St. Petersburg 197101, Russia.

Phone: +7(812) 607-02-54, **Journal site:** <http://nanojournal.ifmo.ru/>,

E-mail: popov1955@gmail.com

AIM AND SCOPE

The scope of the journal includes all areas of nano-sciences. Papers devoted to basic problems of physics, chemistry, material science and mathematics inspired by nanosystems investigations are welcomed. Both theoretical and experimental works concerning the properties and behavior of nanosystems, problems of its creation and application, mathematical methods of nanosystem studies are considered.

The journal publishes scientific reviews (up to 30 journal pages), research papers (up to 15 pages) and letters (up to 5 pages). All manuscripts are peer-reviewed. Authors are informed about the referee opinion and the Editorial decision.

CONTENT

MATHEMATICS

W. Borrelli, R. Carlone

Bifurcating standing waves for effective equations in gapped honeycomb structures 5

V.V. Kuidin, V.V. Zalipaev, D. R. Gulevich

Discrete spectrum Analysis using Laplace transform and Volterra equations (DALV-method) 15

PHYSICS

P.V. Mokrushnikov, V.Ya. Rudyak, E.V. Lezhnev

Mechanism of gas molecule transport through erythrocytes' membranes by kinks-solitons 22

D. Chevizovich, A.V. Chizhov, Z. Ivić, A.A. Reshetnyak

On the long-distance charge transport in DNA-like macromolecules 32

S. Leble

Domain wall evolution at nanowires in terms of 3D LLG equation initial-boundary problem 42

Ya.A. Fofanov, I.V. Pleshakov, A.V. Prokof'ev, E.E. Bibik

Weak polarization-optical responses of diluted magnetic nanofluid probed by laser radiation with polarization modulation 60

Priyanka, Savita Gill

Study of nonclassicality in fifth harmonic generation nonlinear optical process 65

I.S. Lobanov, A.I. Trifanov, E.S. Trifanova, I.Y. Popov, E. Fedorov, K.V. Pravdin, M.A. Moskalenko

Photon generation in resonator with time dependent boundary conditions 73

CHEMISTRY AND MATERIAL SCIENCE

A.A. Ostroushko, K.V. Grzhegorzhevskii, S.Yu. Medvedeva, I.F. Gette, M.O. Tonkushina, I.D. Gagarin, I.G. Danilova

Physicochemical and biochemical properties of the Keplerate-type nanocluster polyoxomolybdates as promising components for biomedical use 81

V.F. Kabanov, A.I. Mikhailov, M.V. Gavrikov Analysis of the energy spectrum of indium antimonide quantum dots with temperature changes	113
M.M. Khalisov, V.A. Lebedev, A.S. Poluboyarinov, A.V. Garshev, E.K. Khrapova, A.A. Krasilin, A.V. Ankudinov Young's modulus of phyllosilicate nanoscrolls measured by the AFM and by the in-situ TEM indentation	118
Information for authors	128

Bifurcating standing waves for effective equations in gapped honeycomb structures

W. Borrelli¹, R. Carlone²

¹Centro De Giorgi, Scuola Normale Superiore, Piazza dei Cavalieri 3, I-56100, Pisa, Italy

²Università “Federico II” di Napoli, Dipartimento di Matematica e Applicazioni “R. Caccioppoli”,
MSA, via Cinthia, I-80126, Napoli, Italy

william.borrelli@sns.it, raffaele.carlone@unina.it

PACS 03.65.-w, 02.30.Rz

DOI 10.17586/2220-8054-2021-12-1-5-14

In this paper, we deal with two-dimensional cubic Dirac equations, appearing as an effective model in gapped honeycomb structures. We give a formal derivation starting from cubic Schrödinger equations and prove the existence of standing waves bifurcating from one band-edge of the linear spectrum.

Keywords: nonlinear Dirac equations, bifurcation methods, existence results, honeycomb structures.

Received: 28 December 2020

Revised: 6 January 2021

1. Introduction

1.1. Motivation and main results

In this paper, we deal with nonlinear massive Dirac equations of the form:

$$(\mathcal{D} + m\sigma_3 - \omega)\psi = h(\psi)\psi \quad \text{on } \mathbb{R}^2, \quad (1)$$

where $\omega \in (-m, m)$ is a frequency in the spectral gap of the Dirac operator $\mathcal{D} + m\sigma_3$, with $m > 0$ (see Section 2). We consider the nonlinearity in (1) of the form:

$$h(z) = \begin{pmatrix} \beta_1|z_1|^2 + 2\beta_2|z_2|^2 & 0 \\ 0 & \beta_1|z_2|^2 + 2\beta_2|z_1|^2 \end{pmatrix}, \quad z \in \mathbb{R}^2, \quad (2)$$

with given parameters $\beta_1, \beta_2 > 0$.

Equation (1) appears as an effective model of wave propagation in two-dimensional honeycomb structures. As proved in [1], if $V \in C^\infty(\mathbb{R}^2, \mathbb{R})$ is a potential having the symmetries of a honeycomb lattice, then the Schrödinger operator:

$$H = -\Delta + V(x), \quad x \in \mathbb{R}^2, \quad (3)$$

exhibits generically conical touching points in its dispersion bands called *Dirac points*. The dynamics of wave packets spectrally concentrated around Dirac points, see [2], is thus effectively described by the *massless* (i.e., $m = 0$) Dirac operator. Adding a perturbation that breaks parity induces a mass term in the effective operator, as proved in [1, Appendix].

An important model in nonlinear optics and in the description of macroscopic phenomena is given by the *nonlinear Schrödinger / Gross-Pitaevski equation* [3–5]:

$$i\partial_t u = Hu + |u|^2 u. \quad (4)$$

This equation, in the approximation described before, leads (at least formally) to the effective cubic nonlinear-ity (2). Indeed, as first computed in [6], the effective equation around Dirac points reads:

$$\begin{cases} \partial_t \Xi_1 + \bar{\lambda}(\partial_{x_1} + i\partial_{x_2})\Xi_2 = i(2\beta_2|\Xi_1|^2 + \beta_1|\Xi_2|^2)\Xi_1, \\ \partial_t \Xi_2 + \lambda(\partial_{x_1} - i\partial_{x_2})\Xi_1 = i(\beta_1|\Xi_1|^2 + 2\beta_2|\Xi_2|^2)\Xi_2, \end{cases} \quad (5)$$

where the parameters $\lambda \in \mathbb{C} \setminus \{0\}$, $\beta_1, \beta_2 > 0$ depend on the potential V in (3).

Setting $\Psi_1 := -\frac{\lambda}{|\lambda|}\Xi_2$, $\Psi_2 := \Xi_1$ and looking for stationary solutions

$$\Psi(t, x) = \psi(x),$$

we get the massless version of (1), i.e. with $m = \omega = 0$. As shown in Section 3, adding a perturbation breaking the parity of the potential V in (3) gives an additional mass term in the effective equation. This corresponds to a gap $(-m, m)$ in the linear spectrum so that we can consider stationary solutions at frequency $\omega \in (-m, m)$, leading to (1).

In [7] the validity of the effective cubic equation is studied. In Section 3 we give a formal derivation of the effective model (1) using a multiscale expansion.

Existence and qualitative properties of solutions to the massless version of (1) have been studied in [8, 9]. The massive case in (1) has been addressed in [10, 11] for a special choice of parameters in (1).

In this paper we partly generalize those results dealing with arbitrary $\beta_1, \beta_2 > 0$ and proving the existence of stationary solutions bifurcating from one edge of the spectral gap of the operator $\mathcal{D} + m\sigma_3$.

We remark that cubic Dirac equations in two dimensions are *critical* for the Sobolev embedding. Such types of equations have been studied also in different contexts. We mention, for instance, problems from conformal spin geometry, for which we refer the reader to [12–15] and references therein, and in the case of coupled systems involving the Dirac operator and critical nonlinearities related to supersymmetric models coupling gravity with fermions, see [16, 17]. The main difficulty in studying those equations comes from the underlying conformal symmetry so that looking for stationary solutions by variational methods one has to deal with the induced loss of compactness, see [10, 11]. This problem can be circumvented, for instance, using a bifurcation argument to find solutions to (1), as done in this paper following [18]. We mention that the same method has been recently used for nonlinear Dirac equations on star graphs [19].

The results given in [10, 11] correspond to the choice of parameters $\beta_1 = 2\beta_2$, so that one can assume $\beta_1 = 1$, $\beta_2 = 1/2$ by scaling. In this paper, we deal with general $\beta_1, \beta_2 > 0$, but this forces us to put restrictions on the frequency ω that will be close to the band-edge at m . More precisely, we focus on the existence of standing waves to (1) of symmetric form:

$$\psi(r, \theta) = \begin{pmatrix} v(r) \\ iu(r)e^{i\theta} \end{pmatrix}, \quad (r, \theta) \in (0, \infty) \times \mathbb{S}^1, \quad (6)$$

(r, θ) being polar coordinates in \mathbb{R}^2 , and u, v real-valued functions. Notice that (6) is the two-dimensional analogue of the *Soler/Wakano ansatz* [20–22].

Theorem 1.1. *Let $\varepsilon := m - \omega$. There exists $\varepsilon_0 > 0$ such that for $\varepsilon \in (0, \varepsilon_0)$ equation (1) admits a solution ψ_ε of the form (6), with*

$$u_\varepsilon(r) = \varepsilon(-f'(\sqrt{\varepsilon}r) + e_1(\sqrt{\varepsilon}r)), \quad v_\varepsilon(r) = \sqrt{\varepsilon}(f(\sqrt{\varepsilon}r) + e_2(\sqrt{\varepsilon}r)), \quad r > 0,$$

where $\|e_j\|_{H^1(\mathbb{R}^2)} \leq C\varepsilon$, $j = 1, 2$, and $f \in H^1(\mathbb{R}^2)$ is the positive ground state of the NLS

$$-\Delta f - f^3 + f = 0, \quad \text{on } \mathbb{R}^2.$$

Remark 1.1. Arguing as in Section 4 one can deal with the regime $-m < \omega < 0$, $\omega \rightarrow -m$. However in that case the limit equation (57) is replaced by the following *defocusing* NLS

$$-\Delta U + U^3 + U = 0, \quad \text{on } \mathbb{R}^2, \quad (7)$$

which has no non-trivial solution in $H^1(\mathbb{R}^2)$. This can be easily seen multiplying the equation by such a solution and integrating by parts.

2. The Dirac operator

The *Dirac operator* is the constant coefficients first order differential operator defined in two dimensions as:

$$\mathcal{D}_m = \mathcal{D} + m\sigma_3 := -i\sigma \cdot \nabla + m\sigma_3. \quad (8)$$

The constant $m > 0$ usually represents the mass of the particle described by the equation. We adopt the notation $\sigma \cdot \nabla := \sigma_1\partial_1 + \sigma_2\partial_2$ and the σ_k 's are the Pauli matrices:

$$\sigma_1 := \begin{pmatrix} 0 & 1 \\ 1 & 0 \end{pmatrix}, \quad \sigma_2 := \begin{pmatrix} 0 & -i \\ i & 0 \end{pmatrix}, \quad \sigma_3 := \begin{pmatrix} 1 & 0 \\ 0 & -1 \end{pmatrix}. \quad (9)$$

The operator \mathcal{D}_m is a self-adjoint operator on $L^2(\mathbb{R}^2, \mathbb{C}^2)$, with domain $H^1(\mathbb{R}^2, \mathbb{C}^2)$ and form-domain $H^{1/2}(\mathbb{R}^2, \mathbb{C}^2)$.

Passing to the Fourier domain $p = (p_1, p_2)$ the Dirac operator (8) becomes the multiplication by the matrix:

$$\widehat{\mathcal{D}}_m(p) = \begin{pmatrix} m & p_1 - ip_2 \\ p_1 + ip_2 & m \end{pmatrix}$$

and then the spectrum is easily found to be:

$$\text{Spec}(\mathcal{D}_m) = (-\infty, -m] \cup [m, +\infty). \quad (10)$$

The above mentioned results can be found, e.g., in [23].

3. Formal derivation of the model

In this section, we give a formal derivation of equation (1) from the corresponding cubic Schrödinger equation with honeycomb potential following the exposition given in [24].

We consider a fixed triangular lattice $\Lambda := \mathbb{Z}v_1 \oplus \mathbb{Z}v_2$, where $v_1, v_2 \in \mathbb{R}^2$ are two linearly independent vectors.

3.1. Honeycomb Schrödinger operators

Consider the Schrödinger operator

$$H := -\Delta + V(x), \quad x \in \mathbb{R}^2. \quad (11)$$

Definition 3.1. *The function $V \in C^\infty(\mathbb{R}^2)$ is called honeycomb potential, see [1], if there exists $x_0 \in \mathbb{R}^2$ such that $\tilde{V}(x) = V(x - x_0)$ has the following properties:*

- (1) \tilde{V} is periodic with respect to some triangular lattice Λ , that is, $\tilde{V}(x + v) = \tilde{V}(x)$, $\forall x \in \mathbb{R}^2, \forall v \in \Lambda$;
- (2) \tilde{V} is even: $\tilde{V}(-x) = \tilde{V}(x)$, $\forall x \in \mathbb{R}^2$;
- (3) \tilde{V} is invariant by $\frac{2\pi}{3}$ counterclockwise rotation:

$$\mathcal{R}[\tilde{V}](x) := \tilde{V}(R^*x) = \tilde{V}(x) \quad \forall x \in \mathbb{R}^2,$$

where R is the corresponding rotation matrix:

$$R = \begin{pmatrix} -\frac{1}{2} & \frac{\sqrt{3}}{2} \\ \frac{\sqrt{3}}{2} & -\frac{1}{2} \end{pmatrix}. \quad (12)$$

Remark 3.1. (Some examples of honeycomb potentials [1])

- (1) **Atomic potentials:** Let $\mathbb{H} = (A + \Lambda) \cup (B + \Lambda)$ be a hexagonal lattice, given by the superposition of two triangular lattices. Consider a radial function $V_0 \in C^\infty(\mathbb{R}^2)$ rapidly decaying at infinity (for instance, with polynomial rate) representing the potential generated by a nucleus located on a vertex of the lattice. The potential

$$V(x) = \sum_{y \in \mathbb{H}} V_0(x - y)$$

is then given by the superposition of atomic potentials, and it is a honeycomb potential (Def. 3.1).

- (2) **Optical lattices:** The envelop ψ of the electric field of a monochromatic beam propagating in a dielectric medium can be described by a Schrödinger equation. More precisely, denoting by z the direction of propagation of the beam and assuming that the refraction index varies only in the transversal directions (x, y) , the function ψ solve the following equation:

$$i\partial_z \psi = (-\Delta + V(x, y)) \psi. \quad (13)$$

In this case, the honeycomb potential is generated using optical interference techniques [25]. A typical example is the potential of the form:

$$V(x, y) \simeq V_0(\cos(k_1 \cdot (x, y)) + \cos(k_1 \cdot (x, y)) + \cos((k_1 + k_2) \cdot x)), \quad V_0 \in \mathbb{R}, k_1, k_2 \in \mathbb{R}^2. \quad (14)$$

For any fixed $k \in \mathbb{R}^2$ consider the following eigenvalue problem with *pseudo-periodic boundary conditions* (see [1] and [26, Sec. XIII.16]):

$$\begin{cases} H\Phi(x; k) = \mu(k)\Phi(x; k), & x \in \mathbb{R}^2 \\ \Phi(x + v; k) = e^{ik \cdot v} \Phi(x; k), & v \in \Lambda. \end{cases} \quad (15)$$

Remark 3.2. The eigenfunctions $\Phi(x; k)$ are of class C^∞ by elliptic regularity theory.

Recall that, given a lattice, its (*first*) Brillouin zone \mathcal{B} is defined as the fundamental cell of the dual lattice. In the case of a honeycomb lattice, both its fundamental cell and its Brillouin zone are hexagonal [1]. An important property of \mathcal{B} is that waves propagating in a periodic medium can be described in terms of *Bloch functions*.

Given $k \in \mathcal{B}$, the resolvent of $H(k)$ is compact and then the spectrum of the operator is real and purely discrete, accumulating at $+\infty$:

$$\mu_1(k) \leq \mu_2(k) \leq \dots \leq \mu_j(k) \leq \dots \uparrow +\infty. \quad (16)$$

Fixing $n \in \mathbb{N}$, one says that $k \mapsto \mu_n(k)$ is the n -th *dispersion band* of the operator H and call n -th *Bloch wave* the function $\Phi_n(x, k)$. The spectrum may also have some gaps, and it can be obtained as union of the images of the dispersion bands of the operator

$$\text{Spec}(H) = \bigcup_{n \in \mathbb{N}} \mu_n(\mathcal{B}). \quad (17)$$

Moreover, the Bloch waves constitute a complete systems, meaning that for all $f \in L^2(\mathbb{R}^2)$:

$$f(x) - \sum_{1 \leq n \leq N} \int_{\mathcal{B}} \langle \Phi_n(\cdot, k), f(\cdot) \rangle_{L^2(\mathbb{R}^2)} \Phi_n(x; k) dk \longrightarrow 0 \quad (18)$$

in $L^2(\mathbb{R}^2)$, for $N \longrightarrow +\infty$ [1, 26].

The Cauchy problem:

$$\begin{cases} i\partial_t u(t, x) = Hu(t, x), & (t, x) \in \mathbb{R} \times \mathbb{R}^2, \\ u(0, x) = u_0(x) \in L^2(\mathbb{R}^2), \end{cases} \quad (19)$$

admits the solution:

$$e^{-iHv t} u_0 = \sum_{n \in \mathbb{N}} \int_{\mathcal{B}} e^{-i\mu_n(k)} \langle \Phi_n(\cdot, k), u_0(\cdot) \rangle_{L^2(\mathbb{R}^2)} \Phi_n(x, k) dk. \quad (20)$$

As a consequence, it is evident that the dynamics (20) are strongly influenced by the behavior of the band functions $\mu_n(\cdot)$, $n \in \mathbb{N}$. In particular, as showed in [2], there exist two bands μ_N, μ_{N+1} that meet at conical points located at the vertices of \mathcal{B} . That is, locally near such a point $K_* \in \mathcal{B}$ there holds:

$$\begin{cases} \mu_{N+1}(k) - \mu_{N+1}(K_*) = |\lambda| |k - K_*| (1 + E_+(k - K_*)), \\ \mu_N(k) - \mu_N(K_*) = -|\lambda| |k - K_*| (1 + E_-(k - K_*)), \end{cases} \quad |k - K_*| < \delta, \lambda \in \mathbb{C}, \lambda \neq 0. \quad (21)$$

Here, $E_{\pm} : U_{\delta} \rightarrow \mathbb{R}$, with $U_{\delta} := \{y \in \mathbb{R}^2 : |y| < \delta\}$, are Lipschitz functions such that $E_{\pm}(y) = O(|y|)$, for $|y| \rightarrow 0$. This means that, to first order, the dispersion relation near $k = K_*$ is a cone. This corresponds to the dispersion relation of the two-dimensional Dirac operator (8), as it can be readily seen in the Fourier domain.

Consider a wave packet $u_0(x) = u_0^{\varepsilon}(x)$ concentrated around a Dirac point K_*

$$u_0^{\varepsilon}(x) = \sqrt{\varepsilon} (\psi_{0,1}(\varepsilon x) \Phi_1(x) + \psi_{0,2}(\varepsilon x) \Phi_2(x)), \quad (22)$$

where Φ_j , $j = 1, 2$, are the Bloch functions at K_* and the functions $\psi_{0,j}$ are some (complex) amplitudes to be determined. Then, the solution of the NLS (57), with initial conditions u_0^{ε} is expected to evolve to leading order in ε still as a modulation of Bloch functions,

$$u^{\varepsilon}(t, x) \underset{\varepsilon \rightarrow 0^+}{\sim} \sqrt{\varepsilon} (\psi_1(\varepsilon t, \varepsilon x) \Phi_1(x) + \psi_2(\varepsilon t, \varepsilon x) \Phi_2(x) + \mathcal{O}(\varepsilon)), \quad t > 0, x \in \mathbb{R}^2, \quad (23)$$

and the amplitudes ψ_j solve the effective equation (5).

Given a Dirac point $K_* \in \mathcal{B}$, let $\mu_* := \mu_N(K_*) = \mu_{N+1}(K_*)$ be the frequency at which the conical crossing occurs. Consider then the NLS:

$$(-\Delta + V - \mu_*)u = |u|^2 u, \quad \mathbb{R}^2. \quad (24)$$

As in (23), one thus looks for solutions to (24) of the form:

$$u^{\varepsilon}(t, x) \underset{\varepsilon \rightarrow 0^+}{\sim} \sqrt{\varepsilon} e^{-t\mu_*} (\psi_1(\varepsilon x) \Phi_1(x) + \psi_2(\varepsilon x) \Phi_2(x) + \mathcal{O}(\varepsilon)), \quad t > 0, x \in \mathbb{R}^2. \quad (25)$$

3.2. Derivation of the massless equation

The aim of this subsection is to formally derive the effective Dirac equation for the amplitudes ψ_j appearing in (25) through a multiscale expansion (see e.g. [7, 27]).

Since the coefficients $\psi_j(\varepsilon x)$ and the Bloch functions $\Phi_j(x)$ vary on different scales, one can consider x and $y := \varepsilon x$, $0 < \varepsilon \ll 1$, as independent variables. Moreover, we look for solution to (24) as formal power series in ε , as follows:

$$u_\varepsilon = \sqrt{\varepsilon} U_\varepsilon(x, y), \quad U_\varepsilon(x, y) = U_0(x, y) + \varepsilon U_1(x, y) + \varepsilon^2 U_2(x, y) + \dots \quad (26)$$

We moreover impose K_* -pseudoperiodicity with respect to x , i.e.

$$U_\varepsilon(x + v, y) = e^{-iK_* \cdot v} U_\varepsilon(x, y), \quad \forall v \in \Lambda, x, y \in \mathbb{R}^2. \quad (27)$$

Similarly, we look for μ of the form:

$$\mu = \mu_\varepsilon = \mu_* + \varepsilon \mu_1 + \varepsilon^2 \mu_2 + \dots \quad (28)$$

Rewriting (24) in terms of U_ε and μ_ε then gives:

$$\left(-(\nabla_x + \varepsilon \nabla_y)^2 + V(x) - \mu_\varepsilon \right) U_\varepsilon(x, y) = \varepsilon |U_\varepsilon(x, y)|^2 U_\varepsilon(x, y). \quad (29)$$

Plugging (26,28) into (29) one finds a hierarchy of equations.

At order $\mathcal{O}(\varepsilon^0)$ we obtain:

$$(-\Delta_x + V - \mu_*) U_0 = 0. \quad (30)$$

Recall that $\ker_{L^2_{K_*}}(-\Delta + V - \mu_*) = \text{Span}\{\Phi_1, \Phi_2\}$, and then by (27) we have:

$$U_0(x, y) = \psi_1(y) \Phi_1(x) + \psi_2(y) \Phi_2(x), \quad (31)$$

where the amplitudes are to be determined solving the next equation in the formal expansion. Here $L^2_{K_*}$ denotes square integrable functions satisfying the pseudo-periodicity condition in (15).

The equation for $\mathcal{O}(\varepsilon)$ terms reads:

$$(-\Delta_x + V - \mu_*) U_1 = (2\nabla_x \cdot \nabla_y + \mu_1) U_0 + |U_0|^2 U_0. \quad (32)$$

By Fredholm alternative, solvability of the above equation requires its right hand side to be L^2 -orthogonal to the kernel of $(-\Delta_x + V - \mu_*)$. Then the functions ψ_j are determined imposing orthogonality to the Bloch functions Φ_k . For simplicity we deal with linear part and the cubic term in the right hand side of (32) separately.

The linear terms can be calculated using the following lemma from [1]:

Lemma 3.1. *Let $\zeta = (\zeta_1, \zeta_2) \in \mathbb{C}^2$ be a vector. Then there exists $\lambda \in \mathbb{C} \setminus \{0\}$ such that we have:*

$$\begin{aligned} \langle \Phi_k, \zeta \cdot \nabla \Phi_k \rangle_{L^2(\Omega)} &= 0, \quad k = 1, 2, \\ 2i \langle \Phi_1, \zeta \cdot \nabla \Phi_2 \rangle_{L^2(\Omega)} &= \overline{2i \langle \Phi_2, \zeta \cdot \nabla \Phi_1 \rangle_{L^2(\Omega)}} = -\bar{\lambda} (\zeta_1 + i\zeta_2), \\ 2i \langle \Phi_2, \zeta \cdot \nabla \Phi_1 \rangle_{L^2(\Omega)} &= -\lambda (\zeta_1 - i\zeta_2). \end{aligned} \quad (33)$$

Notice that: $(\nabla_x \cdot \nabla_y) U_0 = \sum_{j=1}^2 \nabla_y \psi_j \cdot \nabla_x \Phi_j$ and then applying Lemma 3.1 with $\zeta = \nabla_y \Phi_j$, $j = 1, 2$ we get:

$$\begin{aligned} 2i \langle \Phi_1, \nabla_y \psi_2 \cdot \nabla \Phi_2 \rangle_{L^2(\Omega)} &= \overline{2i \langle \Phi_2, \nabla_y \psi_2 \cdot \nabla \Phi_1 \rangle_{L^2(\Omega)}} = -\bar{\lambda} (\partial_{y_1} + i\partial_{y_2}) \psi_2, \\ 2i \langle \Phi_2, \nabla_y \psi_1 \cdot \nabla \Phi_1 \rangle_{L^2(\Omega)} &= -\lambda (\partial_{y_1} - i\partial_{y_2}) \psi_1. \end{aligned} \quad (34)$$

Thus, we see that taking the $L^2(\Omega)$ scalar product of the linear part in the right hand side of (32) with the Bloch functions Φ_j gives the linear part of (5). We now want to show that the cubic nonlinearity in (5) is obtained calculating the same product for the cubic term in (32). By symmetry taking this projection many terms vanish. The cubic term reads:

$$|U_0|^2 U_0 = \sum_{1 \leq j, k, l \leq 2} \psi_j \psi_k \bar{\psi}_k \Phi_j \Phi_k \bar{\Phi}_l. \quad (35)$$

Let us consider, for instance, the term: $\psi_1 \psi_1 \overline{\psi_2} \Phi_1 \Phi_1 \overline{\Phi_2}$ and then project it onto Φ_1 . We compute

$$\begin{aligned}
\langle \Phi_1, \Phi_1 \Phi_1 \overline{\Phi_2} \rangle_{L^2(\Omega)} &= \int_{\Omega} \overline{\Phi_1(x)} \Phi_1(x) \Phi_1(x) \overline{\Phi_2(x)} dx \\
&= \int_{R\Omega} \overline{\Phi_1(R^*y)} \Phi_1(R^*y) \Phi_1(R^*y) \overline{\Phi_2(R^*y)} dy \\
&= \int_{R\Omega} \tau \overline{\Phi_1(y)} \tau \Phi_1(y) \tau \Phi_1(y) \overline{\tau \Phi_2(y)} dy \\
&= \tau^2 \int_{\Omega} \overline{\Phi_1(x)} \Phi_1(x) \Phi_1(x) \overline{\Phi_2(x)} dx = \tau^2 \langle \Phi_1, \Phi_1 \Phi_1 \overline{\Phi_2} \rangle_{L^2(\Omega)},
\end{aligned} \tag{36}$$

where R is the rotation matrix (12), and we used that $\mathcal{R}\Phi_1 = \tau\Phi_1$ and $\mathcal{R}\Phi_2 = \overline{\tau}\Phi_2$ with $\tau = \exp(2i\pi/3)$, see [1]. From (36) we get

$$(1 - \tau^2) \langle \Phi_1, \Phi_1 \Phi_1 \overline{\Phi_2} \rangle_{L^2(\Omega)} = 0,$$

and thus

$$\langle \Phi_1, \Phi_1 \Phi_1 \overline{\Phi_2} \rangle_{L^2(\Omega)} = 0.$$

Iterating this calculations one can check that:

$$\begin{cases} \langle \Phi_1, |U_0|^2 U_0 \rangle_{L^2(\Omega)} = (2\beta_2 |\psi_1|^2 + \beta_1 |\psi_2|^2) \psi_1 \\ \langle \Phi_2, |U_0|^2 U_0 \rangle_{L^2(\Omega)} = (\beta_1 |\psi_1|^2 + 2\beta_2 |\psi_2|^2) \psi_2, \end{cases} \tag{37}$$

thus recovering the cubic term in (5), with:

$$\beta_1 := \int_{\Omega} |\Phi_1|^4 dx = \int_{\Omega} |\Phi_2|^4 dx, \quad \beta_2 := \int_{\Omega} |\Phi_1|^2 |\Phi_2|^2 dx. \tag{38}$$

It is then easy to see that the stationary version of (5) (i.e. $\partial_t \Xi_1 = \partial_t \Xi_2 = 0$) appears as compatibility condition for the solvability of (32), combining (34, 37) and taking $\mu_1 = 0$ in (32).

3.3. Derivation of the effective mass term

The same multiscale argument as in the previous Section allows to derive the mass term in (5), induced by a suitable perturbation.

As shown in [1, Appendix], breaking the \mathcal{PT} symmetry lifts the conical degeneracy in the dispersion relation of a honeycomb Schrödinger operator $(-\Delta + V)$ admitting Dirac points. Let us consider the following equation:

$$(-\Delta + V + \varepsilon W - \mu_*) u = |u|^2 u, \tag{39}$$

that is, we consider a potential perturbation of (24) where we add a linear term W breaking parity. More precisely, we assume that W is *odd*:

$$W(-x) = -W(x), \quad \forall x \in \mathbb{R}^2. \tag{40}$$

In this case, compared to the analysis in the previous Section, we get an additional term at order $\mathcal{O}(\varepsilon)$ corresponding to the potential εW in (39). Then, we have to compute the projections:

$$\langle W U_0, \Phi_k \rangle_{L^2(\Omega)} = \sum_{j=1}^2 \psi_j \langle W \Phi_j, \Phi_k \rangle_{L^2(\Omega)}, \quad k = 1, 2. \tag{41}$$

Recall that

$$\Phi_2(x) = \overline{\Phi_1(-x)}, \tag{42}$$

and this relation allows us to compute:

$$\begin{aligned}
\langle W \Phi_2, \Phi_1 \rangle_{L^2(\Omega)} &= \int_{\Omega} (W \Phi_2)(x) \overline{\Phi_1(x)} dx = \int_{\Omega} W(x) \overline{\Phi_1(-x)} \overline{\Phi_1(x)} dx \\
&= \int_{-\Omega} W(-y) \overline{\Phi_1(y)} \overline{\Phi_1(-y)} dy = - \int_{\Omega} (W \Phi_2)(y) \overline{\Phi_1(y)} dy \\
&= - \langle W \Phi_2, \Phi_1 \rangle_{L^2(\Omega)},
\end{aligned} \tag{43}$$

where we have also used (40). We thus obtain:

$$\langle W\Phi_2, \Phi_1 \rangle_{L^2(\Omega)} = \langle W\Phi_1, \Phi_2 \rangle_{L^2(\Omega)} = 0. \quad (44)$$

Moreover, arguing as in (43) one easily finds:

$$\langle W\Phi_1, \Phi_1 \rangle_{L^2(\Omega)} = -\langle W\Phi_2, \Phi_2 \rangle_{L^2(\Omega)}, \quad (45)$$

and then:

$$\begin{aligned} \sum_{j=1}^2 \psi_j \langle W\Phi_j, \Phi_1 \rangle_{L^2(\Omega)} &= \psi_1 \langle W\Phi_1, \Phi_1 \rangle_{L^2(\Omega)} \\ \sum_{j=1}^2 \psi_j \langle W\Phi_j, \Phi_2 \rangle_{L^2(\Omega)} &= -\psi_2 \langle W\Phi_1, \Phi_1 \rangle_{L^2(\Omega)}. \end{aligned} \quad (46)$$

Assuming that $m := \langle W\Phi_1, \Phi_1 \rangle_{L^2(\Omega)} > 0$, we obtain the mass term in (5).

4. Proof of the main result

In this section, we prove the existence of branches of bound states for (1) that bifurcate from the trivial solution at the positive band-edge of the spectrum of \mathcal{D} . Those solutions are constructed from bound states of a suitable nonlinear Schrödinger equation (57), which (after scaling) gives the asymptotic profile as $\omega \rightarrow m$.

We start by rewriting (1) componentwise. Setting $\psi = (\psi_1, \psi_2)^T$, equation (1) becomes the system:

$$\begin{cases} -i(\partial_1 - i\partial_2)\psi_2 = (\beta_1|\psi_2|^2 + 2\beta_2|\psi_1|^2)\psi_1 - (m - \omega)\psi_1, \\ -i(\partial_1 + i\partial_2)\psi_1 = -(2\beta_2|\psi_2|^2 + \beta_1|\psi_1|^2)\psi_2 - (m + \omega)\psi_2, \end{cases} \quad (47)$$

that can be regarded as a functional equation of the form:

$$\mathcal{H}(\psi_1, \psi_2) = 0,$$

where $\mathcal{H} : X \times X \rightarrow L^2(\mathbb{R}^2, \mathbb{C}^2)$ is the map defined by:

$$\mathcal{H}(\psi_1, \psi_2) = \begin{pmatrix} -i(\partial_1 - i\partial_2)\psi_2 - (\beta_1|\psi_2|^2 + 2\beta_2|\psi_1|^2)\psi_1 + (m - \omega)\psi_1 \\ -i(\partial_1 + i\partial_2)\psi_1 + (2\beta_2|\psi_2|^2 + \beta_1|\psi_1|^2)\psi_2 + (m + \omega)\psi_2 \end{pmatrix},$$

with

$$X := H^1(\mathbb{R}^2, \mathbb{C}). \quad (48)$$

In what follows, we shall consider the subspace

$$X_r \subset X \times X \quad (49)$$

given by functions of the form (6). For simplicity they will be denoted by (u, v) , where those functions are the radial factors in (6).

4.1. Rescaling the equation

Plugging the ansatz (6) in (47) leads to the follows system for the real valued functions u, v :

$$\begin{cases} -u' + \frac{u}{r} = (\beta_1 u^2 + 2\beta_2 v^2)v - (m - \omega)v, \\ v' = -(2\beta_2 u^2 + \beta_1 v^2)u - (m + \omega)u. \end{cases} \quad (50)$$

Now set $\varepsilon := (m - \omega)$, and consider the following rescaling

$$u_\varepsilon(r) = \varepsilon f(\sqrt{\varepsilon}r), \quad v_\varepsilon(r) = \sqrt{\varepsilon}g(\sqrt{\varepsilon}r), \quad r > 0, \quad (51)$$

so that, by (50), after some straightforward computations we find the equations for $f(\rho), g(\rho)$:

$$\begin{cases} f' + \frac{f}{\rho} = (\varepsilon\beta_1 f^2 + 2\beta_2 g^2)g - g, \\ g' = -(2\beta_2 \varepsilon^2 f^2 + \beta_1 \varepsilon g^2)f - (2m - \varepsilon)f, \end{cases} \quad (52)$$

where we also used the fact that $\varepsilon := m - \omega$ and then $m + \omega = 2m - \varepsilon$.

Remark 4.1. The branch point of the solutions is given by $\varepsilon = 0$. The equivalence between (50) and (52) is valid only for $\varepsilon > 0$, while (52) makes sense for arbitrary $\varepsilon \in \mathbb{R}$.

4.2. Solutions of the rescaled problem

Our goal is to apply the implicit function theorem to prove the existence of a local branch of solutions to (52).

To this aim, we rewrite reformulate the problem as follows. We define the map:

$$\mathcal{F} : \mathbb{R} \times X_r \longrightarrow L^2(\mathbb{R}) \times L^2(\mathbb{R}),$$

with X_r in (49), and acting as:

$$\mathcal{F}(\varepsilon, u_\varepsilon, v_\varepsilon) := \begin{pmatrix} f' + \frac{f}{\rho} - (\varepsilon\beta_1 f^2 + 2\beta_2 g^2)g + g \\ g' + (2\beta_2 \varepsilon^2 f^2 + \beta_1 \varepsilon g^2)f + (2m - \varepsilon)f \end{pmatrix}. \quad (53)$$

Therefore, the original problem is equivalent to the following:

$$\begin{cases} (\varepsilon, u_\varepsilon, v_\varepsilon) \in \mathbb{R} \times X_r, \\ u_\varepsilon, v_\varepsilon \neq 0, \\ \mathcal{F}(\varepsilon, u_\varepsilon, v_\varepsilon) = 0. \end{cases} \quad \varepsilon > 0. \quad (54)$$

Remark 4.2. In order to simplify the notation, without loss of generality, we take $m = 1/2$ and $\beta_2 = 1/2$.

Proposition 4.1. *There exists $\varepsilon_0 > 0$ such that (54) admits a solution for $\varepsilon \in (-\varepsilon_0, \varepsilon)$.*

Remark 4.3. The above proposition is equivalent to the main result stated in Theorem 1.1. Then we equivalently prove the former.

4.2.1. *Solutions for $\varepsilon = 0$.* Take $\varepsilon = 0$. Looking for non-trivial solutions of (54) in X_r we get:

$$\begin{cases} f' + \frac{f}{\rho} = g^3 - g, \\ g' = -f, \end{cases} \quad (55)$$

see Remark 4.2. Then (f, g) solves the following nonlinear Schrödinger equation:

$$\begin{cases} -g'' - \frac{1}{\rho}g' - g^3 + g = 0, \\ f = -g'. \end{cases} \quad (56)$$

Since $\frac{\partial^2}{\partial \rho^2} + \frac{1}{\rho} \frac{\partial}{\partial \rho}$ is the radial part of the two-dimensional Laplacian, one immediately recognizes that g must be a radial solution of the following elliptic equation:

$$-\Delta U - U^3 + U = 0 \quad \text{on } \mathbb{R}^2. \quad (57)$$

It is well known that such equation admits a unique positive radial *ground state solution* U , which is smooth and exponentially decaying at infinity [28, Thm. 8.1.5]. Given such function, we shall consider the solution to (56) given by:

$$(u_0, v_0) = (U, V), \quad V = -U'. \quad (58)$$

4.2.2. *Solutions for small ε .* In order to prove existence of solutions of (54) for small values of ε we have to check the assumptions of the implicit function theorem.

It is not hard to verify that the map \mathcal{F} is of class C^1 , and then we need to prove the following:

Lemma 4.1. *The differential of \mathcal{F} with respect to (u, v) -variables, $D_{(u,v)}\mathcal{F}$, evaluated at $(0, u_0, v_0)$ is an isomorphism.*

The proof of this lemma requires the results that are contained in the following lemmas.

Lemma 4.2. *The operator $D_{(X,Y)}\mathcal{F}(0, u_0, v_0) : X_r \rightarrow L^2(\mathbb{R}^2, \mathbb{R}^2)$ is injective.*

Proof. We need to prove that $\ker\{D_{(u,v)}\mathcal{F}(0, u_0, v_0)\}$ is trivial. For this reason let us consider the linearization of (55) at $(0, u_0, v_0)$ and $(h, k) \in \ker D_{(u,v)}\mathcal{F}(0, u_0, v_0)$, so that

$$D_{(u,v)}\mathcal{F}(0, u_0, v_0)[h, k] := \begin{pmatrix} k' + \frac{k}{\rho} + h - u_0^2 h \\ h' + k \end{pmatrix} = 0. \quad (59)$$

Then h solves

$$-h'' - \frac{1}{\rho}h' - u_0^2h + h = 0$$

that is, h lies in the kernel of the linearization of (57) at the ground state solution U . By known results [29], such kernel is empty and thus $h \equiv 0$ and $k \equiv 0$, proving the Lemma. \square

Now we want to prove that $D_{(u,v)}\mathcal{F}(0, u_0, v_0)$ is surjective, using the Fredholm alternative [30, Thm. 6.6]. Namely, using classical arguments from perturbation theory of linear operators, the claim follows showing that $D_{(u,v)}\mathcal{F}(0, u_0, v_0)$ is given by the sum of an isomorphism and a compact operator.

By (59), let:

$$D_{(u,v)}\mathcal{F}(0, u_0, v_0) = J + K(u_0), \quad (60)$$

where $J, K(u_0) : X_r \rightarrow L^2(\mathbb{R}^2, \mathbb{R}^2)$ are defined as

$$J[h, k] := \left(k' + \frac{k}{\rho} + h, h' + k \right)^T, \quad (61)$$

and

$$K(U)[h, k] := (u_0h, 0)^T. \quad (62)$$

Lemma 4.3. *The operator $J : X_r \rightarrow L^2(\mathbb{R}^2, \mathbb{R}^2)$ is an isomorphism.*

Proof. The operator J is clearly continuous, so that we only need to prove injectivity and surjectivity.

Step (i): J is injective. Assume $(h, k)^T \in X_r$ solves $J[h, k] = 0$. The argument in the proof of Lemma 4.2 gives:

$$-h'' + \frac{1}{\rho}h' + h = 0,$$

i.e.

$$-\Delta h + h = 0,$$

so that multiplying by h and integrating by parts one immediately sees $h \equiv 0$. By (61) we also get $k \equiv 0$.

Step (ii): J is surjective. Let $a, b \in L^2(\mathbb{R}^2)$. We want to prove that there exists $(h, k)^T \in X_r$ such that

$$J[h, k] = (a, b)^T, \quad (63)$$

that is, such that:

$$\begin{cases} k' + \frac{k}{\rho} + h = a, \\ h' + k = b. \end{cases}$$

Assuming that $b \equiv 0$, arguing as in *Step (i)*, we have to find a weak solution $h_1 \in H^1(\mathbb{R}^2)$ of

$$-\Delta h_1 + h_1 = a. \quad (64)$$

The existence of such function is an immediate application of the Lax–Milgram Lemma [30, Cor. 5.8]. Then taking $k_1 = -h_1'$, the pair $(h_1, k_1)^T \in X_r$ solves (63) with $b \equiv 0$. The same argument, exchanging k and h , allows to find a solution $(h_2, k_2)^T \in X_r$ of (63) with $a \equiv 0$. By linearity of J we thus get the claim. \square

Lemma 4.4. *The operator $K(u_0) : X_r \rightarrow L^2(\mathbb{R}^2, \mathbb{R}^2)$ is compact.*

Proof. Let $((h_n, k_n)^T)_n \subset X_r$ be a bounded sequence.

Note that, up to subsequences,

$$(h_n, k_n) \longrightarrow (h, k) \quad \text{in } L^2_{loc}(\mathbb{R}^2, \mathbb{R}^2). \quad (65)$$

On the other hand, since the soliton u_0 tends to zero at infinity, for all $\eta > 0$ there exists $M_\eta > 0$ such that $u_0(x) < \eta$ if $|x| > M_\eta$. Thus,

$$\begin{aligned} \|K(u_0)[h_n, k_n] - K(u_0)[h, k]\|_{L^2(\mathbb{R}^2)} &= \|u_0^2(h_n - h)\|_{L^2(\mathbb{R}^2 \setminus B_{M_\eta})} \\ &\quad + \|u_0^2(h_n - h)\|_{L^2(B_{M_\eta})} \leq C\eta^2 + o(1), \quad \text{as } n \rightarrow \infty. \end{aligned}$$

where $B_{M_\eta} := \{|x| \leq M_\eta\} \subset \mathbb{R}^2$. Then

$$\lim_{n \rightarrow \infty} \|K(u_0)[h_n, k_n] - K(u_0)[h, k]\|_{L^2(\mathbb{R}^2)} \leq C\eta^2, \quad \forall \eta > 0,$$

so that the statement follows. \square

Now, we can combine all the previous results to prove Proposition 4.1.

Proof of Proposition 4.1. Notice that $D_{(X,Y)}\mathcal{F}(0, u_0, v_0)$ is clearly continuous, and it is injective by Lemma 4.2. On the other hand, see (60), Lemmata 4.3 and 4.4 show that:

$$D_{(X,Y)}\mathcal{F}(0, u_0, v_0) = J + K$$

is the sum of an isomorphism and of a compact operator. Then:

$$D_{(X,Y)}\mathcal{F}(0, u_0, v_0) = J + K = J(I + J^{-1}K).$$

Since J is an isomorphism, the map $(I + J^{-1}K)$, which is of the form identity plus compact, is also injective. Then the claim follows by Fredholm's alternative [30, Thm. 6.6]. \square

The proof of Theorem 1.1 immediately follows, as we can now prove Proposition 4.1.

Proof of Proposition 4.1. There holds $\mathcal{F}(0, u_0, v_0) = 0$ and by Proposition 4.1, the differential $D_{(u,v)}\mathcal{F}(0, u_0, v_0)$ is an isomorphism. Then the claim follows by the implicit function theorem. \square

References

- [1] Fefferman C.L., Weinstein M.I. Honeycomb lattice potentials and dirac points. *J. Amer. Math. Soc.*, 2012, **25**, P. 1169–1220.
- [2] Fefferman C.L., Weinstein M.I. Wave packets in honeycomb structures and two-dimensional Dirac equations. *Comm. Math. Phys.*, 2014, **326**, P. 251–286.
- [3] Erdős L., Schlein B., Yau H.-T. Derivation of the cubic non-linear Schrödinger equation from quantum dynamics of many-body systems. *Invent. Math.*, 2007, **167**, P. 515–614.
- [4] Moloney J., Newell A. *Nonlinear optics*. Westview Press, Advanced Book Program, Boulder, CO, 2004.
- [5] Pitaevskii L., Stringari S. Bose-Einstein condensation. *International Series of Monographs on Physics*, The Clarendon Press, Oxford University Press, Oxford, 2003, **116**.
- [6] Fefferman C.L., Weinstein M.I. Waves in honeycomb structures. *Journ'ees 'equations aux d'eriv'ees partielles*, 2012, 12, 12 p.
- [7] Arbunich J., Sparber C. Rigorous derivation of nonlinear Dirac equations for wave propagation in honeycomb structures. *J. Math. Phys.*, 2018, **59**, 011509.
- [8] Borrelli W. Weakly localized states for nonlinear Dirac equations. *Calc. Var. Partial Differential Equations*, 2018, **57**, P. 57–155.
- [9] Borrelli W., Frank R.L. Sharp decay estimates for critical Dirac equations. *Trans. Amer. Math. Soc.*, 2020, **373**, P. 2045–2070.
- [10] Borrelli W. Stationary solutions for the 2D critical Dirac equation with Kerr nonlinearity. *J. Differential Equations*, 2017, **263**, P. 7941–7964.
- [11] Borrelli W. Symmetric solutions for a 2D critical Dirac equation. ArXiv e-prints, 2020, arXiv:2010.04630.
- [12] Ammann B., Grosjean J.-F., Humbert E., Morel B. A spinorial analogue of Aubin's inequality. *Math. Z.*, 2008, **260**, P. 127–151.
- [13] Grosse N. On a conformal invariant of the Dirac operator on noncompact manifolds. *Ann. Global Anal. Geom.*, 2006, **30**, P. 407–416.
- [14] Isobe T. Nonlinear Dirac equations with critical nonlinearities on compact Spin manifolds. *J. Funct. Anal.*, 2011, **260**, P. 253–307.
- [15] Maalaoui A. Infinitely many solutions for the spinorial Yamabe problem on the round sphere. *Nonlinear Differential Equations Appl. NoDEA*, 2016, **23**, 25.
- [16] Borrelli W., Maalaoui A. Some properties of Dirac-Einstein bubbles. *J. Geometric Analysis*, 2020, <https://doi.org/10.1007/s12220-020-00503-1>.
- [17] Maalaoui A., Martino V. Characterization of the Palais-Smale sequences for the conformal Dirac-Einstein problem and applications. *J. Differential Equations*, 2019, **266**, P. 2493–2541.
- [18] Ounaies H. Perturbation method for a class of nonlinear Dirac equations. *Differential Integral Equations*, 2000, **13**, P. 707–720.
- [19] Borrelli W., Carlone R., Tentarelli L. On the nonlinear Dirac equation on noncompact metric graphs. *Journal of Differential Equations*, 2021, **278**, P. 326–357.
- [20] Cazenave T., V´azquez L. Existence of localized solutions for a classical nonlinear Dirac field, *Comm. Math. Phys.*, 1986, **105**, P. 35–47.
- [21] Cuevas-Maraver J., Kevrekidis P.G., et al. Stability of solitary waves and vortices in a 2D nonlinear Dirac model. *Phys. Rev. Lett.*, 2016, **116**, 214101.
- [22] Esteban M.J., S´er´e E. Stationary states of the nonlinear Dirac equation: a variational approach. *Comm. Math. Phys.*, 1995, **171**, P. 323–350.
- [23] Thaller B. *The Dirac equation*, Texts and Monographs in Physics, Springer-Verlag, Berlin, 1992.
- [24] Borrelli W. L'equation de Dirac en physique du solide et en optique non lin´eaire. PhD thesis, Universit´e Paris-Dauphine PSL, (2018).
- [25] Peleg O., Bartal G., et al. Conical diffraction and gap solitons in honeycomb photonic lattices. *Phys. Rev. Lett.*, 2007, **98**, 103901.
- [26] Reed M., Simon B. *Methods of modern mathematical physics. IV. Analysis of operators*, Academic Press [Harcourt Brace Jovanovich, Publishers], New York-London, 1978.
- [27] Ilan B., Weinstein M.I. Band-edge solitons, nonlinear Schrödinger/Gross–Pitaevskii equations, and effective media. *Multiscale Model. Simul.*, 2010, **8**, P. 1055–1101.
- [28] Cazenave T. *Semilinear Schrödinger equations*. Courant Lecture Notes in Mathematics, New York University, Courant Institute of Mathematical Sciences, New York; American Mathematical Society, Providence, RI, 2003, **10**.
- [29] Chang S.-M., Gustafson S., Nakanishi K., Tsai T.-P. Spectra of linearized operators for NLS solitary waves. *SIAM J. Math. Anal.*, 2007–2008, **39**, P. 1070–1111.
- [30] Brezis H. *Functional analysis, Sobolev spaces and partial differential equations*. Universitat, Springer, New York, 2011.

Discrete spectrum Analysis using Laplace transform and Volterra equations (DALV-method)

V. V. Kuidin, V. V. Zalipaev, D. R. Gulevich

ITMO University, St. Petersburg 197101, Russia

vladislav.kujdin@metalab.ifmo.ru

PACS 02.70.Hm, 02.30.Hq, 03.65.Ge

DOI 10.17586/2220-8054-2021-12-1-15-21

The theory of excitons in two dimensional materials including graphene and transition metal dichalcogenides (TMD) is complicated, as there appears a screened interaction in equations. Such interaction can be represented as Keldysh potential. The exact solution does not seem to exist yet. The method of searching appropriate solutions to equations of quantum mechanics is believed to solve this problem by using Laplace transform of tempered distributions and Volterra equations. The method is to seek solution as a Laplace transform of some tempered distribution that satisfies the appropriate Laplace spectral equation which, under Laplace transform, gives us the initial equation. Due to Paly–Wigner–Schwarz theorem, the image functions behavior depends on the geometry of original one support. In addition, the homogenous Volterra equation does not have nontrivial continuous solution. These constraints together with the fact that the studied equations turn out to be Volterra equations of III kind lead to a method that seems to solve a wide class of quantum mechanics equations.

Keywords: discrete spectrum, Laplace transform, Volterra equation, Schrödinger equation.

Received: 10 January 2021

Revised: 3 February 2021, 12 February 2021

1. Introduction

In the past years, the spectral theory of differential operators has attained extensive results for various differential operators. The qualitative theory for second-order differential equations has been systematically presented e.g. in [1]. The results on spectral theory of differential equations has been presented in [2, 3]. The asymptotic analysis has been developed for calculating spectrum of quantum mechanics operators [4].

However, there are few methods for exact calculation of discrete spectrum even for the most studied Schrödinger equation that can be utilized by physicists. The most used methods remain perturbation theory, semiclassical analysis and computational methods. Thus, the computationally simple method for computing discrete spectrum of quantum mechanics operators is of great necessity. One of the best rigorous approaches to calculating discrete spectrum widely used is Frobenius method, which is used to calculate the discrete spectrum and corresponding wave functions of an electron in hydrogen atom and constant magnetic and electric fields. Nevertheless, the Frobenius method fails when a non-fuchsian potentials (Keldysh potential), i.e. the potentials with non-fuchsian singularities, are studied.

Classical Laplace transform has been used to calculate discrete spectrum of Schrödinger equation with particular radially symmetric potentials. The original second-order differential equation is transformed to another differential or difference equation [5–11]. The fractional differential equations has been studied e.g. in [12]. The study of Schrödinger equation with Coulomb potential and a pseudoharmonic potential using the Laplace transform has been elaborated in [6, 10]. The one-dimensional equation with periodic potentials having finite number of Fourier coefficients has been studied in [13]. The above papers utilized classical Laplace transform to reduce the original spectral problem to a more treatable one. However, most of studied equations can be reduced to Fuchsian ones by an appropriate substitution.

The main concept in DALV-method presented in this paper is to treat the solutions to Schrödinger equation as the Laplace transform of some generalized functions, whose properties have been systematically studied in [14]. In this paper, we attempt to derive a method to analyze the Schrödinger equation with a wide class of radially symmetric potentials. On the contrary to above papers, DALV-method utilizes the inverse Laplace transform to convert the original differential equation to convolutional equation with the solution being a generalized function.

The Laplace transform of a generalized function with certain properties of the support exhibits the required asymptotic behaviour (Theorem (3.10.2) [14]), which is the main starting point for presented method. A distribution whose Laplace transform is a function f will be called *Laplace spectral function of f* . The equation for the Laplace spectral function of a solution to given differential equation will be denoted as *Laplace spectral equation*. The latter turns out to be a homogenous *III kind Volterra equation*, whose spectral properties has been studied in [15–17]. The

coefficients of the initial equation need to have smooth Laplace spectral functions (up to a factor $\theta(s)$) for the corresponding Laplace spectral equation to become a Volterra equation with smooth kernel. Some potentials with smooth Laplace spectral functions are given in Table 1. The homogenous Volterra equation's solution properties along with the behaviour of weight function lead to the choice of a particular ansatz, which, after being applied to the spectral equation, results in the system of algebraic and integral equations for ansatz elements. The singular points of the solution corresponds with the eigenvalue, so the spectrum can be calculated without calculating the eigenfunction. As a result, the formula for energy levels is obtained and the equations for corresponding eigenfunctions are presented.

2. Preliminaries

2.1. Laplace transform of generalized functions

According to Zemanian [14], we will introduce Laplace transform of a regular compactly supported generalized function as follows:

$$\mathcal{L}_{s \rightarrow r} F \stackrel{\text{def}}{=} (F, e^{-rs}) = \int_{\mathbb{R}} F(s) e^{-rs} ds. \quad (1)$$

The definition can be expanded to tempered distributions supported on \mathbb{R}_+ . Throughout the whole paper, we will utilize tempered distributions with semibounded supports, namely $\text{supp}(f) \subset \mathbb{R}_+$. The above definition is valid for such distributions, as for every $r > 0$ the function $\eta(s)e^{-rs}$, $\eta \in C^\infty(\mathbb{R})$, $\eta([-1, \infty)) = 1$, $\text{supp}(\eta) \subset [-T, +\infty)$ for some $T \geq 2$ is in Schwartz class, so the definition (1) is correct as

$$(F, e^{-rs}) = (F, \eta(s)e^{-rs}). \quad (2)$$

The definition does not depend on η when we apply a semibounded distribution to it since $\partial_n \eta(s)e^{-rs} = \partial_n e^{-rs}$, $s \geq 0$, $n = 0, 1, 2, \dots$. In fact, η is added rather for technical reasons so that the tempered distribution acts on the function from Schwartz class as the theory of tempered distributions demands it.

Throughout the whole paper, we will utilize tempered distributions with semibounded supports, namely $\text{supp}(f) \subset \mathbb{R}_+$.

All well-known properties of Laplace transform can be proved for Zemanian's definition:

$$\begin{aligned} \mathcal{L}_{s \rightarrow r} F^{(n)}(s) &= r^n (\mathcal{L}_{s \rightarrow r} F)(r), \quad n = 0, 1, 2, \dots, \\ \mathcal{L}_{s \rightarrow r} s^n F(s) &= (-1)^n (\mathcal{L}_{s \rightarrow r} F)^{(n)}(r), \quad n = 0, 1, 2, \dots, \\ \mathcal{L}_{s \rightarrow r} F(s-a) &= e^{-ar} (\mathcal{L}_{s \rightarrow r} F)(r), \quad a \in \mathbb{R}. \end{aligned}$$

Another property of Laplace transform to be used in this paper is the Laplace transform of a convolution:

$$\mathcal{L}_{s \rightarrow r}(F * G) = \mathcal{L}_{s \rightarrow r} F \cdot \mathcal{L}_{s \rightarrow r} G.$$

2.2. Laplace spectral function and the integrability condition

The main concept of DALV-method is to consider the solution to Schrödinger equation as the Laplace transform of some tempered distribution. The equation for this distribution will be called *Laplace spectral equation* and the distribution whose Laplace transform is some function f will be called *Laplace spectral function of f* . Unlike Fourier transform, Laplace transform is not an isometry on $L_2(\mathbb{R})$. Therefore, the integrability of the wave-function should somehow be interpreted in terms of its Laplace spectral function.

When treating the Schrödinger equation in \mathbb{R}^n , the radial part of wavefunction should satisfy the integrability condition:

$$\int_0^\infty r^{n-1} |R(r)|^2 dr < \infty. \quad (3)$$

First assume that $R(r) = (F, e^{-rs})$ and F is a smooth compactly supported function. Observe that an integral:

$$\int_0^\infty r^{n-1} e^{-rs} dr$$

exists only when $s > 0$. In this case, we can change the order of integration and the integral in (3) can be rewritten as:

$$\int_0^\infty r^{n-1} |R(r)|^2 dr = \Gamma(n) \int_{\mathbb{R}_+} \frac{F(s) * \overline{F(s)}}{s^n} ds, \quad \text{supp}(F) \subset (0, +\infty). \quad (4)$$

TABLE 1. Various potentials and their Laplace spectral functions. $\theta(s)$ – Heaviside theta function, $J_0(r), Y_0(r)$ – Bessel functions of first and second type respectively, $H_0(r)$ – Struve function

	Potential	Spectral function
Coulomb potential	$V(r) = \frac{1}{r}$	$K(s) = \theta(s)$
Shifted Coulomb potential	$V(r) = \frac{1}{\sqrt{r^2 + a^2}}$	$K(s) = \theta(s)J_0(as)$
Keldysh potential	$V(r) = \frac{\pi}{2} (H_0(r) - Y_0(r))$	$K(s) = \frac{\theta(s)}{\sqrt{1 + s^2}}$
“Centripetal potential”	$V(r) = \frac{1}{r^2}$	$K(s) = \theta(s)s = s_+$

This gives us the integrability condition for a function with smooth compactly supported Laplace spectral function:

$$\int_{\mathbb{R}_+} \frac{F(s) * \overline{F(s)}}{s^n} ds < \infty. \quad (5)$$

A few crucial conclusions can be made from this result. First, the support of F can only lie on the right semiaxis \mathbb{R}_+ . Second, the function F has to vanish in the neighborhood of zero. A similar result is obtained for tempered distributions, but with certain technical subtleties.

Since $R(r) = (F, e^{-rs})$, $\text{supp}(F) \subset \mathbb{R}_+$, we can rewrite (3) using the notion of generalized functions:

$$\int_0^\infty (F * \overline{F}, r^{n-1} e^{-rs}) dr < \infty. \quad (6)$$

Observe now the integral

$$\int_a^\infty r^{n-1} e^{-rs} dr = \frac{\Gamma(n, as)}{s^n}, \quad s > 0,$$

where $\Gamma(n, as)$ is an incomplete gamma function. Again, since $\eta\Gamma(n, as)$ with the above mentioned η is from Schwartz space and $\text{supp}(F * \overline{F}) \subset \mathbb{R}_+$ if $\text{supp}(F) \subset \mathbb{R}_+$, we can formulate the condition (3) in terms of spectral functions:

$$\lim_{a \rightarrow 0} \left(\frac{F * \overline{F}}{s^n}, \Gamma(n, as) \right) < \infty. \quad (7)$$

In terms of Laplace transformable generalized functions [14], the above inequality means that the Laplace transform of a distribution $s^{-n}(F * \overline{F})$ is defined at point zero (clearly, $\Gamma(n, 0) = \Gamma(n) = \text{const}$).

3. Laplace spectral equation, associated with Schrödinger equation

The main equation studied in this paper is the radial part of the Schrödinger equation with radially symmetric potential $V(r)$ having a smooth Laplace spectral function. This equation is reduced to one-dimensional equation:

$$-\frac{1}{2}f''(r) + \left(V(r) + \frac{l(l+1)}{2r^2} \right) f(r) = Ef(r), \quad r > 0. \quad (8)$$

The corresponding Laplace spectral equation, assuming that

$$2V(r) + \frac{l(l+1)}{r^2} = \int_0^\infty e^{-rs} (2K(s) + l(l+1)s) ds = \int_0^\infty e^{-rs} K_{eff}(s) ds$$

with a smooth function $K(s)$ and $F : f(r) = \mathcal{L}_{s \rightarrow r} F$ being the Laplace spectral function of f reads:

$$\theta(s)K_{eff}(s) * \theta(s)F(s) = (s^2 - s_0^2)F(s). \quad (9)$$

Where s_0 , $-s_0^2 = 2E$, is a spectral parameter. It is well known that the discrete spectrum is to be sought in \mathbb{R}_- , so s_0 is to be sought in \mathbb{R} . The function $(s^2 - s_0^2)$ has two zeros $\pm s_0$, but $\text{supp}(F) \subset \mathbb{R}_+$, so we assume further that $s_0 \geq 0$. The factor $\theta(s)$ before $F(s)$ is added for symmetry. In order to justify the equation (9), one can apply Laplace transform to it:

$$\mathcal{L}_{s \rightarrow r} \theta(s) K_{eff}(s) * \theta(s) F(s) = \left(2V(r) + \frac{l(l+1)}{r^2} \right) \mathcal{L}_{s \rightarrow r} F, \quad (10)$$

$$\mathcal{L}_{s \rightarrow r} ((s^2 - s_0^2) F(s)) = (\mathcal{L}_{s \rightarrow r} F)'' + 2E \mathcal{L}_{s \rightarrow r} F. \quad (11)$$

Rearranging the terms, we end up with the original equation (8).

The form of the equation assumes the solution to have singularities at least at point $s = s_0$. Moreover, the regular part of solution has to be zero in the interval $(0, s_0)$, since for $s \in (0, s_0)$ the equation can be reduced to homogenous Volterra one with regular kernel. The support of the Laplace spectral function being separated from 0 gives us the appropriate behaviour of the wavefunction in the neighborhood of infinity. The only problem to be resolved would then be the behaviour of Laplace spectral function in the neighborhood of infinity, that correlates with the behaviour of wavefunction near 0.

The singularity at point $s = s_0$ is believed to be accounted for by a set of some specific generalized functions. However, this set does not necessarily account for the regular part of solution. Therefore, the solution shall be constructed in view of the above. The ansatz for the solution can be chosen the following:

$$F(s) = \theta(s - s_0) \chi(s - s_0) + \sum_{n=-\lceil \gamma \rceil}^N A_n \varphi_{-\gamma-n}(s - s_0), \quad \gamma > 0, N \in \mathbb{N}, \quad (12)$$

$$\varphi_a(s) = \begin{cases} \frac{\theta(s) s^{a-1}}{\Gamma(a)}, & a > 0, \\ \varphi_{a+N}^{(N)}, & a < 0, a + N > 0, N \in \mathbb{N}. \end{cases} \quad (13)$$

Where $\varphi_{a+N}^{(N)}$ is a generalized derivative of φ_{a+N} . Here, χ is a continuous function and the sum characterizes the singularity of solution. The sum is finite since we seek solution in the set of tempered distributions having finite order. The functions $\varphi_a(s)$ are the kernels of a fractional *Riemann–Liouville derivatives*. Their main properties are shown in [18] and their Laplace transforms are

$$\mathcal{L}_{s \rightarrow r} \varphi_{-\gamma-n}(s - s_0) = e^{-s_0 r} r^{\gamma+n}. \quad (14)$$

Note that $\varphi_a(s)$ has singularity at $s = 0$, whenever $a < 1$. Therefore, we attempt to extract singularities of a spectral function by applying such ansatz. The possibility to separate singular part from regular one by proposed linear combination remains an open problem for now. Although, in some cases, such ansatz might give reliable values for spectrum and corresponding eigenfunctions. However, in order to account for all singularities at point $s = s_0$, the more generic representation of a singular part might be needed:

$$F_{sing}(s) = \int_0^N A(\alpha) \varphi_{-\alpha+1}(s - s_0) d\alpha. \quad (15)$$

The algebraic iteration formulae would then become difference equation for $A(\alpha)$. In this paper, we utilize the ansatz (12) to show, that it gives an exact solution for Coulomb interaction.

4. Singular and regular parts

When convolving $\theta(s)K(s)$ with $\varphi_{-\gamma-n}(s - s_0) = \varphi_{1-\{\gamma\}}^{(\lceil \gamma \rceil + n)}(s - s_0)$, where $\lceil \gamma \rceil$ – *ceiling function* and $\{\gamma\} = \gamma - \lceil \gamma \rceil$, we get:

$$\theta(s)K(s) * \varphi_{1-\{\gamma\}}^{(\lceil \gamma \rceil + n)}(s - s_0) = (\theta(s)K(s))^{(\lceil \gamma \rceil + n)} * \varphi_{1-\{\gamma\}}(s - s_0).$$

Differentiation of $\theta(s)K(s)$ results in the linear combination of delta functions. The following formula:

$$(\theta(s)K(s))^{(\lceil \gamma \rceil + n)} = \theta(s)K^{(\lceil \gamma \rceil + n)}(s) + \sum_{k=1}^{\lceil \gamma \rceil + n} C_{\lceil \gamma \rceil + n}^k \delta^{(k-1)}(s) K^{(\lceil \gamma \rceil + n - k)}(s),$$

where $C_{\lceil \gamma \rceil + n}^k$ is a binomial coefficient, gives us regular and singular terms. The former becomes the nonhomogeneity for a regular integral equation, the latter gives coefficients for an algebraic system. The expression $\delta^{k-1}(s) K^{(\lceil \gamma \rceil + n - k)}(s)$ needs to be calculated as a multiplication of Dirac delta function and a smooth function. After applying the ansatz (12) to equation (9), the latter splits into two parts: singular and regular ones. The singular

part could be resolved into the iterative system of equations for A_n , whereas the regular one gives us the equation for χ . After some algebraic manipulations, we obtain the system

$$\sum_{j=n-\lceil\gamma\rceil+1}^N A_j K_{eff}^{(j+\lceil\gamma\rceil-n-1)}(0) = \quad (16)$$

$$= (\gamma - \lceil\gamma\rceil + n + 2)(\gamma - \lceil\gamma\rceil + n + 1)A_{n-\lceil\gamma\rceil+2} - 2s_0(\gamma - \lceil\gamma\rceil + n + 1)A_{n-\lceil\gamma\rceil+1},$$

for $n = 0, \dots, N + \lceil\gamma\rceil - 1$. The requirement $A_N \neq 0$, and the requirement $A_{N+k} = 0, k \in \mathbb{N}$, gives us the formula for s_0 :

$$s_0 = -\frac{K_{eff}(0)}{2(N + \gamma)} \Leftrightarrow E_N = -\frac{K_{eff}^2(0)}{8(N + \gamma)^2}. \quad (17)$$

The search of γ can be described the following: the iterative system (16) has to zero out at some point. The possibility for γ to have multiple solutions (not exactly positive), or no solutions at all, requires further study.

The equation (16) gives us the formulae for coefficients:

$$A_{n-1} = \frac{\gamma + N}{K_{eff}(0)(N + m)} \left(((\gamma + n + 1)(\gamma + n) - K'_{eff}(0)) A_n - \sum_{j=n+1}^N A_j K_{eff}^{(j-n)}(0) \right) \quad (18)$$

The coefficient A_N is chosen arbitrarily. Since A_n and $\chi(s)$ depend linearly on A_N , the whole solution is unique up to a constant factor. This makes A_N the norming factor. The term $\chi(s)$ from formula (12) is found from the equation

$$\int_0^z K(z-t)\chi(t)dt + G(z) = z(z + 2s_0)\chi(z), \quad z > 0 \quad (19)$$

with $G(z)$ obtained from convolution of kernel with singular part of solution:

$$G(z) = \sum_{n=-\lceil\gamma\rceil}^N \frac{A_n}{\Gamma(1 - \{\gamma\})} \int_0^z \frac{d^{\lceil\gamma\rceil+n} K_{eff}(t)}{dt^{\lceil\gamma\rceil+n}} \frac{dt}{(z-t)^{\{\gamma\}}}. \quad (20)$$

The equation (19) is a *Volterra equation of III kind*. The theory of integral equations of III kind has not been fully developed comparing to that for integral equations of I and II kinds. Fredholm equations of III kind has been studied, for example, in [15]. The authors showed that the solution of such equation has singularities at points, where the weight function vanishes. In the above case, the operator

$$\mathcal{K}\varphi(z) = \int_0^z \frac{K_{eff}(z-t)}{z(z + 2s_0)} \varphi(t)dt = \int_0^1 \frac{K_{eff}(z(1-x))}{(z + 2s_0)} \varphi(zx)dx \quad (21)$$

belongs to the class of *cordial operators*, whose spectral properties has been systematically studied in [16,17]. According to those papers, the spectrum of operator (21) in continuous functions is $\sigma_0(\mathcal{K}) = -(N + \gamma)(\lambda + 1)^{-1}, \text{Re}\lambda \geq 0$. Therefore, the equation (19) that can be written as

$$\chi(z) = \mathcal{K}\chi(z) + \frac{G(z)}{z(z + 2s_0)} = \mathcal{K}\chi(z) + \hat{G}(z), \quad z > 0 \quad (22)$$

has a unique continuous solution $\chi(z)$, once \hat{G} is continuous at zero. However, if $\gamma \notin \mathbb{Z}$, the free term in (22) has a weak singularity. In this case, the theory in [17] is to be generalized for $L_1(\mathbb{R}_+)$ space.

5. Coulomb potential

The spectral function of a coulomb potential $V(r) = \frac{Z}{r}$ is a constant $K(s) = Z$ (it actually is a Heaviside function, but the multiplication by one is already taken into consideration), therefore all its derivatives vanish and the formulae for A_n contain only two adjacent coefficients. The system (16) zeroes out at coefficient A_{-1} when $\gamma = l + 1$, so the system (16) becomes an iteration formula

$$A_n = \frac{(n + 1)(2l + n + 2)}{-2Z + 2s_0(l + n + 1)} A_{n+1}, \quad (23)$$

which is exactly the formula for coefficients of a polynomial part of hydrogen atom wavefunction. The formula (17) becomes a well-known Rydberg formula

$$s_0 = \frac{Z}{(N + l + 1)}. \quad (24)$$

The regular equation (19) becomes trivial, as (20) equals to zero. Therefore, we obtain the eigenvalues and eigenfunctions:

$$E_N = -\frac{Z^2}{2(N + l + 1)^2}, \quad f_{N,l}(r) = r^{l+1} e^{-s_0 r} \sum_{n=0}^N A_n r^n.$$

6. Generalizations

The proper analysis of Schrödinger equation, however, has to be conducted explicitly without substitutions like $R(r) = r^{-1}f(r)$, so there would be no additional assumptions on Laplace spectral function behaviour. Then the Laplace spectral equation belongs to a wider class of equations:

$$\sum_{\alpha,\beta} s^\alpha (\theta(s) K^{\alpha\beta}(s) * \theta(s) s^\beta F(s)) = a(s, s_0(E)) F(s).$$

In fact, a wide range of pseudodifferential equations belongs to this class, including Dirac-type equations (after reducing the latter to the scalar equation). Indeed, the operator

$$AF = \sum_{\alpha,\beta} s^\alpha (\theta(s) K^{\alpha\beta}(s) * \theta(s) s^\beta F(s)),$$

after Laplace transform, gives us the operator

$$\mathcal{L}_{s \rightarrow r} A \psi = \sum_{\alpha,\beta} \frac{\partial^\alpha}{\partial r^\alpha} V^{\alpha\beta}(r) \frac{\partial^\beta}{\partial r^\beta} \psi(r).$$

This gives the opportunity to cover a wide class of spectral problems by means of DALV-method.

7. Conclusion

The approach to analyzing a spectral problem in real space by treating a solution as the Laplace transform of a tempered distribution is believed to give extensive results in quantitative analysis of discrete spectrum of differential operators. The study of Laplace spectral equations gives identical results for already solved equation for hydrogen atom. The discrete linear combination of Riemann–Liouville kernels can be replaced with continuous one, following the logic of Fourier transform theory evolution. Moreover, the equation (9) could be obtained for a wider class of differential and even pseudodifferential operators on \mathbb{R}_+ . The analysis of a Dirac-type matrix differential operators with DALV-method gives a convincing formulae for spectrum that could result in the rise of a self-sustained theory. Nevertheless, the rigorous proofs are to be elaborated for the method to become purely mathematical.

Acknowledgements

The work is supported by the Russian Science Foundation under the Grant No. 18-12-00429.

References

- [1] Titchmarsh E.G., Teichmann T. Eigenfunction expansions associated with secondorder differential equations, part 2. *PhT*, 1958, **11**(10), P. 34.
- [2] Teschl G. *Mathematical Methods in Quantum Mechanics: With Applications to Schrödinger Operators*. Graduate studies in mathematics. American Mathematical Society, 2009.
- [3] Dunford N., Schwartz J.T. *Linear Operators, Part 2: Spectral Theory, Self Adjoint Operators in Hilbert Space*. Wiley Classics Library, Wiley, 1988.
- [4] Fedoryuk M.V., Maslov V.P. *Quasiclassical approximation for quantum mechanics equations*, 1976.
- [5] Englefield M.J. Solution of Schrödinger equation by Laplace transform. *Journal of The Australian Mathematical Society*, 1968, **8**(3), P. 557–567.
- [6] Englefield M.J. Solution of coulomb problem by Laplace transform. *Journal of Mathematical Analysis and Applications*, 1974, **48**(1), P. 270–275.
- [7] Altuğ Arda and Ramazan Sever. Exact solutions of the Schrödinger equation via Laplace transform approach: pseudoharmonic potential and mietype potentials. *Journal of Mathematical Chemistry*, 2012, **50**(4), P. 971–980.
- [8] Douglas R.M., Pimentel and Antonio S De Castro. A Laplace transform approach to the quantum harmonic oscillator. *European Journal of Physics*, 2012, **34**(1), P. 199.
- [9] Ginyih Tsaur and Jyhpyng Wang. A universal Laplace transform approach to solving Schrödinger equations for all known solvable models. *European Journal of Physics*, 2013, **35**(1), P. 015006.

- [10] Tapas Das and Altüg Arda. Exact analytical solution of the ndimensional radial Schrödinger equation with pseudoharmonic potential via Laplace transform approach. *Advances in High Energy Physics*, **2015**, 2015.
- [11] Yangqiang Ran, Lihui Xue, Sizhu Hu, and RuKeng Su. On the coulombtype potential of the onedimensional Schrödinger equation. *Journal of Physics A: Mathematical and General*, 2000, **33**(50), P. 9265.
- [12] Naber M. Time fractional Schrödinger equation. *Journal of Mathematical Physics*, 2004, **45**(8), P. 3339–3352.
- [13] Michael E. Clarkson and Huw O Pritchard. A Laplace transform solution of Schrödingers equation using symbolic algebra. *International journal of quantum chemistry*, 1992, **41**(6), P. 829–844.
- [14] Zemanian A.H. *Generalized integral transformations*, 1968.
- [15] Warnock R.L. Bart G.R. Linear integral equations of the third kind. *SIAM Journal on Mathematical Analysis*, 1973, **4**(4), P. 609–622.
- [16] Vainikko G. Cordial Volterra integral equations 1. *Numerical Functional Analysis and Optimization*, 2009, **30**(910), P. 1145–1172.
- [17] Vainikko G. Cordial Volterra integral equations 2. *Numerical Functional Analysis and Optimization*, 2010, **31**(2), P. 191–219.
- [18] Vladimirov V.S. *Generalized functions in mathematical physics*, Nauka, Moscow, 1979. English transl, Mir, Moscow, 1979.

Mechanism of gas molecule transport through erythrocytes' membranes by kinks-solitonsP. V. Mokrushnikov¹, V. Ya. Rudyak^{1,2}, E. V. Lezhnev¹¹Novosibirsk State University of Architecture and Civil Engineering,
Leningradskaya, 113, Novosibirsk, 630008, Russia²Novosibirsk State University, Pirogova, 1, Novosibirsk, 630090, Russia
pavel.mokrushnikov@bk.ru, valery.rudyak@mail.ru, lionlev@yandex.ru**PACS 87.16.Dg, 87.16.Uv, 87.15.He****DOI 10.17586/2220-8054-2021-12-1-22-31**

A model of kinks appearance in the lipid bilayer membrane of erythrocytes, which are responsible for gas molecule transport, in particular, oxygen, is proposed. It was shown that the kinks arise due to the simultaneous action of transverse and tensile longitudinal mechanical stresses compressing the membrane. This model explains the membrane's permeability sharp increase for gases during an erythrocyte passage through the microcapillary network with the compressive transverse mechanical stresses sharply increasing in its membrane. It was found that the equation of kinks motion has a soliton solution, so that a kink-soliton is formed in the bilayer of the erythrocyte membrane. The developed model is consistent with the previously experimentally established fact that the native erythrocyte membranes in the bloodstream undergo a structural transition, when small changes in blood pH, hormone concentration, and temperature dramatically change the conformation of the biomembranes and its functions by changing the mechanical stress field in the biomembrane.

Keywords: biomembrane, diffusion, kinks, mechanical stress in biomembranes, microcapillary, nanosystem, erythrocyte.

Received: 15 November 2020

Revised: 20 December 2020

1. Introduction

Gas molecule transfer (O_2 , CO , CO_2 , NH_4) through an erythrocyte's membranes is an important physiological process. Biomembranes usually consist of two lipids layers, where proteins are embedded. This is a typical nanosystem, since the thickness of lipid layers does not usually exceed 10 nm. The structural state of the biomembrane is very complex. In the normal state, the membrane is in a liquid crystalline state, but a phase transition to the gel phase can occur in it, depending on the external conditions. In general, lipids perform rather complex movements, including lateral diffusion, rotational movement around the axis, and some others. The lateral diffusion coefficient of spin-labeled or fluorescent phospholipid probes can be analyzed by several methods: electronic paramagnetic resonance, nuclear magnetic resonance and fluorescence. The root-mean-square displacement of such a probe is determined by the Einstein relation: $\bar{l}^2 = 4Dt$ (two-dimensional system). In this case, the diffusion coefficient values were found to be quite high: $D = 10^{-11} - 10^{-12} \text{ m}^2/\text{s}$ [1].

Gas molecule transport through the biomembrane should be determined by the same mechanisms as the diffusion probe. It was experimentally established that the erythrocyte's membrane permeability for gas molecules is not lower than the water layer permeability of the same thickness [2]. This is rather strange, since the dynamic viscosity of the lipid bilayer, which forms most of the erythrocyte membrane surface, is from 30 to 100 mPa·s, and water is about 1 mPa·s. Indeed, the diffusion coefficient D of the spherical particle with radius r is determined by the Einstein–Stokes formula: $D = kT/6\pi\mu r$, where k is the Boltzmann constant, T is the temperature, and μ is the medium viscosity coefficient. This leads to the fact, that diffusion resistance of the lipid bilayer should also be greater than the corresponding value for the same water layer. The data of measurements of the oxygen molecules permeability through monolayer artificial lipid membranes are in agreement with this conclusion. Their permeability is shown to be significantly lower than that of a water layer of similar thickness [3, 4].

The observed facilitated diffusion of oxygen molecules are attempted to explain by the fact that the main stream of oxygen molecules passes through the proteins' membrane of aquaporin AQP1 in a number of papers [5–8]. Currently, aquaporins have also been associated with the transport of CO , CO_2 , O_2 , NH_4 [9–11]. Such a mechanism actually takes place, but it does not explain the sharp increase in the gas molecule's transport through the membrane during the erythrocyte's passage through the microcapillary chain and into lungs alveoli. There must also be a mechanism (or mechanisms) regulating this flux.

Facilitated gaseous diffusion is necessary through the erythrocyte's membranes when the hemoglobin of the erythrocyte is saturated with oxygen in the lungs capillaries. It is known that in this case, about a third of the oxygen, carried by it, penetrates into the erythrocyte cytoplasm in a quarter of a second [12]. There is no known mechanism that

allows such a large amount of oxygen to be transferred through the membrane in such a short time. There is another problem with gas exchange in the cardiovascular system. Gas exchange is not desirable in a case, when erythrocytes pass through the arteries and veins. It should occur during the passage of erythrocytes through microcapillaries, penetrating tissues and through the lungs alveoli. Otherwise, oxygen entered the bloodstream, increases the concentration of reactive oxygen species in the blood, which leads to an increase in lipid peroxidation of the cell membranes in blood vessel walls.

It was previously suggested that the gaseous diffusion in the lipid bilayer can occur with the help of kinks running along the hydrocarbon chains of phospholipids, that is, bends arising in the hydrocarbon chains [13, 14]. It was believed that kinks arise due to the energy of thermal vibrations of phospholipids. While paying tribute to such a mechanism, one should note its obvious shortcomings. First of all, the indicated fluctuating nature of kink formation determines their obvious instability. It is unclear how the kinks appearance synchronization occurs in the hydrocarbon chain, which should determine the directional transport of gas molecules by kinks along the hydrocarbon chain.

The aim of this paper is to study the mechanism of the kinks' appearance in the hydrocarbon chain of phospholipids. It is shown that they arise as a result of mechanical transverse compression of the erythrocyte membrane during its passage through the microcapillary layer and through the lungs alveoli. The mathematical model describing the kinks' evolution is formulated and it is established that not simple kinks, but the kinks-solitons are formed. The models of kink-solitons, running along the infinite hydrocarbon chain of the erythrocyte membrane lipids and along a real chain of finite length, are analyzed.

2. Equation of a hydrocarbon chain motion

In order to study the transport of gas molecules by erythrocytes, it is first necessary, to analyze their passage through the corresponding membrane, through the corresponding lipid bilayer. So, we should consider a hydrocarbon chain section of a phospholipid molecule with saturated bonds. It consists of n carbon groups and the distance between them is determined by the valence bonds and the corresponding angles. A section of such a hydrocarbon chain of three CH_2 -groups (groups $i, i+1, i-1$) is shown in Fig. 1, where θ_i is the bond angle, and φ_i is the angle of internal rotation. The bond lengths and bond angles θ_i remain constant (Fig. 1). The polymer molecule conformation is determined by the angles of rotation around C–C bonds, or angles of internal rotation [15]. These are the angles between two planes formed by bond pairs $(i-1, i)$ and $(i, i+1)$.

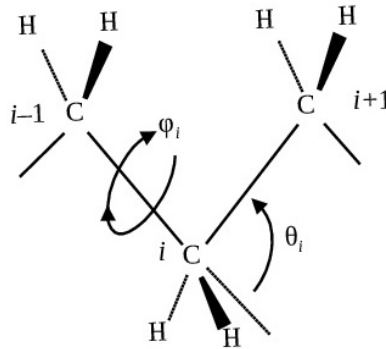


FIG. 1. A hydrocarbon chain section with saturated bonds: i is a number of CH_2 -group of atoms, θ_i is the bond angle, φ_i is the angle of internal rotation

The erythrocytes roll up into cylinders, passing through microcapillaries [16]. If there are no stretching regions in the lipid bilayer, then the double hydrocarbon tails of phospholipid molecules in the biomembrane are in a completely trans-configuration. All angles are zero, and the hydrocarbon chain is a linear structure in the trans-conformation. This is illustrated in Fig. 2a, which is a side view of the double hydrocarbon tails of phospholipid molecules in the trans-configuration.

On the contrary, in the general case, when erythrocytes pass through the microcapillary, longitudinal mechanical tensile stresses G and mechanical compressive stresses P increase in the direction transverse to the membrane plane in their plasma membranes (see Fig. 2b). The hydrocarbon tail loses its stability, its links begin to rotate under the action of the transverse mechanical compression stress and the longitudinal mechanical tensile stress. This leads to the bending of the phospholipid chain and a kink formation. As a result of membrane compression, its thickness decreases by $h = 0.127$ nm (see Fig. 2b).

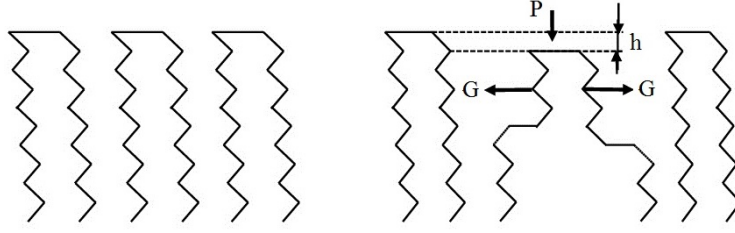


FIG. 2. Side view of double hydrocarbon tails of phospholipid molecules in a biomembrane, which are in trans-configuration (a) and in the presence of transverse and longitudinal mechanical stresses (b)

The appearance of a kink is due to the rotation of CH_2 groups around the OX axis by an angle Ψ_i (see Fig. 3), which arises under the action of transverse and longitudinal mechanical stresses. The rotation of each CH_2 -group is determined by the forces moment \mathbf{N}_{i1} , created by the interaction between this hydrocarbon chains group of neighboring phospholipid molecules. In addition, it is necessary to take into account the forces moment \mathbf{N}_{i2} , created during steric interaction of hydrogen atoms during rotation of CH_2 -groups i and $(i + 1)$ and groups i and $(i - 1)$ around C–C bonds. Finally, one should take into account the forces moment \mathbf{N}_{i3} , created by the interaction of the membrane electric field and the induced dipole moment of the C–C bond. Thus, the equation of the i -th group motion has the following form:

$$J \frac{\partial^2 \Psi_i}{\partial t^2} = \mathbf{N}_{i1} + \mathbf{N}_{i2} + \mathbf{N}_{i3}, \quad (1)$$

where J – an inertia moment i -th CH_2 -groups around the axis OX (Fig. 1).

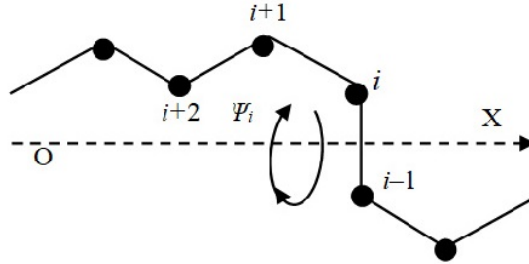


FIG. 3. The kink is moved by turning the CH_2 -group number i around the axis rotation OX by the angle Ψ_i . The OX axis is directed along the hydrocarbon chain

Let us consistently consider the moments \mathbf{N}_{i1} , \mathbf{N}_{i2} , \mathbf{N}_{i3} in eq. (1). In the trans-configuration of the hydrocarbon chain $\Psi_i = 0$. On the other hand, in gauche(+)-trans-gauche(–)-configurations $\Psi_i = \pi$. The forces moment, created by the interaction of neighboring hydrocarbon chains \mathbf{N}_{i1} is maximum at $\Psi_i = \pi/4, 3\pi/4, 5\pi/4$ and $7\pi/4$ and is equal to zero at $\Psi_i = 0, \Psi_i = \pi/2, \pi$ and $3\pi/4$. Indeed, at $\Psi_i = 0$ or $\Psi_i = \pi$, the arm of force \mathbf{F} acting between the i -th CH_2 -group and the hydrocarbon chains of neighboring phospholipid molecules in the process of rotating around OX axis rotation is equal to zero. When $\Psi_i = \pi/2$ or $3\pi/2$, the force \mathbf{F} is equal to zero. Thus, this forces moment is equal to: $\mathbf{N}_{i1} = K_F \sin(2\Psi_i)$, where $K_F = Fl$, here l is the length of the C–C bond, and \mathbf{F} is the force, tending to rotate the CH_2 -group i around the C–C bond by Ψ_i angle (see Fig. 3). This force can be estimated using Young's modulus of longitudinal tension \mathbf{E}_{\parallel} of a biomembrane [17]. Further, it will be assumed that $K_F = \text{const}$.

There is an electric field with strength E , which causes the polarization of the C–C bonds of phospholipid molecules in the native membrane of the erythrocyte. Each C–C bond acquires an electric dipole moment. Let us denote the electric dipole moment between carbon atoms $(i - 1)$ and i as \mathbf{p}_{i-1} , between $i, (i + 1)$ as \mathbf{p}_i , and between $(i + 1), (i + 2)$ as \mathbf{p}_{i+1} . Two positions of these three dipoles are shown in Fig. 4 with arrows, when a kink passes through them at $\Psi_i = 0$ and $\Psi_i = \pi$. The dashed lines indicate the force lines of the electric field strength \mathbf{E} in the membrane. The interaction energy of the electric dipole \mathbf{p} with the electric field is equal to $W_0 = -\mathbf{p} \cdot \mathbf{E} = -pE \cos(\alpha)$, where α is the angle between \mathbf{E} and \mathbf{p} vectors. The dipole modulus equals to $p = \varepsilon_0 \beta \cos \alpha$, where β is the polarizability coefficient of the C–C bond and ε_0 is the electrical constant. The energy W_0 is determined by the angle α . When the three dipoles rotate around the OX axis from $\Psi_i = 0$ to $\Psi_i = \pi$ for \mathbf{p}_{i-1} dipole, the angle α changes from $\pi/3$

to $\pi/2$, for \mathbf{p}_{i-1} dipole, the angle α does not change and is equal to $\pi/3$, for \mathbf{p}_{i+1} the angle α varies from $\pi/2$ to $\pi/3$. When $\Psi_i = \pi/2$ for \mathbf{p}_{i-1} and \mathbf{p}_{i+1} , the angle $\alpha = 75^\circ$. Between the states of three dipoles \mathbf{p}_{i-1} , \mathbf{p}_i , \mathbf{p}_{i+1} at $\Psi_i = \pi$ and at $\Psi_i = 0$ there is an energy barrier with a height $\Delta W_E = \varepsilon_0 \beta E^2$ created by the interaction of these three dipoles with the electric field of the membrane. Thus, it is easy to establish that the forces moment \mathbf{N}_{i2} is equal to $\mathbf{N}_{i2} = -KE \sin(2\Psi_i)$.

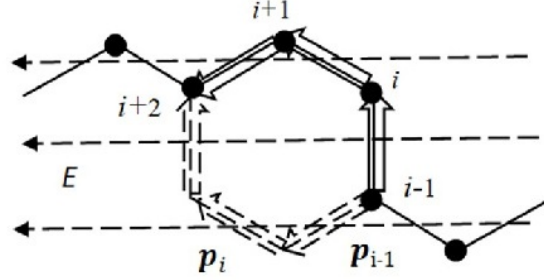


FIG. 4. Two positions of three dipoles \mathbf{p}_{i-1} , \mathbf{p}_i , \mathbf{p}_{i+1} at $\Psi_i = 0$ (flat dashed arrows) and $\Psi_i = \pi$ (flat solid arrows) in the membrane electric field \mathbf{E}

The force moment \mathbf{N}_{i3} is created by the i -th atomic group interaction with the neighboring groups $(i-1)$ and $(i+1)$ (see Fig. 3). It appears because of the barrier ΔE in the interaction energy of neighboring atomic CH_2 -groups, which appears during these groups rotation around C–C bonds. The barrier arises as a result of steric repulsion of closely spaced valence unbonded hydrogen atoms of neighboring CH_2 -groups. The energy minimum occurs if two pairs of hydrogen atoms of neighboring CH_2 -groups are in a crossed state ($(\Psi_{i-1} - \Psi_i) = 0$ or π), and the maximum corresponds to shaded conformations ($(\Psi_{i-1} - \Psi_i) = \pi$). For a saturated hydrocarbon chain, ΔE barrier changes from 12 to 17 kJ/mol, depending on the link and the length position of the hydrocarbon chain [17]. If the difference in the angles of neighboring groups rotation is small or at least less $\pi/2$ ($\Psi_{i-1} - \Psi_i \leq \pi$), then we can approximately assume that the forces moments, created by the interaction of atomic group i with atomic groups $(i-1)$ and $(i+1)$ are respectively equal to $\chi(\Psi_{i-1} - \Psi_i)$ and $\chi(\Psi_{i+1} - \Psi_i)$, where χ is some constant determined by the following relation: $\chi = \Delta E / (\pi/2)^2$. Here ΔE is the barrier value in the energy of neighboring atomic CH_2 -groups interaction, which appears during these groups rotation around C–C bonds. Therefore, the total moment turns out to be equal to $N_{i2} = \chi(\Psi_{i+1} - 2\Psi_i + \Psi_{i-1})$.

Substituting the obtained expressions for the moments into eq. (1), we obtain:

$$J \frac{\partial^2 \Psi_i}{\partial t^2} = \chi(\Psi_{i+1} - 2\Psi_i + \Psi_{i-1}) + (K_F - K_E) \sin 2\Psi_i, \quad i = 1, 2, \dots, N, \quad (2)$$

where N is the number of atomic groups in the simulated hydrocarbon chain.

3. Soliton solution for the equation of a kink motion

Let us first consider the evolution of a sufficiently long hydrocarbon chain. The number of CH_2 -groups is large and the chain length is much greater than the distance between them in such a chain. In order to qualitatively describe its evolution, one needs to go to the limit, directing the distance between groups to zero. In fact, this is equivalent to considering an infinite chain. So, if we denote the distance between neighboring atomic groups by l and put $\chi = Kl^{-2}$, we will assume that K remains a finite constant as $l \rightarrow 0$ (this is a kind of the thermodynamic limit transition analogue [18], if we remind that the number of groups tends to infinity). Directing the OX axis along the hydrocarbon tails, it is easy to see that eq. (2) is reduced to the sine-Gordon differential equation [19]:

$$J \frac{\partial^2 \Psi}{\partial t^2} - K \frac{\partial^2 \Psi}{\partial x^2} - (K_F - K_E) \sin 2\Psi = 0. \quad (3)$$

We will find a solution to this equation in the form of $f(\xi)$ function, where $\xi = x \pm Vt$, x is the coordinate along OX and V is the kink velocity. Substituting this solution into (3), after simple transformations we find

$$\frac{1}{2} \left(\frac{\partial f}{\partial \xi} \right)^2 + \frac{(K_F - K_E)}{2(JV^2 - K)} \cos(2f) = \gamma, \quad (4)$$

where $\gamma = \text{const.}$

Equation (4) is the equation of an oscillator moving in a potential well $U(f) = U_0 \cos(2f)$, where $U(f) = U_0 \cos(2f)$, and $U_0 = (K_F - K_E)/[2(JV^2 - K)]$. At $\gamma < -U_0$ the equation has no solution. On the other hand, if $-U_0 < \gamma < U_0$, then the oscillator performs periodic oscillations inside one of the potential well. Finally, for $\gamma = -U_0$, the solution describes a soliton, i.e. isolated perturbation tending to constant values at infinity: $\lim_{\xi \rightarrow \pm\infty} f(\xi) = \text{const}$. Thus the soliton solution of the eq. (4) has the following form:

$$\tan(f/2) = \exp\{\pm 2\sqrt{\gamma}(\xi + \xi_0)\}, \quad (5)$$

where $\xi_0 = \text{const}$. The dependence of the function f from $(x - Vt)$ is presented in Fig. 5, here h is the width of the kink-soliton.

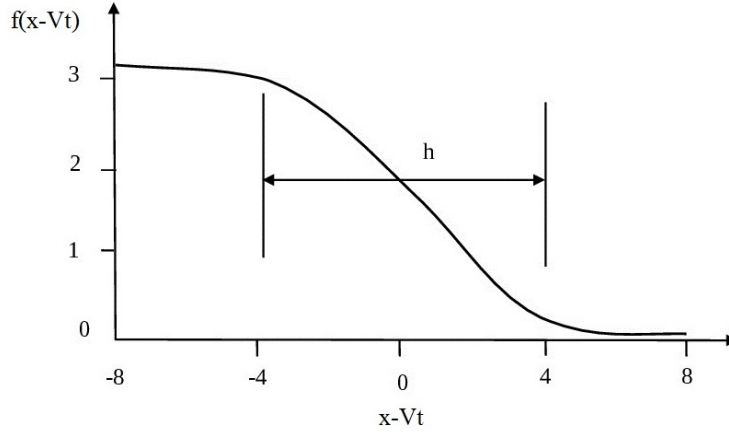


FIG. 5. The form of solution (5) for $2\sqrt{\gamma} = V = 1$

For the kinks-solitons appearance in the hydrocarbon chain, such a chain must be subjected to mechanical compression with a strictly defined value of transverse pressure \mathbf{P} . In this case, the phospholipid is compressed by Δ , and then straightens and the kink-soliton runs along it. So, in order to do it, the work A of the mechanical pressure \mathbf{P} , compressing the membrane in the transverse direction must be equal to the energy of the kink-soliton W and the kinetic energy, transferred by the kink-soliton at the velocity V of a gas molecule with mass m . We estimate the work A using Young's modulus of transverse compression \mathbf{E}_\perp of the biomembrane. The energy of the kink-soliton is calculated the same way, as it is done in [19]. In order to do it, we find the density of the Hamiltonian from eq. (3), and then calculate the energy of the kink-soliton in an infinite hydrocarbon chain. The width of the kink is equal to h (Fig. 5). At this distance, the angle of f rotation varies from 0 to π . This is done under the following conditions:

$$\gamma = \frac{(K_F - K_E)}{2(JV^2 - K)}, \quad \frac{E_\perp S \Delta^2}{2L} = W \frac{mV^2}{2}, \quad \sqrt{\gamma} = \ln 2, \quad (6)$$

where S is lipid cross-sectional area, and L is its length.

From conditions (6), it is possible to estimate velocity of the kink-soliton, its energy W , and the value of critical compression Δ . In order to do this, it is necessary to evaluate the constants K , K_F , K_E . The force \mathbf{F} , tending to rotate the CH_2 -group i around the C-C bond, can be estimated using the Young's modulus of longitudinal tension E_\parallel of the biomembrane $F = \varepsilon E_\parallel S_1$, where S_1 is the area, occupied by the CH_2 -group, and ε is the relative membrane elongation. Setting $\varepsilon = 0.01$, $E_\parallel = 5 \cdot 10^8 \text{ N/m}^2$, $S_1 = 0.084 \text{ N}\cdot\text{m}^2$, $l = 0.15 \text{ nm}$ [17], we get $K_F = 0.628 \cdot 10^{-22} \text{ N}\cdot\text{m}$.

The polarizability is $\beta = 1.25 \cdot 10^{-30} \text{ m}^3$, and the electric field strength in the erythrocyte membrane is $E \approx 5 \cdot 10^7 \text{ V/m}$ for C-C bonds, [17]. Substituting these values into the expression for $K_E = (2\Delta W_E/\pi)$, we get $K_E = 2.044 \cdot 10^{-27} \text{ N}\cdot\text{m}$. We estimate the constant χ by the formula $\chi = \Delta E/(\pi/2)^2$, where ΔE is the value of the barrier in the interaction energy of neighboring atomic CH_2 -groups, which appears when these groups rotate around C-C bonds. Taking $\Delta E = 12.5 \text{ kJ/mol}$, we find that $\chi = 0.843 \cdot 10^{-20} \text{ N}\cdot\text{m/rad}$. Therefore the constant $K = \chi l^2$ is equal to the following value $K = 1.897 \cdot 10^{-40} \text{ N}\cdot\text{m}^3/\text{rad}$. The inertia moment of the CH_2 -group around the OX axis rotation (Fig. 3) $J = Ml^2$, where M is the mass of the CH_2 -group. Substituting the corresponding value values, we find $J = 0.544 \cdot 10^{-45} \text{ kg}\cdot\text{m}^2$. The velocity of the kink-soliton is $V = 591 \text{ m/s}$.

The energy of the kink-soliton W is calculated from the density of the Hamiltonian H corresponding to the eq. (3):

$$W = \int_{-\infty}^{+\infty} H dx, \quad H = \frac{1}{2} \left[j \left(\frac{\partial f}{\partial t} \right)^2 + \frac{K}{l} \left(\frac{\partial f}{\partial x} \right)^2 - \frac{(K_F - K_E)}{l} 2 \sin^2 f \right], \quad (7)$$

where $j = (Ml^2)/2$ is the linear density of the inertia moment of the hydrocarbon chain. Substituting solution (5) and relations (6) into (7), we find:

$$W = 2jV^2 \sqrt{\gamma} + \frac{2K}{l} \sqrt{\gamma} - \frac{(K_F - K_E)}{l\sqrt{\gamma}} = \frac{2.772K}{lh}. \quad (8)$$

Thus, the energy of the kink-soliton depends only on the barrier value ΔE of the interaction energy of neighboring atomic CH_2 -groups, which appears during these groups rotation around C–C bonds. Substituting the corresponding values, we obtain $W = 2.703 \cdot 10^{-20}$ J, and the critical compression of the phospholipid is equal to $\Delta = 1.28$ nm.

4. Modeling the kinks-solitons in silico motion

In the previous section, a kink was shown to arise in a hydrocarbon chain as a result of its mechanical deformation. Its dynamics are described by a soliton (5) in the approximation of an infinite chain: the kink-soliton moves along the hydrocarbon chain. Such kinks-solitons, which appear in the lipid bilayer as a result of structural changes in biomembranes, can indeed determine the real mechanism of gas molecules transporting. At the same time, it is obvious that in a real situation the hydrocarbon chain has a finite size. Do the kinks-solitons form in such a chain, and if so, how do their characteristics depend on the parameters of the system modeled? This section is devoted to answering these questions. In silico simulation of the dynamics of a finite-length acyl chain is performed here. Situations are simulated when the number of links in the hydrocarbon chain is limited and when three of the bonds are unsaturated (C=C).

Equation (2) of motion about the axis of the OX i th CH_2 -group has the form:

$$J \frac{\partial^2 \Psi_i}{\partial \tau^2} - A (\Psi_{i+1} - 2\Psi_i + \Psi_{i-1}) - B \sin 2\Psi_i = 0, \quad i = 1, 2, \dots, N. \quad (9)$$

Here, the time is normalized to the time $\tau_0 = 10^{-12}$ s, it is determined by the interaction time of the neighboring CH_2 -groups of the hydrocarbon chain, which is of the order of l/V . It is easy to establish that this time in this case is $0.26 \cdot 10^{-12}$ s. The coefficient $A = (\chi\tau_0^2/J)$ included in (9) is determined by the forces moment acting between neighboring CH_2 -groups as a result of steric interaction of hydrogen atoms as they rotate around C–C bonds. For the erythrocyte membrane, $A = 15.5$ for a single C–C bond. For a link with a double C=C bond, rotation around it is very difficult (the height of the energy barrier ΔE is about 270 kJ/mol) and $A = 334.5$.

Coefficient $B = (K_F - K_E) \tau_0^2 J^{-1}$ depends on the moment of forces, created by the interaction of the i -th CH_2 -group and hydrocarbon chains of neighboring lipid molecules, rotating around the OX axis (see Fig. 4). Taking into account the estimates given above, $B = 0.1154$.

The equations system (9) was solved by the fourth order Runge–Kutta method. The initial angle Ψ_{10} and the corresponding angular velocity ω_{10} were set as the initial state of the system for the first link. The rest of links at the initial moment of time had zero angle of rotation and angular velocity. Since a finite chain was considered, boundary links (zero and $(n + 1)$ -th) were introduced, which parameters values were fixed.

The evolution of a hydrocarbon chain, consisting of 20 CH_2 -groups, is shown in Fig. 6. This evolution is described by the rotation angle Ψ (radians) of each of the groups. Here, the group number is indicated along the abscissa axis, time was measured in times τ_0 , and the constants in eq. (9) were equal to $A = 15.5$ and $B = 0.1154$. A kink forms in the hydrocarbon chain at time $\tau = 0.5$, which further transforms into a kink-soliton, spreading along the chain at V velocity. Thus, the kink-soliton is formed in the hydrocarbon chain, moving at a given velocity along it. The deformation process of the erythrocyte membrane during its passage through the microcapillary layer and through the lungs alveoli is periodic. The kink-soliton is formed periodically in the considered hydrocarbon chain.

Coefficient B in eq. (9) is determined by coefficients K_F and K_E , which depend on the membrane conformation. With some change in the composition of membrane lipids, for example, with an increase or decrease in cholesterol concentration, the B coefficient will change. It is important to understand how this can affect the formation and motion of the kink-soliton. In order to find out, solutions of eq. (9) were constructed for a hydrocarbon chain of 20 groups at a fixed coefficient $A = 15.5$. Coefficient B varied from 0.1 to 0.35. It was found that the kink-soliton appeared in the indicated range, its energy did not depend on the coefficient B . This was consistent with formula (8), indeed, if we substitute the definition of A coefficient in it, we get the following value $B = (2.772JA) / (\tau_0^2 h)$.

It is important to understand what happens when the coefficient A changes. For this purpose, parametric calculations were carried out with the constant coefficient $B = 0.11544$, where A varied from 15.5 to 45. It was found that

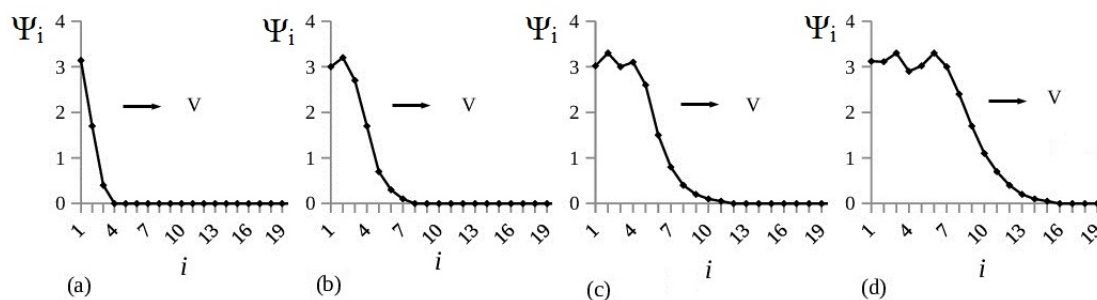


FIG. 6. Evolution of the rotation angle of the hydrocarbon chain CH_2 -groups at different times $\tau = 0.5, 1, 1.5, 2$ (from left to right)

a kink-soliton always appeared in this case as well. The dependence of the dimensionless value of the kink-soliton energy $W_A = W/W_i$, where W_i is the kink-soliton energy at $A = 15.5$, is shown in Fig. 7. The energy of a soliton is directly proportional to the coefficient A , which agrees with formula (8).

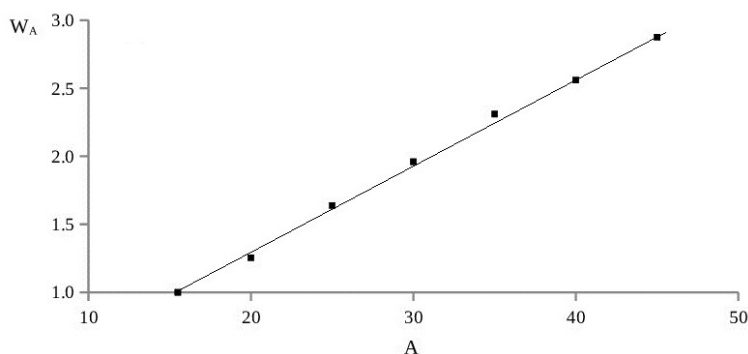


FIG. 7. Dependence of the kink-soliton dimensionless energy W_A on the coefficient A

In phospholipid molecules, along with saturated $\text{C}-\text{C}$ bonds, there can be links with a $\text{C}=\text{C}$ double bond. The modeling has shown that, the kink-soliton is also formed in the presence of such bonds, but its structure and properties change significantly. A comparison of the kink-soliton's energy distribution over individual groups is shown in Fig. 8. Here the values of the relative energy W/W_m (W is the rotational motion energy of the i -th CH_2 -group, W_m is the maximum energy of the fourth CH_2 -group rotational motion) of the rotational motion of each CH_2 -group saturated (Fig. 8a) and unsaturated (Fig. 8b) a hydrocarbon chain during a soliton passing along it are given.

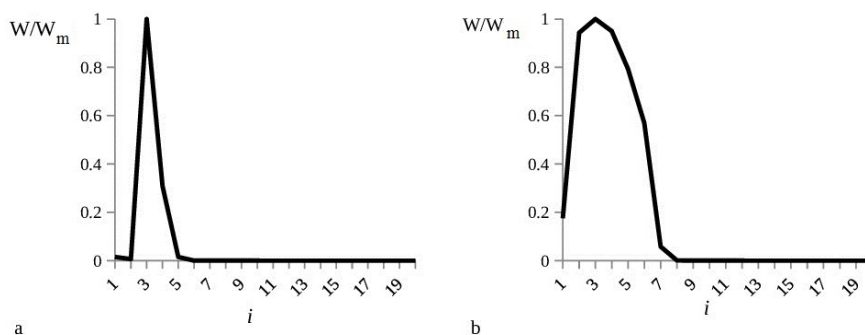


FIG. 8. Energy of each saturated CH_2 -group rotational motion (a) and unsaturated (b) hydrocarbon chain during a soliton passing along it

The links 2, 3, 4 are with a double bond $\text{C}=\text{C}$ in the unsaturated chain, the rest is with a single $\text{C}-\text{C}$ bond. The presented picture corresponds to the time $\tau = 1$ (see Fig. 6b), when the link number 4 has the highest angular velocity (and kinetic energy). The group number is again plotted along the abscissa axis. In the presence of a single bond, a

soliton is actually formed by four groups 3, 4, 5, 6 (see Fig. 6b). Group 4 has the maximum energy, the energy of the 5th group is about 30 % of the maximum, and groups 3 and 6 have very low relative energies. On the other hand, in the presence of double bonds, groups 1, 2, 6, 7 also have a sufficiently high energy. The kink-soliton is formed not by four, but by five groups.

The difference between a soliton in an unsaturated hydrocarbon chain and a soliton in a saturated chain is that, the CH₂-groups, connected by a double bond continue to oscillate with large amplitude, taking up part of the soliton energy after the soliton has passed the front. This is not observed in the saturated chain; after the soliton passes the front, the CH₂ groups vibrate with very small amplitude. Thus, the soliton is "blurred" in the unsaturated chain, and it is necessary to give the former greater energy for its existence. A stronger transverse compression of the erythrocyte membrane is necessary during the erythrocyte passaging through the microcapillaries. In this case, in the erythrocyte membrane from saturated and unsaturated phospholipids, kink-solitons will appear in saturated chains, and will not do it in unsaturated chains. Therefore, gaseous transport through the membrane should decrease with an increase in the concentration of unsaturated lipids in it. It is known that when animals hibernate, the lipid bilayer of the erythrocyte membranes is enriched with lipids with unsaturated bonds in hydrocarbon chains. According to the developed model, this contributes to a decrease in oxygen permeability for these membranes.

5. Discussion of the obtained results and concluding remarks

Let us consider the above approximations, before discussing the obtained results. Eqs. (2) and (7) describe the interactions between hydrocarbon chain links of phospholipids in the lipid bilayer of the erythrocyte membrane approximately. First, the interaction of the lipid hydrocarbon chain links with membrane proteins is not considered. Meanwhile, membrane proteins make up approximately 50 % of the erythrocyte membranes mass; they strongly affect the conformation of the membranes lipid bilayer [20]. Secondly, considering the forces moment N_{i3} in eq. (1), we neglected the steric interaction of hydrogen atoms during rotation of the i -th CH₂-group with groups $(i + 2)$, and $(i - 2)$, etc., leaving only the moment of forces, created due to the steric interaction of hydrogen atoms during the rotation of two neighboring CH₂-groups (i -th and $(i + 1)$ -th) and two neighboring CH₂-groups (i -th and $(i - 1)$ -th) around C-C bonds. Meanwhile, more distant CH₂-groups also affect the rotation of the i -th CH₂-group. This error is easy to estimate. The steric interaction of hydrogen atoms is due to Van Der Waals forces (dipole-dipole induced interaction) between them. These forces are inversely proportional to the distance between atoms to the sixth power. Therefore, the exact value of χ_e coefficient in eq. (2) is: $\chi_e = \chi(1 + 2^{-6} + 3^{-6} + \dots)$. The difference between the exact value of this coefficient and that used in eqs. (2) and (7) is less than 2 %. Thus, the model, developed here, is quite adequate. In principle, of course, it is not difficult to take into account subsequent contributions to χ_e , however this will not lead to significant changes in the final results.

Now, let us consider the possibilities of the kink-soliton model for describing processes actually observed in practice. With an increase in cholesterol concentration in biomembranes, their permeability to oxygen molecules decreased. This was established by the method of molecular dynamics [21] and by measuring the biomembrane permeability of a human eye's corneal cells [22–26], the Chinese hamster's ovary cells [27] using electron paramagnetic resonance. These data are quite explainable by the kink-soliton model of oxygen molecule transport. Indeed, cholesterol molecules can easily move along the membrane, being incorporated into the biomembrane, increasing the interaction energy between the hydrocarbon chains of the bilayer molecules and creating mechanical compressive stresses in the membrane. The chains are in the trans-configuration, and their transition to the gauche-trans-gauche-configuration turns out to be difficult (Fig. 2). Cholesterol hindered the appearance of kinks-solitons, and the membrane permeability decreased, coming up to the hydrocarbon chains of phospholipids.

After all, it was experimentally established that the oxygen permeability was lower in the protein-lipid domains of cytoplasmic membranes than in the areas between them [27]. The same fact was found for artificial lipid membranes, enriched with cholesterol [28]. This difference can be explained by the fact that mechanical compression deformations prevail in the protein-lipid domains of biomembranes, and tensile deformations prevail in the areas between them [20]. The kinks-solitons formation is hindered in protein-lipid domains, while the kinks-solitons are more often formed in the regions between them and the oxygen permeability for these regions is higher.

Further, it was found that by using the electron paramagnetic resonance method, the inclusion of a cis- or trans-double bond in the C9–C10 position of the alkyl chain reduced oxygen transfer at all sites of the membrane in the absence of cholesterol [14]. If oxygen were transported through the membrane only due to passive diffusion, then the presence of a double bond in the alkyl chain should have increased the oxygen transfer. Double bonds created kinks in the alkyl chain; the lipid bilayer was more friable than the lipid bilayer of phospholipids with saturated bonds in the alkyl chain. Passive diffusion through a more friable lipid bilayer should be higher, but the experiment showed the opposite fact. The model of oxygen molecule transportation using kinks-solitons, presented in this paper, explains the results of this experiment. Turning around is facilitated (the energy barrier height is about 12.5 kJ/mol) for a link

with a saturated C–C bond. On the other hand, for a link with a C=C double bond, such a turn is difficult, on the contrary (the height of the energy barrier is about 270 kJ/mol of energy). Therefore, the frequency of the kink-soliton occurrence becomes very low. It is known that when fish start hibernation, the lipid bilayer of the plasma membranes of their cells is enriched with phospholipids with unsaturated bonds in hydrocarbon chains [29]. This helps to reduce the oxygen permeability of these membranes.

Mechanical stresses in membranes affect the ability of erythrocytes to fold when they pass through micro capillaries [30]. These stresses change under the influence of exogenous and endogenous factors: hormones [31, 32], nanoparticles [33–36], blood plasma proteins [37], vitamin E [38]. Apparently, the change in the microviscosity of the erythrocyte membranes is one of the mechanisms of a human body adaptation to the harsh conditions of the Far North. The native membrane of an erythrocyte in blood undergoes a structural transition under physiological parameters of blood [39]. Small changes in blood pH, hormone concentration, and temperature dramatically change the biomembranes conformation, thus altering its functions by changing the field of mechanical stress in the biomembrane [39,40]. The model of the kinks-solitons in the lipid bilayer developed corresponds to this general principle. A slight increase in the transverse mechanical pressure on the membrane causes a change in its structure and a sharp increase in the diffusion of gas molecules through it. The existence of kinks-solitons in a biomembrane can apparently be detected by the nuclear magnetic resonance method [41].

Longitudinal mechanical compressive stresses prevail in the erythrocyte membranes, when they pass through arteries and veins, which diameter is larger than erythrocytes [19,31]. There are no conditions for the kinks-solitons formation. The membrane permeability is low for gas molecules.

On the contrary, when the erythrocyte passes through the microcapillary bed, for which the diameter is smaller than the diameter of red blood cells, it folds and the erythrocyte membrane is affected by both transverse compression and longitudinal mechanical tension (see Fig. 2). In addition, contractions of smooth muscle cells of microcapillaries occur with a high frequency, leading to radial mechanical displacements of the microvessels walls [32,42,43]. There are the conditions for the membrane to shrink to a critical value Δ , the kinks-solitons begin to run along the hydrocarbon tails of phospholipids, moving gas molecules with their bends. The permeability of the erythrocyte membrane increases sharply.

According to the developed model, the biomembrane electric field has very little effect on the kinks-solitons appearance, since $K_E \ll K_F$. But, what else can affect the passage of the erythrocytes through capillaries on the gas molecules transport through the membrane? The microcapillary diameter is often less than the diameter of an erythrocyte. The erythrocyte folds into a tube and passes through the capillary. In this case, the boundary layer of immiscible water adjacent to the membrane from the outside is almost completely stripped off the erythrocyte surface. The total permeability for gas molecules from the erythrocyte and into the erythrocyte increases. At the same time, a slight decrease in blood plasma pH occurs in the peri-membrane layer. Red blood cells receive additional force pushing them along the microcapillary layer [44].

Acknowledgements

This work was financially supported by the Russian Foundation for Basic Research (Grant No. 19-01-00399).

References

- [1] Bahri M.A., Heine B.J., Hans P., et al. Quantification of lipid bilayer effective microviscosity and fluidity effect induced by propofol. *Biophys. Chem.*, 2005, **114**, P. 53–61.
- [2] Kreuzer F., Yahr W.Z. Influence of red cell membrane on diffusion of oxygen. *J. Appl. Physiol.*, 1960, **15**, P. 1117–1122.
- [3] Blank M. Monolayer permeability and the properties of natural membranes. *J. Phys. Chem.*, 1962, **66** (10), P. 1911–1918.
- [4] Ivanov I.I., Loktyushkin A.V., et al. Oxygen channels of the erythrocyte membrane. *Doklady biochemistry and biophysics*, 2007, **414** (1), P. 137–140.
- [5] Denker B.M., Smith B.L., Kuhajda F.P., Agre P. Identification, purification, and partial characterization of a novel Mr 28,000 integral membrane protein from erythrocytes and renal tubules. *J. Biol. Chem.*, 1988, **263** (30), P. 15634–15642.
- [6] Preston G.M., Carroll T.P., Guggino W.B., Agre P. Appearance of water channels in *Xenopus* oocytes expressing red cell CHIP 28 protein. *Science*, 1992, **256** (5055), P. 385–387.
- [7] Saparov S.M., Liu K., Agre P., Pohl P. Fast and selective ammonia transport by aquaporin-8. *J. Biol. Chem.*, 2007, **282** (8), P. 5296–5301.
- [8] Endeward V., Cartron J.P., Ripoché P., Gros G. RhAG protein of the Rhesus complex is a CO₂ channel in the human red cell membrane. *FASEB J.*, 2008, **22** (1), P. 64–73.
- [9] Agre P., Preston G.M., et al. Aquaporin CHIP: the archetypal molecular water channel. *Am. J. Physiol.*, 1993, **265** (4), P. 463–476.
- [10] Cooper G.J., Boron W.F. Effect of PCMBs on CO₂ permeability of *Xenopus* oocytes expressing aquaporin 1 or its C189S mutant. *Am. J. Physiol.*, 1998, **275** (6), P. 1481–1486.
- [11] Endeward V., Musa-Aziz R., et al. Evidence that aquaporin 1 is a major pathway for CO₂ transport across the human erythrocyte membrane. *FASEB J.*, 2006, **20** (12), P. 1974–1981.
- [12] Endeward V., Gros G. Low carbon dioxide permeability of the apical epithelial membrane of guinea-pig colon. *J. Physiol.*, 2005, **567** (1), P. 253–265.

- [13] Träuble H. The movement of molecules across lipid membranes: A molecular theory. *J. Membr. Biol.*, 1971, **4** (1), P. 193–208.
- [14] Subczynski W.K., Hyde J.S., Kusumi A. Effect of alkyl chain unsaturation and cholesterol intercalation on oxygen transport in membranes: a pulse ESR spin labeling study. *Biochemistry*, 1991, **30** (35), P. 8578–8590.
- [15] Flory P.J., Volkenstein M. Statistical mechanics of chain molecules. *Biopolymers*, 1969, **5**, P. 699–700.
- [16] Secomb T.W., Pries A.R. Blood viscosity in microvessels: experiment and theory. *Comptes Rendus Physique*, 2013, **14** (6), P. 470–478.
- [17] Rubin A.B. *Biophysics*. Nauka, Moscow, 2004, 469 p.
- [18] Rudyak V.Ya. *Statistical Aerohydrodynamics of Homogeneous and Heterogeneous Media. Vol. 2. Hydromechanics*, NSUACE, Novosibirsk, 2005, 468 p.
- [19] Dodd R.K., Eilbeck J.C., Gibbon J.D., Morris H.C. *Solitons and Nonlinear Wave Equations*. Academic Press, New York, 1982, 697 p.
- [20] Panin L.E., Mokrushnikov P.V., Kunitsyn V.G., Zaitsev B.N. The interaction mechanism of cortisol and catecholamines with structural components of erythrocyte membranes. *Journal of physical chemistry B*, 2010, **114**, P. 9462–9473.
- [21] Angles G., Dotson R., Bueche K., Pias S.C. Predicted Decrease in Membrane Oxygen Permeability with Addition of Cholesterol. *Adv. Exp. Med. Biol.*, 2017, **977**, P. 9–14.
- [22] Subczynski W.K., Widomska J., Mainali L. Factors Determining the Oxygen Permeability of Biological Membranes: Oxygen Transport Across Eye Lens Fiber-Cell Plasma Membranes. *Adv. Exp. Med. Biol.*, 2017, **977**, P. 27–34.
- [23] Widomska J., Raguz M., Subczynski W.K. Oxygen permeability of the lipid bilayer membrane made of calf lens lipids. *Biochim. Biophys. Acta*, 2007, **1768** (10), P. 2635–2645.
- [24] Subczynski W.K., Widomska J., Feix J.B. Physical properties of lipid bilayers from EPR spin labeling and their influence on chemical reactions in a membrane environment. *Free Radic. Biol. Med.*, 2009, **46** (6), P. 707–718.
- [25] Subczynski W.K., Raguz M., et al. Functions of cholesterol and the cholesterol bilayer domain specific to the fiber-cell plasma membrane of the eye lens. *J. Membr. Biol.*, 2012, **245** (1), P. 51–68.
- [26] Mainali L., Raguz M., O'Brien W.J., Subczynski W.K. Properties of membranes derived from the total lipids extracted from the human lens cortex and nucleus. *Biochim. Biophys. Acta*, 2013, **1828** (6), P. 1432–1440.
- [27] Khan N., Shen J., et al. Plasma membrane cholesterol: a possible barrier to intracellular oxygen in normal and mutant CHO cells defective in cholesterol metabolism. *Biochemistry*, 2003, **42** (1), P. 23–29.
- [28] Kawasaki K., Yin J.J., et al. Pulse EPR detection of lipid exchange between protein-rich raft and bulk domains in the membrane: Methodology development and its application to studies of influenza viral membrane. *Biophys. J.*, 2001, **80** (2), P. 738–748.
- [29] Mokrushnikov P.V., Panin L.E., et al. Interaction of corundum and quartz nanocrystals with erythrocyte membranes. *Biophysics*, 2011, **56** (6), P. 1074–1077.
- [30] Kozelskaya A.I., Panin A.V., et al. Morphological changes of the red blood cells treated with metal oxide nanoparticles. *Toxicology in Vitro*, 2016, **37**, P. 34–40.
- [31] Panin L.E., Mokrushnikov P.V., Kunitsyn V.G., Zaitsev B.N. Interaction mechanism of anabolic steroid hormones with structural components of erythrocyte membranes. *Journal of physical chemistry B*, 2011, **115**, P. 14969–14979.
- [32] Bagayev S.N., Zakharov V.N., et al. Transcapillary exchange regulation by pulse blood pressure. *Russian Journal of Biomechanics*, 2008, **12** (3), P. 7–14.
- [33] Mokrushnikov P.V., Dudarev A.N., et al. Effects of native and oxidized apolipoprotein A-I on lipid bilayer microviscosity of erythrocyte plasma membrane. *Journal Biochemistry (Moscow), Supplement Series A: Membrane and Cell Biology*, 2017, **11** (1), P. 48–53.
- [34] Mokrushnikov P.V. A Mechanism of the Interaction of Metal Oxide Nanoparticles with Biological Membranes. *Biophysics*, 2020, **65** (1), P. 65–69.
- [35] Popov A.L., Savintseva I.V., et al. Cytotoxicity analysis of gadolinium doped cerium oxide nanoparticles on human mesenchymal stem cells. *Nanosystems: physics, chemistry, mathematics*, 2018, **9** (3), P. 430–438.
- [36] Popov A.L., Savintseva I.V., et al. PVP-stabilized tungsten oxide nanoparticles (WO₃) nanoparticles cause hemolysis of human erythrocytes in a dose-dependent manner. *Nanosystems: physics, chemistry, mathematics*, 2019, **10** (2), P. 199–205.
- [37] Poteryaeva O.N., Russkikh G.S., et al. Hormonal status, lipid profile and membranes microviscosity of north residents. *Journal of Ural Medical Academic Science*, 2014, **2** (48), P. 149–152.
- [38] Mokrushnikov P.V., Osipova L.P., Gol'tsova T.V., Rozumenko A.A. Erythrocyte membranes microviscosity in the population of Samburg village Yamalo-Nenets Autonomous Okrug. *Yakut medical journal*, 2016, **2** (54), P. 15–16.
- [39] Mokrushnikov P.V., Panin L.E., et al. *Structural transitions in erythrocyte membranes (experimental and theoretical models)*. NGASU, Novosibirsk, 2019, 286 p.
- [40] Mokrushnikov P.V. *Mechanical Stresses in the Lipid Bilayer of Erythrocyte Membranes*. In: "Lipid Bilayers: Properties, Behavior and Interactions" edited by Mohammad Ashrafuzzaman, Nova Science Publishers, NY, 2019, P. 43–91.
- [41] Filippov A., Oradd G., Lindblom G. Lipid lateral diffusion in ordered and disordered phases in raft mixtures. *Biophys. J.*, 2004, **86**, P. 891–896.
- [42] Bagayev S.N., Fomin Yu.N., et al. Investigation of transcapillary exchange by the laser method. *Laser Physics*, 2005, **15** (9), P. 1292–1298.
- [43] Bagayev S.N., Zakharov V.N., et al. Investigation of the physical mechanisms of blood microcirculation and transcapillary exchange using a phase-sensitive laser method. *Russian Journal of Biomechanics*, 2006, **10** (3), P. 22–40.
- [44] Mokrushnikov P.V. The influence of δH on the surface tension of suspended erythrocytes. *The Siberian Scientific Medical Journal*, 2010, **1**, P. 38–46.

On the long-distance charge transport in DNA-like macromolecules

D. Chevizovich¹, A. V. Chizhov^{2,3}, Z. Ivić¹, A. A. Reshetnyak⁴

¹University of Belgrade, Vinča Institute of Nuclear Sciences,
Laboratory for Theoretical and Condensed Matter Physics,
P.O. BOX 522, Belgrade, 11001, Serbia

²Laboratory of Radiation Biology, Joint Institute for Nuclear Research,
Joliot-Curie, 6, Dubna, 141980, Russia

³Dubna State University, Universitetskaya, 19, Dubna, 141980, Russia

⁴Institute of Strength Physics and Materials Science SB RAS,
Academicheskoy ave., 2/4, Tomsk, 634021, Russia

cevizd@vinca.rs

PACS 87.15.hj, 05.60.Gg, 05.45.Yv, 87.10.-e,

DOI 10.17586/2220-8054-2021-12-1-32-41

In this paper, we investigate the possibility of stable migration of charge carriers over long distances in DNA-like macromolecular structures in the form of an adiabatic soliton and derive the conditions for the formation of solitons. We find two types of soliton solutions: symmetric and antisymmetric. Comparing the energy of both types of soliton solutions with the energy of free extra charge, we find the region of the system parameters in which the soliton states are more energetically favorable than the states of quasi-free charges. At the same time, which of the two mentioned soliton solutions corresponds to an energetically favorable state depends on the ratio of the energy parameters of the molecular structure.

Keywords: charge migration, DNA, soliton, adiabatic polaron, interchain coupling.

Received: 22 December 2020

Revised: 25 December 2020

1. Introduction

Deoxyribonucleic acid (DNA) is a stable macromolecular structure that carries the genetic information of living organisms. This molecule stores significant amounts of information that plays a key role in the functioning of a living cell, such as that related to the synthesis of vital proteins, for example. The primary structure of DNA consists of two polynucleotide chains, each of which is made up of a series of nucleotides linked to each other via phosphate PO_4 and hydroxyl OH groups, which are located on the sugar components. Specific nucleotide residues are purine and pyrimidine bases: adenine (A), guanine (G), thymine (T) and cytosine (C). The bases of one strand are linked to the complementary base belonging to other strand by a network of hydrogen bonds: adenine is linked to thymine (A–T) by double hydrogen bond, and guanine is linked to cytosine (G–C) by a triple hydrogen bond. In this way, a double-stranded DNA macromolecule is formed. The secondary structure of DNA is the double helix. For the biological functionality of DNA the primary and secondary structures are responsible [1, 2].

The appearance and migration of an extra charge in DNA can have a major impact on the functioning of this molecule [1, 3–7]. For example, one source of DNA damage can be the oxidative stress process and UV irradiation, when an electron is removed from nucleotide and an extra positive charge (hole) is created. A major target for oxidants is guanine, since it has the lowest ionization potential compared to other DNA bases. The oxidative stress

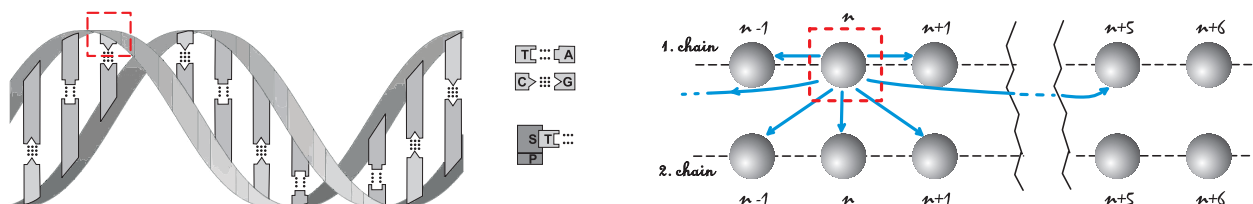


FIG. 1. Left panel: Schematic structure of the double helix DNA macromolecule. The backbone of the DNA strand is made of alternating phosphate and sugar groups. Right panel: Simplified structure of DNA-like macromolecule. Nucleotide bases are presented by spheres, regularly distributed along the strains. The most probable directions of charge migration from a given nucleotide (enabled by the overlapping of electron π -orbitals between neighboring nucleotides) are marked with arrows.

on guanine can reduce fidelity in the replication of DNA molecule and, consequently, such a process is the source of genomic mutations [2–4]. Further, the overlap of electronic π -orbitals of neighboring nucleotide groups will lead to delocalization of the charge along the chain and its capture by a neighboring nucleotide, having a lower oxidation potential. Because guanine has the lowest oxidation potential, the migration of the extra charge will occur along the guanines and all other nucleotides will represent potential barriers for its movement. Due to the fact that multi-guanine sequences have a lower ionization potential than a single guanine, the formed positive charge must migrate to guanine clusters, sometimes over long distances [1, 3, 4]. The mentioned mechanism can cause the appearance of the mutation not only at the place where the oxidative stress process occurred, but at any place along the DNA chain. Compared to the migration of positive charge that occurs in the process of the oxidative stress on guanine, much less is known about electron migration via base radical anions. The bases that are most easily reduced are T and C, whose reduction potentials are very similar. Therefore, it was assumed that the migration mechanism might involve all base pairs as charge carriers [3]. As a consequence, the question arises about the mechanism of the stable long range charge migration in DNA molecule, as well as in molecules that have a structure similar to DNA. Two mechanisms of charge migration in DNA are most often mentioned in the literature. The first is based on a tunnelling effect, but this mechanism cannot explain the long-distance charge migration. The second mechanism is based on the π -orbital overlap between neighboring nucleotide groups which leads to charge delocalization along the chain and its capture by the neighboring nucleotide [1, 3, 4, 8, 9]. It leads to charge migration as a series of successive jumps from one nucleotide base to the neighboring one. This mechanism corresponds to the transport of the Holstein nonadiabatic polaron, which, in principle, is able to explain the stable long-range charge transport [10, 11].

To form such a quasiparticle, the macromolecule must satisfy certain conditions for basic energy parameters of a structure: phonon energy, energy of the extra charge transitions from one to the adjacent structure elements (which is related to the values of the transfer integrals for the extra charge), and the strength of interaction of the extra charge with the phonon subsystem (which is related to the value of the particle–phonon coupling constant χ and determines the polaron binding energy E_b) [7, 10, 12–16]. Investigations devoted to the determination of the values of these parameters in DNA as well as in other biological macromolecules is still ongoing, but, according to various results, estimated values of these parameters (especially those concerning χ) explore the whole regime ranging from weak to strong coupling limit [17, 18]. Therefore, in addition to the hopping mechanism of the quasi-free and non-adiabatic (small) polaron migration, it is necessary to consider other possibilities.

In this paper, we consider the possibility that an induced charged particle (due to interaction with phonons of the structure) forms an adiabatic polaron (soliton). For this purpose, a simple molecular structure in the form of a double helix with identical structural elements is considered, in which the difference between different nucleotide residues is ignored and it is assumed that each of them can be a target for an extra charge with the same efficiency.

Here, we assume that the π -orbital overlap can occur not only between two adjacent structural elements belonging to the same chain (which causes migration along the same chain), but also between two structural elements belonging to different chains. The assumptions made allow us to obtain a simple analytical model that can give a much clearer picture of the charge migration process in DNA-like molecules, but can also serve as a starting point for more accurate numerical calculations.

2. The model

We consider an extra charge (exciton in general) in a structure consisting of the two coupled identical macromolecular chains, each of which is composed of $N \gg 1$ structural elements (molecular groups). The physics of charge migration in such a structure is usually described in the framework of common tight binding model, modified here in order to incorporate the interchain coupling of charge excitations on different chains. The helical structure is taken into account in such a way that we allow delocalization of the charge from the n -th node (where it is located) to the node that is close to its current position due to the helical form of the macromolecule ($n \pm \delta$ node). For DNA macromolecule, $\delta = 5$ (see Fig. 1). As a consequence, we allow the charge to be able to migrate from n -th to $n \pm 1$ node as well as from n -th to $n \pm \delta$ -node along the same chain. In addition, due to the spatial proximity, we allow the charge to migrate from n -th node of one chain to n -th and $n \pm 1$ -th nodes placed on another chain. We take into account the charge coupling with acoustic phonon modes. Only local exciton–phonon coupling is considered. Under these conditions, the model Hamiltonian has the form:

$$\hat{H} = \hat{H}_e + \hat{H}_{ph} + \hat{H}_{int}, \quad (1)$$

where the exciton Hamiltonian is:

$$\begin{aligned}\hat{H}_e = & \mathcal{E}_0 \sum_{n,j} \hat{a}_{n,j}^\dagger \hat{a}_{n,j} - J_1 \sum_{n,j} \hat{a}_{n,j}^\dagger (\hat{a}_{n+1,j} + \hat{a}_{n-1,j}) \\ & + J_\delta \sum_{n,j} \hat{a}_{n,j}^\dagger (\hat{a}_{n+\delta,j} + \hat{a}_{n-\delta,j}) + L_1 \sum_{n,j} \hat{a}_{n,j}^\dagger \hat{a}_{n,3-j} \\ & + L_2 \sum_{n,j} \hat{a}_{n,j}^\dagger (\hat{a}_{n+1,3-j} + \hat{a}_{n-1,3-j}),\end{aligned}\quad (2)$$

the phonon Hamiltonian is:

$$\hat{H}_{ph} = \sum_{q,j} \hbar\omega_q \hat{b}_{q,j}^\dagger \hat{b}_{q,j}, \quad (3)$$

and, finally, the Hamiltonian of exciton–phonon interaction is:

$$\hat{H}_{int} = \frac{1}{\sqrt{N}} \sum_{n,q,j} F_q e^{iqnR_0} \hat{a}_{n,j}^\dagger \hat{a}_{n,j} (\hat{b}_{q,j} + \hat{b}_{-q,j}^\dagger). \quad (4)$$

Here n labels the lattice sites along the strands, and it takes the values from $-N/2$ to $N/2$. Index j enumerates molecular strands ($j = 1, 2$), R_0 is the distance between two adjacent structural elements of the same chain, operators $\hat{a}_{n,j}^\dagger$ ($\hat{a}_{n,j}$) correspond to the exciton creation (annihilation) operators on n -th site of the j -th strand, and $\hat{b}_{q,j}^\dagger$ ($\hat{b}_{q,j}$) correspond to the phonon creation (annihilation) operators of the q -th phonon mode (q is the phonon wave vector) on the j -th strand. \mathcal{E}_0 is the energy of charge excitation on the corresponding (n, j) molecule, J_1 is the transfer integral between the neighboring molecules on the same strand (we adopt that $J_1 > 0$), while J_δ is the transfer integral between sites n and $n \pm \delta$ on the same strand, which originates from the helical structure of the macromolecule. Finally, L_1 and L_2 are the transfer integrals between the nearest ($(n, j) \leftrightarrow (n, 3-j)$) and the first neighboring ($(n, j) \leftrightarrow (n \pm 1, 3-j)$) molecules on different chains. In the case of Peierls dielectrics, it is commonly adopted that $L_1 < 0$, but in some substances it may be of the opposite sign or it may alternate along a chain [19]! Here, we adopt that J_1, J_δ, L_1 , and L_2 have the same values along the structure. We adopt that J_1 is positive, while other transfer integrals can be either positive or negative.

The interaction of the charge with the phonon subsystem is determined through the exciton–phonon coupling parameter F_q . The form of this parameter depends on the phonon's nature. In what follows, we will assume that the mechanical oscillations of both chains are mutually independent, which can be justified by the fact that the interaction energies of adjacent two structural elements of different molecular chains are significantly less than the interaction energies of two adjacent structural elements belonging to the same chain. In addition, we suppose that the electron interacts with acoustic phonon modes only [20–22]. For that reason, the exciton–phonon coupling parameter has the form: $F_q = 2i\chi\sqrt{\hbar/2M\omega_q} \sin(qR_0)$, where $\omega_q = \omega_0 \sin qR_0/2$ is the phonon frequency, and $\omega_0 = 2\sqrt{\kappa/M}$ is the characteristic phonon energy. Here, parameter χ is the strength of exciton–phonon interaction, κ is the stiffness of the particular chain, and M is the mass of the molecular group at the chain site n . Finally, we adopt the linear dispersion law for phonons: $\omega_q = c|q|$, where $c = \omega_0 R_0/2$.

In order to discuss the stable long-distance charge migration along the DNA structure, we suppose that, due to the charge–phonon interaction, the extra charge forms a soliton-like large polaron. The nature of the formed polaron quasiparticle, in the case of macromolecular structures, depends on the values of the basic energy parameters, such as the transfer integrals J_1 of the charge transfer between the nearest neighboring molecular group along the same chain (here, we suppose that the interchain transfer integral L is lower than J_1 and, consequently, its influence on the polaron formation is neglected), so called the polaron binding energy $E_b = 1/N \sum_q |F_q|^2 / \hbar\omega_q = 8\chi^2 / M\omega_0^2$, and the characteristic phonon energy $\hbar\omega_0$. The concept of a large polaron is applicable to structures that satisfy the following condition [7, 12, 13, 23, 24]:

$$2J_1 \gg E_b \gg \hbar\omega_0. \quad (5)$$

Here, the adiabatic condition ($2J_1 \gg \hbar\omega_0$) ensures that the fluctuations of charge and macromolecular subsystems are uncorrelated, and they can be neglected [7, 23, 24]. As a consequence, the mean values of the products of the charge and phonon operators may be factorized, and theoretical treatment can be carried out within the semiclassical approximation, for example, in the framework of the Pekar variational ansatz [12, 23, 24]. Physically, this means that the deformation of the lattice formed due to the interaction of excitons with the phonon subsystem is slow compared to the exciton subsystem, and it can not follow the quasiparticle motion (deformation of the lattice forms a “frozen” structure). The strong coupling condition $E_b \gg \hbar\omega_0$ ensures that the potential well that appears due to the lattice distortion (and which captures the extra charge) is deep enough to prevent the destruction of the formed polaron state

(it provides the polaron stability). On the other hand, this coupling should not be very strong in order to allow the polaron to span a large number of lattice sites, when continuum approximation is applicable. Such a condition is satisfied in the case when $2J_1 \gg E_b$ [12, 13]. On the basis of existing data, it seems that the mentioned criteria are satisfied for many biological macromolecular structures, including DNA. As usual, in most conjugated polymers, the typical values of the phonon energies are in the range 0.12 eV in polyacene molecule, 0.2 eV in double-strand polyacene, and 17 meV in alpha-helix structure. In the case of DNA, phonon energies are about $\hbar\omega_0 = 1$ meV [25]. Typical values for the intersite transfer integral are approximately 2.5 eV in conjugated polymers, while in alpha-helix its value is estimated on the order of few eV. According to different calculations, the values of the electron and hole transfer integrals in DNA are about $J_1 \approx 0.1$ eV [18, 26]. The values for the charge-phonon coupling parameter lie in the entire range from the weak to the strong charge-phonon coupling limit. They are estimated in several eV/Å: for polyacene $\chi \approx 4.1$ eV/Å, and for DNA χ ranges from 0.3 eV/Å to 2.3 eV/Å [17].

In order to describe the process of ST in structures consisting of two or more chains, it is necessary to introduce additional parameters which will take into account additional interactions between the chains and other interactions arising from additional geometric properties of the structure (helical geometry, for example): $p_1 = L_1/J_1$, $p_2 = L_2/J_1$, and finally, $p_\delta = J_\delta/J_1$.

To study the dynamics of our system, we use the simple time dependent extension of the Pekar variational ansatz, that allows the simple factorization of charge and phonon variables [23, 24, 27, 28]:

$$|\psi\rangle = \sum_{n,j} \psi_{n,j}(t) \hat{a}_{n,j}^\dagger |0\rangle_e \otimes |\beta(t)\rangle, \quad (6)$$

where $|\beta(t)\rangle = \prod_{q,j} |\beta_{q,j}(t)\rangle$ is the multimode phonon coherent state, and $|\beta_{q,j}(t)\rangle$ is the eigenfunction of the phonon annihilation operator: $\hat{b}_{q,j}(t) |\beta_{q,j}(t)\rangle = \beta_{q,j}(t) |\beta_{q,j}(t)\rangle$. Due to the conservation of the probability for the quasiparticle, exciton amplitudes are normalized. So that:

$$\sum_{n,j} |\psi_{n,j}(t)|^2 = 1. \quad (7)$$

The functions $\psi_{n,j}(t)$ and $\beta_{q,j}(t)$ are treated as dynamical variables. In order to find exciton and phonon amplitudes, as a first step we find the explicit form of the functional $\mathcal{H} = \langle \psi | \hat{H} | \psi \rangle$:

$$\begin{aligned} \mathcal{H} = & \mathcal{E}_0 \sum_{n,j} \psi_{n,j}^* \psi_{n,j} - J_1 \sum_{n,j} \psi_{n,j}^* (\psi_{n+1,j} + \psi_{n-1,j}) \\ & + J_\delta \sum_{n,j} \psi_{n,j}^* (\psi_{n+\delta,j} + \psi_{n-\delta,j}) + \sum_{q,j} \hbar\omega_q \beta_{q,j}^* \beta_{q,j} \\ & + L_1 \sum_{n,j} \psi_{n,j}^* \psi_{n,3-j} + L_2 \sum_{n,j} \psi_{n,j}^* (\psi_{n+1,3-j} + \psi_{n-1,3-j}) \\ & + \frac{1}{\sqrt{N}} \sum_{n,q,j} F_q e^{iqnR_0} \psi_{n,j}^* \psi_{n,j} (\beta_{q,j} + \beta_{-q,j}^*). \end{aligned} \quad (8)$$

Equations of motion for dynamical variables $\psi_{n,j}(t)$ and $\beta_{q,j}(t)$ are:

$$i\hbar\dot{\psi}_{n,j} = \frac{\partial \mathcal{H}}{\partial \psi_{n,j}^*}, \quad i\hbar\dot{\beta}_{q,j} = \frac{\partial \mathcal{H}}{\partial \beta_{q,j}^*}.$$

In the continuum limit:

$$\psi_{n,j}(t) \rightarrow \psi_j(x, t), \quad nR_0 \rightarrow x, \quad \sum_n \rightarrow \int \frac{dx}{R_0},$$

we have:

$$\begin{aligned} i\hbar\dot{\psi}_j(x, t) = & (\mathcal{E}_0 - 2J_1 + 2J_\delta) \psi_j(x, t) - (J_1 - \delta^2 J_\delta) R_0^2 \frac{\partial^2 \psi_j(x, t)}{\partial x^2} \\ & + L_2 R_0^2 \frac{\partial^2 \psi_{3-j}(x, t)}{\partial x^2} + (L_1 + 2L_2) \psi_{3-j}(x, t) \\ & + \frac{1}{\sqrt{N}} \sum_q F_q e^{iqx} \psi_j(x, t) (\beta_{q,j}(t) + \beta_{-q,j}^*(t)), \end{aligned} \quad (9)$$

and the equation of motion for the phonon amplitudes are:

$$i\hbar\dot{\beta}_{q,j}(t) = \hbar\omega_q\beta_{q,j}(t) + \frac{F_{-q}}{\sqrt{N}} \int_{-\infty}^{+\infty} \frac{dx}{R_0} e^{-iqx} |\psi_j(x, t)|^2. \quad (10)$$

In the obtained system of equations (9) and (10) we have coupled charge and vibrational amplitudes. Since our goal is to analyze the properties of the extra charge, the first step we must take is to eliminate from the Eq. (9) the variables that describe the phonon subsystem. Because we investigate the extra charge propagation in the form of a stable “wave pulse” (soliton form), we assume that the charge probability densities depend on t and x through coordinate $\xi = x - vt$: $|\psi(x, t)|^2 = |\psi(x - vt)|^2$, where v is the soliton velocity. In this case, Eq. (10) becomes an ordinary differential equation of the first order, and it can be easily integrated. The general solution of this equation has the form: $\beta_{q,j}(t) = \beta_{q,j}^{\text{homog}}(0)e^{-i\omega_q \cdot t} + \beta_{q,j}^{\text{coh}}(t)$. Here, the first term is the homogeneous solution corresponding to the incoherent part of lattice displacement coming from free lattice modes, and it can be disregarded in the adiabatic treatment [7, 29, 30]. Since we search for a stable stationary polaron solution, the main contribution to the polaron formation comes from the particular solution. The particular solution of the phonon equation of motion attains the form:

$$\beta_{q,j}^{\text{coh}}(t) = -\frac{1}{\sqrt{N}} \frac{F_{q,j}^*}{\hbar\omega_q} \frac{1}{1 - \frac{qv}{\omega_q}} \int \frac{dx}{R_0} e^{-iqx} |\psi_j(x, t)|^2. \quad (11)$$

After substitution of the obtained phonon amplitudes (11) into (9), we obtain the system of the two coupled nonlinear Schrödinger equations (NSE) for polaron amplitudes $\psi_1(x, t)$ and $\psi_2(x, t)$:

$$i\hbar\dot{\psi}_j = -(J_1 - \delta^2 J_\delta) R_0^2 \frac{\partial^2 \psi_j}{\partial x^2} + L_2 R_0^2 \frac{\partial^2 \psi_{3-j}}{\partial x^2} + (L_1 + 2L_2) \psi_{3-j} - \frac{2E_b}{1 - v^2/c^2} |\psi_j|^2 \psi_j. \quad (12)$$

Physically irrelevant term $(\mathcal{E}_0 - 2J_1 + 2J_\delta) \psi_j(x, t)$ is absorbed by the transformation $\psi_j(x, t) \rightarrow e^{(\mathcal{E}_0 - 2J_1 + 2J_\delta) \cdot t} \psi_j(x, t)$.

The resulting expression (12) depends on J_1 and J_δ only through the corrected transfer integral $J = J_1 - \delta^2 J_\delta$. Therefore, one can see that, in the framework of the presented model, J_δ corrects only the value of the exciton transfer integral J_1 . Since the overlap of the π -orbitals between the n -th and $n \pm \delta$ -th nodes in the chain is very small, the value of the corrected J is rather close to J_1 .

3. Soliton solutions

Thus, we have the system of two partial differential equations (12) for two unknown functions $\psi_1(x, t)$ and $\psi_2(x, t)$. Similar systems of equations have been studied in various problems, especially in biophysics and nonlinear optics [7, 31–34]. Apart from two trivial cases, namely, $\psi_1(x, t) \neq 0, \psi_2(x, t) = 0$ and $\psi_1(x, t) = 0, \psi_2(x, t) \neq 0$, the explicit solutions of such systems have not yet been fully examined, and they are generally unknown. Nevertheless, their properties may be examined by means of various approximate approaches. In this sense, the average profile approximation can be very useful as it allows analytical calculations, the accuracy of which has been demonstrated by comparison with numerical analysis [32–34]. The main idea of this approach is the assumption that the solutions of the coupled system of NSE are not substantially different from those of the uncoupled ones. Consequently, the stationary solutions of the above equations (12) can be sought in the form:

$$\psi_j(x, t) = A_j \cdot \underbrace{e^{i(kx - \Omega t)}}_{\psi(x, t)} \cdot \phi(x - vt) = A_j \psi(x, t). \quad (13)$$

Here, A_j is the real amplitude of the soliton propagating along the molecular chain j , k is the wave vector of the soliton carrier wave, Ω is the frequency of the carrier wave, v is the soliton speed. The real function $\phi(x - vt)$ is the envelope of the extra charge wave function, which we looking for in the form of a wave pulse. This means that the initial conditions for envelope function are (in the “moving” coordinate frame, where $\xi = x - vt$):

$$\begin{aligned} \lim_{\xi \rightarrow \pm\infty} \phi(\xi) &= \lim_{\xi \rightarrow \pm\infty} \frac{d\phi(\xi)}{d\xi} = 0, \\ \lim_{\xi \rightarrow 0} \phi(\xi) &= \phi_0, \quad \lim_{\xi \rightarrow 0} \frac{d\phi(\xi)}{d\xi} = 0. \end{aligned} \quad (14)$$

Since we accept the assumption that the DNA macromolecule is made up of two identical molecular strands, we can assume that the soliton wave has identical form on both macromolecular chains and it is $\psi(x, t)$ in (13). The normalization condition for the extra charge function in the continuum approximation becomes:

$$\sum_j \int_{-\infty}^{+\infty} \frac{dx}{R_0} \psi_j^*(x, t) \psi_j(x, t) = \sum_j A_j^2 \cdot \int_{-\infty}^{+\infty} \frac{d\xi}{R_0} \phi^2(\xi) = 1.$$

If we additionally require that the envelope of the electronic wave function is normalized, the normalization condition becomes:

$$\sum_j A_j^2 = 1, \quad \frac{1}{R_0} \int_{-\infty}^{+\infty} d\xi \phi^2(\xi) = 1. \quad (15)$$

So, relations (12), (13), (14) and (15) are the mathematical framework for our study on the possible existence of solitons in DNA-like macromolecular structures. Let us analyze these equations and see under what conditions soliton solutions can occur. After substituting (13) into (12) and separating the real and imaginary parts of obtained equations, from the imaginary part we find the set of algebraic equations for amplitudes A_1 and A_2

$$\begin{aligned} A_1 (\hbar v - 2kR_0^2 J) + A_2 \cdot 2kR_0^2 L_2 &= 0, \\ A_1 \cdot 2kR_0^2 L_2 + A_2 (\hbar v - 2kR_0^2 J) &= 0. \end{aligned} \quad (16)$$

The resulting system of algebraic equations has a nontrivial solution in the case when the determinant of the system is equal to zero. This condition yields two kinds of solutions, with the wave vector of the carrier wave in the form:

$$k = \frac{m^* v}{\hbar}, \quad (17)$$

where the parameter m^* can be considered as the soliton's effective mass. One of the solutions corresponds to the symmetric form for the amplitudes $A_1 = A_2 = 1/\sqrt{2}$, with the soliton's effective mass $m^* = \frac{\hbar^2}{2(J - L_2)R_0^2}$. Another solution corresponds to an antisymmetric representation for the amplitudes $A_1 = -A_2 = 1/\sqrt{2}$, with the soliton's effective mass $m^* = \frac{\hbar^2}{2(J + L_2)R_0^2}$.

The real part of Eq. (12) after substituting Eq. (13) into it determines the differential equation for the soliton envelope $\phi(x - vt)$, which, in the moving coordinate framework, attains the form:

$$\phi_{\xi\xi}(\xi) - \alpha\phi(\xi) + \gamma\phi^3(\xi) = 0, \quad (18)$$

where $\gamma = \frac{G}{2R_0^2(J - L_2)}$ with $G = \frac{2E_b}{1 - v^2/c^2}$, and $\alpha = k^2 + \frac{L - \hbar\Omega}{R_0^2(J - L_2)}$ in the case of the symmetric amplitudes, while, for the antisymmetric amplitudes, we have $\gamma = \frac{G}{2R_0^2(J + L_2)}$, $\alpha = k^2 - \frac{L + \hbar\Omega}{R_0^2(J + L_2)}$, and $L = L_1 + 2L_2$.

As we mentioned, the pulse shape of the charge envelope function can be expected under the boundary conditions (14). In both cases (symmetric and antisymmetric), the nonlinear differential equation (18) has the soliton solution when $\alpha > 0$ and $\gamma > 0$. In this case, we have the following soliton solution:

$$\phi(\xi) = \frac{\phi_0}{\cosh(\sqrt{\alpha}\xi)}, \quad \phi_0^2 = 2\alpha/\gamma, \quad (19)$$

where ϕ_0 is the soliton amplitude, and $\xi = x - vt$. In the case of the symmetric solution we have:

$$\begin{aligned} \phi_0^2 &= \frac{G}{16(J - L_2)}, \\ \alpha &= \frac{\gamma}{2} \cdot \phi_0^2 = \frac{G^2}{64R_0^2(J - L_2)^2}, \\ \hbar\Omega &= \frac{\hbar^2 v^2}{4R_0^2(J - L_2)} - \frac{G^2}{64(J - L_2)} + L, \end{aligned} \quad (20)$$

while in the antisymmetric case, we obtain:

$$\begin{aligned}\phi_0^2 &= \frac{G}{16(J + L_2)}, \\ \alpha &= \frac{\gamma}{2} \cdot \phi_0^2 = \frac{G^2}{64R_0^2(J + L_2)^2}, \\ \hbar\Omega &= \frac{\hbar^2 v^2}{4R_0^2(J + L_2)} - \frac{G^2}{64(J + L_2)} - L.\end{aligned}\tag{21}$$

Bearing in mind the definition of γ in (18), for $J > 0$, $J \gg |L_{1,2}|$, one can conclude that $v < c$ (“subsonic” soliton solution). It should be noted that the state of the considered system is determined by the set of parameters (E_b , J_1 , L_1 , L_2 , J_δ). These parameters depend on the physical properties of the macromolecule under consideration. In fact, the soliton’s velocity should be added to the parameters that determine the state of the system. This parameter is “external” in the sense that it does not depend on the physical properties of the macromolecule itself, but it is determined either by the environment (for example, by the fact that the ensemble of induced charges is in thermal equilibrium with the environment in which the macromolecule is placed), or by some other way (during a chemical reaction, during an experiment, etc.).

4. Energy spectra for soliton

4.1. Energy spectra of linear excitations

Let us now examine the energetic stability of the soliton solution. For this purpose, we have to find the soliton energies for all obtained solutions and compare them with the energy of the quasi-free exciton (charge) state, i.e. the energy corresponding to the functional \mathcal{H} , defined by (8), but in the absence of the exciton–phonon coupling. Let us first find the energy of free exciton states: setting $F_q = 0$, taking the exciton amplitudes in the form $\psi_j(x, t) = A_j \cdot e^{-\frac{i}{\hbar}\mathcal{E}(k)\cdot t + ikx}$ and put them into equation of motion for the exciton amplitude (9), we obtain the linear system of equations for amplitudes A_1 and A_2 in the form:

$$\begin{aligned}\left[\mathcal{E}(k) - \mathcal{E}_0 + 2J_1 \left(1 - \frac{R_0^2 k^2}{2} \right) - 2J_\delta \left(1 - \frac{\delta^2 R_0^2 k^2}{2} \right) \right] \cdot A_j \\ - \left[L_1 + 2L_2 \left(1 - \frac{R_0^2 k^2}{2} \right) \right] \cdot A_{3-j} = 0.\end{aligned}\tag{22}$$

It should be noted that k appearing in (22) is the wave vector of free quasiparticle in a periodic structure with the spatial period R_0 , and, consequently, $k \in [-\pi/R_0, \pi/R_0]$. This parameter should not be confused with the parameter of the same notation, defined by the relation (17), which represents the wave vector of the soliton carrier wave. The obtained system of equations has nontrivial solutions provided that the determinant of the system is equal to zero. From this condition, we find that the energy spectrum for quasi-free excitons has two bands:

$$\begin{aligned}\mathcal{E}_{A,S}^{free}(k) &= \mathcal{E}_0 - 2J_1 \left(1 - \frac{R_0^2 k^2}{2} \right) + 2J_\delta \left(1 - \frac{\delta^2 R_0^2 k^2}{2} \right) \\ &\mp \left[L_1 + 2L_2 \left(1 - \frac{R_0^2 k^2}{2} \right) \right].\end{aligned}\tag{23}$$

The sign “−” in (23) corresponds to the antisymmetric solution of (22) (denoted by A), while the sign “+” corresponds to the symmetric solution of (22) (denoted by S). We can see that the spectrum of the linear excitations splits into two bands: symmetric and antisymmetric ones, separated by the energy gap. The width of this gap depends on the transfer integrals L_1 and L_2 only. The corresponding eigenstates are the linear superpositions of the exciton states belonging to different strands. As a consequence, the quasi-free exciton states are hybrid states, fully delocalized, in which the particle probability density is uniformly distributed over both strands.

It is useful to express all energies in term of parameters $S = E_b/\hbar\omega_0$ and $B = 2J/\hbar\omega_0$. The bottom of the energy band of a quasi-free exciton, in the case of the exciton symmetric (antisymmetric) state (since $|L_2| < J_1$) is:

$$\begin{aligned}\bar{\mathcal{E}}_A^{free} &= \frac{\mathcal{E}_0}{\hbar\omega_0} - B(1 - p_\delta + p_1 + 2p_2), \\ \bar{\mathcal{E}}_S^{free} &= \frac{\mathcal{E}_0}{\hbar\omega_0} - B(1 - p_\delta - p_1 - 2p_2).\end{aligned}\tag{24}$$

Here, $\bar{\mathcal{E}}_{A,S}^{free} = \mathcal{E}_{A,S}^{free}/\hbar\omega_0$ is the bottom of the energy of the antisymmetric (symmetric) quasi-free exciton state, normalized by the characteristic phonon energy $\hbar\omega_0$.

4.2. Energy spectra of soliton

The mean value of the exciton Hamiltonian (2) in the continuum approximation is:

$$\begin{aligned} \mathcal{H}_e = \langle \psi | \hat{H}_e | \psi \rangle &= (\mathcal{E}_0 - 2J_1 + 2J_\delta) \sum_j \int \frac{dx}{R_0} |\psi_j|^2 \\ &- JR_0^2 \sum_j \int \frac{dx}{R_0} \left\{ \psi_j^* \frac{\partial^2 \psi_j}{\partial x^2} \right\} + (L_1 + 2L_2) \sum_j \int \frac{dx}{R_0} \left\{ \psi_j^* \psi_{3-j} \right\} \\ &+ L_2 R_0^2 \sum_j \int \frac{dx}{R_0} \left\{ \psi_j^* \frac{\partial^2 \psi_{3-j}}{\partial x^2} \right\} - \frac{2E_b}{1 - v^2/c^2} \sum_j \int \frac{dx}{R_0} |\psi_j|^4. \end{aligned} \quad (25)$$

After substitution (13) into (25), we express the mean value of the exciton Hamiltonian in terms of the soliton amplitudes A_j :

$$\begin{aligned} \mathcal{H}_e &= (\mathcal{E}_0 - 2J_1 + 2J_\delta) + (J_1 - \delta^2 J_\delta) R_0^2 k^2 \\ &+ \alpha (J_1 - \delta^2 J_\delta) R_0^2 - \frac{2\phi_0^4 \gamma R_0}{3\sqrt{\alpha}} (J_1 - \delta^2 J_\delta) \\ &+ \left[(L_1 + 2L_2) - L_2 R_0^2 k^2 - \alpha L_2 R_0^2 + \frac{2\phi_0^4 \gamma R_0}{3\sqrt{\alpha}} L_2 \right] \cdot \sum_j A_j A_{3-j} \\ &- \frac{4G}{3} \frac{\phi_0^4 \gamma R_0}{\sqrt{\alpha}} \sum_j A_j^4. \end{aligned} \quad (26)$$

To obtain the above equation, we used the results of the following integrals:

$$I_1 = \int_{-\infty}^{+\infty} \frac{d\xi}{R_0} \phi^2(\xi) = 1$$

(as a consequence of the normalization conditions),

$$I_2 = \int_{-\infty}^{+\infty} \frac{d\xi}{R_0} \phi(\xi) \phi_\xi(\xi) = 0, \quad I_3 = \int_{-\infty}^{+\infty} \frac{d\xi}{R_0} \phi^4(\xi) = \frac{4}{3} \cdot \frac{\phi_0^4}{R_0 \sqrt{\alpha}}, \quad I_4 = \int_{-\infty}^{+\infty} \frac{d\xi}{R_0} \phi(\xi) \phi_{\xi\xi}(\xi) = \frac{2}{3} \cdot \frac{\phi_0^4 \gamma}{R_0 \sqrt{\alpha}} - \alpha.$$

In the case of the antisymmetric solution, the soliton energy expressed in terms of the set of the basic system parameters, normalized to the energy $\hbar\omega_0$, in the ‘‘subsonic’’ limit ($v/c \ll 1$), is:

$$\begin{aligned} \bar{\mathcal{E}}_A^{sol} &= \left\{ \frac{\mathcal{E}_0}{\hbar\omega_0} - \frac{B}{2} (2 + p_1 + 2p_2) + \frac{S^2}{24B} \cdot \frac{1}{1 + p_2} - \frac{S^3}{3B^2} \cdot \frac{1}{(1 + p_2)^2} \right\} \\ &+ \frac{v^2}{c^2} \left\{ \frac{1}{8B} \cdot \frac{1}{1 + p_2} + \frac{S^2}{12B} \cdot \frac{1}{1 + p_2} - \frac{S^3}{B^2} \cdot \frac{1}{(1 + p_2)^2} \right\}. \end{aligned} \quad (27)$$

At the same time, the normalized energy of the symmetric soliton is:

$$\begin{aligned} \bar{\mathcal{E}}_S^{sol} &= \left\{ \frac{\mathcal{E}_0}{\hbar\omega_0} - \frac{B}{2} (2 - p_1 - 2p_2) + \frac{S^2}{24B} \cdot \frac{1}{1 - p_2} - \frac{S^3}{3B^2} \cdot \frac{1}{(1 - p_2)^2} \right\} \\ &+ \frac{v^2}{c^2} \left\{ \frac{1}{8B} \cdot \frac{1}{1 - p_2} + \frac{S^2}{12B} \cdot \frac{1}{1 - p_2} - \frac{S^3}{B^2} \cdot \frac{1}{(1 - p_2)^2} \right\}. \end{aligned} \quad (28)$$

The obtained relations (27) and (28) make it possible to analyze the energy stability of soliton solutions and, consequently, represent the basic result of the presented analysis. Comparing them with the corresponding energies of quasi-free excitons (24), one can conclude whether the formation of a soliton is more favorable in comparison with the state of a quasi-free charge from the energy point of view. For our purpose, it is important to investigate the values of the system parameters that provide the condition $E^{Sol} < E^{free}$ in the region where $B > S$. The results are shown in Figs. 2 and 3. The left panels of the figures demonstrate that the stable soliton solutions of extra charge can be formed in DNA-like structures with small values of $|p_1|$, i.e. $|L_1| \ll |J|$, and in which the adiabatic parameter B is not very much higher than the coupling constant S . Moreover, it can be seen that antisymmetric solitons are more favorable when the transfer integrals of the same strand J and different chains $L_{1,2}$ have the same signs ($p_{1,2} > 0$), while symmetric ones might be realized when their signs are different ($p_{1,2} < 0$).

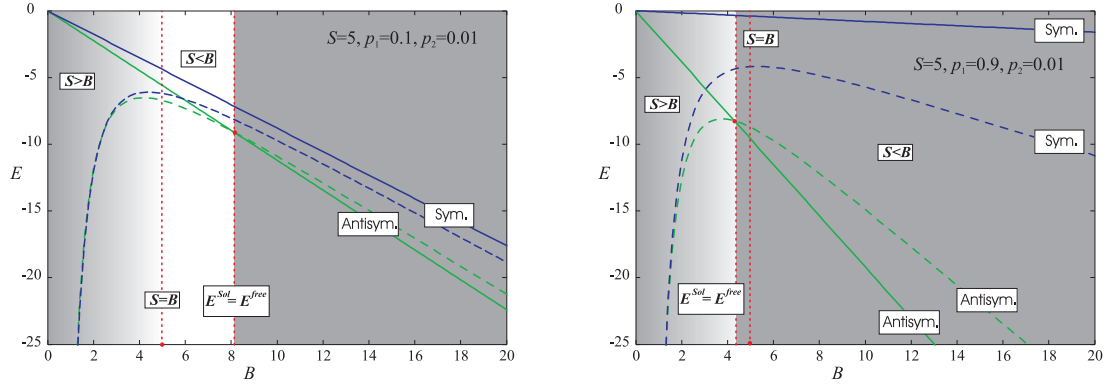


FIG. 2. The dependence of the soliton energy on the adiabatic parameter B for $S = 5$, $p_\delta = 0$, $v/c = 0$, and $p_1 = 0.1$, $p_2 = 0.01$ (left panel), $p_1 = 0.9$, $p_2 = 0.01$ (right panel). Full lines correspond to the energy of the free extra charge, while the dashed ones correspond to the energy of the soliton.

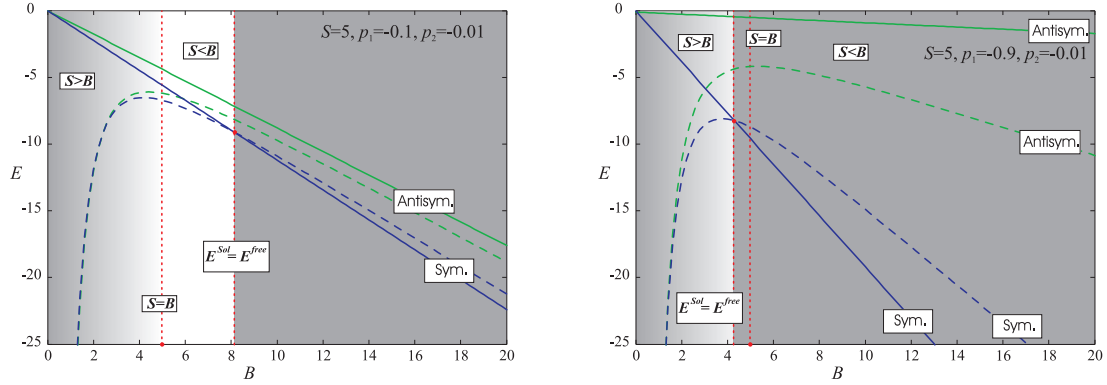


FIG. 3. The same as in Fig. 2 with $p_1 = -0.1$, $p_2 = -0.01$ on the left panel, and $p_1 = -0.9$, $p_2 = -0.01$ on the right panel.

5. Conclusion

In this paper, the possibility of stable long-distance migration of charge carriers in DNA-like macromolecular structures in the form of an adiabatic soliton was investigated. We derived the conditions for the formation of two types of soliton solutions: symmetric and antisymmetric. Analysis of the soliton energy spectra showed that when the transfer integrals of the same strand J and different chains $L_{1,2}$ have the same signs ($p_{1,2} > 0$), then it is more favorable for antisymmetric solitons, while the symmetric ones might be realized when signs of the transfer integrals are different ($p_{1,2} < 0$). It should also be noted that the formation of stable soliton solutions of both types can occur in structures only with small values of $|p_1|$, i.e. $|L_1| \ll |J|$, and in which the adiabatic parameter B is not very much higher than the coupling constant S . In addition, according to the presented model, the helical structure of DNA-like macromolecules does not have a large effect on the formation of solitons because of the large helix pitch. This only affects the effective decrease in the overlap integral J_1 , i.e. to the parameter B .

Acknowledgements

This work is partly supported by the Serbian Ministry of Education and Science under contracts Nos. III-45010 and OI-171009, the COST action No. 17139, and the Project within the Cooperation Agreement between the JINR, Dubna, Russian Federation, and Ministry of Education and Science of Republic of Serbia.

References

- [1] Dekker C., Ratner M.A. Electronic properties of DNA. *Phys. World*, 2001, **14** (8), P. 29–33.
- [2] Rakovic D. *Osnovi biofizike*. IASC&IEFPG, Beograd, 2008, 368 p. (in Serbian).
- [3] Giese B. Long-Distance Charge Transport in DNA: The Hopping Mechanism. *Acc. Chem. Res.*, 2000, **33** (9), P. 631–636.

- [4] Schuster G.B. Long-Range Charge Transfer in DNA: Transient Structural Distortions Control the Distance Dependence. *Acc. Chem. Res.*, 2000, **33** (4), P. 253–260.
- [5] Heller A. Spiers Memorial Lecture. On the hypothesis of cathodic protection of genes. *Faraday Discuss.*, 2000, **116**, P. 1–13.
- [6] Davydov A.S. Solitons in molecular systems. *Phys. Scr.*, 1979, **20** (2), P. 387–394.
- [7] Cevizovic D., Ivic Z., Przulj Z., Tekic J., Kapor D. Interchain coupling effects on large acoustic polaron in two parallel molecular chains. *Chem. Phys.*, 2013, **426**, P. 9–15.
- [8] Giese B. Electron transfer in DNA. *Curr. Opin. Chem. Biol.*, 2002, **6** (5), P. 612–618.
- [9] Hawke L.G.D., Kalosakas G., Simserides C. Electronic parameters for charge transfer along DNA. *Eur. Phys. J. E*, 2010, **32** (3), P. 291–306.
- [10] Holstein T. Studies of polaron motion: Part I. The molecular-crystal model. *Annals of Physics*, 1959, **8** (3), P. 325–342.
- [11] Cevizovic D., Ivic Z., Galovic S., Reshetnyak A., Chizhov A. On the vibron nature in the system of two parallel macromolecular chains: The influence of interchain coupling. *Phys. B*, 2016, **490**, P. 9–15.
- [12] Rashba E.I. Self-trapping of excitons. *Excitons*, North-Holland, Amsterdam: 1982. P. 543–602.
- [13] Brown D.W., Ivic Z. Unification of polaron and soliton theories of exciton transport. *Phys. Rev. B*, 1989, **40** (14), P. 9876–9887.
- [14] Emin D. Self-trapping in quasi-one-dimensional solids. *Phys. Rev. B*, 1986, **33** (6), P. 3973–3975.
- [15] Yarkony D., Silbey R. Variational approach to exciton transport in molecular crystals. *J. Chem. Phys.*, 1977, **67** (12), P. 5818–5827.
- [16] Lang I.G., Firsov Yu.A. Kinetic theory of semiconductors with low mobility. *Soviet Physics JETP*, 1963, **16** (5), P. 1301–1312.
- [17] Maniadis P., Kalosakas G., Rasmussen K.O., Bishop A.R. Polaron normal modes in the Peyrard–Bishop–Holstein model. *Phys. Rev. B*, 2003, **68** (17), 174304 (11 p).
- [18] Kalosakas G. Charge transport in DNA: Dependence of diffusion coefficient on temperature and electron-phonon coupling constant. *Phys. Rev. E*, 2011, **84** (5), 051905 (6 p).
- [19] Baeriswyl D., Maki K. Interchain order, soliton confinement, and electron-hole photogeneration in *trans*-polyacetylene. *Phys. Rev. B*, 1988, **38** (12), P. 8135–8141.
- [20] Davydov A.S. *Biologiya i Kvantovaya Mehanika*. Naukova Dumka, Kiev, 1979. P. 142–216. (In Russian).
- [21] Davydov A.S. The theory of contraction of proteins under their excitation. *J. Theor. Biol.*, 1973, **38** (3), P. 559–569.
- [22] Emin D. On the existence of free and self-trapped carriers in insulators: an abrupt temperature-dependent conductivity transition. *Adv. Phys.*, 1973, **22** (1), P. 57–116.
- [23] Pekar S.I. *Issledovaniya po elektronnoi teorii kristalov*. Gostekhizdat, Moskva, 1951. 256 p. (in Russian).
- [24] Pekar S.I. Autolocalization of the electron in an inertially polarizable dielectric medium. *Zh. Eksp. Teor. Fiz.*, 1946, **16**, P. 335–343.
- [25] Zdravkovic S., Sataric M. Parameter selection in a Peyrard–Bishop–Dauxois model for DNA dynamics. *Phys. Lett. A*, 2009, **373** (31), P. 2739–2745.
- [26] Kitoh–Nishioka H., Ando K. Charge–Transfer Matrix Elements by FMO-LCMO Approach: Hole Transfer in DNA with Parameter Tuned Range–Separated DFT. *Chem. Phys. Lett.*, 2015, **621**, P. 96–101.
- [27] Dauxois T., Peyrard M. *Physics of Solitons*. Cambridge University Press, Cambridge, 2004. 436 p.
- [28] Firsov Yu.A. *Polarons*. Ed. Yu. A. Firsov, Nauka, Moskva, 1975. 423 p. (in Russian).
- [29] Wang X., Brown D.W., Lindberg K., West B. Alternative formulation of Davydov theory of energy transport in biomolecular systems. *Phys. Rev. A*, 1988, **37** (9), P. 3557–3566.
- [30] Ivic Z., Zekovic S., Przulj Z. Radiative decay of the one-dimensional large acoustic polaron. *Phys. Lett. A*, 2002, **306** (2–3), P. 144–152.
- [31] Kevrekidis P.G., Frantzeskakis D.J., Carretero–Gonzalez R. (Eds.) *Emergent nonlinear phenomena in Bose–Einstein condensates*. Springer, Berlin, 2008. 405 p.
- [32] Kivshar Yu.S., Agrawal G.P. *Optical Solitons: From Fibers to Photonic crystals*. Academic Press, New York: 2003. 540 p.
- [33] Shi X., Malomed B.A., Ye F., Chen X. Symmetric and asymmetric solitons in a nonlocal nonlinear coupler. *Phys. Rev. A*, 2012, **85** (5), 053839 (8 p).
- [34] Akhmediev N.N., Ostrovskaya E.A. Elliptically polarized spatial solitons in cubic gyrotropic materials. *Opt. Commun.*, 1996, **132** (1–2), P. 190–204.

Domain wall evolution at nanowires in terms of 3D LLG equation initial-boundary problem

S. Leble

Immanuel Kant Baltic Federal University, 236041 Kaliningrad, Russia

lebleu@mail.ru

PACS 75.70.Cn, 05.30.d, 02.20.a**DOI 10.17586/2220-8054-2021-12-1-42-59**

A theory of a domain wall creation and propagation is built on a linearized version of the transformed Landau–Lifshitz–Gilbert equation. The Lakshmanan–Nakamura stereo-graphic transform, after extra exponential transformation, and, next – linearization partially save information of the original nonlinearity that allows one to keep the domain wall dynamics, form and properties. For cylindrical-symmetric wire geometry, the conventional orthonormal Bessel basis, combined with projecting operators technique applied to subspaces of directed propagation of domain walls is constructed. The physically significant problems of the dynamics switching at points far and close from a wire ends are formulated and its solutions are presented in the frame of the Fourier method. Stationary solutions are found and the wall structure along the wire and propagation plots are drawn.

Keywords: Nanowire magnetization dynamics, domain wall creation, Landau–Lifshitz–Gilbert equation, Lakshmanan–Nakamura transform, initial-boundary problem.

Received: 11 January 2021

Revised: 25 January 2021

1. Introduction

The problem of domain wall (DW) creation and propagation was studied in many sources theoretically, e.g. in [1], and experimentally [1–5]. Historically, starting from the seminal Brown paper [6]: “striking success of micromagnetics has been its contribution to the theory of single-domain particles.” The concept goes back to the 1930 paper of Frenkel–Dorfman [7], where they concluded from energy considerations that “if a particle is sufficiently small, it will not break up into domains but will be uniformly magnetized”.

Brown equations [6] has a direct link to Landau–Lifshitz ones [8], see, e.g. [9]. Touching the DW creation and dynamics paradigm, that in its minimal 1D version relates the one-domain case, we have a simple stationary problem solution [10]. In more complicated cases the Landau–Lifshitz–Gilbert (LLG) equation can describe the dynamics of a DW in the magnetic core of circular cross-section at amorphous nanowires and glass-coated bistable microwires [11, 12]. The DW propagation is characterized by high velocity propagation [13] and, therefore, there are several important applications [14, 15]. Numerous applications are realized for magnetoelectric effects that are observed in special structures [16]. For a general exposition of the field, look [17]. The 1D-2D-3D LLG equations may be derived from Heisenberg chain equation by transition to continuous description and Gilbert term account [18]. The anisotropy term may also be added as phenomenological.

The Landau–Lifshitz equation, by Lakshmanan–Nakamura stereographic projection of the unit sphere of spin onto a complex plane [19], with extra exponential map [20] is transformed to nonlinear complex equation, convenient for further DW dynamics investigations [11]. In [19] it is shown that the effect of the Gilbert damping term is a mere rescaling of time by a complex constant. There are important results obtained for the complete LLG equations, including exact solutions, for example, ones, built by the Hirota method [21] and by a direct method [20]. These solutions, however do not satisfy the boundary conditions, that follow from general electrodynamics. Let us mention that a presence of stress field in amorphous medium influence the DW dynamics [24] so as defects influence implies a modification of the LLG equation to account the magnetic inhomogeneities that manifests in a DW acceleration [25].

We consider a DW creation as Barkhausen jump [9, 22] example at nano- or microwire either far from end by pulse, or switching action of constant external magnetic field by the wires’ end. These two problems are formulated on base of the transformed 3DLLG equation and, next, linearized the result. The isotropic matter version of the LLG equation parameters are chosen as independent on coordinates; for this case of physics, review [11]. Such a choice of the equations’ approximation allows one to choose the correct boundary conditions in the context of the mentioned matter electrodynamics [23].

List the content by sections, in

- Sec. 2. We start with nonlinear LLG Lakshmanan–Nakamura-exponential transform, writing the resulting equation in cylindrical coordinates, convenient for circular cross-section wires geometry account.

- Sec. 3. Derivation of boundary conditions at surfaces of the cylindrical wire.
- Sec. 4. We write the problem solution in terms of cylindrical functions series by Fourier method (division of variables). We also derive and study the dispersion relations and build projecting operators on dispersion branches subspaces, related to DW propagation direction.
- Sec. 5. Two physically significant problems of a DW creation are formulated. The first is related to DW generation by a local pulse, by a few-turn coil, far from ends and, the second, study a DW generation at ends by homogeneous field switching on. For the first case, we formulate and solve a Cauchy problem with initial δ -distribution of magnetization.
- Sec. 6 is devoted to the stationary solution and magnetization vector presentation for a DW translation's mode. The result is illustrated by figures of the magnetization z -profiles.

2. 3DLLG for unit magnetization vector density

2.1. From Heisenberg chain equation to LLG

Starting from Heisenberg chain equations, with anisotropy and Gilbert terms account, we go to continuous description [18, 23], i.e. introduce the spin density field, re-scaled as $\vec{S} \rightarrow \vec{m}$, to unit magnetization vector field, having:

$$-\frac{\partial \vec{m}}{\partial t} = J \vec{m} \times \nabla^2 \vec{m} + K(\vec{m} \cdot \vec{n}) \vec{m} \times \vec{n} + \gamma \vec{m} \times \vec{H} - \alpha \vec{m} \times \frac{\partial \vec{m}}{\partial t}, \quad (1)$$

where $\gamma = \mu g \mu_B$ is gyromagnetic ratio, the product of the magnetic permeability μ , Landé g -factor and Bohr magneton μ_B ; $\alpha \ll 1$ is the damping Gilbert parameter, $J > 0$ is the isotropic exchange energy coupling constant, K is the strength of an effective easy-axis anisotropy, $\vec{H} = (0, 0, H)$ – applied longitudinal magnetic field, \vec{n} is the unit vector along z , see, e.g. [11].

2.2. Transformations of 3DLLG (1)

Following [11, 19] it is useful to introduce a complex variable $\Omega(\vec{r}, t)$ such that:

$$\exp(\Omega) = \frac{m^x + im^y}{1 + m^z}. \quad (2)$$

The structure of magnetization field then is defined mainly by the mentioned form of (2), while (1) transforms as:

$$(i + \alpha)\Omega_t + J\nabla^2\Omega + \left(K - J(\nabla\Omega)^2\right) \tanh\left(\frac{\Omega + \Omega^*}{2}\right) = \gamma H. \quad (3)$$

Such form yields a possibility to obtain interesting, physically reasonable particular solutions [11, 20]. Generally, the variable Ω is convenient to formulate an initial-boundary problem of a DW evolution, via an inversion of the transform (2). It opens the way to particular (in relation to LLG) linearization of the problem, that we study in this work.

Cylindrical variables for the Laplacian yields:

$$\nabla^2 = \Delta_{\perp} + \frac{\partial^2}{\partial z^2}, \quad (4)$$

where:

$$\Delta_{\perp} = \Delta_{\rho} + \frac{1}{\rho^2} \frac{\partial^2}{\partial \varphi^2}, \quad (5)$$

in which:

$$\Delta_{\rho} = \frac{1}{\rho} \frac{\partial}{\partial \rho} \rho \frac{\partial}{\partial \rho}. \quad (6)$$

The linearization of the equation (3) gives:

$$(\alpha + i)\Omega_t + J\nabla^2\Omega + K\Re\Omega = \gamma H. \quad (7)$$

Let us conventionally split the general solution $\Omega^i = \Omega' + \Omega^i$: to the general one Ω' for homogeneous equation:

$$(\alpha + i)\Omega'_t + J\nabla^2\Omega' + K\Re\Omega' = 0, \quad (8)$$

and a particular solution for the inhomogeneous one:

$$(\alpha + i)\Omega_t^i + J\nabla^2\Omega^i + K\Re\Omega^i = \gamma H. \quad (9)$$

3. On statement of problem. Boundary conditions. Transverse modes

3.1. Real/Imaginary parts division

3.1.1. *Homogeneous equation and magnetization field.* Let the solution of the homogeneous equation is presented as:

$$\Omega' = R + iS, \quad (10)$$

using the inverse to (2) relations we write:

$$\Re\Omega' = R = \ln\left(\frac{1 - m^z}{1 + m^z}\right) = \ln(1 - m^z) - \ln(1 + m^z), \quad (11)$$

$$\exp[2i\Im\Omega'] = \exp[2iS] = \frac{m^x + im^y}{m^x - im^y}.$$

3.1.2. *Boundary conditions for real and imaginary parts of Ω' .* Let us take a body of a magnetic surrounded by dielectric. The magnetization vector \vec{M} is introduced as:

$$\vec{B} = \vec{H} + 4\pi\vec{M}. \quad (12)$$

The continuity of the normal component of the vector \vec{B} yields:

$$H_{ni} + 4\pi M_{ni} = H_{ne} + 4\pi M_{ne}, \quad (13)$$

index "i" marks internal, "e" – external vectors with respect to an interface under consideration. Suppose the magnetization of the (external) medium, that is labeled by e , is zero, then:

$$H_{ni} + 4\pi M_{ni} = H_{ne}. \quad (14)$$

Similarly, from the continuity of the tangent component of the vector \vec{H} we derive that:

$$H_{ti} = B_{ti} - 4\pi M_{ti} = H_{te} = B_{te}. \quad (15)$$

For an isotropic paramagnetic inside the body $\vec{B}_i = \mu_i\vec{H}_i$, while for the external one $\vec{B} = \vec{H}$, hence:

$$\mu_i H_{ti} - 4\pi M_{ti} = H_{te} = H_{te}, \quad (16)$$

therefore:

$$\frac{4\pi}{\mu_i - 1} M_{ti} = H_{ti} = H_{te}, \quad (17)$$

$$M_{ti} = \frac{\mu_i - 1}{4\pi} H_{te}. \quad (18)$$

For the normal component, similarly:

$$B_{ne} = B_{ni} = H_{ni} + 4\pi M_{ni} = \mu_i H_{ni} = H_{ne}, \quad (19)$$

$$M_{ni} = (\mu_i - 1)H_{ni} = \frac{\mu_i - 1}{4\pi\mu_i} H_{ne}. \quad (20)$$

The relations (21) and (20) pave the way to a boundary conditions for magnetic moment formulation.

A ferromagnetic boundary vicinity is characterized by "incomplete" number of nearest neighbours and, hence, lower exchange forces sum. It is hence have properties of a paramagnetic layer [23].

For the case of a wire lying along z -axis in a solenoid with the magnetic field $\vec{H}||z$, co-axially, the normal component of \vec{M} is zero. Hence:

$$m_\rho|_{\rho=\rho_0} = 0.$$

The tangential components m_z, m_ϕ are proportional to external (solenoid) magnetic field. If the field is strictly parallel z ,

$$m_\phi|_{\rho=\rho_0} = 0.$$

If, however, on the basis of:

$$M_{ti} = \frac{\mu_i - 1}{4\pi} H_{te}, \quad (21)$$

taking $\mu_i - 1 \approx 0$ into account, by (11), we suppose:

$$\Re\Omega'(\varphi, \rho, z, t)|_{\rho=\rho_0} = R(\varphi, \rho_0, z, t) = 0, \quad (22)$$

where ρ_0 is the wire radius. Note, that nonzero condition may also be incorporated into the statement of problem.

4. Fourier method application

4.1. Division of variables

The basic system for the Re/Im, or R, S parts of the complex field Ω' reads:

$$\alpha R_t + KR + J\nabla^2 R = S_t, \quad (23)$$

$$R_t + \alpha S_t + J\nabla^2 S = 0. \quad (24)$$

It allows the division of variables, put $R = R_d + c.c.$, same for S :

$$R_d(\varphi, \rho, z, t) = \exp[i\nu\varphi]\Sigma(\rho) Z(z, t), S_d = \exp[i\nu\varphi]\Sigma(\rho) W(z, t), \quad (25)$$

which gives for (24):

$$\Sigma Z_t + \alpha \Sigma W_t + J \left(W \Delta_\rho \Sigma - W \frac{\nu^2}{\rho^2} \Sigma + \frac{\partial^2 W}{\partial z^2} \Sigma \right) = 0.$$

Next step, after division by ΣZ is:

$$\frac{Z_t}{Z} + \alpha \frac{W_t}{W} + J \left(\frac{\Delta_\rho \Sigma}{\Sigma} - \frac{\nu^2}{\rho^2} + \frac{W_{zz}}{W} \right) = 0. \quad (26)$$

The equation (23) transforms similarly.

4.2. Spectral problem

Conventionally, we put:

$$\frac{\Delta_\rho \Sigma}{\Sigma} - \frac{\nu^2}{\rho^2} = -\lambda,$$

or, rewriting it as:

$$\Delta_\rho \Sigma - \frac{\nu^2}{\rho^2} \Sigma = -\lambda \Sigma, \quad (27)$$

we arrive at the Bessel equation. We should add zero boundary conditions for Z at ρ_0 , see (22), having:

$$\Sigma(\rho_0) = 0. \quad (28)$$

Also, adding the finite-value condition at $\rho = 0$, we have the Bessel basis.

Otherwise, the standard manipulations yields:

$$\rho^2 \frac{\partial^2 \Sigma}{\partial \rho^2} + \rho \frac{\partial \Sigma}{\partial \rho} - \nu^2 \Sigma + \lambda \rho^2 \Sigma = 0, \quad (29)$$

denoting: $\lambda \rho^2 = r^2$, one goes to the Bessel equation for:

$$J_\nu(r) = J_\nu(\sqrt{\lambda} \rho). \quad (30)$$

If $\sqrt{\lambda} = \beta$

$$\int_0^{\rho_0} J_\nu(\beta_{\nu,n} \rho) J_\nu(\beta_{\nu,m} \rho) d\rho = N_{\nu n} \delta_{nm} \quad (31)$$

the spectrum $\beta_{\nu,m}(\rho_0)$, for each ν is determined by the equation:

$$J_\nu(\beta \rho_0) = 0, \quad \beta_{\nu,m}(\rho_0) \rho_0 = \epsilon_m(\nu), \quad (32)$$

therefore:

$$\lambda_{\nu,m} = \beta_{\nu,m}^2 = \frac{\epsilon_m^2(\nu)}{\rho_0^2}. \quad (33)$$

So, $\epsilon_m(\nu)$ are the zeros of the Bessel functions. In the case of $\nu = 0$, $\epsilon_1(0) \approx 2.4$, hence $\lambda_{0,1} = \frac{(2.4)^2}{\rho_0^2}$. Taking $\rho_0 =$

$100 \text{ nm} = 10^{-7} \text{ m}$, we get $\lambda_{0,1} = \frac{(2.4)^2}{10^{-14}} \approx 5.8 \times 10^{14}$. A method of the zeros evaluation for J_ν is suggested [26], where the values are also listed.

4.3. Unit expansion

Let us write the unit expansion, that is necessary for in-homogeneous (with nonzero rhs) equation (9) solution, using the Bessel function $J_0(r)$ as example. For the function $f(r)$, $r \in [0, 1]$, for $\nu = 0$, the following expansion is valid:

$$f(r) = \sum_{m=1}^{\infty} a_m J_0(\epsilon_m(0)r), \quad (34)$$

with the coefficients, defined by:

$$a_n = \frac{1}{N_{0n}} \int_0^1 f(r) J_0(\epsilon_n(0)r) r dr. \quad (35)$$

If $f(\rho) = 1$, $\rho \leq \rho_0$, one has:

$$a_n = \frac{1}{N_{0n}} \int_0^1 J_0(\epsilon_n(0)r) r dr. \quad (36)$$

By the textbook formula:

$$\int_0^a J_0(r) r dr = a J_1(a), \quad (37)$$

for $\epsilon_n(0) = \kappa$:

$$\int_0^a J_0(\kappa r) r dr = \frac{1}{\kappa^2} \int_0^{a/\kappa} J_0(r) r dr = \frac{a}{\kappa^3} J_1(a/\kappa). \quad (38)$$

For $a = 1$:

$$\int_0^1 J_0(\kappa r) r dr = \frac{1}{\kappa^3} J_1(1/\kappa) = \frac{J_1(\frac{1}{\epsilon_n(0)})}{\epsilon_n^3(0)}, \quad (39)$$

plugging it in (36) gives the expression for a_n

Generally, orthonormal basis consists of the functions:

$$\Sigma_\nu(\rho) = \frac{1}{\sqrt{N_{01}}} J_\nu(\sqrt{\lambda_{\nu,m}} \rho) = \frac{1}{\sqrt{N_{01}}} J_\nu\left(\frac{\epsilon_m(\nu)}{\rho_0} \rho\right). \quad (40)$$

For the equation (26), the relation (29) account yields:

$$Z_t + \alpha W_t + J(-\lambda W + W_{zz}) = 0. \quad (41)$$

Next, similarly, (23) reads:

$$\alpha Z_t + K Z + J(-\lambda Z + Z_{zz}) = W_t. \quad (42)$$

Multiplying (41) by α and subtracting, we have:

$$\alpha^2 W_t + J\alpha(-\lambda W + W_{zz}) - K Z - J(-\lambda Z + Z_{zz}) = -W_t.$$

Next, multiplying (42) by α and adding, gives:

$$(1 + \alpha^2) Z_t + J(-\lambda W + W_{zz}) + \alpha K Z + \alpha J(-\lambda Z + Z_{zz}) = 0.$$

Finally, we arrive at the system:

$$Z_t = \frac{J\lambda W - K Z \alpha - J W_{zz} - J\alpha Z_{zz} + J Z \alpha \lambda}{1 + \alpha^2}, \quad W_t = \frac{J Z_{zz} + K Z - J Z \lambda - J\alpha W_{zz} + J\alpha \lambda W}{1 + \alpha^2}, \quad (43)$$

which constitutes the mode evolution system. In matrix form it reads:

$$\begin{pmatrix} Z \\ W \end{pmatrix}_t = \frac{J}{1 + \alpha^2} \begin{pmatrix} -\frac{K}{J}\alpha - \alpha\partial_{zz} + \alpha\lambda & \lambda - \partial_{zz} \\ \partial_{zz} + \frac{K}{J} - \lambda & -\alpha\partial_{zz} + \alpha\lambda \end{pmatrix} \begin{pmatrix} Z \\ W \end{pmatrix}. \quad (44)$$

After Fourier transformation by z , in k -representation $Z \rightarrow \tilde{Z}, \dots$, the evolution in k -domain is described by:

$$\begin{pmatrix} \tilde{Z} \\ \tilde{W} \end{pmatrix}_t = \frac{J}{1 + \alpha^2} \begin{pmatrix} -w\alpha + \alpha k^2 + \alpha\lambda & \lambda + k^2 \\ -k^2 + w - \lambda & \alpha k^2 + \alpha\lambda \end{pmatrix} \begin{pmatrix} \tilde{Z} \\ \tilde{W} \end{pmatrix}, \quad (45)$$

where it is denoted: $w = \frac{K}{J}$.

4.4. On dispersion/attenuation

4.4.1. *Dispersion equation.* The dispersion equation reads:

$$\det \begin{pmatrix} -w\alpha + \alpha k^2 + \alpha\lambda - i\omega & \lambda + k^2 \\ -k^2 + w - \lambda & \alpha k^2 + \alpha\lambda - i\omega \end{pmatrix} = 0. \quad (46)$$

Let us denote $\lambda + k^2 = \mu$, $\alpha\mu - i\omega = \varkappa$, having:

$$\det \begin{pmatrix} -w\alpha + \varkappa & \mu \\ -\mu + w & \varkappa \end{pmatrix} = 0. \quad (47)$$

Solving the equation (47) with respect to ω , gives dispersion branches ω_{\pm} .

4.4.2. *Dispersion branches.* The roots of the quadratic Eq. (47) are expressed as:

$$\omega_{\pm} = \pm \frac{i}{2} \sqrt{4w(k^2 + \lambda) + w^2\alpha^2 - 4(k^2 + \lambda)^2} - \frac{1}{2}i\alpha(k^2 - w + \lambda). \quad (48)$$

If $4w(k^2 + \lambda) + w^2\alpha^2 - 4(k^2 + \lambda)^2 > 0$, the solution oscillates. The ω_{\pm} are complex if:

$$4w(k^2 + \lambda) + w^2\alpha^2 - 4(k^2 + \lambda)^2 < 0, \quad (49)$$

which gives damping contributions, eventual cut of guide propagation. Otherwise, the borders of the range are defined by:

$$4w(k^2 + \lambda) + w^2\alpha^2 - 4(k^2 + \lambda)^2 = 0,$$

the condition (49) holds if either

$$k^2 < \frac{w}{2} \left(1 - \sqrt{\alpha^2 + 1}\right) - \lambda < 0,$$

which is impossible for real k , or:

$$k^2 > \frac{w}{2} \left(1 + \sqrt{\alpha^2 + 1}\right) - \lambda. \quad (50)$$

4.5. Dynamical projectors

4.5.1. *Evolution operator in k -domain.* Returning to original form of the evolution operator:

$$L_k = \frac{J}{1 + \alpha^2} \begin{pmatrix} -\frac{K}{J}\alpha + \alpha k^2 + \alpha\lambda & \lambda + k^2 \\ -k^2 + \frac{K}{J} - \lambda & \alpha k^2 + \alpha\lambda \end{pmatrix},$$

denoting, as before, $w = \frac{K}{J}$, $\lambda + k^2 = \mu$, we arrive to more compact form, omitting the constant factor, that do not

contribute in the projectors (to eigen subspaces of L_k) expressions. We write:

$$L'_k = \begin{pmatrix} -w\alpha + \alpha\mu & \mu \\ w - \lambda & \alpha\mu \end{pmatrix}, \quad (51)$$

that enters the algorithm below, see the key formula (57).

4.5.2. *Eigenvector matrix.* The eigenvectors of (51) with unit lower component are evaluated as:

$$\left\{ \begin{array}{c} \frac{1}{2\mu - 2w} \left(w\alpha + \sqrt{w^2\alpha^2 + 4w\mu - 4\mu^2} \right) \\ 1 \end{array} \right\} \leftrightarrow \alpha\mu - \frac{1}{2}w\alpha - \frac{1}{2}\sqrt{w^2\alpha^2 + 4w\mu - 4\mu^2},$$

$$\left\{ \begin{array}{c} \frac{1}{2\mu - 2w} \left(w\alpha - \sqrt{w^2\alpha^2 + 4w\mu - 4\mu^2} \right) \\ 1 \end{array} \right\} \leftrightarrow \alpha\mu - \frac{1}{2}w\alpha + \frac{1}{2}\sqrt{w^2\alpha^2 + 4w\mu - 4\mu^2}.$$

Denoting:

$$q^2 = 4w(k^2 + \lambda) + w^2\alpha^2 - 4(k^2 + \lambda)^2, \quad p = 2\mu - 2w, \quad (52)$$

we write the eigenmatrix as:

$$\Psi = \begin{pmatrix} \frac{1}{p}(w\alpha + q) & \frac{1}{p}(w\alpha - q) \\ 1 & 1 \end{pmatrix}. \quad (53)$$

4.5.3. *Algorithm of projectors construction.* Denoting $\tilde{\Lambda} = \text{diag}\{\lambda_i\}$ the diagonal eigenvalue matrix, Ψ - eigenmatrix, we transform the eigenproblem in k -domain:

$$\tilde{L}\Psi = \Psi\tilde{\Lambda}, \quad (54)$$

that is, by the way, the definition of Ψ , too:

$$\tilde{L} = \Psi\tilde{\Lambda}\Psi^{-1}, \quad (55)$$

or, in components, it gives the spectral decomposition of the matrix \tilde{L} :

$$\tilde{L}_{ij} = \Psi_{ik}\tilde{\Lambda}_{kl}\Psi_{lj}^{-1} = \Psi_{ik}\lambda_k\Psi_{kj}^{-1} = \sum_k \lambda_k\Psi_{ik}\Psi_{kj}^{-1} = \sum_s \lambda_s(\tilde{P}^s)_{ij}. \quad (56)$$

Where \tilde{P}^s are the k -transforms of the dynamic projecting operators [27]:

$$(\tilde{P}^s)_{ij} = \Psi_{is}\Psi_{sj}^{-1}, \quad (57)$$

with the inverse to (53):

$$\Psi^{-1} = \begin{pmatrix} \frac{1}{2} \frac{p}{q} & \frac{1}{2q}(q - w\alpha) \\ -\frac{1}{2} \frac{p}{q} & \frac{1}{2q}(q + w\alpha) \end{pmatrix}.$$

Reading the relation (57), let us do the first step of the first projector construction in the form:

$$P^1 = \begin{pmatrix} \frac{w\alpha + q}{p} \\ 1 \end{pmatrix} \begin{pmatrix} \frac{1}{2} \frac{p}{q} & \frac{1}{2q}(q - w\alpha) \end{pmatrix} = \begin{pmatrix} \frac{1}{2q}(q + w\alpha) & \frac{1}{2pq}(q + w\alpha)(q - w\alpha) \\ \frac{1}{2} \frac{p}{q} & \frac{1}{2q}(q - w\alpha) \end{pmatrix}.$$

Acting by the projector P^1 to the basic vector gives:

$$\begin{pmatrix} \frac{1}{2q}(q + w\alpha) & \frac{1}{2pq}(q + w\alpha)(q - w\alpha) \\ \frac{1}{2} \frac{p}{q} & \frac{1}{2q}(q - w\alpha) \end{pmatrix} \begin{pmatrix} Z \\ W \end{pmatrix} =$$

$$\begin{pmatrix} \frac{1}{2} \frac{Z}{q}(q + w\alpha) + \frac{1}{2pq}W(q + w\alpha)(q - w\alpha) \\ \frac{1}{2} \frac{Z}{q} + \frac{1}{2q}W(q - w\alpha) \end{pmatrix} = \begin{pmatrix} \frac{(q + w\alpha)}{p}\Pi \\ \Pi \end{pmatrix},$$

where the notation for the new field Π is introduced:

$$\Pi = \frac{p}{2q}Z + \frac{q - w\alpha}{2q}W. \quad (58)$$

Going to the second step, in the direct analogy, we have:

$$P^2 = \begin{pmatrix} \frac{w\alpha - q}{p} \\ 1 \end{pmatrix} \begin{pmatrix} -\frac{1}{2} \frac{p}{q} & \frac{1}{2q} (q + w\alpha) \end{pmatrix} = \begin{pmatrix} \frac{1}{2q} (q - w\alpha) & -\frac{1}{2pq} (q + w\alpha) (q - w\alpha) \\ -\frac{1}{2} \frac{p}{q} & \frac{1}{2q} (q + w\alpha) \end{pmatrix},$$

acting by the projector P^2 to the basic vector gives:

$$\begin{pmatrix} \frac{1}{2q} (q - w\alpha) & -\frac{1}{2pq} (q + w\alpha) (q - w\alpha) \\ -\frac{1}{2} \frac{p}{q} & \frac{1}{2q} (q + w\alpha) \end{pmatrix} \begin{pmatrix} Z \\ W \end{pmatrix} = \begin{pmatrix} \frac{1}{2} \frac{Z}{q} (q - w\alpha) - \frac{1}{2pq} W (q + w\alpha) (q - w\alpha) \\ \frac{q + w\alpha}{2q} W - \frac{1}{2} Z \frac{p}{q} \end{pmatrix} = \begin{pmatrix} \frac{(q - w\alpha)}{p} \Lambda \\ \Lambda \end{pmatrix},$$

where the second field:

$$\Lambda = \frac{q + w\alpha}{2q} W - \frac{p}{2q} Z. \quad (59)$$

is introduced. The inverse to (58,59) reads as:

$$W = \Pi + \Lambda, \quad (60)$$

$$Z = \frac{1}{p} (-q\Lambda + q\Pi + w\alpha\Lambda + w\alpha\Pi). \quad (61)$$

4.5.4. *Evolution dynamics splitting.* Returning to the complete form of the evolution operator:

$$L_k = \frac{J}{1 + \alpha^2} \begin{pmatrix} -w\alpha + \alpha\mu & \mu \\ -\mu + w & \alpha\mu \end{pmatrix},$$

we define the evolution vector as:

$$\phi = \begin{pmatrix} Z \\ W \end{pmatrix},$$

having:

$$\phi_t = L_k \phi. \quad (62)$$

To split the problem, let us act by operators $P^{1,2}$ to Eq. (62), that commute with L_k . Hence. on a way to the variable Π we obtain:

$$P^s \phi_t = L_k P^s \phi,$$

while the right side for $s = 1$ gives:

$$L_k P^1 \phi = \frac{J}{1 + \alpha^2} \begin{pmatrix} -w\alpha + \alpha\mu & \mu \\ -\mu + w & \alpha\mu \end{pmatrix} \begin{pmatrix} \frac{(q + w\alpha)}{p} \Pi \\ \Pi \end{pmatrix} = \frac{J}{1 + \alpha^2} \begin{pmatrix} \mu\Pi - \frac{1}{p} \Pi (w\alpha - \alpha\mu) (q + w\alpha) \\ \alpha\mu\Pi + \frac{1}{p} \Pi (w - \mu) (q + w\alpha) \end{pmatrix}.$$

Reading the second line, we see, that:

$$\Pi_t = \frac{J}{1 + \alpha^2} \frac{-q\mu + w^2\alpha + qw + p\alpha\mu - w\alpha\mu}{p} \Pi = \beta\Pi, \quad (63)$$

where:

$$p = 2k^2 - 2w + 2\lambda, \quad \mu = \lambda + k^2, \quad \beta = J \frac{-q\mu + w^2\alpha + qw + p\alpha\mu - w\alpha\mu}{p(1 + \alpha^2)}.$$

Finally, the function:

$$\Pi = C \exp(\beta t) \quad (64)$$

solves the equation (63). Similar, for Λ -state, we evaluate:

$$L_k P^2 \phi = \frac{J}{1 + \alpha^2} \begin{pmatrix} -w\alpha + \alpha\mu & \mu \\ -\mu + w & \alpha\mu \end{pmatrix} \begin{pmatrix} -\frac{(q - w\alpha)}{p} \Lambda \\ \Lambda \end{pmatrix} = \begin{pmatrix} J\Lambda \frac{\mu}{\alpha^2 + 1} + J\Lambda(w\alpha - \alpha\mu) \frac{q - w\alpha}{\alpha^2 + 1} \\ J\alpha\Lambda \frac{\mu}{\alpha^2 + 1} - \frac{J}{p} \Lambda(w - \mu) \frac{q - w\alpha}{\alpha^2 + 1} \end{pmatrix},$$

which gives:

$$J\alpha\Lambda \frac{\mu}{\alpha^2 + 1} - \frac{J}{p} \Lambda(w - \mu) \frac{q - w\alpha}{\alpha^2 + 1} = \frac{J(q + p\alpha)\mu + w(\alpha w - q - \alpha\mu)}{\alpha^2 + 1} \Lambda,$$

arriving at the equation:

$$\Lambda_t = \frac{J(q + p\alpha)\mu + w(\alpha w - q - \alpha\mu)}{p(\alpha^2 + 1)} \Lambda = \eta \Lambda,$$

and its solution:

$$\Lambda = D \exp(\eta t),$$

where:

$$\eta = J \frac{(q + p\alpha)\mu + w(\alpha w - q - \alpha\mu)}{p(\alpha^2 + 1)}.$$

4.6. The solution of (45) pick up

4.6.1. *One-term Ω' .* For the reader's convenience, we reproduce the result of Fourier one-term contribution via: (25):

$\Sigma(\rho) = N_{\nu, m}^{-1/2} J_\nu(\frac{\epsilon_m(\nu)}{\rho_0} \rho)$, $\Omega' = R + iS$. We further skip the normalizing factor and c.c. term, having

$$R(\varphi, \rho, z, t) = \exp[i\nu\varphi] J_\nu(\frac{\epsilon_m(\nu)}{\rho_0} \rho) Z(z, t), \quad S = \exp[i\nu\varphi] J_\nu(\frac{\epsilon_m(\nu)}{\rho_0} \rho) W(z, t),$$

adding results yields:

$$\Omega'_{\nu m}(k) = R + iS = \exp[i\nu\varphi] J_\nu(\epsilon_m(\nu) \frac{\rho}{\rho_0}) (Z + iW). \quad (65)$$

Going to the Π, Λ variables, we transform:

$$Z + iW = \left(\frac{q + w\alpha}{p} + i \right) C \exp(\beta t) + \left(\frac{-q + w\alpha}{p} + i \right) D \exp(\eta t). \quad (66)$$

4.6.2. *Final expression.* Taking the expressions for parameters (52), we rewrite:

$$q = \sqrt{w^2 \alpha^2 + 4k^2 w - 4k^4 - 4 \frac{\epsilon_m^4}{\rho_0^4} + 4w \frac{\epsilon_m^2}{\rho_0^2} - 8k^2 \frac{\epsilon_m^2}{\rho_0^2}}, \quad (67)$$

$$p = 2k^2 - 2w + 2\lambda = 2k^2 - 2w + 2 \frac{\epsilon_m^2(\nu)}{\rho_0^2}, \quad (68)$$

which should be plugged in:

$$\begin{aligned} \beta &= J \frac{\mu(p\alpha - q - w\alpha) + w^2\alpha + qv}{p(1 + \alpha^2)}, \\ \eta &= J \frac{\mu(p\alpha + q - w\alpha) + w^2\alpha - qw}{p(1 + \alpha^2)}. \end{aligned} \quad (69)$$

For the *one-(transversal)-mode solution* at z -domain we obtain:

$$\Omega'_{\nu m}(z, t) =$$

$$N_{\nu, m}^{-1/2} J_\nu(\epsilon_m(\nu) \frac{\rho}{\rho_0}) e^{i\nu\phi} \int dk e^{-ikz} \left(\left(\frac{w\alpha + q}{p} + i \right) C e^{\beta t} + \left(\frac{w\alpha - q}{p} + i \right) D e^{\eta t} \right) + c.c. \quad (70)$$

5. Two problems

5.1. Initiation of DW in experiment

A comprehensive review on nanowires and nanotubes physics was published recently [28, 29]. It contains a description of the synthesis, magnetic properties and applications of magnetic cylindrical nanowires and nanotubes, including single domain wall statics and dynamics, with very rich set of references. By "nano" the authors conventionally consider diameters reasonably smaller than a micrometer. One possibility to govern magnetoresistance by light is studied theoretically in [30]. In a real experiments a DW creation is realized either in the vicinity of a distant point from the ends [5] or at the end point vicinity [31]. In the first case, the DW is excited by a few-turns coin, the measurement of its velocity is performed by similar coins shifted left and right, that pick up Faraday pulses. A similar approach is used to measure the velocity in the second case as well, as it allows one to estimate the DW length via the coin voltage form [31], The measurements of DW velocity exhibits conventionally a linear dependence on magnetic field [32], however the presence of magnetic inhomogeneities forces a DW acceleration [5, 25].

A statement of problem at a vicinity of a wire end implies account of so-called "stray field" [23].

5.2. Cauchy problem for a DW excitation far from ends

Let us consider the simplest case of complete cylindrical symmetry of solution, i.e. ϕ -independent solution, that fixes the case $\nu = 0$, taking the first Bessel mode, which determines the radial dependence.

As an initial condition, let us choose the delta-impulse posed at the $z = 0$ point, chosen far from a wire ends. It mimics the excitation of the DW pair by a current pulse at a few-turn coin. Omitting the Bessel function factor $J_0(\epsilon_1(0)\frac{\rho}{\rho_0})$ at (70), we impose the following condition:

$$\Omega''_{01}(z, 0) = \int dk \exp[-ikz] \left(\left(\frac{q + w\alpha}{p} + i \right) C + \left(\frac{-q + w\alpha}{p} + i \right) D \right) = \delta(z).$$

It yields:

$$\int dz \exp[ik'z] \int dk \exp[-ikz] \left(\left(\frac{q + w\alpha}{p} + i \right) C + \left(\frac{-q + w\alpha}{p} + i \right) D \right) = \int dz \exp[ik'z] \delta(z) = 1,$$

$$\left(\left(\frac{q(k) + w\alpha}{p(k)} + i \right) C + \left(\frac{-q(k) + w\alpha}{p(k)} + i \right) D \right) = 1.$$

It gives the following relations:

1. Zero imaginary part, that gives $D = -C$.
2. The real one reads: $C \frac{2q(k)}{p(k)} = 1$, or $C(k) = \frac{p(k)}{2q(k)}$.

Then, plugging the results into the relation (70), we arrive at:

$$\Omega''_{01}(z, t) = \frac{1}{2} \int dk \exp[-ikz] \left[\left(\frac{q + w\alpha}{q} + i \frac{p}{q} \right) \exp(\beta t) - \left(\frac{-q + w\alpha}{q} + i \frac{p}{q} \right) \exp(\eta t) \right].$$

Let us introduce new parameters: $A = \frac{J\alpha}{1 + \alpha^2} \frac{\mu(p - w) + w^2}{p}$, $B = \frac{Jq}{1 + \alpha^2} \frac{-\mu\alpha + w}{p}$, having:
 $\beta = A + B$, $\eta = A - B$.

Finally, in new notations,

$$\Omega''_{01}(z, t) = \frac{1}{2} \int dk \exp[-ikz + At] \left[\left(\frac{w\alpha}{q} + 1 + i \frac{p}{q} \right) \exp(Bt) - \left(\frac{w\alpha}{q} - 1 + i \frac{p}{q} \right) \exp(-Bt) \right].$$

The parameters in the approximation $\alpha \ll 1$, simplify as:

$$q = w \sqrt{\alpha^2 + 4 \frac{k^2}{w} - 4 \left(\frac{k^2}{w} \right)^2},$$

$$\mu = k^2 + \lambda_{0,1}, \quad \frac{p}{2w} = \frac{k^2}{w} + \frac{\lambda_{0,1}}{w} - 1,$$

$$A \approx J\alpha \frac{(k^2 + \lambda_{0,1})(2k^2 - 3w + 2\lambda_{0,1}) + w^2}{2k^2 - 2w + 2\lambda_{0,1}},$$

$$B \approx Jq \frac{-\mu\alpha + w}{p}.$$

The linearity of the equations allows one to build more general solution as the mode superposition.

5.3. DW dynamics, forced by magnetic field

5.3.1. *Inhomogeneous system.* Basic linear complex in-homogeneous equation is written as:

$$\mathcal{L}\Omega^l = (\alpha + i)\Omega_t^l + J\nabla^2\Omega^l + K\Re\Omega^l = \gamma H, \quad (71)$$

where: $\Omega^l = R^l + iS^l$, that, adding and subtracting results for real and imaginary parts, yields:

$$\begin{aligned} \left(\alpha + \frac{1}{\alpha}\right) S_t^l + J\nabla^2 S^l - \frac{1}{\alpha} K R^l + \frac{J}{\alpha} \nabla^2 R^l &= -\frac{\gamma}{\alpha} H, \\ \left(\alpha + \frac{1}{\alpha}\right) R_t^l + K R^l + J\nabla^2 R^l + \frac{1}{\alpha} J\nabla^2 S^l &= \gamma H. \end{aligned}$$

Simplifying for the case of small relaxation term, $\alpha \ll 1$, we arrive at the system:

$$\begin{aligned} R_t^l + \alpha K R^l + \alpha J\nabla^2 R^l + J\nabla^2 S^l &= \alpha\gamma H, \\ S_t^l + \alpha J\nabla^2 S^l - K R^l - J\nabla^2 R^l &= -\gamma H. \end{aligned}$$

Next, let us conventionally transform it to the matrix notation:

$$\begin{pmatrix} R^l \\ S^l \end{pmatrix}_t + \begin{pmatrix} \alpha K + \alpha J\nabla^2 & J\nabla^2 \\ -K - J\nabla^2 & \alpha J\nabla^2 \end{pmatrix} \begin{pmatrix} R^l \\ S^l \end{pmatrix} = \begin{pmatrix} \alpha\gamma H \\ -\gamma H \end{pmatrix}.$$

The general solution of the inhomogeneous system (c.c. and normalizing factor omitted) is given by two equalities:

$$R^l(\varphi, \rho, z, t) = \sum_{\nu, m} \exp[i\nu\varphi] J_\nu(\epsilon_m(\nu)r) Z_{m\nu}^l(z, t), \quad (72)$$

$$S^l = \sum_{\nu, m} \exp[i\nu\varphi] J_\nu(\epsilon_m(\nu)r) W_{m\nu}^l(z, t). \quad (73)$$

Putting unit expansion at r.h.s., for example, for a given ν :

$$H(z, t) = \sum_{m=1} a_{m\nu}(z, t) J_\nu(\epsilon_m(\nu)r) \exp[i\nu\varphi], \quad (74)$$

we arrive at the two-component inhomogeneous system, transformed to matrix form. For such a transverse mode, the system reads:

$$\begin{pmatrix} Z_{m\nu}^l(z, t) \\ W_{m\nu}^l(z, t) \end{pmatrix}_t + \alpha J \begin{pmatrix} w - \lambda_{m\nu} + \partial_{zz} & \frac{1}{\alpha}(-\lambda_{m\nu} + \partial_{zz}) \\ \lambda_{m\nu} - \partial_{zz} - \frac{w}{\alpha} & -\lambda_{m\nu} + \partial_{zz} \end{pmatrix} \begin{pmatrix} Z_{m\nu}^l(z, t) \\ W_{m\nu}^l(z, t) \end{pmatrix} = \begin{pmatrix} \alpha\gamma a_{m\nu}(z, t) \\ -\gamma a_{m\nu}(z, t) \end{pmatrix}.$$

5.3.2. *Inhomogeneous system projecting.* Now, it is convenient to apply projecting operators, in k -domain, putting:

$$a_{m\nu}(z, t) = \int dk \exp[-ikz] \tilde{a}_{m\nu}(k, t), \quad (75)$$

and, similar to homogeneous case, it is written:

$$\begin{pmatrix} \tilde{Z}_{m\nu}^l(k, t) \\ \tilde{W}_{m\nu}^l(k, t) \end{pmatrix}_t + \alpha J \begin{pmatrix} w - \lambda_{m\nu} - k^2 & \frac{1}{\alpha}(-\lambda_{m\nu} - k^2) \\ \lambda_{m\nu} + k^2 - \frac{w}{\alpha} & -\lambda_{m\nu} - k^2 \end{pmatrix} \begin{pmatrix} \tilde{Z}_{m\nu}^l(k, t) \\ \tilde{W}_{m\nu}^l(k, t) \end{pmatrix} = \begin{pmatrix} \alpha\gamma \tilde{a}_{m\nu}(k, t) \\ -\gamma \tilde{a}_{m\nu}(k, t) \end{pmatrix}. \quad (76)$$

Denoting again, $\lambda_{m\nu} + k^2 = \mu$, we simplify the evolution operator for the approximate system as:

$$L = \alpha J \begin{pmatrix} w - \mu & -\frac{\mu}{\alpha} \\ \mu - \frac{w}{\alpha} & -\mu \end{pmatrix}. \quad (77)$$

Let us show Maple-made eigenvectors and eigenvalues:

$$\left\{ \begin{array}{c} -\frac{w\alpha - \sqrt{w^2\alpha^2 + 4w\mu - 4\alpha\mu^2}}{2w - 2\alpha\mu} \\ 1 \end{array} \right\} \leftrightarrow \frac{1}{2\alpha^2} (w\alpha^2 - 2\alpha^2\mu) - \frac{1}{2\alpha} \sqrt{w^2\alpha^2 + 4w\mu - 4\alpha\mu^2},$$

$$\left\{ \begin{array}{c} -\frac{w\alpha + \sqrt{w^2\alpha^2 + 4w\mu - 4\alpha\mu^2}}{2w - 2\alpha\mu} \\ 1 \end{array} \right\} \leftrightarrow \frac{1}{2\alpha} \sqrt{w^2\alpha^2 + 4w\mu - 4\alpha\mu^2} + \frac{1}{2\alpha^2} (w\alpha^2 - 2\alpha^2\mu).$$

Going to the more compact form, we denote:

$$-\frac{w\alpha}{2w - 2\alpha\mu} \left(1 - \sqrt{1 + \frac{4\mu}{w\alpha^2} - \frac{4\mu^2}{w^2\alpha}} \right) = r(1 - s),$$

where:

$$r = -\frac{w\alpha}{2w - 2\alpha\mu}, \quad s = \sqrt{1 + \frac{4\mu}{w\alpha^2} - \frac{4\mu^2}{w^2\alpha}}. \quad (78)$$

5.3.3. *The projectors and its application.* The projector matrices are built by formula: (57) on base of the eigenmatrix of the evolution operator L , see (77)

$$\Psi = \begin{pmatrix} r(1 - s) & r(1 + s) \\ 1 & 1 \end{pmatrix},$$

and its inverse:

$$\begin{pmatrix} -\frac{1}{2rs} & \frac{1}{2s}(s+1) \\ \frac{1}{2rs} & \frac{1}{2s}(s-1) \end{pmatrix}.$$

We write both projecting matrices as:

$$\pi_1 = \begin{pmatrix} r(1 - s) \\ 1 \end{pmatrix} \begin{pmatrix} -\frac{1}{2rs} & \frac{1}{2s}(s+1) \end{pmatrix} = \begin{pmatrix} \frac{1}{2s}(s-1) & -\frac{1}{2s}r(s^2-1) \\ -\frac{1}{2rs} & \frac{1}{2s}(s+1) \end{pmatrix},$$

$$\pi_2 = \begin{pmatrix} r(1 - s) \\ 1 \end{pmatrix} \begin{pmatrix} \frac{1}{2rs} & \frac{1}{2s}(s-1) \end{pmatrix} = \begin{pmatrix} -\frac{1}{2s}r(s-1) & -\frac{1}{2s}r(s-1)^2 \\ \frac{1}{2rs} & \frac{1}{2s}(s-1) \end{pmatrix}.$$

The action of $\pi_{1,2}$ to the matrix equation (76), using the shorthand for the evolution vector:

$$\begin{pmatrix} \tilde{Z} \\ \tilde{W} \end{pmatrix},$$

gives:

$$\alpha J \begin{pmatrix} w - \mu & -\frac{\mu}{\alpha} \\ \mu - \frac{w}{\alpha} & -\mu \end{pmatrix} \begin{pmatrix} \frac{1}{2s}(s-1) & -\frac{1}{2s}r(s^2-1) \\ -\frac{1}{2rs} & \frac{1}{2s}(s+1) \end{pmatrix} \begin{pmatrix} \tilde{Z} \\ \tilde{W} \end{pmatrix} =$$

$$\begin{pmatrix} \frac{1}{2s}\tilde{Z}(s-1) - \frac{1}{2s}r\tilde{W}(s^2-1) \\ \frac{1}{2s}\tilde{W}(s+1) - \frac{1}{2rs}\tilde{Z} \end{pmatrix}.$$

The conventional notation:

$$\frac{(s+1)}{2s}\tilde{W} - \frac{1}{2rs}\tilde{Z} = \pi, \quad (79)$$

gives for the upper component, proportional to π : $-(s-1)r\pi$. The projecting operator at z -domain is the integral operator with the kernel, that is expressed via r, s , as well as the formula for π is built as integral transform [27].

Approximate equations for long wave range (small k) is obtained by expansion the matrix elements of π in k - power series.

5.4. Relaxation equation in k -domain

The result in terms of the new variable π , see (79), we obtain, introducing the shorthand $\tilde{a}_{m\nu}(k, t) = a$, whence the equation (76) projection reads as:

$$\alpha J \begin{pmatrix} w - \mu & -\frac{\mu}{\alpha} \\ \mu - \frac{w}{\alpha} & -\mu \end{pmatrix} \begin{pmatrix} -(s-1)r\pi \\ \pi \end{pmatrix} = \begin{pmatrix} -\pi J\mu - \pi Jr\alpha(w - \mu)(s-1) \\ -\pi J\alpha\mu - \pi Jr\alpha\left(\mu - \frac{w}{\alpha}\right)(s-1) \end{pmatrix} =$$

$$\begin{pmatrix} \frac{1}{2s}(s-1) & -\frac{1}{2s}\frac{r}{s}(s-1)(s+1) \\ -\frac{1}{2rs} & \frac{1}{2s}(s+1) \end{pmatrix} \begin{pmatrix} \alpha\gamma a \\ -\gamma a \end{pmatrix} =$$

$$\begin{pmatrix} \frac{1}{2} \frac{a}{q} \alpha \gamma (s-1) + \frac{1}{2} \frac{a}{s} r \gamma (s-1)(s+1) \\ -\frac{1}{2} \frac{a}{s} \gamma (s+1) - \frac{1}{2} \frac{a}{rs} \alpha \gamma \end{pmatrix}.$$

Plugging the expression for π (79) one arrives at the *relaxation equation*:

$$\pi_t + J(-\alpha\mu - sw + s\alpha\mu + rsw - rs\alpha\mu)\pi = -\frac{1}{2}\gamma \frac{r + \alpha + rs}{sr} a.$$

Denoting:

$$o = J(-\alpha\mu - sw + s\alpha\mu + rsw - rs\alpha\mu), \quad h = -\frac{1}{2}\gamma \frac{r + \alpha + rs}{rs} a, \quad (80)$$

where h is proportional to magnetic field, see (74). We transform:

$$\pi_t + o\pi = h, \quad e^{-ot} (\pi e^{ot})_t = h,$$

having the solution for time-dependent homogeneous magnetic field switching at k -domain:

$$\pi e^{ot} = \int_0^t h(\tau) e^{o\tau} d\tau, \quad \pi = e^{-ot} \int_0^t h(\tau) e^{o\tau} d\tau.$$

For the constant magnetic field $h(\tau) = h\theta(\tau)$ and the zero initial condition gives:

$$\pi = e^{-ot} \int_0^t h e^{o\tau} d\tau = \frac{h}{o} (1 - e^{-ot}), \quad (81)$$

then, for a real o , o^{-1} is relaxation time of k -mode.

5.4.1. *Back to the z -domain.* The inverse Fourier transform gives:

$$\Pi_{m\nu}(z, t) = \frac{h}{2\pi} \int dk \exp[-ikz] \frac{(1 - e^{-o(k)t})}{o(k)}.$$

Plugging $r = -\frac{w\alpha}{2w - 2\alpha\mu}$, $\mu = \lambda_{m\nu} + k^2$ into o , we obtain the frequency:

$$o = -\frac{1}{2} J\alpha (-w + 2\lambda_{m\nu} + sw + 2k^2). \quad (82)$$

The dependence of o on k^2 for real s is presented at Fig. 1, and, at the range of imaginary s at Fig. 2. The "left" variable is introduced in similar way via the projecting by π_2 .

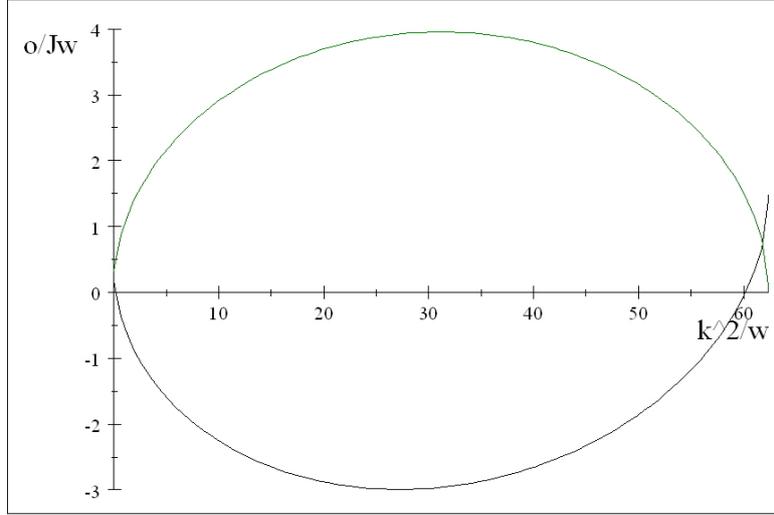


FIG. 1. The dependence of o/K on k^2/w (black) is presented at range of real root expression (green) for the values of parameters $\nu = 0, m = 1$.

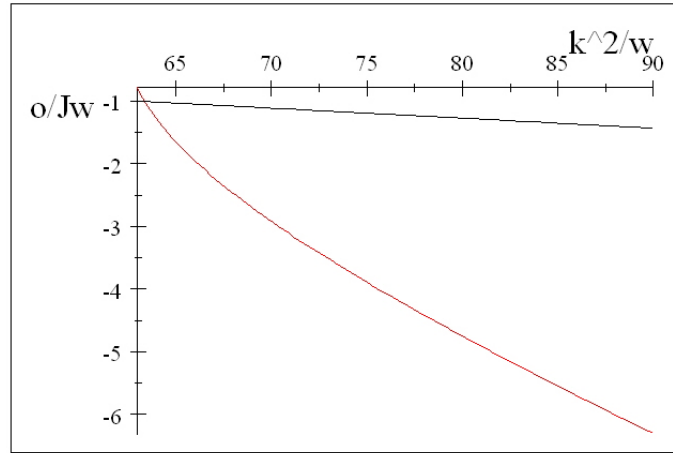


FIG. 2. The dependence of the real part of o/K on k^2/w (black) and its imaginary part (red) is presented at range of imaginary root expression for the same parameters values.

6. Stationary solution

6.1. Homogeneous equation

Stationary solutions for $\alpha \ll 1$ of the system:

$$Z_t = J\lambda W - KZ\alpha - JW_{zz} - J\alpha Z_{zz} + JZ\alpha\lambda,$$

$$W_t = JZ_{zz} + KZ - JZ\lambda - J\alpha W_{zz} + J\alpha\lambda W,$$

is conventionally expressed in terms of the coordinate $\xi = z - ct$. We write: $Z_t = -cZ_\xi$, $Z_{zz} = Z_{\xi\xi}$, and get

$$-cZ_\xi = J\lambda W - KZ\alpha - JW_{\xi\xi} - J\alpha Z_{\xi\xi} + JZ\alpha\lambda,$$

$$-cW_\xi = JZ_{\xi\xi} + KZ - JZ\lambda - J\alpha W_{\xi\xi} + J\alpha\lambda W,$$

which is the system of linear ODE. Its solution is searched by plugging the functions: $Z = A \exp(b\xi)$, $W = B \exp(b\xi)$ into the system, having:

$$-cbA = J\lambda B - KA\alpha - Jb^2B - J\alpha b^2A + JA\alpha\lambda, \quad (83)$$

and:

$$-cbB = Jb^2A + KA - J\lambda A - J\alpha b^2B + J\alpha\lambda B. \quad (84)$$

Solving the: equation (83) with respect to B , gives for $b^2 \neq \lambda$:

$$B = \frac{1}{J\lambda - Jb^2} (AK\alpha - Abc - AJ\alpha\lambda + AJb^2\alpha).$$

Next, if, $-J\lambda + Ja^2 \neq 0$, plugging B in (84) yields:

$$J^2b^4\alpha^2 + J^2b^4 - 2J^2b^2\alpha^2\lambda - 2J^2b^2\lambda + J^2\alpha^2\lambda^2 + J^2\lambda^2 - 2Jb^3c\alpha + KJb^2\alpha^2 + KJb^2 + 2Jbc\alpha\lambda - KJ\alpha^2\lambda - KJ\lambda + b^2c^2 - Kbc\alpha = 0.$$

From this equation it follows the relation, that determine link between the velocity of the k -mode c and b . Solving it with respect to c we write:

$$c = \frac{1}{2b} \left(K\alpha - 2J\alpha\lambda + 2Jb^2\alpha \pm \sqrt{-4J^2\lambda^2 + K^2\alpha^2 - 4J^2b^4 + 8J^2b^2\lambda + 4JK\lambda - 4JKb^2} \right).$$

Plugging Z, W into the expression for Ω , we write the transverse mode term as:

$$Z + iW = A \exp(b\xi) \left[1 + \frac{i}{J\lambda - Jb^2} (K\alpha - bc - J\alpha\lambda + Jb^2\alpha) \right]. \quad (85)$$

We denote the roots of the under-square-root bi-quadratic expression as:

$$\frac{1}{2} \left(\lambda - \sqrt{\lambda^2 - 2J\lambda^2 + J^2\lambda^2 + K^2 + \frac{K^2\alpha^2}{J} + 2K\lambda - 2JK\lambda + J\lambda - K} \right) = d_1, \quad (86)$$

$$\frac{1}{2} \left(\lambda + \sqrt{\lambda^2 - 2J\lambda^2 + J^2\lambda^2 + K^2 + \frac{K^2\alpha^2}{J} + 2K\lambda - 2JK\lambda + J\lambda - K} \right) = d_2, \quad (87)$$

arriving at:

$$c = -\frac{1}{2b} \left(K\alpha - \sqrt{-4J(b^2 - d_1)(b^2 - d_2)} - 2J\alpha\lambda + 2Jb^2\alpha \right).$$

We see, that the rhs is real, if b^2 lies between the roots $d_{1,2}$. If the roots are both positive, the case takes place for a real b , otherwise b may be as real for $b^2 > 0$, as imaginary, if $b^2 < 0$. For a convenience of plotting, we rearrange the formula for the velocity as:

$$\frac{c}{b} = -\frac{d_1}{2b^2} \left(\frac{K\alpha}{d_1} - \sqrt{4J \left(\frac{b^2}{d_1} - 1 \right) \left(\frac{d_2}{d_1} - \frac{b^2}{d_1} \right)} - \frac{2J\alpha\lambda}{d_1} + 2J\alpha \frac{b^2}{d_1} \right). \quad (88)$$

The plot of $\frac{c}{b}$ as the function of $\frac{b^2}{d_1} \in [0, 1]$, or $b \in [0, \sqrt{d_1}]$, is presented at the Fig. 3 for the following parameters

choice: $K = 7.77 \times 10^6$, $J = 1.5 \times 10^{-11}$ in SI units and $\alpha = 0.016$, see, e.g. [11]; next, we take: $\lambda_{0,1} = \frac{(2.4)^2}{\rho_0^2}$.

For estimation we choose $\rho_0 = 100 \text{ nm} = 10^{-7} \text{ m}$, hence we get $\lambda_{0,1} \approx 5.8 \times 10^{14}$. It results in $d_1 = -8.2121 \times 10^6$, $d_2 = 5.8 \times 10^{14}$.

6.1.1. Inhomogeneous equation. The rhs of mode evolution equation (76) in the case of constant magnetic field may be written as a shorthand $\begin{pmatrix} \alpha\gamma\tilde{a}_{m\nu}(k, t) \\ -\gamma\tilde{a}_{m\nu}(k, t) \end{pmatrix} = \begin{pmatrix} \alpha\gamma a \\ -\gamma a \end{pmatrix}$, where $\tilde{a}_{m\nu}$ is defined by (74). Its particular solution, determined by constants $Z = A$, $W = B$ satisfies the system:

$$\begin{aligned} J\lambda B - KA\alpha + JA\alpha\lambda + \alpha\gamma a &= 0, \\ KA - JA\lambda + J\alpha\lambda B - \gamma a &= 0. \end{aligned} \quad (89)$$

From the first equation of (89), we have:

$$B = \frac{1}{J\alpha\lambda} (a\gamma - AK + AJ\lambda).$$

Plugging it to the second one yields:

$$\frac{1}{\alpha} (a\gamma - AK + AJ\lambda) - AK\alpha + a\alpha\gamma + AJ\alpha\lambda = 0,$$

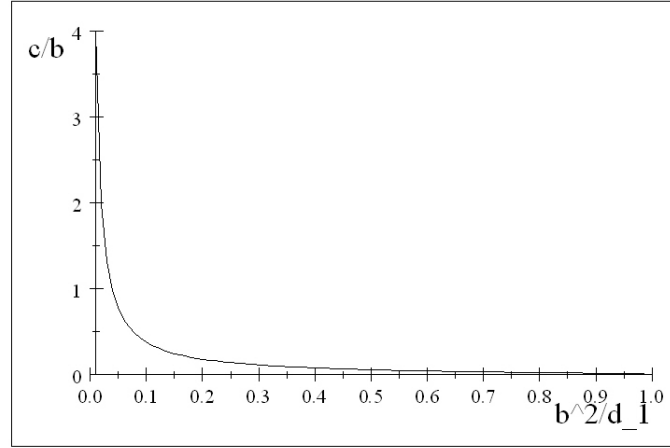


FIG. 3. The dependence of the DW velocity c on b^2/d_1 within the range of real c , for $b > 0$, for the chosen parameters values.

which gives:

$$A = a \frac{\gamma}{K - J\lambda}, \quad B = 0.$$

The general solution of an initial-boundary problem for (71) is, as was mentioned, the sum of general solution, see (72,73), of homogeneous equation and the particular solution, defined by (89).

6.2. Magnetization vector

6.2.1. *The magnetization vector components, general relations.* In Cartesian coordinates the components of the magnetization vector are expressed in terms of complex field Ω as follows:

$$\begin{aligned} m^z &= \frac{\exp(-\Re\Omega) - \exp(\Re\Omega)}{\exp(\Re\Omega) + \exp(-\Re\Omega)}, \\ m^x &= \frac{\exp(\Omega) + \exp(\Omega^*)}{1 + \exp[2\Re\Omega]}, \\ m^y &= -i \frac{\exp(\Omega) - \exp(\Omega^*)}{1 + \exp[2\Re\Omega]}. \end{aligned} \quad (90)$$

In cylindrical coordinates, the components appear as combinations of the Cartesian ones as:

$$\begin{aligned} m_z &= m^z, \\ m_\rho &= m^x \cos \phi + m^y \sin \phi, \\ m_\phi &= m^x \sin \phi + m^y \cos \phi, \end{aligned} \quad (91)$$

for the geometry, see Fig. 4.

6.2.2. *The domain wall.* In approximations that were described through the presented text:

$$m^z \simeq \frac{1 - \exp(2\Re\Omega')}{\exp(2\Re\Omega') + 1} = \frac{\exp(-R) - \exp(R)}{\exp(R) + \exp(-R)} = \tanh R,$$

where:

$$R(\varphi, \rho, z, t) = \sum_{\nu, m} \exp[i\nu\varphi] J_\nu(\epsilon_m(\nu) \frac{\rho}{\rho_0}) Z_{m\nu}^l(z, t) + c.c.$$

The stationary solution motion is depicted at the Fig. 5, it shows the change of direction of magnetization to the opposite one at asymptotic "right" and "left" sides of a DW center ($\rho = 0$).

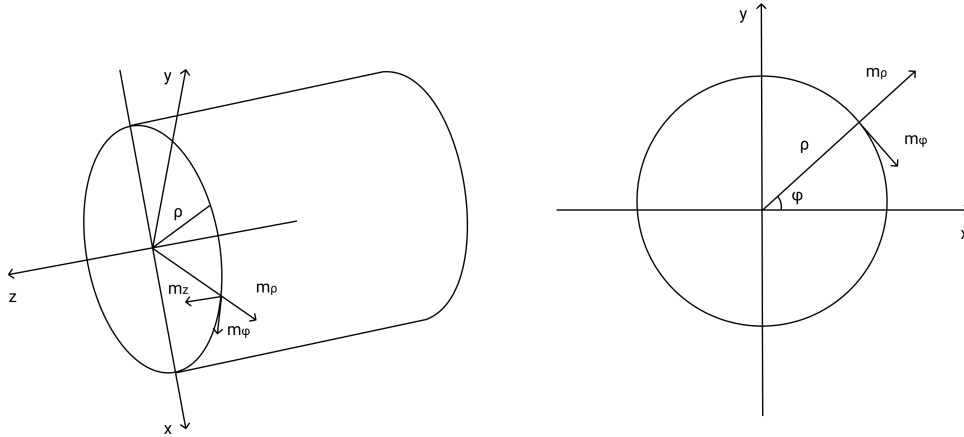


FIG. 4. Geometry. Vector \vec{m} components in cylindrical coordinates, $\rho < \rho_0$

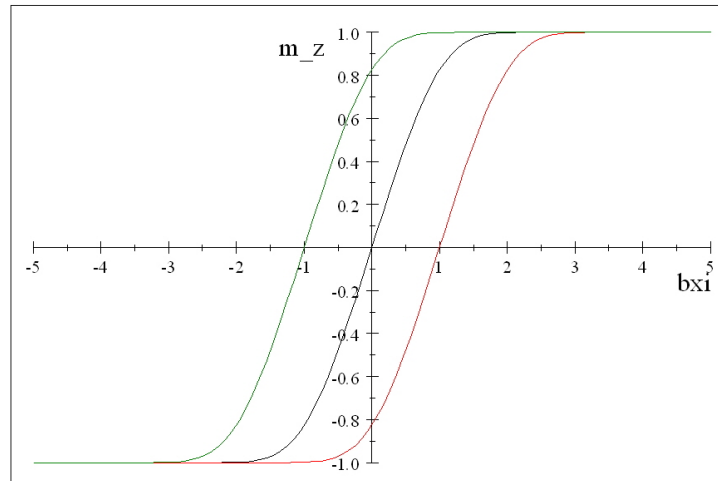


FIG. 5. The stationary wall motion plot at $b\xi = -1$ (green), 0 (black), 1 (red) for $m_z(\xi)$, $\nu = 0$, $n = 1$, $\rho = 0$

7. Conclusion

A detailed scheme for a DW creation dynamics, in terms of boundary-initial problems for zero and nonzero external magnetic fields, is proposed. The solutions of the problems are presented in the form of a combination of projections onto eigen subspaces of the evolution operators in k - and x -domains in respect to Fourier transformation. The problem may be reformulated within the proposed scheme for anisotropy coefficient depending on ρ , ϕ , as well as for coordinate-dependent external magnetic field.

Acknowledgements

The author thanks V. Rodionova for fruitful discussions.

References

- [1] Ipatov M., Zhukova V., Zvezdin A.K., Zhukov A. Mechanisms of the ultrafast magnetization switching in bistable amorphous microwires, *J. Appl. Phys.*, 2000, **106**, 103902.
- [2] Chizhik A.A., Zhukov A., Gonzalez A., Stupakiewicz A. Control of reversible magnetization switching by pulsed circular magnetic field in glass-coated amorphous microwires. *Applied Physics Letters*, 2018, **112** (7), 072407.
- [3] Stupakiewicz A., Chizhik A., et al. Ultrafast Magnetization Dynamics in Metallic Amorphous Ribbons with a Giant Magnetoimpedance Response. *Physical Review Applied*, 2020, **13**, 044058.

- [4] Badarneh M.H.A.G., Kwiatkowski J., Bessarab P.F. Mechanisms of energy efficient magnetization switching in a bistable nanowire. *Nanosystems: Physics, Chemistry, Mathematics*, 2020, **11** (3), P. 294–300.
- [5] Rodionova V., Zhukova M., et al. The defects influence on domain wall propagation in bistable glass-coated microwires. *Physica B*, 2012, **407**, P. 1446–1449.
- [6] Brown Jr. W.F. Micromagnetics, Domains, and Resonance. *J. Appl. Phys.*, 1959, **106**, 103902.
- [7] Frenkel I., Dorfman J.N. Spontaneous and Induced Magnetisation in Ferromagnetic Bodies. *Nature*, 1930, **126**, P. 274–278.
- [8] Landau L., Lifshitz E. On the theory of the dispersion of magnetic permeability in ferromagnetic bodies. *Phys. Z. Sowjetunion*, 1935, **8** (153), P. 101–114.
- [9] Aharoni A. *Introduction to the Theory of Ferromagnetism*, Clarendon Press, Oxford, 1996, 192 p.
- [10] Schryer N.L., Walker L.R. The motion of 180° domain walls in uniform dc magnetic fields. *J. Appl. Phys.*, 1974, **45**, 5406.
- [11] Vereshchagin M., Baraban I., Leble S., Rodionova V. Structure of head-to-head domain wall in cylindrical amorphous ferromagnetic microwire and a method of anisotropy coefficient estimation. *Journal of Magnetism and Magnetic Materials*, 2020, **504**, 166646.
- [12] Leble S. *Waveguide Propagation of Nonlinear Waves. Impact of Inhomogeneity and Accompanying Effects*, Springer, 2019, 288 p.
- [13] Varga R., Zhukov A., et al. Fast magnetic domain wall in magnetic microwires. *Phys. Rev. B*, 2006, **74**, 212405.
- [14] Chizhik A.I., Zhukov A., Gonzalez J., and Stupakiewicz A. . Basic study of magnetic microwires for sensor applications: Variety of magnetic structures”. *Journal of Magnetism and Magnetic Materials*, 2017, **422** 299 – 303,
- [15] Omelyanchik A., Gurevich A., et al. Ferromagnetic glass-coated microwires for cell manipulation. *Journal of Magnetism and Magnetic Materials*, 2020, **242–245**, P. 216–223.
- [16] Amirov A., Baraban I., Panina L., Rodionova V. Direct Magnetolectric Effect in a Sandwich Structure of PZT and Magnetostrictive Amorphous Microwires. *Materials*, 2020, **13** (4), 916.
- [17] Vázquez M. *Magnetic Nano- and Microwires: Design, Synthesis, Properties and Applications*. Woodhead Publishing Series in Electronic and Optical Materials. Elsevier Science, 2015.
- [18] Lakshmanan M. The fascinating world of the Landau–Lifshitz–Gilbert equation: an overview. *Phil. Trans. R. Soc. A*, 2011, **369**, P. 1280–1300.
- [19] Lakshmanan M., Nakamura K. Landau–Lifshitz Equation of Ferromagnetism: Exact Treatment of the Gilbert Damping. *Phys. Rev. Lett.*, 1984, **53**, 2497.
- [20] Vereshchagin M. Structure of domain wall in cylindrical amorphous microwire. *Physica B: Condensed Matter*, 2018, **549**, P. 91–93.
- [21] Janutka A., Gawroński P. Structure of magnetic domain wall in cylindrical microwire. *IEEE Transactions on Magnetics*, 2015, **51** (5), P. 1–6.
- [22] Huening F., Backes A. Direct observation of large Barkhausen jump in thin Vicalloy wires. *IEEE Magnetics Letters*, 2020, **11**, 2506504.
- [23] Leble S. *Practical Electrodynamics with Advanced Applications*, IOP Publishing, 2020.
- [24] Baraban I., Leble S., Panina L., Rodionova V. Control of magneto-static and -dynamic properties by stress tuning in Fe–Si–B amorphous microwires with fixed dimensions. *Journal of Magnetism and Magnetic Materials*, 2019, **477**, P. 415–419.
- [25] Leble S.B., Rodionova V.V. Dynamics of Domain Walls in a Cylindrical Amorphous Ferromagnetic Microwire with Magnetic Inhomogeneities. *Theor. Math. Phys.*, 2020, **202**, P. 252–264.
- [26] Kerimov M.K. Studies on the zeros of Bessel functions and methods for their computation. *Comput. Math. and Math. Phys.*, 2014, **54**, P. 1337–1388.
- [27] Leble S., Perelomova A. *Dynamical projectors method in hydro- and electrodynamics*, CRC Press, Taylor and Francis group, 2018.
- [28] Stano M., Fruchart O. Magnetic Nanowires and Nanotubes, *Handbook of Magnetic Materials*, 2018, DOI: 10.1016/bs.hmm.2018.08.002.
- [29] Alam J., Bran C., et al. Cylindrical micro and nanowires: Fabrication, properties and applications. *Journal of Magnetism and Magnetic Materials*, 2020, **513**, 167074.
- [30] Popov I.Y. On the possibility of magnetoresistance governed by light. *Nanosystems: physics, chemistry, mathematics*, 2013, **4** (6), P. 795–799.
- [31] Chizhik A., Gonzalez J., Zhukov A., Gawroński P. Study of length of domain walls in cylindrical magnetic microwires. *Journal of Magnetism and Magnetic Materials*, 2020, **512**, 167060.
- [32] Corte-León P., Gonzalez-Legarreta L., et al. Controlling the domain wall dynamics in Fe-, Ni- and Co-based magnetic microwires. *Journal of Alloys and Compounds*, 2020, **834**, 155170.

Weak polarization-optical responses of diluted magnetic nanofluid probed by laser radiation with polarization modulation

Ya. A. Fofanov¹, I. V. Pleshakov², A. V. Prokof'ev², E. E. Bibik³

¹Institute for Analytical Instrumentation RAS, 26 Rizhsky ave.,
St. Petersburg, 190103, box 207, Russian Federation

²Ioffe Institute, 26 Politechnicheskaya str., St. Petersburg, 194021, Russian Federation

³St. Petersburg State Institute of Technology (Technical University),
26 Moskovsky ave., 190013, St. Petersburg, Russian Federation

ivanple@yandex.ru

PACS 78.20.Ls; 75.50.Mm; 42.60.-v

DOI 10.17586/2220-8054-2021-12-1-60-64

A sensitive laser registration of weak polarization-optical responses was used for the investigations of dilute magnetic nanofluids. Criteria for weak and strong signals for probing of sample by laser radiation with deep modulation of polarization were considered. The magneto-optical responses of a kerosene-based fluid with magnetite nanoparticles were investigated over a wide (five orders of magnitude) range of concentrations. Weak polarization responses for this nanofluid were observed at record low volume concentrations of nanoparticles up to 10^{-7} .

Keywords: magnetic nanofluid, laser probing, magnetooptics, weak polarization-optical response.

Received: 4 February 2021

Revised: 15 February 2021

1. Introduction

Magnetic nanofluids have attracted the attention of researchers to this day, and the particular interest in them is associated with the emergence of a number of new proposals for their application in optoelectronics, biomedicine, and other areas [1]. The main properties of these materials were established several decades ago [1–5], however they cannot be considered quite definitively studied. At present, magnetic nanofluids continue to be investigated from different points of view and by different methods, among which, optical analyses take an important place [1–5].

Approaches based on the use of light polarization are very informative and successfully complement magneto-metric experiments [2–5]. In particular, the use of polarization modulation seems to be promising [6], and this has already been demonstrated in the study of different objects [7–12], although as applied to magnetic nanofluids the advantages of this method were not widely used.

Nonstationary laser polarization-optical probing in the original combination with a differential photodetection scheme allows one to achieve a very high sensitivity of optical measurements up to a threshold that is limited only by natural (quantum, photonic) noise of radiation [13–15]. Earlier, by the methodology developed on this basis, we investigated the polarization characteristics of various objects, including optical elements with a high degree of optical and structural homogeneity [16], magnetically ordered materials [17], and perfect optical crystals, including those with a modified crystal structure [15]. A preliminary polarization-optical diagnostics of magnetic fluids was also performed [18]. This paper presents the results of a study of weak polarization responses obtained for a wide range of concentrations in experiments with magnetic nanofluid probing by laser radiation with polarization modulation.

2. Experimental details

2.1. Setup

A simplified diagram of the experimental setup adapted for the study of magnetic nanofluids is shown in Fig. 1 (see also [16–18]). Probing laser radiation ($\lambda = 0.63\mu$) passes through a polarization modulator, a cuvette with a magnetic nanofluid, and enters a polarization analyzer, where polarization-sensitive optical detection and preliminary processing of the photosignal performed, and then the signal enters the registration system and the computer. A cuvette with a magnetic fluid is placed in a transverse magnetic field H , which is created by solenoids. This field is linearly swept at values ranging from -45 to $+45$ Oe.

The analytical signal of the experimental setup, i.e., the observed polarization-optical response φ can be represented as follows: $\varphi = \varphi_0 \sin \Delta$. Here, φ_0 is a scale factor that takes into account, in particular, the degree of polarization modulation; Δ is the phase difference of two orthogonal linearly polarized components of the probing

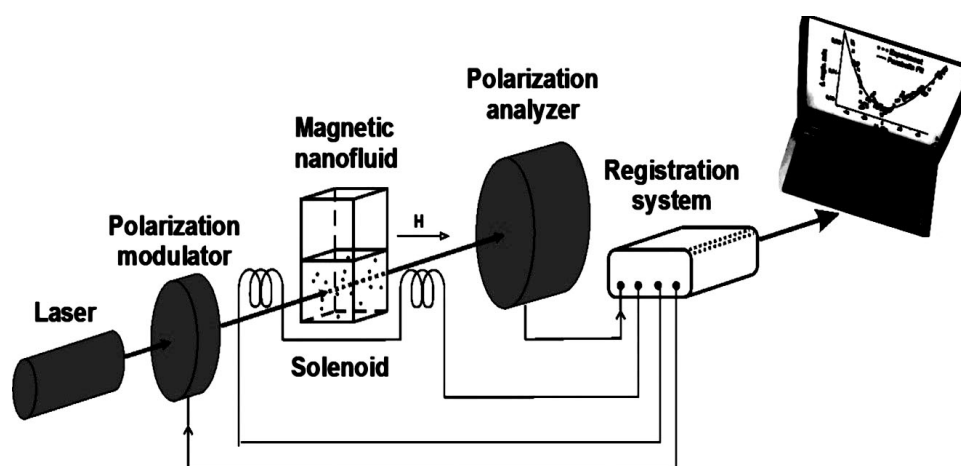


FIG. 1. Experimental setup

light arising as a result of passing through the object under study. Thus, the measured quantity is birefringence (linear optical anisotropy) of the magnetic fluid induced by an external magnetic field [16–18]. Further, we assume that the scale of the output signals is calibrated in units of the measured anisotropy (in our case, in angular minutes). A detailed description of the measurement and calibration procedures is given in [16–18].

2.2. Weak polarization responses

In a number of practical cases it is important to investigate samples with small optical anisotropy [16–19]. Our proposed natural criterion for the smallness of anisotropy is based on the inequality $\Delta \ll 1$ rad [14]. When it is so, $\sin \Delta \sim \Delta$ and the dependence $\varphi(\Delta)$ becomes linear. The degree of linearity of the function $\varphi(\Delta)$ depends on how well this inequality is fulfilled. In the opposite case, when $\Delta > 1$ rad, the anisotropy under study should be considered strong.

Polarization responses φ corresponding to weak anisotropy Δ might also be called weak signals (weak responses), in spite of this, the output signals can be quite large in absolute terms. Except to linearity, the region of weak signals has another very useful property – the additivity of responses: the total response of a system of samples φ_{Σ} is equal to the sum of their individual responses φ_i : $\varphi_{\Sigma} = \sum_i \varphi_i$ [16].

The threshold value of the measured birefringence Δ_{th} , determined by the natural noise of the photo registration process, is rather small and, according to the criterion considered above, is in the area of weak responses. Thus, for the power of the used laser is on the order of 1 mW, the value of Δ_{th} is about $1.5 \cdot 10^{-4}$ ang. min. (respectively, the value of φ_{th} is also about $1.5 \cdot 10^{-4}$ ang. min.) [13, 14, 19, 20]. In practice, the minimum value of the recorded response can often be limited, for example, by fluctuations of the laser radiation parameters used and other instrumental factors, which requires careful organization of the measuring procedure [17, 18, 21].

To register weak polarization responses, we have provided the ability of precise adjustment of the transmission coefficient of the optoelectronic path in the range of more than three orders of magnitude with retention the calibration. Also, the accumulation of the signal during the implementation of series of multiple, up to twenty times, scanning of the magnetic field was provided.

2.3. Samples

The investigation was carried out on the kerosene-based magnetite solutions, prepared by the technique, described in [22] (the samples were the same as was used in [18, 23]). The solid phase, dispersed in carrying fluid consisted of Fe_3O_4 particles with a characteristic size of about 10 nm, coated by a surfactant (oleic acid). It is well known that at such sizes, ferrimagnetically ordered magnetite particles are single-domain and, in total, represent a system of independent magnetic moments that can be affected by an external magnetic field [1, 3]. Thus, this two-component liquid (solid phase and solvent) is a nanostructure with magnetic properties. An important manifestation of the latter is that under the field action, this magnetic nanostructure takes on an optical anisotropy. This phenomenon of forming the optically anisotropic medium becomes possible due to the fact that magnetic particles themselves have a shape anisotropy and they can also accumulate into elongated agglomerates [2–4].

The material was a colloid synthesized by hydrolysis of iron chloride and sulfate solutions with ammonia followed by extraction of magnetite nanoparticles with a solution of oleic acid. This technology makes it possible to obtain a

ferrofluid containing particles with a surface covered with a layer of surfactant (the thickness of which is much less than the diameter of their magnetic core) and an easily determined volume concentration of the solid phase [22].

Our experiments on observing field-induced birefringence started from the sample with concentration of $1 \cdot 10^{-2}$ (which ensured sufficient transparency of the nanofluid in a 1 cm-thick cuvette), with its further successive dilutions up to $1 \cdot 10^{-7}$.

3. Experimental results

In Fig. 2 the dots show the measured polarization response vs H , for the nanofluid with initial concentration. To obtain a quantitative estimate of its value, a parabolic approximation was applied, which is shown in figure by the solid line. As one can see, it gives a fairly good agreement with the experiment, although there are some minor deviations. (A more detailed analysis of the similarity of the observed functions $\varphi(H)$, as well as a comparative analysis of their analytical approximations over a range of three orders of magnitude on concentration were carried out in [18, 24, 25].) Fig. 3 depicts the similar dependencies for the sample with minimal investigated concentration.

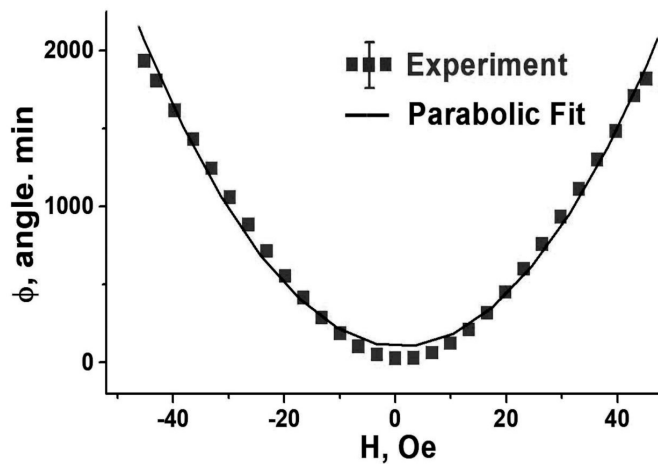


FIG. 2. Polarization responses for the concentration of $1 \cdot 10^{-2}$

The scatter of experimental data in this case can be explained by instrumental factors and, probably, by intrinsic fluctuations in the studied nanofluid.

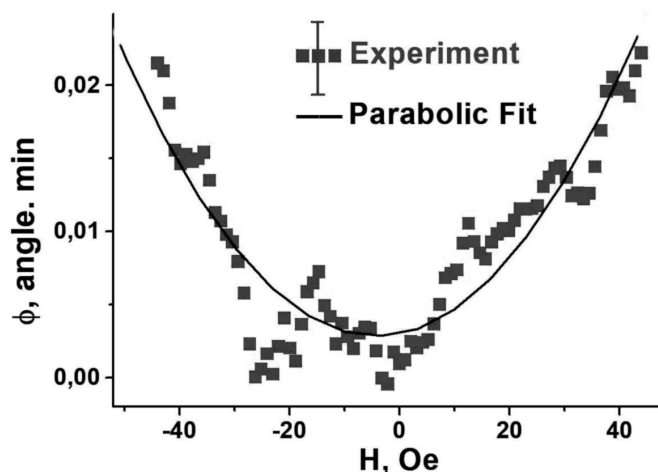


FIG. 3. Polarization responses for the concentration of $1 \cdot 10^{-7}$

From the obtained results, it is obvious that the value of parabolic fitting function taken at some fixed H can be regarded as magnitude of the response φ (further we used $H = 43$ Oe). In Fig. 4 the dependence of φ on concentration is shown; the figure also shows it is a linear approximation. Note that the measurement at the end of the range with minimal concentration indicates a very high sensitivity of the method used.

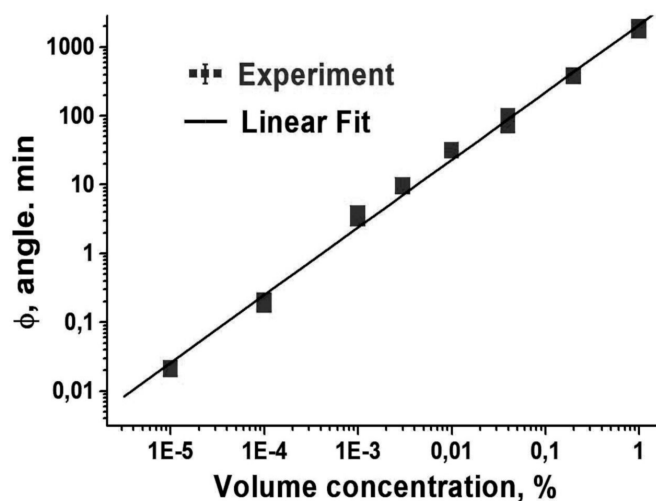


FIG. 4. Polarization response versus concentration of magnetic nanoparticles ($H = 43$ Oe)

4. Discussion

The similarity of $\varphi(H)$ functions over a very wide range suggests the physical mechanism of birefringence in a magnetic nanofluid to be generally the same for both relatively large (10^{-2}) and very small (10^{-7}) concentrations of solid phase. At low concentrations, the nature of polarization responses cannot be entirely determined by the aggregates of nanoparticles induced by the field (we do not exclude, however, that this effect to some extent is present). This means, that for large concentrations, this mechanism may not be the only one. (In more detail, this fact is discussed in [18, 24, 25]).

Frequently used model for the birefringence in magnetic nanofluids is based on the idea of the orientation of individual nanoparticles in magnetic field [1–4]. In the theory developed in [2, 4] the total anisotropy of the fluid is determined by the sum of contributions from individual non-spherical particles, taking into account their orientation with respect to the field direction. Such a model results in linear dependence of Δ on the number of magnetic particles.

This concept is in accordance with the linearity of the experimentally observed dependence $\varphi(\Delta)$ and with additivity of weak polarization responses for magnetic nanofluid under study (see also [18, 24, 25]). It is possible that up to those concentrations that in this work are considered as high, the influence of aggregates is still small. Further clarification of the proportion between contributions from aggregates and individual particles can probably be obtained by studying the dynamic characteristics of the investigated medium.

5. Conclusion

Our experiments have demonstrated a very high potency of the probing a magnetic nanofluid by laser radiation with polarization modulation. This way made it possible to detect the optical responses for a record low concentration of the solid phase (10^{-7}).

It was found that over a very wide range of changes in the concentrations of the solid phase in nanofluids, at low magnetic fields ($H < 45$ Oe), birefringence is determined by one dominant mechanism, which is most likely associated with the anisotropy of the particle's shape.

In our opinion, the approach used in this work can be extended further, for example, to magnetic fluids modified by different additives, to impurity centers and defects in solids, biological tissues and others.

This work was performed in the framework of State tasks 075-01073-20-00 on the topic No. 0074-2019-0007 of the Ministry of Science and Higher Education of the Russian Federation.

References

- [1] Scherer C., Figueiredo Neto A.M. Ferrofluids: Properties and applications. *Braz. J. Phys.*, 2005, **35**(3A), P. 718–727.
- [2] Skibin Yu.N., Chekanov V.V., Raker Yu.L. Birefringence in a ferromagnetic liquid. *Sov. Phys. JETP*, 1977, **45**(3), P. 496–499.
- [3] Davis H.W., Llewellyn J.P. Magnetic birefringence of ferrofluids: I. Estimation of particle size. *J. Phys. D: Appl. Phys.*, 1979, **12**(2), P. 311–319.
- [4] Scholten P.C. The origin of magnetic birefringence and dichroism in magnetic field. *IEEE Trans. Magn.*, 1980, **16**(2), P. 221–225.
- [5] Zhao Y., Lv R., Zhang Y., Wang Q. Novel optical devices based on the transmission properties of magnetic fluid and their characteristics. *Opt. Lasers Eng.*, 2012, **50**(9), P. 1177–1184.

- [6] Badoz J., Billardon M., Canit J.C., Russel M.F. Sensitive devices to determine the state and degree of polarization of a light beam using a birefringence modulator. *J. Opt.*, 1977, **8**(6), P. 373–384.
- [7] Jaspersen S.N., Schnatterly S.E. An improved method for high reflectivity ellipsometry based on a new polarization modulation technique. *Rev. Sci. Instrum.*, 1969, **40**(6), P. 761–767.
- [8] Shindo Y., Mizuno K., Sudani M., Hayakawa H., Ohmi Y., Sakayanagi N., Takeuchi N. New polarization-modulation spectrometer for simultaneous circular dichroism and optical rotatory dispersion measurements. II. Design, analysis, and evaluation of prototype model. *Rev. Sci. Instrum.*, 1989, **60**(12), P. 3633–3639.
- [9] Acher O., Bigan E., Dreviron B. Improvements of phase-modulated ellipsometry. *Rev. Sci. Instrum.*, 1989, **60**(1), P. 65–77.
- [10] Gupta V.K., Kornfield J.A., Ferencz A., Wegner G. Controlling molecular order in “Hairy-rod” Langmuir-Blodgett films: A polarization-modulation microscopy study. *Science*, 1994, **265**(5174), P. 940–942.
- [11] Shindo Y., Kani K., Horinaka J., Kuroda R., Harada T. The application of polarization modulation method to investigate the optical homogeneity of polymer films. *J. Plast. Film Sheeting*, 2001, **17**(2), P. 164–183.
- [12] Osborn K.D., Singh M.K., Urbauer R.J.B., Johnson C.K. Maximum-likelihood approach to single-molecule polarization modulation analysis. *ChemPhysChem*, 2003, **4**(9), P. 1005–1011.
- [13] Fofanov Ya.A. Threshold sensitivity in optical measurements with phase modulation. Proceedings of the Conference. Tenth All-Union Symposium and School on High-Resolution Molecular Spectroscopy. *Proc. SPIE*, 1992, **1811**, P. 413–414.
- [14] Fofanov Ya.A., Sokolov I.M., Pleshakov I.V., Vetrov V.N., Prokofiev A.V., Kuraptsev A.C., Bibik E.E. On the criteria for strong and weak polarization responses of ordered objects and systems. Proceedings of the XI International Symposium on Photon Echo and Coherent Spectroscopy (PECS-2017), Svetlogorsk (Russia), 2017, *EPJ Web Conf.*, **161**, P. 01003.
- [15] Fofanov Ya., Vetrov V., Ignatenkov B. Laser polarization-optical sounding of optical crystals and ceramics. Proceedings of 2018 International Conference Laser Optics (ICLO), St. Petersburg, 2018, P. 406–406.
- [16] Sokolov I.M., Fofanov Ya.A. Investigations of the small birefringence of transparent objects by strong phase modulation of probing laser radiation. *J. Opt. Soc. Am. A.*, 1995, **12**(7), P. 1579–1588.
- [17] Fofanov Ya.A., Pleshakov I.V., Kuz'min Yu. I. Laser polarization-optical detection of the magnetization process of a magnetically ordered crystal. *J. Opt. Technol.*, 2013, **80**(1), P. 64–67.
- [18] Fofanov Ya.A., Pleshakov I.V., Prokof'ev A.V., Bibik E.E. Investigation of polarization magneto-optic responses of a low-concentration ferrofluid. *Tech. Phys. Lett.*, 2016, **42**(10), P. 1054–1056.
- [19] Fofanov Ya.A. Nonlinear and fluctuation phenomena under conditions of strong selective reflection in inclined geometry. In *Advances in Optoelectronics Research*. Nova Science Publishers, USA, 2014, P. 75–114.
- [20] Klyshko D.N., Masalov A.V. Photon noise: observation, squeezing, interpretation. *Phys.-Uspekhi*, 1995, **38**(11), 1203–1230.
- [21] Sokolov I.M., Fofanov Ya.A. Suppression of excess noise of polarization-modulated probe light in measurements of weak optical birefringence. *Optics and spectroscopy*, 1999, **86**(5), P. 745–752.
- [22] Bibik E.E., Matyugullin B.Ya., Raikher Yu.L., Shliomis M.I. Magnetostatic properties of magnetite colloids. *Magneto hydrodynamics*, 1973, **9**(1), P. 58–62.
- [23] Prokof'ev A.V., Pleshakov I.V., Bibik E.E., Kuz'min Yu.I. An optical investigation of the geometric characteristics of aggregates formed by particles of magnetic fluid. *Tech. Phys. Lett.*, 2017, **43**(2), P. 194–196.
- [24] Fofanov Ya.A., Manoilov V.V., Zarutskii I.V., Kuraptsev A.S. Statistical analysis of the data of highly sensitive laser polarization-optical probing of magnetic nanofluids. *J. Opt. Technol.*, 2020, **87**(2), P. 94–99.
- [25] Fofanov Ya.A., Manoylov V.V., Zarutskiy I.V., Kuraptsev A.S. Laser polarization-optical diagnostics of ordered objects and structures. *Bull. Russ. Acad. Sci.: Phys.*, 2020, **84**(3), P. 263–266.

Study of nonclassicality in fifth harmonic generation nonlinear optical process

Priyanka, Savita Gill*

Department of Applied Science, University Institute of Engineering and Technology,
Kurukshetra 136119, India

Chauhan7101@gmail.com, *Savita2015@kuk.ac.in

DOI 10.17586/2220-8054-2021-12-1-65-72

We have examined non classical effect i.e. higher order single mode antibunching and intermodel antibunching and higher order sub-poissonian photon statistics (HOSPS) in fifth harmonic generation non linear optical process using short time interaction technique. We have found that nonclassical effects directly depend on number of photons prior to interaction with non linear medium. The higher the number of photons present prior to an interaction, the higher will be the nonclassicality in the system. It is additionally found that stoke mode doesn't fulfill the condition of single mode antibunching and HOSPS in fifth harmonic generation process. To examine the optical nonlinearity of nanoparticles, there are significant research efforts concerning the estimation of higher order nonlinear susceptibility which can be utilized as a source for the generation of higher order harmonic generation nonlinear optical processes [19].

Keywords: higher order sub-poissonian photon statistics, single mode and intermodel antibunching, optical processes.

Received: 6 February 2021

Revised: 18 February 2021

1. Introduction

It is conceivable to characterize a state as a nonclassical state that does exclude any classical analog [1–3]. A radiation field is supposed to be nonclassical if the Glauber Sudarshan P-function of the field becomes more negative than the delta function. The investigation of nonclassical properties of a designed quantum state is a vital field in quantum state designing and quantum information processsing, since the presence of nonclassical qualities gives quantum supremacy [4,5]. Some notable instances of nonclassical are antibunching and sub-Poissonian photon statistics. Investigation of these nonclassical properties is consistently significant in field of their intriguing applications with regards to field of quantum computing, quantum communication and quantum cryptography [6–10]. All the above actual frameworks are experimentally feasible and are effectively seen at nonlinear optics research centers [11, 12]. After the cooperation, photon statistics can be achieved experimentally using homodyne detection procedure [13, 14]. The improvements in nanotechnology and nanoscience have given new freedoms to non linear optics. Over the most recent couple of many years, a number of studies on non linear optical properties of novel materials have been performed due to the capability of these materials in optical equipment applications [15–18]. The most impressive strategy to quantify the higher order susceptibilities is Z-scan technique [19] which can be utilized as a source of generations of higher order harmonic generation non linear optical processes. Numerous different creators have additionally predicted upgraded optical nonlinearities, arising because of quantum confinement impacts, regarding the relating mass materials [20–22]. Generation of third, fifth and seventh harmonics by filamentation of mid-infrared laser pulses in air was as of late tentatively noticed [23–26].

These two nonclassical effects may have lower and higher order renditions, investigation of lower order nonclassicality in a quantum state is accounted for in writing since its origin, yet premium in higher order is generally new and promising from an experimental perspective [27]. Out of these higher order nonclassical impacts, higher order squeezing has been focused on in detail [28–31] yet higher order sub-Poissonian photon statistics (HOSPS) and higher order antibunching (HOA) has not yet been concentrated definitely. The concept of HOA was introduced by Lee [32] and it has been anticipated in a two photon coherent state [32, 33, 33], and a shadowed negative binomial state [34]. Yet, HOA has all the earmarks of being an extremely uncommon wonder. Recently, Prakash and Mishra have set up broad measure for HOSPS in a real system [35].

Remembering these realities, the current investigation shows that higher order single mode antibunching, intermodel antibunching, and HOSPS can be found in fifth harmonic generation process, and in this process, they appear simultaneously. In this paper, section 2 gives the condition of nonclassicality of the nonlinear optical system. Section 3 will introduce a second order solution of equation of motion of fifth harmonic generation process and show the presence of higher order single mode antibunching, intermodel antibunching and HOSPS and their immediate relationship with pump photons present in the system. In section 6 is committed to conclusion.

2. Criteria of nonclassicality of a nonlinear optical system

2.1. Criteria for single mode and intermodel antibunching

HOA is communicated in wording factorial moment of number operator. HOA criteria for single mode was presented by Lee is given as [32]:

$$R(m, l) = \frac{\langle N_x^{m-1} \rangle \langle N_x^{l+1} \rangle}{\langle N_x^m \rangle \langle N_x^l \rangle} - 1 < 0, \quad (1)$$

where N is numerical operator. $\langle N^{(k)} \rangle = \langle N(N-1)(N-2)\dots(N-k+1) \rangle$ is the k^{th} factorial moment of number operator. Integers l and m fulfilling condition $l \leq m \leq 1$ and x subscript denotes specific mode. $m = 1$ is chosen by Ba An [33] and criteria of l^{th} order antibunching is reduced to:

$$\langle N_x^{l+1} \rangle < \langle N_x^l \rangle \langle N_x \rangle \quad (2)$$

by streamlining equation (2) and acquire condition of l^{th} order antibunching as

$$d(l) = \langle N_x^{l+1} \rangle - \langle N_x \rangle^{l+1} < 0 \quad (3)$$

furthermore, intermodel antibunching criteria is given as:

$$D_{ab} = (\Delta N_{ab})^2 = \langle a^\dagger a b^\dagger b \rangle - \langle a^\dagger a \rangle \langle b^\dagger b \rangle < 0, \quad (4)$$

where equation (3) gives us the condition to single mode antibunching and equation (4) gives us the conditions for intermodel antibunching. Accordingly, we can say that single photon source utilized in quantum cryptography ought to fulfill the criteria given in equation (3) of HOA [36].

2.2. Condition for Higher Order sub-Poissonian Photon Statistics (HOSPS)

Prakash and Mishra [35] provides condition of $(l-1)^{th}$ order HOSPS is given as:

$$D(l-1) = \sum_{k=0}^l \sum_{i=0}^{l-k} {}^l C_k (-1)^k S_2(l-k, i) \langle N^i \rangle \langle N \rangle^k - \sum_{k=0}^l \sum_{i=0}^{l-k} {}^l C_k (-1)^k S_2(l-k, i) \langle N \rangle^{k+i} < 0, \quad (5)$$

where $S_2(l, k)$ is a Stirling number of the second order. The criteria for second order subpoissonian photon statistics for which $l = 3$ is given as:

$$D(2) = \langle N^3 \rangle + 2 \langle N \rangle^3 - 3 \langle N^2 \rangle \langle N \rangle + 3 \langle N^2 \rangle - 3 \langle N \rangle^2 < 0, \quad (6)$$

equation (6) is the criteria of second order sub-Poissonian photon statistics.

3. Fifth harmonic generation process

To examine higher order single mode antibunching, intermodel antibunching and HOSPS, we have picked fifth harmonic generation process so that absorption of five photons, each having frequency ω_1 with emission of one photon of frequency ω_2 where $\omega_2 = 5\omega_1$. Hamiltonian for the said process is

$$H = \omega_1 a^\dagger a + \omega_2 b^\dagger b + g(a^5 b^\dagger + a^\dagger b^5), \quad (7)$$

where g is the coupling constant, a^\dagger (a), b^\dagger (b) are the creation (annihilation) operators, respectively. $A = a \exp i\omega_1 t$, $B = b \exp i\omega_2 t$ are the slowly varying operators at frequencies ω_1 and ω_2 .

3.1. Time evolution of pump mode A

Time evolution of operator in pump mode A is given by Heisenberg equation of motion as:

$$\frac{dA}{dt} = \frac{\partial A}{\partial t} + i[H, A], \quad (8)$$

we obtain:

$$\dot{A} = -5igA^4 B \quad (9)$$

and

$$\dot{B} = -igA^5. \quad (10)$$

Now using the short time approximation technique, expanding $A(t)$ using Taylor's series expansion and taking terms up to $g^2 t^2$ as:

$$A(t) = A - 5igtA^4 B + \frac{5}{2}g^2 t^2 (20A^{\dagger 3} A^4 N_B + 120A^{\dagger 2} A^3 N_B + 240A^\dagger A^2 N_B + 120AN_B - A^{\dagger 4} A^5). \quad (11)$$

Using equation (11), the numerical operator $N_A(t) = A^\dagger(t)A(t)$ is given as:

$$N_A(t) = A^\dagger A - 5igt(A^{\dagger 5}B - A^5B^\dagger) + 5g^2t^2(25A^{\dagger 4}A^4N_B + 200A^{\dagger 3}A^3N_B + 600A^{\dagger 2}A^2N_B + 600A^\dagger AN_B + 120N_B - A^{\dagger 5}A^5) \quad (12)$$

To study antibunching, initially we assume a quantum state which is the product of coherent state $|\alpha\rangle$ for pump mode A and vacuum state $|0\rangle$ for stokes mode B i.e.

$$|\psi\rangle = |\alpha\rangle_A |0\rangle_B. \quad (13)$$

Using equation (13) in equation (12), we get expectation value of $\langle N_A(t) \rangle_\alpha$ is given as:

$$\langle N_A(t) \rangle_\alpha = |\alpha|^2 - 5g^2t^2 |\alpha|^{10}, \quad (14)$$

where $A|\alpha\rangle = \alpha|\alpha\rangle$. By using straight forward description we can get:

$$\langle N_A^2(t) \rangle_\alpha = \langle A^{\dagger 2}(t)A^2(t) \rangle = |\alpha|^4 - 10g^2t^2(|\alpha|^{12} + 2|\alpha|^{10}), \quad (15)$$

and

$$\langle N_A^3(t) \rangle_\alpha = |\alpha|^6 - 5g^2t^2(3|\alpha|^{14} + 12|\alpha|^{12} + 12|\alpha|^{10}), \quad (16)$$

and

$$\langle N_A^4(t) \rangle_\alpha = |\alpha|^8 - 20g^2t^2(|\alpha|^{16} + 6|\alpha|^{14} + 12|\alpha|^{12} + 24|\alpha|^{10}), \quad (17)$$

and

$$\langle N_A^5(t) \rangle_\alpha = |\alpha|^{10} - 5g^2t^2(5|\alpha|^{18} + 40|\alpha|^{16} + 120|\alpha|^{14} + 120|\alpha|^{12} + 24|\alpha|^{10}), \quad (18)$$

now using equations (14–18) in equation (3), we get:

$$d_A(1)_\alpha = -20g^2t^2 |\alpha|^{10}, \quad (19)$$

and

$$d_A(2)_\alpha = -60g^2t^2(|\alpha|^{12} + |\alpha|^{10}), \quad (20)$$

and

$$d_A(3)_\alpha = -120g^2t^2(|\alpha|^{14} + 2|\alpha|^{12} + |\alpha|^{10}), \quad (21)$$

and

$$d_A(4)_\alpha = -40g^2t^2(5|\alpha|^{16} + 15|\alpha|^{14} + 15|\alpha|^{12} + 3|\alpha|^{10}). \quad (22)$$

Equations (19–22) show that the fifth harmonic generation process satisfies the criterion for normal and higher order antibunching.

To study higher order antibunching, we have taken the initial state which is the product of vacuum state $|0\rangle$ for pump mode A and $|\beta\rangle$ for stokes mode B i.e.:

$$|\psi\rangle = |0\rangle_A |\beta\rangle_B. \quad (23)$$

Now taking expectation values of $N_A(t)$, $N_A^2(t)$, $N_A^3(t)$, $N_A^4(t)$ and $N_A^5(t)$ in pump mode A, with respect to condition (23), is given as:

$$\langle N_A(t) \rangle_\beta = 600g^2t^2 |\beta|^2, \quad (24)$$

$$\langle N_A^2(t) \rangle_\beta = 2400g^2t^2 |\beta|^2, \quad (25)$$

$$\langle N_A^3(t) \rangle_\beta = 7200g^2t^2 |\beta|^2, \quad (26)$$

$$\langle N_A^4(t) \rangle_\beta = 14400g^2t^2 |\beta|_{(27)}^2, \quad (27)$$

$$\langle N_A^5(t) \rangle_\beta = 14400g^2t^2 |\beta|^2. \quad (28)$$

Using equations (24–28) in equation (3), we get normal and higher order antibunching in pump mode A with respect to $|0\rangle|\beta\rangle$ is given as:

$$d_A(1)_\beta = 2400g^2t^2 |\beta|^2, \quad (29)$$

$$d_A(2)_\beta = 7200g^2t^2 |\beta|^2, \quad (30)$$

$$d_A(3)_\beta = 14400g^2t^2 |\beta|^2, \quad (31)$$

$$d_A(4)_\beta = 14400g^2t^2 |\beta|^2. \quad (32)$$

Equations (29–32) show that neither normal antibunching nor higher order antibunching is present in pump mode A with respect to the quantum state $|0\rangle|\beta\rangle$.

Now using equations (12, 13 and 23) in equation (6), we get:

$$D(2)_\alpha = -120g^2t^2 |\alpha|^{10}, \quad (33)$$

$$D(2)_\beta = 0. \quad (34)$$

We obtain a negative value in equation (33) with respect to the quantum state $|\psi\rangle = |\alpha\rangle_A |0\rangle_B$, which shows the higher order non-classicality, i.e. HOSPS, exists in pump mode A.

3.2. Time evolution of stoke mode B:

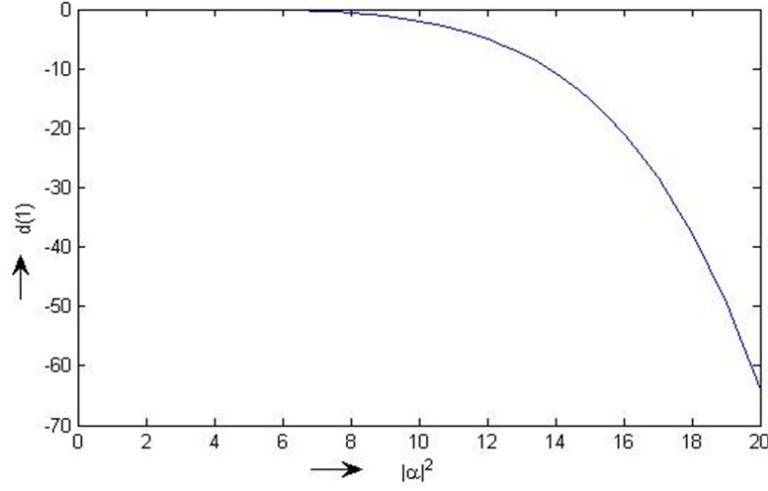


FIG. 1. Variation of normal antibunching $d(1)$ with $|\alpha|^2$ in fifth harmonic generation process (taking $g^2 t^2 \approx 10^{-6}$)

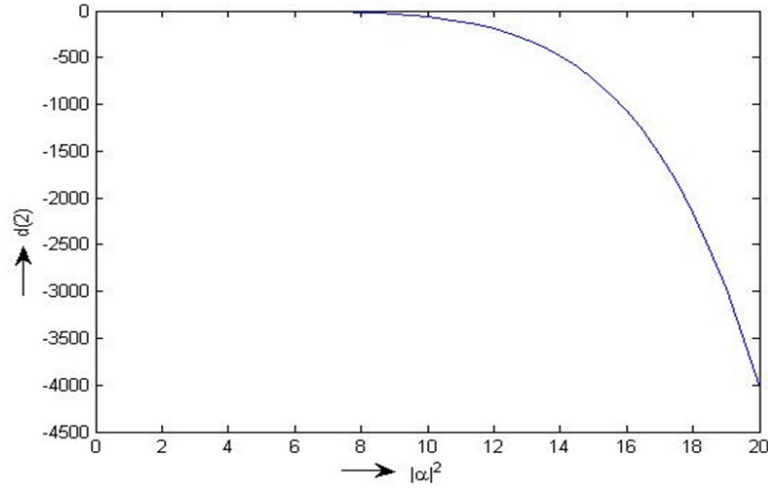


FIG. 2. Variation of second order antibunching $d(2)$ with $|\alpha|^2$ in fifth harmonic generation process (taking $g^2 t^2 \approx 10^{-6}$)

Using Heisenberg equation of motion, we get:

$$\dot{A} = -5igA^{+4}B, \quad \dot{B} = -igA^5. \quad (35)$$

Using Taylor's series expansion, time evolution of B operator is given as:

$$B(t) = B - igtA^5 - \frac{5}{2}g^2t^2[5A^{\dagger 4}A^4B + 40A^{\dagger 3}A^3B + 120A^{\dagger 2}A^2B + 120A^{\dagger}AB + 24B], \quad (36)$$

where $N_A = A^+A$, $N_B = B^+B$ and $N_C = C^+C$.

The number operator in B mode is given as:

$$N_B(t) = B^\dagger(t)B(t),$$

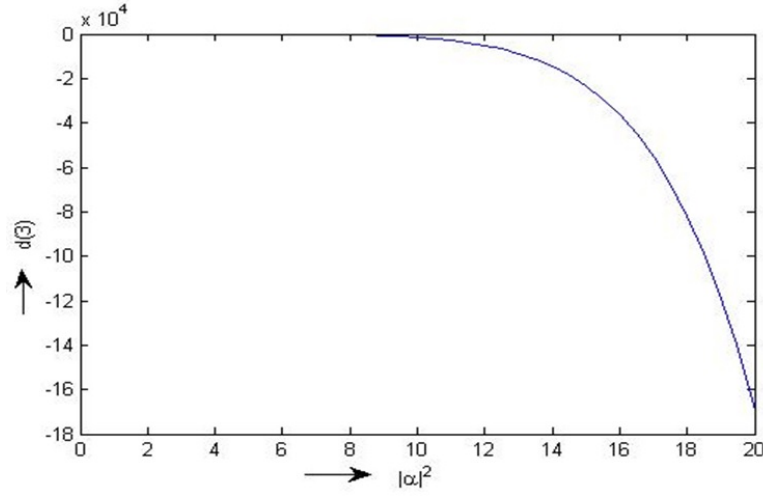


FIG. 3. Variation of third order antibunching $d(3)$ with $|\alpha|^2$ in fifth harmonic generation process (taking $g^2t^2 \approx 10^{-6}$)

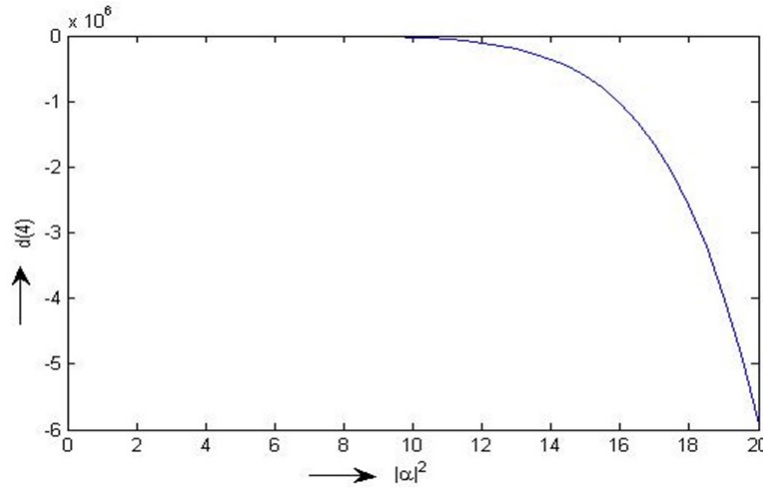


FIG. 4. Variation of fourth order antibunching $d(4)$ with $|\alpha|^2$ in fifth harmonic generation process (taking $g^2t^2 \approx 10^{-6}$)

$$N_B(t) = B^\dagger B -igt(A^5 B^\dagger - A^{\dagger 5} B) - 5g^2t^2(5A^{\dagger 4} A^4 N_B + 40A^{\dagger 3} A^3 N_B + 120A^{\dagger 2} A^2 N_B + 120A^\dagger A N_B + 24N_B) + g^2t^2 A^{\dagger 5} A^5. \quad (37)$$

The expectation value of $N_B(t)$ with respect to the initial condition $|\alpha\rangle |0\rangle$ is given as:

$$\langle N_B(t) \rangle_\alpha = g^2t^2 |\alpha|^{10}. \quad (38)$$

Now, the expectation value of $N_B^2(t)$, $N_B^3(t)$, $N_B^4(t)$ and $N_B^5(t)$ is given as:

$$\langle N_B^2(t) \rangle_\alpha = 0, \quad (39)$$

and

$$\langle N_B^3(t) \rangle_\alpha = 0, \quad (40)$$

and

$$\langle N_B^4(t) \rangle_\alpha = 0, \quad (41)$$

and

$$\langle N_B^5(t) \rangle_\alpha = 0. \quad (42)$$

Now, using equations (38-42) in equation (3), we get:

$$d_B(1)_\alpha = 0, \quad (43)$$

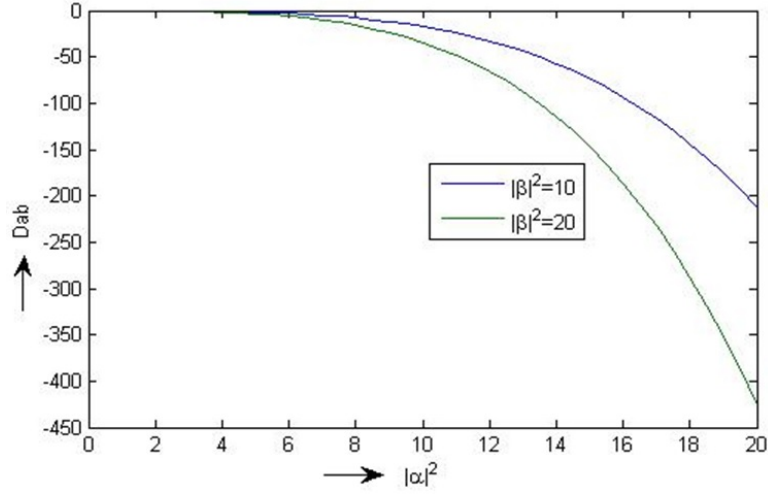


FIG. 5. Variation of intermodel antibunching D_{ab} with $|\alpha|^2$ in fifth harmonic generation process (taking $g^2t^2 \approx 10^{-6}$)

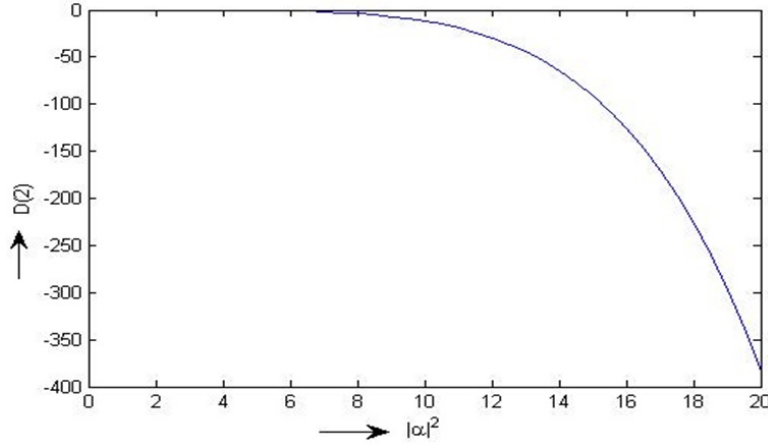


FIG. 6. Variation of higher order sub-Poissonian photon statistics $D(2)$ with $|\alpha|^2$ in fifth harmonic generation process (taking $g^2t^2 \approx 10^{-6}$)

$$d_B(2)_\alpha = 0, \quad (44)$$

$$d_B(3)_\alpha = 0, \quad (45)$$

$$d_B(4)_\alpha = 0. \quad (46)$$

using initial condition (23), we obtain expectation values of $N_B(t)$, $N_B^2(t)$, $N_B^3(t)$, $N_B^4(t)$ and $N_B^5(t)$ in stoke mode B is given as:

$$\langle N_B(t) \rangle_\beta = |\beta|^2 - 120g^2t^2 |\beta|^2, \quad (47)$$

$$\langle N_B^2(t) \rangle_\beta = |\beta|^4 - 240g^2t^2 |\beta|^4, \quad (48)$$

$$\langle N_B^3(t) \rangle_\beta = |\beta|^6 - 360g^2t^2 |\beta|^6, \quad (49)$$

$$\langle N_B^4(t) \rangle_\beta = |\beta|^8 - 480g^2t^2 |\beta|^8, \quad (50)$$

$$\langle N_B^5(t) \rangle_\beta = |\beta|^{10} - 600g^2t^2 |\beta|^{10}, \quad (51)$$

using equations (47–51) in equation (3), we obtain the normal and higher order antibunching in B mode with respect to $|0\rangle |\beta\rangle$ is given as:

$$d_B(1)_\beta = 0, \quad (52)$$

$$d_B(2)_\beta = 0, \quad (53)$$

$$d_B(3)_\beta = 0, \quad (54)$$

$$d_B(4)_\beta = 0. \quad (55)$$

Equations (43–46) and (52–55) show that neither normal antibunching nor higher order antibunching is present in stoke mode B with respect to quantum states $|\alpha\rangle|0\rangle$ and $|0\rangle|\beta\rangle$ respectively.

Now, using equations (13, 23 and 37) in equation (6), we get:

$$D(2)_\alpha = 0, \quad (56)$$

$$D(2)_\beta = 0. \quad (57)$$

Equations (56–57) show that higher order non-classicality i.e. HOSPS is absent in stoke mode B.

Further, using the conditions for intermodel antibunching described in equation (4) and using equations (12) and (37), we obtain following closed expression of D_{ab} :

$$D_{ab} = -100g^2t^2(|\alpha|^2|\beta|^2)[|\alpha|^6 + 6|\alpha|^4 + 12|\alpha|^2 + 6]. \quad (58)$$

Equation (58) show that intermodel antibunching exist in fifth harmonic generation non linear optical process.

4. Results

The presence of single mode and intermodel antibunching and HOSPS in fifth harmonic generation nonlinear process appeared in equations (19,20,21,22,58,33) respectively. On the off chance that we plot a graph between HOA such as $d(1)$, $d(2)$, $d(3)$, $d(4)$, intermodel antibunching say D_{ab} and HOSPS say $D(2)$ with photon number in pump mode A i.e. $|\alpha|^2$ respectively, it is clear that higher order single mode antibunching, intermodel antibunching and HOSPS increase non linearly with an increase in $|\alpha|^2$. Further, it is obvious from the figures that nonclassicality increases as we go towards the higher order of antibunching.

5. Conclusion

We have revealed normal as well as higher order non-classicality with regards to single mode antibunching and intermodel antibunching and higher order sub-Poissonian photon statistics (HOSPS) in pump mode in fifth harmonic generation nonlinear optical process. HOA as well as HOSPS isn't seen in stoke mode in fifth harmonic generation nonlinear optical process. Along these lines, from the results, we can presume that the higher the number of photons present prior to interaction, the higher will be the nonclassicality in the system.

References

- [1] Meystre P., Sargent M. *Elements of Quantum Optics*, 2nd edn, Berlin, Springer, 1991.
- [2] Dodonov V.V. Nonclassical states in quantum optics: a 'squeezed' review of the first 75 years. *Journal of Optics B: Quantum and Semiclassical Optics*, 2002, **4**.
- [3] Hanbury Brown R., Twiss R. Q. Correlation between photons in two coherent beams of light. *Nature*, 1956, **177**(4497), P. 27-29.
- [4] Harrow Aram W., Montanaro A. Quantum computational supremacy. *Nature*, 2017, **549**(7671), P. 203–209.
- [5] Neill C., Roushan P., Kechedzhi K., Boixo S., Isakov S.V., Smelyanskiy V., Megrant A., Chiaro B., Dunsworth A., Arya K. A blueprint for demonstrating quantum supremacy with superconducting qubits. *Science*, 2018, **360**(6385), P. 195–199.
- [6] Abbott B. P., Abbott R., Abbott T. D., Abernathy M. R., Acernese F., Ackley K., Adams C., Addesso P., Adhikari R. X. et al. Gw151226. Observation of gravitational waves from a 22-Solar mass binary black hole coalescence. *Physical Review Letters*, 2016, **116**(24), P. 241103(1-14).
- [7] Madsen L. S., Usenko V. C., Lassen M., Filip R., Andersen U.L. Continuous variable quantum key distribution with modulated entangled states. *Nature communications*, 2012, **3**(1), P. 1038(1-6).
- [8] Bennett C.H. et al. Entanglement-Assisted Classical Capacity of Noisy Quantum Channels. *Physical Review Letters*, 1993, **83**(15), P. 3081–3084.
- [9] Braunstein S.L., Kimble H.J. Dense coding for continuous variables. *Physical Review A*, 2000, **61**(4), P. 042302(1-4).
- [10] Braunstein et. al. Universal Teleportation with a Twist. *Physical Review Letters*, 2000, **84**(15), P. 3486–3489.
- [11] Bachor H.A. A guide to experiments in quantum optics (Weinheim: Wiley-VCH) chapters 8 and 10.
- [12] Vogel W., Welsch D., Wallentowitz S. *Quantum optics: an introduction* 2nd edition. Berlin, Wiley-VCH, chapter 6.
- [13] Erenso D., Vyas R., Singh S. Higher-order sub-Poissonian photon statistics in terms of factorial moments. *Journal of Optical Society B*, 2002, **19**(6), P. 1471–1475.
- [14] Vyas R., Singh S. Photon-counting statistics of the degenerate optical parametric oscillator. *Physical Review A*, 1989, **40**(9), 5147–5159.
- [15] Kreibitz U., Vollmer M. Optical properties of metal clusters. *Springer Series in Materials Science*, 1995, **25**, P. 278–279.
- [16] Seongmin J.U., Wateker P.R., Jeong S. Nonlinear optical properties of zinc doped germane silicate glass optical fibre. *Journal of Nonlinear Optical Physics and Materials*, 2011, **19**(4), P. 791–799.
- [17] Xie R.H. *Handbook of advanced electronic and photonic materials and devices*. H.S. Nalwa (Ed.), Elsevier, 2000, **9**, P. 267–307.
- [18] Shuklina A.I., Smirnov A.V., Fedorov B.A., Kirillova S.A., Almjashaeva O.V. Structure of nanoparticles in the ZrO₂–Y₂O₃ system, as obtained under hydrothermal conditions. *Nanosystems: Physics, Chemistry, Mathematics*, 2020, **11**(6), P. 729–738.
- [19] Xie R.H., Rao Q., Ensen L. *Encyclopedia of nanoscience and nanotechnology*. Nalwa H.S., American Scientific, Los angles, 2003.
- [20] Roussignol P.H., Ricard D., Flytzanis C.H.R. Quantum confinement mediated enhancement of optical kerr effect in CdS_x Se_{1-x} semiconductor microcrystallites. *Applied Physics B*, 1990, **51**(6), P. 437–442.

- [21] Hanamura E. Very large optical nonlinearity of semiconductor microcrystallites. *Physical Review B*, 1988, **37**(3), P. 1273–1279.
- [22] Cotter D., Burt M.G., Manning R.J. Below-band-gap third-order optical nonlinearity of Nanometer -size semiconductor crystallites. *Physical Review Letters*, 1992, **68**(8), P. 1200–1203.
- [23] Jni J., Yao J., Zeng B., Chu W., Li G., Zhang H., Jing C., Chin S. L., Cheng Y., Xu Z. Comparative investigation of third- and fifth-harmonic generation in atomic and molecular gases driven by midinfrared ultrafast laser pulses. *Physics Review A*, 2011, **84**(5), P. 063846(1-4).
- [24] Ariunbold G.O., Polynkin P., Moloney J.V. Third and Fifth harmonic generation by tightly focused femtosecond pulses at 2.2 μm wavelength in air. *Optics Express*, 2012, **20**(2), P. 1662–1667.
- [25] Kartashov D., Alisauskas S., Pugzlys A., Voronin A.A., Zheltikov A.M., Baltuska A. Third- and fifth-harmonic generation by mid-infrared ultrashort pulses: beyond the fifth- order nonlinearity. *Optics Letter*, 2012, **37**(12), P. 2268–2270.
- [26] Nath A., Dharmadhikari J.A., Dharmadhikari A.K., Mathur D. Seventh harmonic generation from tightly focused 2 μm ultrashort pulses in air. *Optics Letter*, 2013, **38**(14), P. 2560–2562.
- [27] Sperling J., Vogel W., Agarwal G.S. Quantum state engineering by click counting. *Physical Review A*, 2014, **89**(4), P. P. 043829(1-10).
- [28] Hong C.K., Mandel L. Higher order squeezing of a quantum field. *Physical Review Letters*, 1985, **54**(4), P. 323–325.
- [29] Hong C.K., Mandel L. Generation of higher order squeezing of quantum electromagnetic fields. *Physical Review A*, 1985, **32**(2), P. 974–982.
- [30] Hillery M. Amplitude-squared squeezing of the electromagnetic field. *Physical Review A*, 1987, **36**(8), P. 3796–3802.
- [31] Priyanka, Gill S. Comparison of non classical effects: quantum phase fluctuation, antibunching and minimum total noise in various non linear optical processes. *Nanosystems: Physics, Chemistry, Mathematics*, 2020, **11**(2), P. 161–170.
- [32] Lee C.K. Higher order criteria for nonclassical effects in photon statistics. *Physical Review A*, 1990, **41**(3), P. P. 1721–1723.
- [33] An B.N. Multimode higher order antibunching and squeezing in trio coherent states. *Journal of Optics B: Quantum and Semiclassical Optics*, 2002, **4**(3), P. 222–227.
- [34] Srinivasan R., Lee C.T. Shadowed negative binomial state. *Physical Letter A*, 1996, **218**(3-6), P. 151–156.
- [35] Prakash H., Mishra D.K. Higher order sub-Poissonian photon statistics and their use in detection of Hong and Mandel squeezing and amplitude-squared squeezing. *Journal of Physics B: Atomic, Molecular and Optical Physics*, 2006, **39**(9), P. 2291–2297.
- [36] Pathak A. A mathematical criterion for single photon sources used in quantum cryptography. *Indian Journal of Physics*, 2006, **80**(5), P. 495–499.

Photon generation in resonator with time dependent boundary conditions

I. S. Lobanov^{1,2}, A. I. Trifanov¹, E. S. Trifanova¹, I. Y. Popov¹, E. Fedorov¹, K. V. Pravdin¹, M. A. Moskalenko¹

¹ITMO University, Kronverkskiy, 49, St. Petersburg, 197101, Russia

²St. Petersburg State University, St. Petersburg, 198504, Russia

lobanov.igor@gmail.com, alextrifanov@gmail.com,
etrifanova@gmail.com, popov1955@gmail.com, fedevg95@mail.ru

PACS 02.30.Jr, 03.65.Ge

DOI 10.17586/2220-8054-2021-12-1-73-80

We present a simulation of Casimir field generation in the 1D cavity with moving walls and arbitrary variation of boundary conditions. We design a numerical scheme based on the finite element method and compare photon generation due to variation of the geometry of the cavity and due to perturbation of the boundary conditions.

Keywords: dynamical Casimir effect, photon generation, numerical modelling.

Received: 19 February 2021

Revised: 23 February 2021

1. Introduction

Quantum parametric processes are very important mechanisms for constructing and manipulating of quantum states in a variety of aspects of quantum science and technologies. The most impressive properties of such processes are stimulation of quantum vacuum and real photon production under conditions near resonant in various quantum systems [1]. One of these is dynamical Casimir effect (DCE)- the process which demonstrates electromagnetic field generation in an empty cavity due to fast moving boundaries or nonadiabatic changing of boundary conditions or medium properties [2–6]. It was predicted in [7] and experimentally approved [8]. A comprehensive review about the theoretical models and possible implementations of DCE as soon as features of Casimir radiation photodetection one can find in [9, 10].

Observation of DCE is accompanied by difficulties in organization of boundary movement with the speed near the speed of light. Alternatively, fast changing of boundary conditions are used [8]. This is possible in superconducting devices like SQUID. It seems possible to realize photon generation under DCE in low-dimensional systems with complex topology [11, 12]. Modelling of DCE meets well known difficulties due to description of non-stationary problems in conditions near resonance. Main analytical results was obtained here in the frameworks of "toys" one-dimensional models with definite boundary movement patterns [13]. Results of applying numerical schemes to these problems may be found in [14, 15]. Consideration of topologically nontrivial structures for realization DCE requires a number of simple analytical models for a chain of one-dimensional connected resonators with different couplings [16, 17, 19, 23–25]. Here, formalism of quantum graphs is widely used [20, 26, 27]. In this way, a number of spectral and transport problems were considered, particularly, with parameter-dependent or time-dependent characteristics (see, e.g., [21, 22, 28–30]).

In this paper, we generalize 1D model of the dynamical Casimir effect developed in [2–6] to take into account arbitrary variation of boundary conditions. We design a numerical scheme based on the finite element method which is simpler in implementation than the spectral decomposition used in the cited papers, especially if the boundary conditions are not trivial. Using the numerical technique, we compare photon generation due to variation of the geometry of the cavity and due to perturbation of the boundary conditions. We demonstrate that effect of the boundary conditions is significant and should be taken into account.

The paper is organized as follows. In Section 2, we recall well-known results obtained for the cavity with moving walls and field quantization inside it. Here, we also introduce changing boundary conditions (smooth switching back and forth from Dirichlet to Neumann) into the non-stationary 1D problem with moving walls and describe parameters in which dynamics will be investigated numerically. Section 3 contains description of numerical scheme, calculation methods and results of numerical modelling. In Section 4, we discuss obtained results and conclude the paper.

2. Electromagnetic field in a cavity with non-stationary geometry

In this section we recall a one-dimensional problem of Casimir radiation in a cavity with moving boundaries in the same way as in [6]. In addition, we develop a formalism which includes the problem of changing the boundary conditions at the both sides of a one dimensional cavity. We start with the wave equation:

$$\partial_t^2 u(x, t) = \partial_x^2 u(x, t), \quad (1)$$

defined on the domain:

$$\Omega = \{(x, t) : t \in \mathbb{R}, -L(t) \leq x \leq L(t)\}, \quad u : \Omega \rightarrow \mathbb{R}. \quad (2)$$

On the infinities the Dirichlet boundary conditions (BC) are fixed with: $L(t) = L$ for $t < 0$ and for $t > T > 0$. The time dependence of the interval length $L(t)$ is assumed to be smooth. On the time interval $0 \leq t \leq T$, the BCs are time dependent and are given by the Robin conditions:

$$\begin{aligned} \alpha_1 u(-L(t), t) &= \partial_x u(-L(t), t), \\ \alpha_2 u(L(t), t) &= -\partial_x u(L(t), t). \end{aligned}$$

As a particular case, we can deal with the Dirichlet conditions. The solution u to the wave equation is assumed to be square integrable over Ω .

One can observe an analogy between our procedure and the solution of 1D stationary scattering problem (if the time is considered as a spatial variable). The general solution to equation (1) for any t can be decomposed over a basis of instantaneous functions $\varphi_k(x, t)$:

$$u(x, t) = \sum_{k=1}^{\infty} c_k(t) \varphi_k(x, t), \quad (3)$$

where functions $\varphi_k(x, t)$ are eigenfunctions of the operator ∂_x^2 with the boundary conditions for the wave equation for fixed time t (with Dirichlet BC):

$$\partial_x^2 \varphi_k(x; t) = -\omega_k^2(t) \varphi_k(x; t).$$

For $t < 0$ and $t > T$ the instantaneous basis is explicitly known, particularly, for the Dirichlet case it is as follows:

$$\omega_k = \frac{\pi k}{L}, \quad \varphi_k(x; t) = \sin \frac{\pi k x}{L}, \quad k \in \mathbb{N}.$$

Then, the functions c_k can be chosen in the form:

$$\begin{cases} c_k(t) = a_{+,k}^< e^{i\omega_k t} + a_{-,k}^< e^{-i\omega_k t} & \text{for } t < 0, \\ c_k(t) = a_{+,k}^> e^{i\omega_k t} + a_{-,k}^> e^{-i\omega_k t} & \text{for } t > T. \end{cases} \quad (4)$$

with coefficients which must form adjoint pairs:

$$a_{+,k}^< = \bar{a}_{-,k}^<, \quad a_{+,k}^> = \bar{a}_{-,k}^>.$$

At the infinities $t \rightarrow \pm\infty$ the decompositions over exponentials do not coincide generally, but they are related by a linear mapping (due to linearity of the wave equation):

$$a_{+,k}^> = A_{k,j} a_{-,k}^< + B_{k,j} a_{+,k}^<, \quad a_{-,k}^> = \bar{B}_{k,j} a_{-,k}^< + \bar{A}_{k,j} a_{+,k}^<.$$

We find the coefficients A and B in the case when all terms in the decomposition (3) equal zero for $t < 0$ except $a_{-,k}^< = 1$, which is:

$$u(x, t) = \psi_k(x, t) := e^{-i\omega_k t} \varphi_k(x; t), \quad t < 0. \quad (5)$$

Here, $\psi_k(x, t)$ does not belong to $L^2(\Omega)$, but it satisfies boundary conditions and satisfies to the wave equation. According to (3), (4) and our assumption of $a^<$ the following is valid for $t > T$:

$$\psi_k(x; t) = \sum_{j=1}^{\infty} (a_{+,j}^> e^{i\omega_j t} + a_{-,j}^> e^{-i\omega_j t}) \varphi_j(x, t) = \sum_{j=1}^{\infty} (A_{k,j} e^{i\omega_j t} + \bar{B}_{k,j} e^{-i\omega_j t}) \varphi_j(x, t). \quad (6)$$

In the interval $0 \leq t \leq T$ the function $\psi_k(x, t)$ may be decomposed over $\varphi_j(x, t)$ in the same way as the function $u(x, t)$ in (3):

$$\psi_k(x, t) = \sum_j q_{k,j}(t) \varphi_j(x, t). \quad (7)$$

Due to (5), the following initial conditions should be satisfied:

$$q_{k,j}(0) = \delta_{j,k}, \quad \dot{q}_{k,j}(0) = -i\omega_k \delta_{j,k}, \quad (8)$$

where $\delta_{k,j}$ is Kronecker delta. Substituting (5) into the wave equation (1), we obtain the following expression for coefficients $q_{k,j}(t)$ [2, 6]:

$$\ddot{q}_{k,j} + \omega_j^2(t)q_{k,j} = 2\lambda(t) \sum_n g_{jn} \dot{q}_{k,n} + \dot{\lambda}(t) \sum_n g_{jn} q_{k,n} + \lambda^2(t) \sum_{n,m} g_{n,j} g_{n,m} q_m, \quad (9)$$

where:

$$\partial_x^2 \varphi_j(x, t) = -\omega_j^2(t) \varphi_j(x, t), \quad \omega_j(t) = \frac{j\pi}{L(t)}, \quad (10)$$

$$g_{mj} = \frac{1}{\lambda(t)} \int_0^{l(t)} \partial_t \varphi_j(x, t) \cdot \varphi_m(x, t) dx, \quad \lambda(t) = \frac{\dot{L}(t)}{L(t)}. \quad (11)$$

Therefore, $q_{k,j}$ can be computed as the solution to the obtained inhomogeneous ODE with coefficients depending on time. For varying length $L = L(t)$, but fixed boundary conditions, all contributions are known explicitly [2, 6, 9]:

$$g_{jj} = 0 \quad \text{and} \quad g_{kj} = (-1)^{k-j} \frac{2kj}{j^2 - k^2} = -g_{jk} \quad \text{for } k \neq j, \quad (12)$$

and analytical solution of (9) may be obtained approximately for a number of boundary motion laws [9, 10]. In general, solution of this equation is expressed through hypergeometric functions and its analysis is quite cumbersome.

According to (6) and (7), q_k is a sum of plain waves for $t > T$:

$$q_{k,j}(t) = A_{k,j} e^{-i\omega_j t} + \bar{B}_{k,j} e^{i\omega_j t}.$$

We will compute the scattering amplitudes $A_{k,j}$ and $B_{k,j}$ in terms of the solution $q_{k,j}$ of the ODE above:

$$\begin{pmatrix} A_{k,j} \\ \bar{B}_{k,j} \end{pmatrix} = \begin{pmatrix} e^{i\omega_j T} & e^{-i\omega_j T} \\ i\omega_j e^{i\omega_j T} & -i\omega_j e^{-i\omega_j T} \end{pmatrix}^{-1} \begin{pmatrix} q_{k,j}(T) \\ \dot{q}_{k,j}(T) \end{pmatrix}.$$

To describe Casimir radiation resulting from the cavity trembling one should perform quantization of the boundary problem (1) following the standard quantization procedure as, for example, in [3]. For these, we introduce corresponding bosonic operators (a^\dagger is adjoint to a)

$$a_{+,k}^<(t) \rightarrow a_k^<\dagger, \quad a_{-,k}^<(t) \rightarrow a_k, \quad (13)$$

$$a_{+,k}^>(t) \rightarrow a_k^>\dagger, \quad a_{-,k}^>(t) \rightarrow a_k. \quad (14)$$

By definition of annihilation and creation operators:

$$a_j^<|0\rangle = 0, \quad a_j^<\dagger|0\rangle = |1\rangle_j.$$

Operators $a_k^>$ and $a_j^<$ are related by Bogoliubov transformation:

$$a_k^> = \sum_j A_{kj} a_j^< + B_{kj} a_j^<\dagger. \quad (15)$$

Mean photon number N_k in mode k and at moment $t > T$ is calculated under assumption that at time $t < 0$ all modes were in a vacuum state $|0\rangle$:

$$N_k = \langle 0|a_k^>\dagger a_k^>|0\rangle = \sum_j \langle 0|(A_{kj} a_j^< + B_{kj} a_j^<\dagger)^\dagger (A_{kj} a_j^< + B_{kj} a_j^<\dagger)|0\rangle. \quad (16)$$

therefore coefficients A_{kj} disappear and we have:

$$N_k = \sum_j B_{kj}^* B_{kj} \langle 0|a_j^< a_j^<\dagger|0\rangle = \sum_j |B_{kj}|^2. \quad (17)$$

3. Numerical modelling of photon generation process

3.1. Numerical procedure

The decomposition of solution to the wave equation over instantaneous basis $\varphi_k(x, t)$ (Fourier method), described in the previous section, was successfully used for analysis of resonator of time-dependent length, see e.g. [3, 4, 9, 10]. However, if the shape of the resonator or the boundary conditions evolve with time, the instantaneous basis is hard to compute explicitly and the method is not useful in practice. For numerical computations with complex geometries and complex boundary conditions the finite element method (FEM) proves to be useful in various fields of science. In the section we apply FEM to analysis of the photon generation.

The crucial part of the computations is solution of the time-dependent wave equation (1) in the time interval $[0, T]$ with the Cauchy conditions at $t = 0$. Knowing the solution at $t = T$ the computation of number of generated photon is straightforward according to (17).

Due to simple geometry, we take advantage of using the basis for all moments of time. For that purpose, we make change of the coordinate $y = x/L(t)$. Making the substitution the wave equation (1) becomes the following equation on the function $v(y) = u(yL(t))$:

$$a^2 v'' = L^2 \ddot{v} - 2y \dot{L} L \dot{v}' + y^2 \dot{L}^2 v'' - (\ddot{L} L - 2\dot{L}^2) y v'.$$

with boundary conditions:

$$\alpha_1(t) L(t) v(-1) = v'(-1), \quad \alpha_2(t) L(t) v(1) = -v'(1),$$

where:

$$\dot{v} = dv/dt, \quad u' = dv/dx, \quad v' = dv/dy,$$

and we substitute second derivatives according to:

$$u' = \frac{du}{dx} = \frac{1}{L} v', \quad u'' = \frac{1}{L^2} v'', \quad \dot{u}(t, x) = \frac{dv(t; L(t)^{-1} x)}{dt} = \dot{v}(t, y) - v'(t, y) \frac{y \dot{L}}{L}.$$

$$\ddot{u}(t, x) = \ddot{v} - 2\dot{v}' \frac{y \dot{L}}{L} + \left(\frac{y \dot{L}}{L} \right)^2 v'' - \left(\frac{\ddot{L}}{L} - 2 \frac{\dot{L}^2}{L^2} \right) y v'.$$

Multiplying the equation by test function $\phi(y)$, integrating by parts and applying boundary conditions, we obtain the wave equation in the weak form:

$$\int_{-1}^1 (L^2 \ddot{v} \phi - 2\dot{L} L y \dot{v}' \phi - \dot{L}^2 y^2 v' \phi' + a^2 v' \phi' - \ddot{L} L y v' \phi) dy + (\dot{L}^2 - a^2) L [\alpha_2 v(1) \phi(1) + \alpha_1 v(-1) \phi(-1)] = 0. \quad (18)$$

We fix a basis b_k in a computational subspace in $L^2[0, 1]$, and decompose all the functions over the basis:

$$\phi(t, y) = \sum_n \phi_n(t) b_n(y), \quad v(t, y) = \sum_n v_n(t) b_n(y).$$

We use basis of continuous functions which are piecewise linear on every interval $[y_n, y_{n+1}]$, $y_n = n/N$, $n = -N \dots N$ such that $b_n(y_k) = \delta_{n,k}$. All the elements can be expressed in term of the following canonical element e :

$$b_n(y) = e(n + y/\Delta), \quad \Delta = 2/(N + 1), \quad e(z) = \begin{cases} 1 - |z|, & |z| < 1, \\ 0, & |z| \geq 0. \end{cases}$$

Then equation (18) takes the form of the following system of linear equations for all j :

$$\sum_k L^2 \ddot{v}_k A_{jk} - 2\dot{L} L \dot{v}_k B_{jk} - \dot{L}^2 v_k D_{jk} + a^2 v_k M_{jk} - \ddot{L} L v_k B_{jk} + (\dot{L}^2 - a^2) L \delta_{jk} [\alpha_1 \delta_{j,-N} + \alpha_2 \delta_{j,N}] = 0,$$

where the constant matrix coefficients can be computed explicitly (doing change $z = y/\Delta$):

$$A_{jk} = \int_{-1}^1 b_k b_j dy = \Delta \int_{-N}^N e(z+k) e(z+j) dz = \Delta \begin{cases} (\delta_{k>-N} + \delta_{k<N})/3, & k = j, \\ 1/6, & |k-j| = 1, \\ 0, & \text{otherwise,} \end{cases}$$

$$B_{jk} = \int_{-1}^1 b'_k b_j y dy = \Delta \begin{cases} (\delta_{k>-N} - \delta_{k<N})(1/6 - k/2), & k = j, \\ -1/3 \pm k/2, & j = k \pm 1, \\ 0, & \text{otherwise,} \end{cases}$$

$$D_{jk} = \int_{-1}^1 b'_k b'_j y^2 dy = \Delta \begin{cases} (\delta_{k>-N}(3k^2 - 3k + 1) + \delta_{k<N}(3k^2 + 3k + 1))/3, & k = j, \\ k^2 \pm k + 1/3, & j = k \pm 1, \\ 0, & \text{otherwise,} \end{cases}$$

$$M_{jk} = \int_{-1}^1 b'_k b'_j dy = \frac{1}{\Delta} \begin{cases} \delta_{k>-N} + \delta_{k<N}, & k = j, \\ 1, & |j - k| = 1, \\ 0, & \text{otherwise.} \end{cases}$$

Grouping terms for given order of derivative, we obtain:

$$L^2 A \ddot{v} - 2 \dot{L} L B \dot{v} + \left(a^2 M - \dot{L}^2 D - \ddot{L} L B \right) v + (\dot{L}^2 - a^2) L (\alpha_1 F_{-N,jk} + \alpha_2 F_N) = 0 \quad \forall j, \quad (19)$$

where non-zero entries of the matrices F_n are only as follows: $F_{n,jk} = \delta_{nj} \delta_{nk}$. The matrices A , B , D and M can be precomputed, since we assume the discretization to be fixed, hence the dependence on the resonator length L and the boundary conditions α_1 , α_2 are explicitly stated in Equation 19. The matrix A is invertible, therefore, the equation can be solved with respect to \ddot{v} . The order of ODE can be reduced introducing $Y = (\dot{v}, v)$, which satisfies:

$$Q(t) \dot{Y} = P(t) Y, \quad Q = \begin{pmatrix} L^2 A & 0 \\ 0 & 1 \end{pmatrix},$$

$$P = \begin{pmatrix} 2 \dot{L} L B & \dot{L}^2 D - a^2 M + \ddot{L} L B + (a^2 - \dot{L}^2) L (\alpha_2 F_N + \alpha_1 F_N) \\ 1 & 0 \end{pmatrix}.$$

We do integration over time using fifth order Radau method with three stages. The method is defined by the following Butcher table:

$$\begin{array}{c|ccc} c_1 & a_{11} & a_{12} & a_{13} \\ c_2 & a_{21} & a_{22} & a_{23} \\ c_3 & a_{31} & a_{32} & a_{33} \\ \hline & b_1 & b_2 & b_3 \end{array} = \begin{array}{c|ccc} 0 & \frac{1}{9} & \frac{-1-\sqrt{6}}{18} & \frac{-1+\sqrt{6}}{18} \\ \frac{3}{5} - \frac{\sqrt{6}}{10} & \frac{1}{9} & \frac{11}{45} + \frac{7\sqrt{6}}{360} & \frac{11}{45} - \frac{43\sqrt{6}}{360} \\ \frac{3}{5} + \frac{\sqrt{6}}{10} & \frac{1}{9} & \frac{11}{45} + \frac{43\sqrt{6}}{360} & \frac{11}{45} - \frac{7\sqrt{6}}{360} \\ \hline \frac{1}{9} & \frac{4}{9} + \frac{\sqrt{6}}{36} & \frac{4}{9} - \frac{\sqrt{6}}{36} & \end{array}$$

For a selected time, step dt , the solution v is updated to the next time step according to:

$$Y(t + dt) = Y(t) + dt \sum_{s=1}^3 b_s K_s.$$

The vectors K_s are solutions to the algebraic system:

$$Q(t + c_s dt) K_s = P(t + c_s dt) [Y(t) + dt \sum_{q=1}^3 a_{sq} K_q] \quad \forall s.$$

All the matrices are tridiagonal, hence, block tridiagonal solver can be used to solve the system. Another option is to solve the linear system using bi-conjugate gradient method, which we adopt here (the matrix B is not symmetric).

3.2. Numerical simulation results

The framework developed above allows us to compare effect of both cavity length and boundary conditions periodic variation on number of generated photons due to dynamical Casimir effect. The correct model of experiment in [8], where the dynamical Casimir effect was observed in a SQUID device, should probably take into account both change of the effective length and boundary conditions, however until now, theorists were focused on the length modulation. However, as we demonstrate below time-dependent boundary conditions give comparable or larger contribution to the photon generation than the time-dependent geometry.

We run simulation of the 1D cavity modeled by a segment $(-L, L)$ where the segment length is modulated according to $L(t) = 1 + A \sin \pi \omega_L t$, A is the amplitude of oscillations (set to 0.1 in our simulations) and ω_L is the oscillation frequency. We use the same dimensionless units as in Equation (1) and set speed of light equals 1. The period of the lowest eigenmode of the resonator is 2 in the unit and we consider the cavity trembling time T of the same magnitude. The velocity of boundary in all the simulations was smaller than 30% of the speed of light. The interval of simulation was taken to be small multiples of the trembling time T . These short time intervals of transition from eigenmodes to the cavity wall induced dynamics of the electromagnetic field is hard to observe in practice, hence our simulation provides some insight into the process.

The boundary conditions are assumed to be of Robin's type (2). The parameters α_1 , α_2 in the conditions oscillate from $+\infty$ (Dirichlet type) to 0 (Neumann type). A sufficiently large value of the parameters gives almost vanishing value on the boundary in the simulation, hence we restrict ourself to variation of α_k in the interval $[10^{-3}, 10^3]$ and its oscillation is defined as follows:

$$\alpha_1 = \exp(7 \cos \pi \omega_\alpha t),$$

where ω_α is the boundary condition oscillation rate. The formula is chosen somewhat arbitrary, but it guarantees symmetry between the Dirichlet and the Neumann conditions. The trembling time T is always an integer multiple K of switching period to ensure the Dirichlet boundary conditions in the beginning and the end of the trembling time interval, that is $T = 2K/\omega_\alpha$.

The solution to the time-dependent wave equation are shown in Fig. 1 for varying length L and in Fig. 2 for varying boundary conditions. The effect of variation in both cases are stronger for higher cavity trembling frequency. For the frequency ω_L of the cavity wall motion few times smaller than ground mode of the cavity, the evolution is adiabatic and the solution u is only slightly affected by the geometry modification. The cavity wall moving faster generates waves and gradually eliminate the ground mode, resulting in Helmholtz-like motion having triangle pattern in Fig. 1, which repeats itself infinitely.

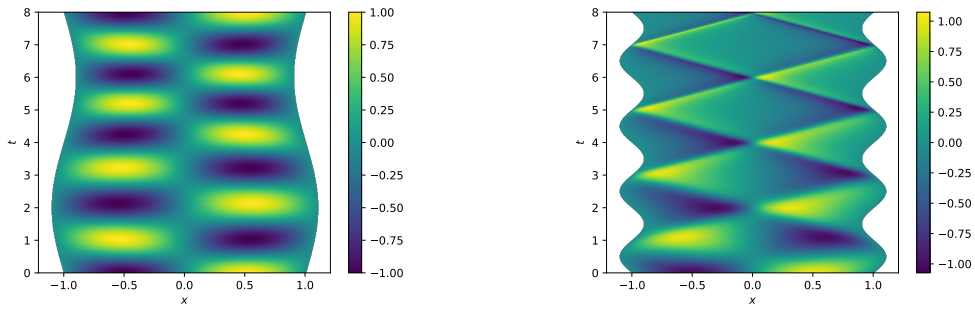


FIG. 1. Evolution of the ground mode of the cavity according to the wave equation with moving boundary for the simulation interval length $T = 8$: (left) adiabatic regime $\omega_L = 0.25$, (right) the cavity wall driven regime $\omega_L = 1$. Heat map shows real part of the solution.

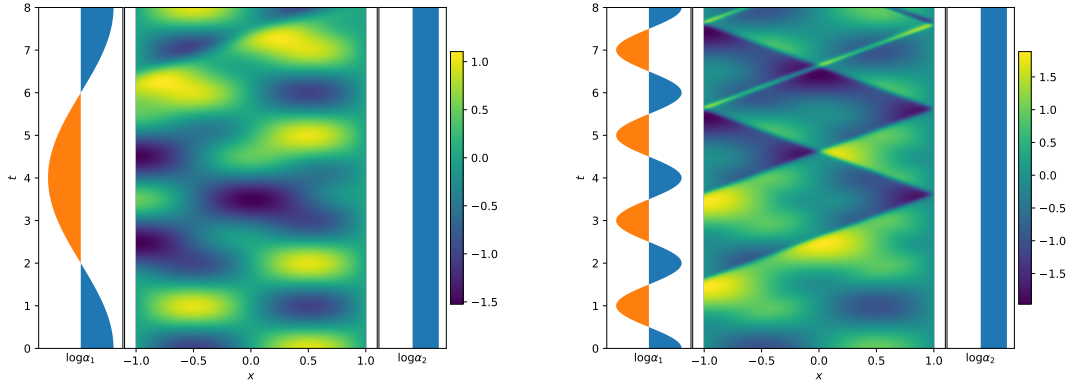


FIG. 2. Solution u to the wave equation with oscillating Robin's boundary condition for the simulation interval length $T = 8$: (left) low frequency regime $\omega_\alpha = 0.25$, (right) the cavity wall driven regime $\omega_\alpha = 1$. Initial conditions correspond to the resonator in the ground state. Heat map shows real part of the solution. The Robin's boundary conditions parameters are shown on left ($\log \alpha_1$) and right ($\log \alpha_2$) panels, initial conditions correspond to the Dirichlet BC, negative values corresponds to the Neumann BC.

The variation of boundary conditions results in change of eigenfrequencies of the resonator, hence noticeably affects dynamics even for small frequencies ω_α . Since we assume time-dependent boundary conditions on single boundary, the symmetry of solution is broken, thus the irregular texture on the heat map. The amplitude of the solution is not conserved in the process, hence number of generated photons is expected to be larger for longer generation period. For rapid boundary conditions switching, the ground state rapidly dissipates on the boundary, and the solution to the wave equation is dominated by wave with source on the boundary of the cavity.

We analyzed 20 lowest modes of the resonator using 201 finite element doing 4th order Runge-Kutta simulation with time step $4 \cdot 10^{-4}$. Then, the average number of photons generated due to the dynamical Casimir effect was estimated according to Equation (17). The computation was repeated for different periods of boundary oscillations, the result are presented in Fig. 3. We computed total number of generated photons for boundary oscillation repeated K times, $K \leq 3$. In all cases, the number of generated photons decreases as trembling time T increases (and therefore oscillation frequency tends to zero). However, the decrease is not monotonic and is quite intricate. The decrease is slower for the variation of the boundary conditions, and total number of photons tends to be smaller for the oscillation of the cavity size.

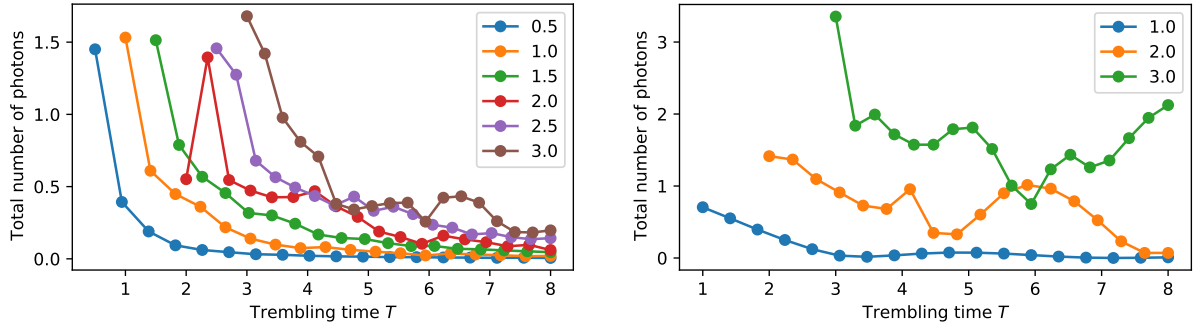


FIG. 3. Average number of generated photons as function of length T of time interval when perturbation to the boundary is applied. Left panel: the cavity length L is varied, right panel: the boundary conditions parameter α_1 is oscillating. Perturbation frequency $\omega = 2K/T$ is matched with T in such a way that K period of oscillation happen during time T . Different lines correspond to different values of K .

The lines with higher K illustrates what happens under repetition of the boundary perturbation. E.g. point for $K = 2$ and $T = 2$ correspond to double repetition of the oscillation for $K = 1$ and $T = 1$. As we see from the left panel in Fig. 3, repetition of the cavity shrinking does not produce more photons then the single perturbation, except for few points. On the contrary, the repetition of oscillation of the boundary conditions do produce new photons, even more the dependence of number of photons on number of repetitions K is faster than linear.

4. Discussion and conclusion

We considered generalized model of dynamic Casimir effect in a trembling cavity taking into account periodic perturbation of boundary conditions. The numerical scheme described in the article for solution of the 1D wave equation with time-dependent geometry and boundary conditions forms a basis for simulation of dynamical Casimir effect relaxing restrictions on the behavior of the boundary. Our numerical simulations demonstrated that boundary conditions oscillation has significant effect on number of generated photons and the number can be even larger than for variation of effective length of the resonator.

The developed numerical scheme based on finite element method can be naturally extended to two and three dimensional cavities, and can be used to simulate experimental settings. Since perturbation of the boundary conditions can be used to boost photon generation, quantum graphs (also called quantum networks) is a natural candidate to increase effectiveness of the generation process.

5. Acknowledgements

The review of quantum non-stationary, multi-mode parametric processes and dynamical Casimir effect in Section 2 was supported by the Ministry of Science and Education of the Russian Federation (Passport No. 2019-0903). Investigation of 1D cavity with moving walls in Section 2 was partially financially supported by grant 20-31-90036 of Russian Foundation for Basic Research. The development of numerical method of simulation of dynamical Casimir effect in Section 3 was funded by Russian Science Foundation (Grant 19-42-06302).

References

- [1] Nation P.D., Johansson J.R., Blencowe M.P. Colloquium: Stimulating uncertainty: Amplifying the quantum vacuum with superconducting circuits. *Rev. Mod. Phys.*, 2012, **84**, P. 1–24.
- [2] Crocce M. Resonant photon creation in a three-dimensional oscillating cavity. *Phys. Rev. A*, 2001, **64** (1), 013808.
- [3] Law C. Effective hamiltonian for the radiation in a cavity with a moving mirror and a time-varying dielectric medium. *Physical Review A*, 1994, **49** (1), P. 433–437.
- [4] Law C. Interaction between a moving mirror and radiation pressure: A hamiltonian formulation. *Physical Review A*, 1995, **51** (3), P. 2537–2541.
- [5] Sassaroli E., Srivastava Y., Widom A. Photon production by the dynamical casimir effect. *Phys. Rev. A*, 1994, **50** (2).
- [6] Dodonov V. Generation and detection of photons in a cavity with a resonantly oscillating boundary. *Phys. Rev. A*, 1996, **53** (4).
- [7] Moore G. Quantum theory of the electromagnetic field in a variable length one dimensional cavity. *Journal of Mathematical Physics*, 1970, **11**, P. 2679.
- [8] Wilson C., Johansson G. Observation of the dynamical Casimir effect in a superconduction circuit. *Nature*, 2011, **479**, P. 376–379.
- [9] Dodonov V. Current status of the dynamical Casimir effect. *Physica Scripta*, 2010, **82**, 038105.
- [10] Dodonov V.V. Fifty years of the dynamical Casimir effect. *Physics*, 2020, **2** (3), P. 67–104.
- [11] Lähteenmäki P., Paraoanu G.S., Hassel J., Hakonen P.J. Dynamical Casimir effect in a Josephson metamaterial. *Proceedings of the National Academy of Sciences*, 2013, **110** (11), P. 4234–4238.
- [12] Svensson I.-M., Pierre M., et al. Microwave photon generation in a doubly tunable superconducting resonator. *Journal of Physics: Conference Series*, 2018, **969**, 012146.
- [13] Good M.R.R., Linder E.V. Slicing the vacuum: New accelerating mirror solutions of the dynamical Casimir effect. *Phys. Rev. D*, 2017, **96**, 125010.
- [14] Li L., Li B.-Z. Numerical solutions of the generalized Moore's equations for a one-dimensional cavity with two moving mirrors. *Physics Letters A*, 2002, **300** (1), P. 27–32.
- [15] Alves D.T., Granhen E.R. A computer algebra package for calculation of the energy density produced via the dynamical casimir effect in one-dimensional cavities. *Computer Physics Communications*, 2014, **185** (7), P. 2101–2114.
- [16] Popov I.Y. Asymptotic series for the spectrum of the Schrödinger operator for layers coupled through small windows. *Theor. Math. Phys.*, 2002, **131** (3), P. 407–418.
- [17] Popov I.Y. Asymptotics of bound states and bands for laterally coupled waveguides and layers. *J. Math. Phys.*, 2002, **43** (1), P. 215–234.
- [18] Popov I., Trifanov A.I., Trifanova E.S. Coupled dielectric waveguides with photonic crystal properties. *Zh. Vychisl. Mat. Mat. Fiz.*, 2010, **50**, P. 1931–1937.
- [19] Nekrashevych V., Teplyaev A. Groups and analysis on fractals, analysis on graphs and its applications. *Amer. Math. Soc.*, 2009, **77**, P. 143–180.
- [20] Korotyaev E. Schrodinger operator with a junction of two 1-dimensional periodic potentials. *Asymptotic Analysis*, 2005, **45**, P. 73–97.
- [21] Matrasulov D.U., Yusupov J.R., Sabirov K.K., Sobirov Z.A. Time-dependent quantum graph. *Nanosystems: Phisycs, Chemistry, Mahematics*, 2015, **6** (2), P. 173–181.
- [22] Lobanov I.S., Nikiforov D.S., et al. Model of time-dependent geometric graph for dynamical Casimir effect. *Indian Journal of Physics*, 2020, DOI 10.1007/s12648-020-01866-5.
- [23] Popov I.Yu., Trifanov A.I., Trifanova E.S. Dielectric waveguides with photonic crystal properties. *Comp. Math. Math. Phys.*, 2010, **50** (11), P. 1830–1836.
- [24] Melikhova A.S., Popov I.Y. Spectral problem for solvable model of bent nanopeapod. *Applicable Analysis*, 2017, **96** (2), P. 215–224.
- [25] Vorobiev A.M., Bagmutov A.S., Popov A.I. On formal asymptotic expansion of resonance for quantum waveguide with perforated semitransparent barrier. *Nanosystems: Phys. Chem. Math.*, 2019, **10** (4), P. 415–419.
- [26] Exner P., Kostenko A., Malamud M., Neidhardt H. Spectral theory of infinite quantum graphs. *Ann. H. Poincare*, 2018, **19**, P. 3457–3510.
- [27] Berkolaiko G., Kuchment P. *Introduction to Quantum Graphs*. AMS, Providence, 2012.
- [28] Eremin D.A., Grishanov E.N., Nikiforov D.S., Popov I.Y. Wave dynamics on time-depending graph with Aharonov-Bohm ring. *Nanosystems: Physics, Chemistry, Mathematics*, 2018, **9** (4), P. 457–463.
- [29] Barseghyan D., Exner P., Khrabustovskyi A., Tater M. Spectral analysis of a class of Schrödinger operators exhibiting a parameter-dependent spectral transition. *J. Phys. A*, 2016, **49**, 165302.
- [30] Fedorov E.G., Popov A.I., Popov I.Y. Metric graph version of the FitzHugh-Nagumo model. *Nanosystems: Physics, Chemistry, Mathematics*, 2019, **10** (6), P. 623–626.

Physicochemical and biochemical properties of the Keplerate-type nanocluster polyoxomolybdates as promising components for biomedical use

A. A. Ostroushko¹, K. V. Grzhegorzhevskii¹, S. Yu. Medvedeva^{1,2}, I. F. Gette²,
M. O. Tonkushina¹, I. D. Gagarin¹, I. G. Danilova^{1,2}

¹Ural Federal University named after the first President of Russia B. N. Yeltsin,
Ekaterinburg, Russia

²Institute of Immunology and Physiology of the Ural Branch of the Russian Academy of Sciences,
Ekaterinburg, Russia

alexander.ostroushko@urfu.ru

DOI 10.17586/2220-8054-2021-12-1-81-112

The paper discusses the results of a research on physicochemical and biochemical properties of the Keplerate-type molybdenum-based nanocluster polyoxometalates (POMs), which show promise in the field of biomedicine as a means of targeted drug delivery, including the transport to immune privileged organs. POMs can be considered as components of releasing systems, including the long-acting ones with feedback (for controlling the drug active component release rate). POMs are promising drugs for the treatment of anemia. Also, the paper deals with the results of studies of POM effect on living systems at the molecular and cellular levels, at that of individual organs, and on the organism as a whole. The mechanism and kinetics of POM destruction and possibilities of stabilization, the oscillatory phenomena manifestation, the formation of POM conjugates with bioactive substances which can be released during the destruction of POM, with polymer components, and with indicator fluorescent dyes, as well as forecasts for further research, are considered.

Keywords: Keplerate-type nanocluster polyoxomolybdates, physicochemical and biochemical properties, impact on living systems, means of targeted delivery, releasing systems, prolonged action.

Received: 27 March 2020

Revised: 14 July 2020, 19 January 2021

Contents

1. Introduction
 - 1.1. Nanoscale components of targeted drug delivery systems.
 - 1.2. Nanocluster polyoxometalates (POMs).
 2. Investigation of the effect of Keplerate-type POMs on living systems at the level of the organism, of individual organs, and at the molecular-cellular level.
 - 2.1. Study of POMs accumulation characteristics and toxicity.
 - 2.2. POMs impact at the cellular-molecular level.
 3. Association of POMs with bioactive substances and polymers.
 4. POMs destruction processes and their stabilization.
 5. Prospects for the creation of POM-based releasing systems with feedback.
 6. Conclusion
- References

1. Introduction

1.1. Nanoscale components of targeted drug delivery systems

The targeted delivery of drugs can employ nanostructured systems that differ in terms of the nature of components and design, to which, for instance, liposomal systems belong [1–13]. Some natural aspects can impede the use of liposomal agents. These aspects include the active capturing of liposomes by macrophages, which results in the limited possibility of drug delivery to some organs and tissues. The capturing also significantly reduces the time of drugs circulation in the organism, thus leading to the liposome membrane degradation under the influence of lipoproteins. In addition, the manufacturing of liposomal products employs rather sophisticated technologies. Various inorganic nanoscale objects are considered as components of targeted drug delivery systems; these include metal, oxide or complex oxide objects, and some other types of nanoparticles [14–25], as well as carbon clusters (fullerenes, nanotubes, graphene, and nanodiamonds) [26–59]. These objects can be used, for instance, as shells or cores of nanocapsules, providing the release of drugs, for example, under local electromagnetic influence. They can play the

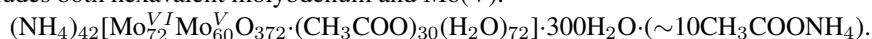
role of carriers of bioactive substances in surface functionalization [44–46, 48, 49, 51–56], or when the porous structure of nanoparticles and clusters is used, including non-magnetic and magnetic systems for delivery, therapy [57–83] and diagnostics [60–68]. The use of carbon clusters and inorganic nanoparticles is associated with the problem of removing such materials from the body after they have performed their function, in order to reduce the xenobiotics load.

Nanocluster polyoxometalates (POMs) can be produced and characterized in terms of composition and structure using fairly simple and proven techniques. Representatives of this class of compounds, in particular molybdenum-containing ones, do not pose a danger to a living organism and are practically non-toxic. They do not accumulate in the body for long, because, for instance, they are capable of gradual decomposition into decay products, which are assimilated as microelements and further evacuated in the course of natural metabolism. For these reasons, POMs are considered as promising materials for targeted delivery of drugs, of long-acting therapeutic agents, including those with feedback for controlling the drug release rate. Also, the advantages of POMs include their solubility in aqueous media and the charge of polyanions, which provides the possibility of iontophoretic delivery. The present review briefly discusses the biochemical properties of the most promising POMs, their ability to associate with biologically active substances, as well as issues related to the processes of POM destruction and stabilization as a key aspects in terms of biomedical application.

1.2. Nanocluster polyoxometalates (POMs)

Various composed and structured POMs, which include both hetero- and isopoly compounds, have found a wide application as catalytic systems, components of hybrid structures, supramolecular assemblies, etc. [84–87]. New types of molybdenum-containing nanocluster polyoxometalates with toroidal [88–91] and fullerene-like structures (Keplerates) containing subnanometer-sized windows and pores [92, 93] (Fig. 1) became known at the turn of the past and present centuries due to studies carried out at the Bielefeld University (Bielefeld, Germany) under the guidance of Prof. A. Müller, whose laboratory synthesized these compounds and confirmed their structure. In comparison with other nanosized particles, such water-soluble clusters have a high ionic charge and are capable of gradual degradation. The discovery of such POMs was, apparently, one of those cases, which are far from rare in the history of science, when such POMs had been most likely obtained in earlier experiments, but the researchers were unaware of their unique structure, which was later deciphered and purposefully reproduced. The POM structure was primarily characterized by single crystal X-ray structure analysis. The everyday scientific practice employs for this purpose reliable and more rapid spectroscopic methods (e.g., IR, Raman, NMR spectroscopy) [94]. The obtaining of giant POM clusters was also confirmed by mass spectrometry (MALDI method) [95]. Among the merits of Prof. Müller's group is the creation of fairly simple and reproducible methods for obtaining POM [93] with a specified structure and composition. In addition to the above-mentioned, basket-like molybdenum-containing POMs [96], with a structure derived from Keplerates, as well as giant clusters named by their creators “nano hedgehog”, “blue lemon” [97, 98] were also obtained.

The structure of these POMs is based on such structural blocks (coordination oxygen polyhedra surrounding multicharged metal cations) such as octahedra, pentagonal bipyramids, which are connected to each other by vertices or edges. In particular, Mo₂ dimolybdenum bridges, Mo₆ and Mo₁₁ blocks should be attributed to basic structural elements. The symmetry of the latter (C₅ or C_s point group) determines the shape of the resulting nanocluster (Keplerate or toroid, respectively). The structure of a POM is stabilized, as a rule, by the organic or inorganic acid residues and water molecules. POMs contain a significant number of molecules of both constitutional and intracuster water. The latter also occupy the internal cavity of Keplerates in the normal state and can exchange with molecules of other substances through the pores. POM synthesis proceeds in the self-assembly mode under conditions of a specified medium acidity and in the presence of a reducing agent, since, for instance, the basic structure of Mo₁₃₂ Keplerate (Fig. 1) includes both hexavalent molybdenum and Mo(V):



There is a possibility to use the basic structure of a POM and substitute ions in it. For instance, the isostructural substitution of Mo(V) with ferric ions leads to the formation of a Mo₇₂Fe₃₀ Keplerate [99] (Fig. 2):



The POMs isolated from the concentrated stock solution are mainly crystalline substances, which may include a fraction of the material in an amorphous state [94]. Upon subsequent dissolution in water, POMs dissociate into Keplerate polyanions and cations (ammonium, sodium and potassium), or do it as a weak acid (Mo₇₂Fe₃₀). The crystallographic size of a Mo₁₃₂ ion is 2.9 nm (Mo₇₂Fe₃₀ is 2.5 nm), while the hydrated Mo₁₃₂ ion in a solution has a size of 3.2 nm. The charge of polyanions depends on the acidity and environment, and can reach –42 and –22 [93, 100] for Mo₁₃₂ and Mo₇₂Fe₃₀, respectively.

The POMs capable, in principle, of changing the energy state of molecules included in their cavity, are considered promising catalytic materials in reactions of fine organic synthesis, membrane technologies, and sensorics [101–113].

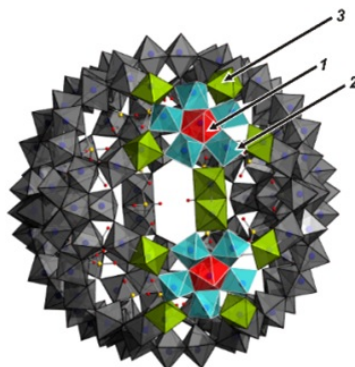


FIG. 1. Structure of Mo_{132} polyoxometalate. The red polyhedron (No. 1) marks the pentagonal MoO_7 bipyramid, linked by common edges with five MoO_6 octahedra (blue, No. 2) – this is the so-called Mo_6 structural unit; Highlighted in green (No. 3) are $\text{Mo}^{\text{V}}\text{O}_6$ polyhedra, which are part of Mo_2 dimolybdenum bridges

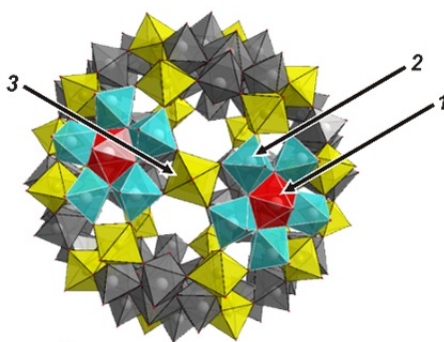
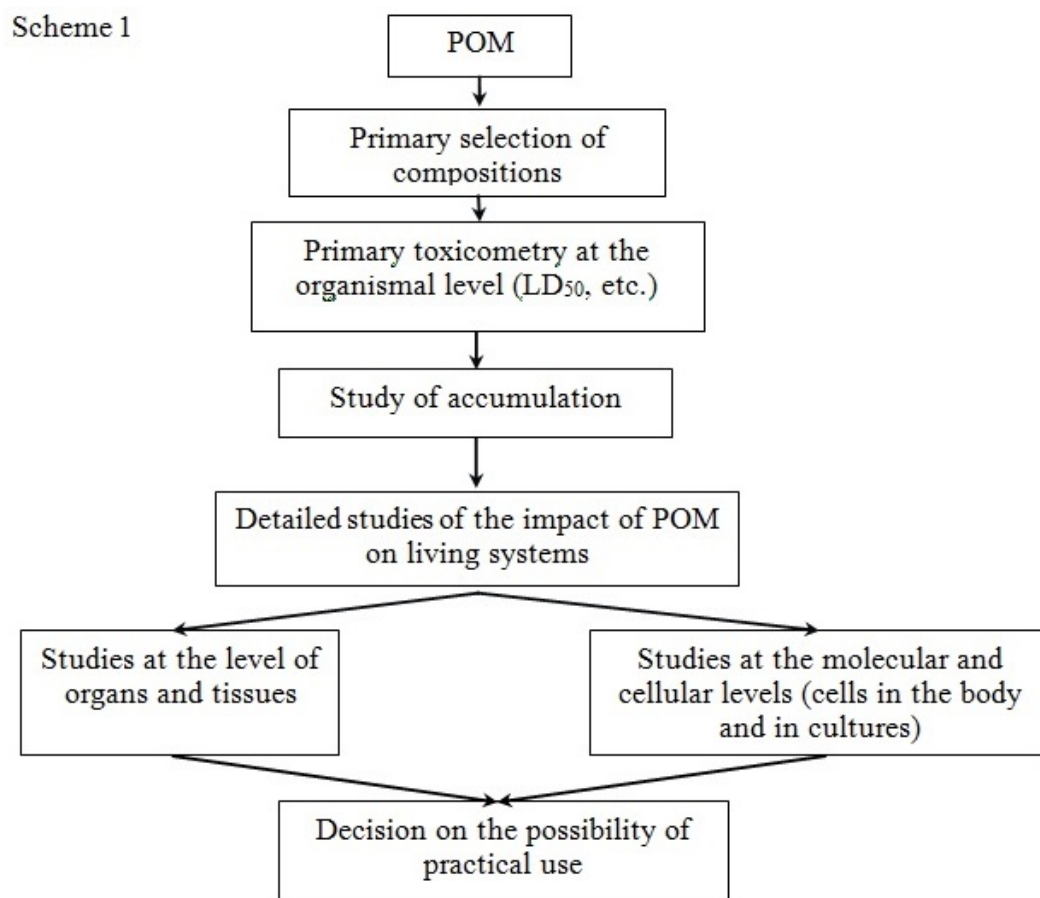


FIG. 2. Structure of $\text{Mo}_{72}\text{Fe}_{30}$ polyoxometalate. Iron-coordinated oxygen polyhedra are marked in yellow (No. 1 is MoO_7 ; 2 is MoO_6 ; 3 is FeO_6)

At the same time, such compounds are also of interest for the biomedical industry (Scheme 1). On the one hand, they can be interesting as individual drugs, because molybdenum and iron are widely known to be used in vitamin and mineral supplements as microelements involved in a number of enzymatic processes of importance for the organism [114]. In addition, it was shown that simpler molybdenum-containing POMs can be used in chemotherapy [115, 116]. On the other hand, the initially predicted possibility of the formation of POM conjugates with bioactive substances, drugs, and metal cations using intra- and extrasphere interactions, the possibility of their transport (including iontophoretic) in the body, adds relevance to the studies of POM in the field of targeted drug delivery and diagnostics [117–131]. These prospects may relate, inter alia, to immunomodulatory and antiviral agents. Important aspects of iontophoretic transport include the potential ability to deliver drugs to lesion areas and body tissues with low degree of vascularization. The very first experimental results showed that these ideas are promising. The low toxicity of Keplerate POMs for the warm-blooded animals, in particular of the iron-containing compounds, has been established on the basis of a set of data [132–137]. When studying the acute and subacute effects of $\text{Mo}_{72}\text{Fe}_{30}$ on rats, no significant negative changes in internal organs were revealed. The animal organism is able to adapt to the action of the named POM, which is confirmed by the absence of a pronounced autoimmune reaction of lymphocytes to hepatocytes during the intramuscular administration of a $\text{Mo}_{72}\text{Fe}_{30}$ preparation in the form of an aqueous solution. There is no long-term and substantial accumulation of POMs and their components in the body (various organs and tissues), as they are excreted by metabolism. This occurs, inter alia, due to the POM degradation into simpler components [106, 137]. The issues of POM toxicity are discussed in more detail below. At the same time, in the case of iontophoretic administration, it is possible to create a temporary $\text{Mo}_{72}\text{Fe}_{30}$ depot localized, for example, in the skin and partly in the subcutaneous fatty tissue, which ensures a prolonged action of POM and its conjugates. In general, the present review is devoted to the

consideration of specific properties and behavior of POMs, as well as to generalization of the results obtained by its authors.



2. Investigation of the effect of Keplerate-type POMs on living systems at the level of the organism, of individual organs, and at the molecular-cellular level

2.1. Study of POMs accumulation characteristics and toxicity

The chosen and studied¹ POMs Mo₁₃₂ and Mo₇₂Fe₃₀ exhibited both similar and different behavior due to their different composition. While the first of them contains Mo(V) in addition to Mo(VI), the second one includes both molybdenum and iron in the highest oxidation states, which makes it promising in terms of low toxicity (no lethality found in animals). The accumulation of Mo₁₃₂ [136] was studied by injecting it into the gastrocnemius muscle of rats at a concentration of $1.5 \cdot 10^{-4}$ mol/L daily for a month. A single dose of POM amounting to 0.15 mg/100 g of the body weight, corresponded to the upper limit of the normal daily intake of molybdenum and to the supposed therapeutic dose. Intact animals served as the control. The absence of the drug and its components accumulation in the liver and bones was established. A sharp decrease in the content of molybdenum in the kidneys was found, the cause of which is, apparently, the excretion of the excessive amount of this element via the urinary tract. Experiments with the Mo₇₂Fe₃₀ polyoxometalate [132, 133, 137] administered at the same dosage, made it possible to establish for this POM the absence of accumulation of molybdenum in the liver, kidneys, bones, and skin of animals, including its hairy part and subcutaneous fatty tissue, since the average values of molybdenum content in the experimental samples after the termination of the procedures did not differ significantly from those in the intact animals.

¹The results of studies of the effect of Keplerate POMs on the animal subject, in particular, the data on transport, accumulation characteristics and toxicity were obtained on outbred rats of both sexes, weighing 200–230 g, kept on the usual diet of the vivarium. The keeping conditions and handling of the animals used in the experiment were in accordance with the principles formulated in Directive 2010/63/EU of the European Parliament and of the European Council of 22 September 2010 on the protection of animals used for scientific purposes (Official Journal of the European Union, 2010). European Parliament, Council, Directive 2010/63/EU of the European Parliament and of the Council of 22 September 2010 on the Protection of Animals Used for Scientific Purposes. *Off. J. Eur. Union.*, 2010, **53**, P. 33–79. doi:10.3000/17252555.L.2010.276.eng.

The histological analysis [132, 137] of animal organs [138] and the results of hematologic studies [134] indicated a relatively higher toxicity of Mo_{132} as compared to $\text{Mo}_{72}\text{Fe}_{30}$. Signs of hepatocyte damage were observed for Mo_{132} . However, the characteristic signs of intensified liver regeneration processes were obviously observed. The histologic analysis of kidney sections from the experimental group of animals after administration of $\text{Mo}_{72}\text{Fe}_{30}$ showed that the structural changes in the organ were minimal. It should be stressed that a weaker toxic effect of iron-molybdenum POMs [133, 139] was confirmed by the analysis of such biochemical parameters [140] characterizing the state of various organs, as aspartate aminotransferase (AST), alanine aminotransferase (ALT), alkaline phosphatase, alpha amylase, urea, and the total protein.

An analysis of peripheral blood parameters [138, 140] of animals allowed one to draw the conclusion that there was no anemia [141] in the group of animals that got Mo_{132} injections, since no significant difference was found in the number of erythrocytes, concentration of hemoglobin, the content and concentration of hemoglobin in erythrocytes in the experimental and intact rats. The total leukocytes in animals that got Mo_{132} injections also did not increase, which indicates the absence of a systemic inflammatory process. The total leukocytes did not significantly increase in the animals within 30 days after $\text{Mo}_{72}\text{Fe}_{30}$ injections, and the leukocyte formula remained almost unchanged, which indicates the absence of inflammation at the organismal level.

An analysis of red blood parameters in rats injected with $\text{Mo}_{72}\text{Fe}_{30}$ yielded a conclusion that there was no anemia – a sign characteristic of many chronic intoxications, since the content of hemoglobin in erythrocytes of experimental rats did not decrease, but increased, on the contrary [108, 139, 142]. Moreover, the experimentally revealed effect of rapid recovery of the hemoglobin level in animals after modeling the post-hemorrhagic anemia [141] is interesting from the point of view of the possible use of POMs in treatment and prevention of iron deficiency anemia, which is confirmed by a patent [142]. The presence of molybdenum in the preparation does not prevent an increase in its effectiveness; besides, molybdenum is effectively removed from the body. Given its lower toxicity, $\text{Mo}_{72}\text{Fe}_{30}$ was subjected to additional studies, in particular, of acute and subacute toxicity [133]. In order to further study the pathways of possible toxic action of POM [133], three methods of Keplerate administration were chosen, that is, the intramuscular, intraperitoneal, and intragastric. The intragastric (1 day) method of administration allowed a significant increase in the POM dose by using not only a POM solution, as in other methods, but also a suspension (concentration of 60 mg/ml). The introduction of the maximum possible dose of POM by the intragastric method was not accompanied by lethality, therefore, the conclusion about low toxicity of the tested compound was confirmed, especially since the amount of POM was 200 times higher than the estimated therapeutic dose of 0.15 mg/100 g.

The blood plasma of rats in all experimental groups [133] showed no increase in the activity of alkaline phosphatase, which is one of the indicators of cholestasis (impaired bile secretion). This fact indicated that the bile-producing function of hepatocytes was preserved after both short and long-term administration of POM. Alkaline phosphatase is also a specific enzyme of osteoblasts, it is involved in mineralization, and the activity of this enzyme is an indicator of changes in the rate of mineral components remodeling in the bone tissue. Molybdates are known of being able to be capable of reducing the activity of phosphatases, probably through the interaction of molybdenum with the cysteine thiol groups and histidine imidazole groups located in the active sites of enzymes [138, 140]. The groups of animals with single intramuscular, intraperitoneal, and intragastric administration of $\text{Mo}_{72}\text{Fe}_{30}$ have shown a relatively small (within 20–25%), but significant decrease in alkaline phosphatase activity [133], possibly due to the inhibitory effect of molybdenum. Just a short-term, 1 day-long, decrease in the activity of alkaline phosphatase eliminates the risk of osteoporosis development after a single administration of Keplerates.

When comparing the average values of other indicators in groups of animals with acute administration of POM (alpha-amylase activity, total protein and creatinine content in blood plasma), no significant differences with those of intact rats were found, which evidences the absence of pronounced changes in the kidneys, liver, and pancreas of animals in these groups [133]. The group with subacute POM administration showed no significant deviations of all the studied biochemical indicators from the norm, which suggested the absence of cytolysis and damage to the liver, kidneys, myocardium, pancreas, and bone tissue after a long (30 days) daily POM administration.

It is important to note that after POM administration by all the studied methods, a significant increase in the content of molybdenum in the blood was recorded [133] after a single POM load. The amount of molybdenum found in the blood 1 day after the administration of Keplerate POMs was proportional to the amount of the injected nanomaterial. A significant decrease in the level of molybdenum in the blood after 1 day compared to the content of the microelement one hour after intramuscular injection, as well as the normalization of the indicator after daily injections of POM within 30 days, was consistent with previously obtained data on the absence of molybdenum accumulation [132, 137, 141]. The absence of molybdenum accumulation [133] in the liver, kidneys, skin, and bone tissue [138] is probably associated with the decomposition and accelerated excretion of the elements constituting POM, which contributes to the normalization of the studied parameters (glucose, aminotransferase, and alkaline phosphatase values) [138] by day 30, a change of which was recorded upon a single injection of POM.

2.2. POMs impact at the cellular-molecular level

Further investigations of $\text{Mo}_{72}\text{Fe}_{30}$ were aimed at studying its effect at the cellular and molecular level, since the use of $\text{Mo}_{72}\text{Fe}_{30}$ as a means of targeted delivery requires knowledge of potential risks and side effects that manifest themselves not only at the macrolevel (in organs and tissues) [138, 140]. For instance, the effect of POM on the content of histone and heat shock proteins in the blood and liver of rats was investigated upon intramuscular injection of this compound into the body [143], since the changes, undetectable by means of assessing traditional indicators, can be identified using other methods. One of the possible mechanisms of the damaging effect of nanoparticles at the molecular level can be their effect on the tertiary structure of proteins. It may be accompanied by immune reactions towards denatured proteins that acquire the properties of antigens alien to the body, by increased proteolysis, apoptosis, necrosis, inflammation, and membrane permeability [144, 145]. Fractions of histone proteins and heat-shock proteins are informative indicators of changes in cells at an early stage of nanoparticles influence before the appearance of the “macrotoxicity” signs. The synthesis of inflammatory factors by lymphocytes depends on the modifications and the amount of histone proteins, the release of which from DNA is essential for the expression of proinflammatory factor genes [146–148]. The disruption of the structure of various body proteins is counteracted by heat shock proteins (Hsp), a class of conservative proteins, whose expression increases with the increasing temperature, the action of toxic substances [150], or under other conditions stressing the cell [149]. Heat shock proteins can act as chaperones, restoring native conformation in other proteins. They can enhance proteolysis, reduce apoptosis, and participate in the transport of other proteins and gene expression [149–152]. The liver is the main organ of detoxication, it is saturated with a large number of specific cells presenting antigens, and it normally deposits iron. Therefore, this organ was chosen as the object of experimental research. The action of most toxicants leads to liver infiltration by lymphocytes coming from the blood. The toxic effect of $\text{Mo}_{72}\text{Fe}_{30}$ in cases of single and repeated administration at the cellular, subcellular and organismal levels was studied as regards the content of histone proteins, heat shock proteins and cytolytic enzymes. The experiment showed no expression of heat shock proteins Hsp70 in the liver cells of intact animals [153], and the expression of Hsp60 was detected on average in about 30 ± 7 cells per unit area. When determining the content of histone proteins in blood lymphocytes [143], during all periods of POM load, no significant changes were found in the fractions of histone proteins, which, according to the literature, regulate the expression of genes of proinflammatory factors [148, 154]. A study of heat shock proteins [143] has detected no Hsp70 in the liver in the groups of both intact and control animals, while Hsp60 were recorded. It indicated the inducible nature of Hsp70 and the constitutive of Hsp60. The normalization of biochemical parameters (characterizing the state of the liver) within 30 days of POM administration [132, 143], gives evidence for the activation of defense systems in the organism. Heat shock proteins restore the native conformation of denatured proteins, which can also segregate proteases, and new proteins are synthesized instead of the segregated ones.

Thus, the single and multiple administration of iron-molybdenum POMs manifested itself at the molecular level only in changes in the content of heat shock proteins [143] involved in the adaptation and maintenance of homeostasis. The studies carried out by a number of authors yielded a suggestion that the absence of an increase in heat shock proteins in response to the action of a stress factor is a violation of adaptation [155, 156]. The action of POM (single and multiple) did not cause a decrease in the amount of histone proteins in blood lymphocytes, which allows an assumption about the absence of autoimmune aggression of these cells against liver tissue. An increase in the amount of Hsp60 and Hsp70 heat shock proteins in rat liver after single and multiple administration of POM can be considered as a way of adaptation, which is confirmed by a study of indicators of cytolysis and synthetic liver function [157, 158].

The content of heat shock proteins in the thymus and spleen was also studied, and it was shown that POM administration is accompanied by an increase in the number of cells containing Hsp60 and Hsp70 heat shock proteins in both organs [108, 132, 159]. The increased expression of heat shock proteins in the thymus [160], despite the presence of a hematothymic barrier, gives reasons to suppose the ability of POM to overcome the histo-hematic barriers of immune privileged organs [161]. Taking into account the results of the ongoing studies [161], it has been shown that POM can also exert a similar effect on other organs with special histo-hematic barriers, in particular, hemoencephalic, hematoophthalmic, hemato-testicular, etc. According to the results of histological studies, the effect of POM on immune privileged organs did not lead to a change in their morphology and structure. There are prospects concerning the transport of medicinal substances with the help of POM across the histo-hematic barriers.

In the course of further investigation of the action of POMs at the cellular level, the effect of $\text{Mo}_{72}\text{Fe}_{30}$ and Mo_{132} on normal and transformed fibroblasts was assessed [162]. The effect of polyoxometalates on cell survival in culture and their cytotoxic action have been studied [163]. Human dermal fibroblasts (HDF) are more resistant to $\text{Mo}_{72}\text{Fe}_{30}$. On the contrary, Mo_{132} causes extensive destruction of the membrane organelles of dermal fibroblasts in the first hours after exposure. Thus, it can be concluded that $\text{Mo}_{72}\text{Fe}_{30}$ is not toxic for normal fibroblasts (it causes only weak changes in cells), while Mo_{132} is toxic for both normal and transformed fibroblasts, and its damaging effect

is more pronounced on transformed fibroblasts. A decrease in the proliferative activity of cells (cell multiplication by division) was recorded. An assessment of the nanocluster toxicity using the MTT test demonstrated a change in the mitochondrial activity after the impact of Mo_{132} . Probably, this type of nanocluster inhibits cellular respiration and causes disruption of energy metabolism in cells. According to the obtained data, the effect of polyoxometalates on cells is selective. The transformed cells accumulated inorganic elements included in the composition of $\text{Mo}_{72}\text{Fe}_{30}$ polyoxometalate (e.g., molybdenum) more intensively than of Mo_{132} . At the same time, iron and molybdenum were absorbed from simpler compounds (iron and molybdenum salts) in smaller amounts, which confirms the selectivity of the action. For instance, 24 hours after the exposure to $\text{Mo}_{72}\text{Fe}_{30}$, the number of transformed cells decreased, and cells with an uncounted cell membrane (indicated by an arrow in Fig. 3) and an increased number of microvilli appeared. This increases the membrane surface, as was recorded by means of optical, electron, and scanning probe microscopy (a comparison of images obtained by different methods is of interest), and can lead, in turn, to an additional increase in its ability to interact with drugs. The obtained results confirm the prospects for the application of POMs in the field of biomedicine, including the use of Mo_{132} in oncological practice [163].

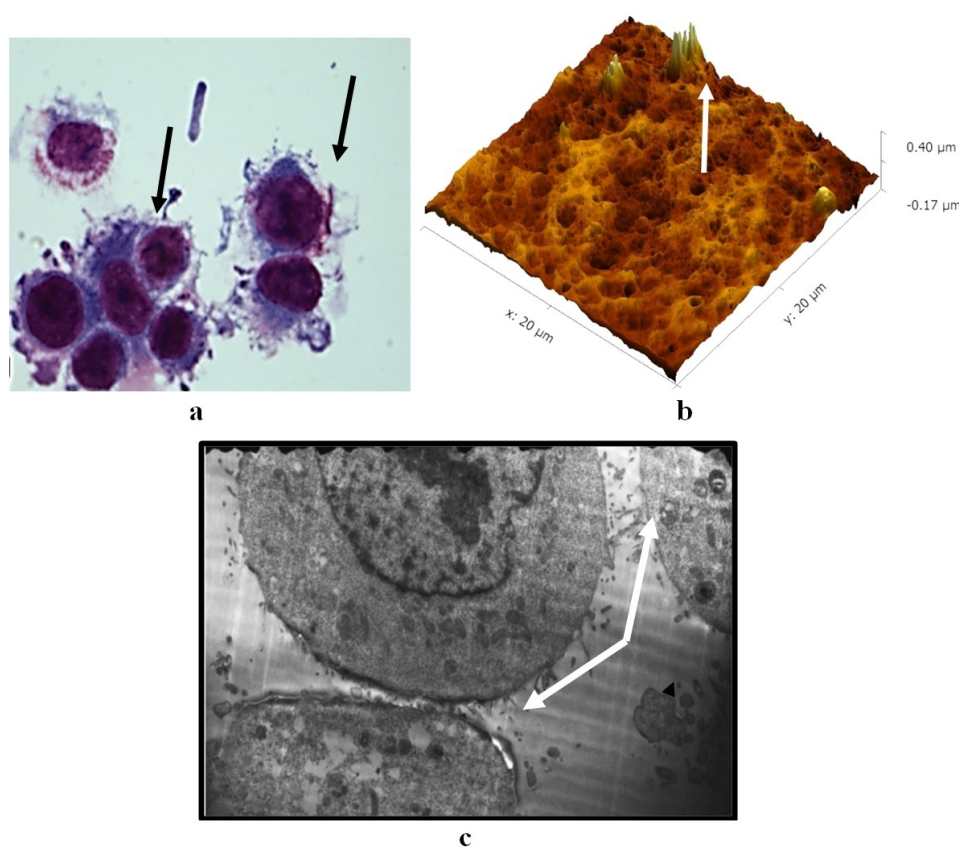


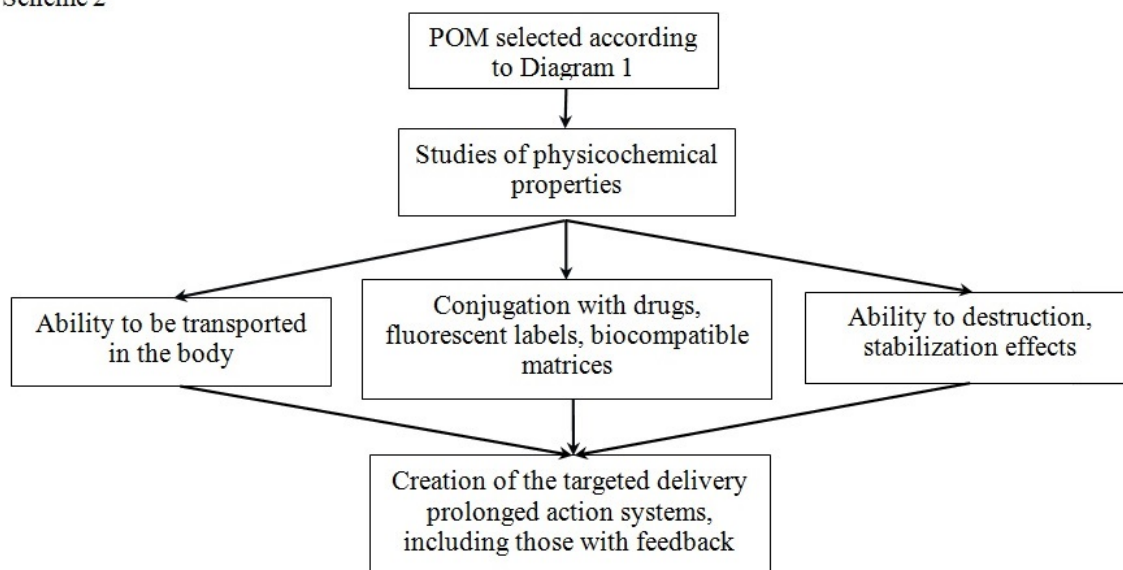
FIG. 3. Transformed fibroblasts after exposure to $\text{Mo}_{72}\text{Fe}_{30}$ POM: a – optical microscopy ($\times 1000$ magnification); b – atomic force microscopy; c – scanning electron microscopy ($\times 15550$ magnification) (equipment of the Ural Center of Shared Use “Modern Nanotechnologies” of the Ural Federal University). The increase in the number of microvilli is indicated by arrows

3. Association of POMs with bioactive substances and polymers

Polyoxometalates that have been selected in the course of research (Scheme 1) as having characteristics that make their practical use in biomedicine promising, are studied for the compliance of their properties to requirements to the materials for targeted drug delivery systems (Scheme 2).

The Keplerate-type POMs and alike, being hydrophilic particles, are able to associate (form conjugates) in their external sphere with diverse substances, which include surfactants (SAs) of various nature [164–171], dyes, photosensitizers [109, 110, 172–174], and polymers [174–179], mainly water-soluble ones. POMs functionalization makes it possible to selectively influence their hydrophilic and hydrophobic properties [110], create catalytic and photocatalytic

Scheme 2



systems with adjustable characteristics, as well as compositions for targeted delivery in biomedicine, controlled by an electric [179] or magnetic field [180, 181]. The hydrophobized POMs acquire an ability to more actively interact with molecules of nonpolar substances and adsorb them [110]. There appears a possibility of formation of ionic associates based on POM and cations of metals (alkaline earths, rare earths, transition metals, including luminescent labels and magnetic resonance imaging (MRI) tags [19, 121–123]), and of cationic surfactants. Weaker, e.g., hydrogen, bonds also actively participate in the interaction of organic compounds with POMs [182]. The formation of POM associates with water-soluble nonionic polymers [174–179, 183–185], including the biocompatible ones, makes it possible to create protective shells on the POM surface, similar to polyethylene glycol (PEG) layers, or to diblock copolymers on nanocapsules [186–194]. In a number of cases, the energy factor (interaction enthalpy) contributes to the formation of these associates. For instance, the enthalpy of POM and polymer interaction is negative over the entire concentration range of the components in the $\text{Mo}_{72}\text{Fe}_{30}$ – polyvinylpyrrolidone (PVP) system [177]. Similar local concentration regions were found for the systems containing polyethylene glycol (PEG) and polyvinyl alcohol (PVA) [183]. In some of the studied systems, the formation of associates is facilitated by the entropy factor [183].

As is noted above, the use of ionic associates of POMs with rare earths as components of diagnostic systems in biomedicine has been proposed [19, 121–123, 195, 196]. In such associates, POM recharging occurs, so the resulting complex can be positively charged [197], unlike the initial POM, and be transferred in an electric field by iontophoresis to the cathode instead of the anode. The structure of a POM is retained in associates [197], which was shown by IR and Raman spectroscopy. A number of drugs, including antibiotics, form bioactive anions in solutions, the association of which directly with POM is prevented by the Coulomb repulsion. The competitive interaction of drug cations with the existing complexing anions also complicates the formation of the cation-POM complexes [197]. On the other hand, there is a way to obtain transportable associates of anionic bioactive substances with POM, for example, through the bridging calcium cations [119, 198]. The discovered POM stabilization in associates with calcium will be discussed below. It is important to note the ability of the Keplerate and compositionally similar toroidal [88–91, 110] POMs to self-association in solutions, i.e., to self-assembly into hollow single-walled globules (Fig. 4) [91, 199], the diameter of which can vary from tens to hundreds of nanometers, depending on concentration, acidity, and dielectric permittivity of the medium [199]. These formations can also be considered as transport units for the targeted delivery of medicinal substances, and the formation of associates, e.g., with surfactants, makes it possible to control the properties of POMs not only at the level of single molecules, but also at the level of globules and aggregates [111, 180, 181].

In the course of investigations, the ratio of components in the formed POM-polymer associates (Fig. 5) was established, which in some cases, is close to the calculated value of the monomolecular coating of POM with polymer chains [175, 178, 184]. Such systems include, for example, associates based on polyvinyl alcohol, PVP with Mo_{132} , and on PVP with $\text{Mo}_{72}\text{Fe}_{30}$. As mentioned above, spontaneous energetically favorable formation of associates occurs in some systems, e.g., of PVP with $\text{Mo}_{72}\text{Fe}_{30}$ (in the entire concentration range of components), as well as in certain concentration ranges - of polyvinyl alcohol and PEG with $\text{Mo}_{72}\text{Fe}_{30}$ [177, 183]. The interaction of POM with polymer macromolecules has specific features, and one of the main ones is the nonlinearity of the associates physicochemical properties dependence on concentration [175, 176, 200, 201]. The oscillating concentration dependencies (Fig. 6–8) are

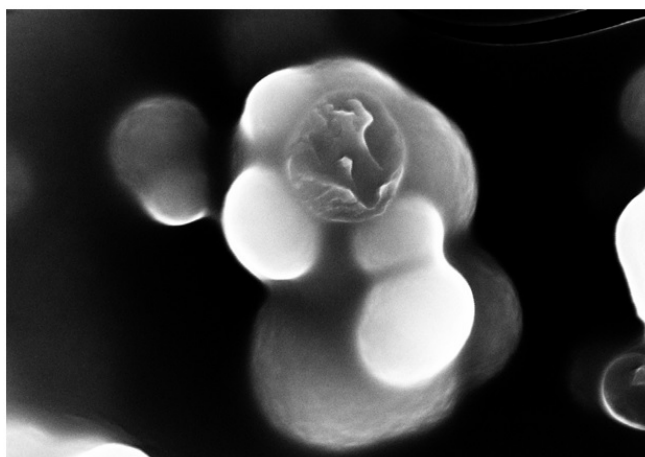


FIG. 4. POM globules, 20000-time magnification. (The electron micrograph was obtained using the equipment of the Ural Center of Shared Use “Modern Nanotechnologies” of the Ural Federal University)

associated with the non-statistical nature of the mutual distribution of the interacting nanoscale components [200,201]. They are observed for such independent characteristics as optical density, solution viscosity, electrical properties, particle size, etc. Obviously, this fact should be taken into account when choosing the ratio of components in associates used for the targeted drug delivery.

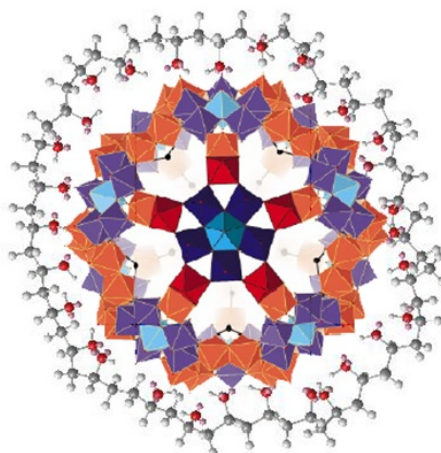


FIG. 5. Diagram of a polymer-salt complex structure [178]

It has been established that $\text{Mo}_{72}\text{Fe}_{30}$ POM forms associates with the drugs that are most promising in terms of targeted delivery. Thiamine chloride (vitamin B1) was considered as a model substance [161, 197]. Thiamine is present in a solution in the form of cations, which get associated with the POM polyanion. It was confirmed by UV/Vis spectroscopy, by measuring the pH of solutions, zeta potential, and the size of the particles in them. In concentrated solutions, colloidal particles get formed along with the solid phase of the resulting conjugates, in which the preservation of the original POM structure and the presence of thiamine are confirmed. To this end, IR and Raman spectroscopy were used. The thiamine-POM ratio in the associates was estimated as 4:1, with the retention of the total negative charge of the conjugate. $\text{Mo}_{72}\text{Fe}_{30}$ associates with substances belonging to the class of immunomodulators, e.g., with 2-morpholino-5-phenyl-6H-1,3,4-thiadiazine bromide [197–202].

$\text{Mo}_{72}\text{Fe}_{30}$ forms conjugates with such an antibiotic as kanamycin sulfate, without reducing the activity of this drug when affecting colibacilli cultures [197]. Also, it was possible to establish that $\text{Mo}_{72}\text{Fe}_{30}$ can associate with insulin in aqueous solutions [197], as well as with amphiphilic protein molecules, such as albumins [161, 197]. This result is of great importance in terms of the possibility of obtaining complexes with POM and with homing peptides for the implementation of bioactive substances targeted delivery to specific cells. Protein molecules, the so-called protein

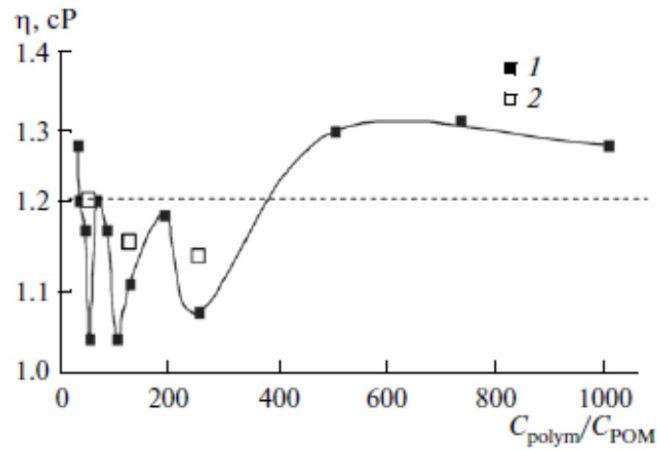


FIG. 6. Dependence of the solutions dynamic viscosity (η) [201] on the ratio of the polyvinylpyrrolidone macromolecular units number per 1 ion of Mo_{132} polyoxometalate (1); 2 – viscosity of the specified POM aqueous solution; the dotted line indicates the viscosity of a 1% pure polymer aqueous solution. ©Pleiades Publishing, Ltd. 2015

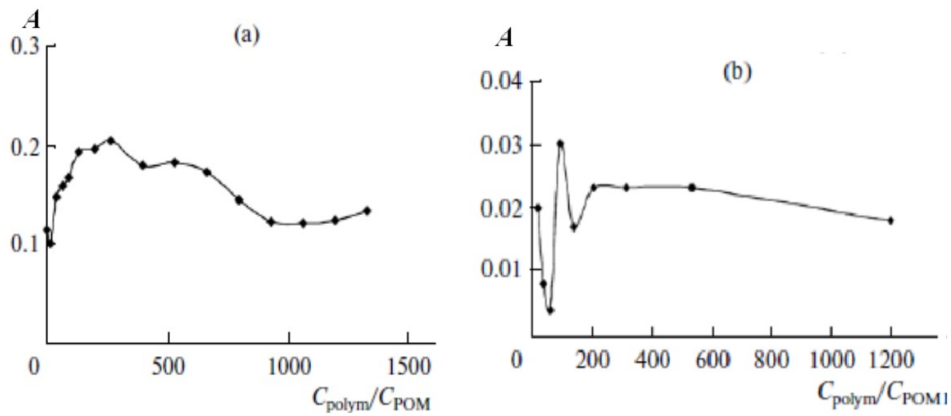


FIG. 7. Optical density (A) ($\lambda = 450$ nm) [201] of Mo_{132} POM and polymer solutions, depending on the molar ratios of the components: a – of polyvinylpyrrolidone ($C_{POM} = 1.5 \cdot 10^{-6}$ mol/L); b – of polyvinyl alcohol ($C_{POM} = 1.5 \cdot 10^{-7}$ mol/L). ©Pleiades Publishing, Ltd. 2015

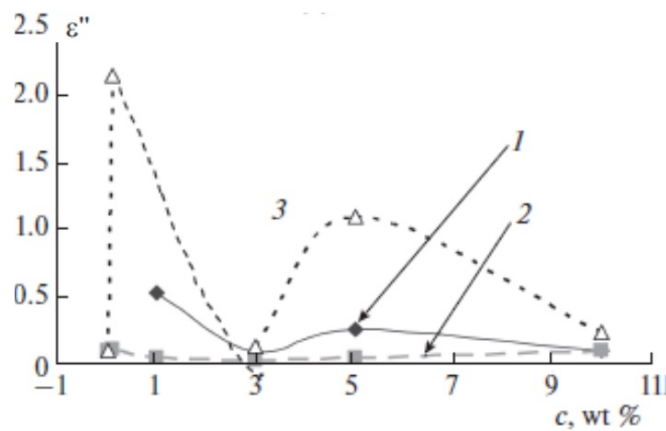


FIG. 8. Concentration dependencies of the dielectric loss factor [175] at the 25 Hz frequency for the PVA-based composites, including (1) Mo_{132} , (2) Mo_{138} , and (3) $Mo_{72}Fe_{30}$. C is the POM content (wt %). ©Pleiades Publishing, Ltd. 2016

corona, significantly influence the biological properties of nanoparticles [203–207]. It should be noted that the blood serum proteins stabilize $\text{Mo}_{72}\text{Fe}_{30}$ [161, 177], in spite of the fact that the serum is an alkaline medium, where the POM is unstable, in principle, which is illustrated by its rapid decomposition in buffer solutions. Stabilization by the natural protein corona opens up prospects for the prolonged action of the POM-based drugs. While in buffer solutions with the corresponding pH 8 $\text{Mo}_{72}\text{Fe}_{30}$ decomposes rapidly, and the effective constant of the POM destruction rate has a value of $2.6 \cdot 10^{-2} \text{ h}^{-1}$ even for the self-aggregated ones, its value is only $1.8 \cdot 10^{-3} \text{ h}^{-1}$ in the composition of conjugates with proteins [96]. The initial experiments aimed at establishing the possibility of obtaining conjugates of $\text{Mo}_{72}\text{Fe}_{30}$ with doxorubicin yielded positive results. Doxorubicin is an anthracycline antitumor antibiotic [208–212] that is actively used in medicine in the treatment of various types of solid tumors. Two main mechanisms of doxorubicin's antitumor activity are proposed in the literature, namely DNA intercalation and disruption of the viral DNA repair, and the generation of free radicals that damage the cell membrane, DNA, and proteins [213]. Along with high efficiency, doxorubicin has high toxicity associated with low selectivity for its action. In addition to high cardiotoxicity, a decrease in bone marrow activity (myelosuppression) is often observed in the course of doxorubicin administration [214]. To date, a significant amount of research has been conducted with the purpose of reducing the toxic effect of doxorubicin on healthy cells by creating means of its targeted delivery. Various types of different systems for the targeted delivery have been considered, in particular, based on liposomes [215–222] (similar forms have already found application in medical practice [223–227]); proteins [228–233]; polymers [234–243]; fullerenes and CNT [35, 244–251]; metal and oxide nanoparticles [52, 76] (gold [250–255], silver [255], and iron oxide [256–260]). The further study of the properties of POM-doxorubicin conjugates should be recognized as promising, given the corresponding properties of POM.

An important aspect of the possible use of POM in the field of biomedicine is the possibility of iontophoretic, including percutaneous, transport of Keplerates and their conjugates into the body. These processes were considered in our previous work [179]. As is noted above, these processes are important, in particular, for the delivery of drugs, e.g., of doxorubicin, to the regions with a low degree of vascularization.

Additional opportunities for the use of $\text{Mo}_{72}\text{Fe}_{30}$ in biomedicine are opened by the preparation of its new coordination compound [261] that can serve as a transportable donor of nitric oxide – a mediator of some important processes in the body [262–267], which include the activation of antiviral and antimicrobial activity, and the cardiotropic action. It is important that the compound $[\text{POM}(\text{NO}_2)_x](\text{NO}_2)_y$ (where $x = 6$, $y = 14 \pm 3$), obtained by the interaction of nitrogen oxides with POM and characterized by a complex of methods, belongs to the group of water-soluble compounds. Iron compounds are used as nitric oxide donor and transport vehicles for its delivery [268–275]. Examples of obtaining other POMs containing nitric oxide can be found in the literature [276–278].

4. POMs destruction process and their stabilization

One of the main above-mentioned properties of POMs is their ability to degrade in diluted solutions [279], which depends on both the POM initial concentration and the pH of the medium. This property can be useful for POM removal from the body after the function of bioactive substances delivery has been performed. The results of studies of thermal stability and destruction of the Keplerate and toroidal type POMs in the solid state using spectroscopic methods are given in [280–286]. At the same time, it was shown that a thorough spectroscopic analysis and a comprehensive interpretation of the results are necessary [280, 286] in order to avoid unreliable conclusions [284] about the POMs' thermal stability. The features of the processes of POMs destruction in solutions have been considered in the earlier performed works [135, 198]. For each of the considered POM, there is a region of stable state in aqueous solutions in terms of POM concentration and medium pH. For Mo_{132} , this region can be clearly illustrated by a diagram (Fig. 9). The region of $\text{Mo}_{72}\text{Fe}_{30}$ stability in sufficiently concentrated solutions is also limited by pH within the 3.7–5.9 range [100, 106]. Under the conditions that exist beyond the range of POM stability, they undergo gradual destruction into simpler components.

UV/Vis spectroscopy was used for studying the kinetics of POM degradation in solution. The time dependencies (τ) of the optical density A (directly proportional to the current POM concentration) obtained [135] for different initial concentrations of $\text{Mo}_{72}\text{Fe}_{30}$ POM were approximated by equations describing reactions of different orders, in order to establish which of them the experimental data obey. A satisfactory agreement with the linear dependence was observed in the $\ln \left(\frac{A_0}{A_\tau} \right) = f(\tau)$ coordinates for $\text{Mo}_{72}\text{Fe}_{30}$ solutions in the domain of relatively low concentrations. The experimental data correlated best with the first order reaction equation. For relatively high $\text{Mo}_{72}\text{Fe}_{30}$ concentrations, the experimental data were approximated by two lines with different slopes (for different time periods). Each of them was linearized in the $\ln \left(\frac{A_0}{A_\tau} \right) = f(\tau)$ coordinates. In this case, the constant of POM decomposition rate in the

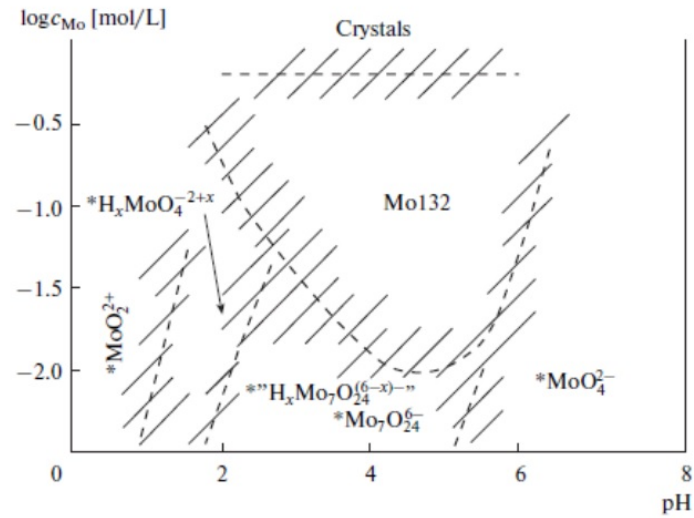


FIG. 9. Hypothetical diagram of Mo₁₃₂ POM stability [184]. ©Pleiades Publishing, Ltd. 2010

first time interval coincided with the constant of Mo₇₂Fe₃₀ destruction rate in low concentration solutions. Such a situation can be explained by a change in the mechanism of the destruction process depending on the concentration and a change in the limiting stage of the general process where inflection between two lines was observed. An example of the experimental data processing is shown in Fig. 10. For comparison, the table also shows the data on the destruction kinetics for a toroid-structured Mo₁₃₈ POM, for which the one-step destruction process in a solution with a relatively high ($2.4 \cdot 10^{-6}$ mol/L) initial POM concentration was satisfactorily described by the first-order reaction equation.

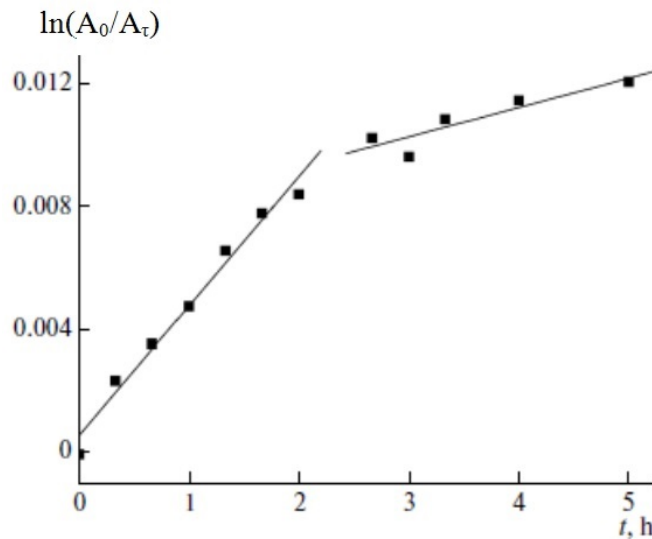


FIG. 10. Kinetics of the Mo₇₂Fe₃₀ Keplerate decomposition [135] in a solution with the initial concentration of $5 \cdot 10^{-6}$ M. ©Pleiades Publishing, Ltd. 2015

In [135], a supposition was made concerning the possible differences in the process of Mo₇₂Fe₃₀ POM destruction at different concentrations. The mentioned POMs tend to form aggregates or hollow globules in solutions [89,199,286–292]. In solutions with high concentrations, aggregation proceeds in such a way that a significant part of the available POM molecules (ions) happens to be bound into aggregates within a relatively short time. In diluted solutions, the relative amount of free POM molecules is more noticeable. Therefore, it can be assumed that the free POM destruction rate constant is higher than that of those bound into globules, in which they are protected due to the presence of bonds between molecules (ions) and a lesser contact with the environment. When the experimental dependencies demonstrate

TABLE 1. Polyoxometalates (k_i) destruction rate constants at the naturally formed acidity of solutions, h^{-1} [135]

Solution concentration, mol/L	Polyoxometalate composition	
	$\text{Mo}_{72}\text{Fe}_{30}$	Mo_{138}
$1 \cdot 10^{-7}$ – $6 \cdot 10^{-7}$	$k_1 = 0.02$	
$1 \cdot 10^{-6}$ – $1 \cdot 10^{-5}$	$k_1 = 0.02$ $k_2 = 0.002$	$k = 0.05$

an inflection within the same initial concentration, a change in the limiting stage occurs, apparently, after the majority of the available free POM molecules have been spent.

The proposed hypothesis is supported by the fact that the constant of the aggregates formation rate [289] (calculated also for the first-order reaction) is lower than the POM decomposition rate constant, and equals $5.4\text{--}7 \cdot 10^{-5} \text{ h}^{-1}$ for $\text{Mo}_{72}\text{Fe}_{30}$, in particular. Therefore, the initially obtained solution should contain at the first stage a sufficiently large number of unbound POM molecules, which decompose faster than the aggregated ones. A relatively faster process of decomposition of free $\text{Mo}_{72}\text{Fe}_{30}$ molecules, which are initially present in a significant amount, can also explain a steeper initial section in the kinetic dependencies of aggregate formation [289]. The rate constant in this section can be estimated as $2.5\text{--}3.9 \cdot 10^{-4} \text{ h}^{-1}$. In this case, it can be assumed that the appearance of iron ions due to the POM destruction leads to acceleration of the aggregation process. The literature indicates a similar effect of cations on the formation of aggregates [291]. At the same time, the existence of singlet POMs in a solution is not typical for the toroid-like Mo_{138} [286]; therefore, its destruction is a one-step process in a certain time interval.

In [289], the ratio between the number of aggregates and singlet nanoclusters was determined, from which the degree of aggregation was calculated. The authors apparently did not take into account a possibility of this ratio increase due to a higher rate of $\text{Mo}_{72}\text{Fe}_{30}$ POM free ions destruction, as well as the change of the total concentration of POM, which could lead to an overestimation of the globule formation rate constant.

Another question that arises is about the mechanism of POM decomposition s included in the aggregates. Do the POM molecules get destroyed directly in the globules, and then the latter disintegrate, or does the preliminary disintegration of the globules occur when the concentration of free POM ions decreases? The destruction of POM in globules could have possibly led to a change in their size; however, according to the data from [289], the size of the existing globules remains practically unchanged. Therefore, it can be assumed that the destruction of POM molecules (ions) into simpler compounds occurs after the preliminary destruction of these globules, which goes along with the decreasing concentration of the studied POM in the course of its decomposition in the solution. Some previously found differences in the kinetics of Mo_{138} POM and $\text{Mo}_{72}\text{Fe}_{30}$ destruction can be associated with both the globules destruction rate, and with the stability of the polyoxometalates themselves. Thus, it was shown in [135] that, depending on the concentration of $\text{Mo}_{72}\text{Fe}_{30}$ POM solutions, the disintegration of single nanoclusters, or the “dissolution” of the existing globules consisting of nanoclusters, can be the limiting stage of the overall destruction process.

The destruction of Mo_{132} has also been investigated [198]. An analysis of the spectrophotometric data from experiments on the destruction of Mo_{132} POM showed that the time dependencies of the optical density and, accordingly, of the POM concentration, have an induction period when the concentration decreases rather slowly. Then the decomposition accelerates, and after passing the interval with the maximum rate, it noticeably slows down again. For this reason, the standard linearization of the data using kinetic reaction equations of various orders (including those at the stages after the induction period) was a failure. Considering the shape of the obtained dependences, it was logical to assume that the destruction proceeds in the autocatalytic reaction mode. A typical picture of the kinetic dependence is shown in Fig. 11a.

The experimental kinetic data obtained at the initial concentration of the studied POM of 10^{-5} mol/L , were processed using an equation that describes the autocatalytic process [293–295]:

$$C = C_0(K_0 + K_c C_0) / (K_c C_0 + K_0 \exp((K_0 + K_c C_0)t)),$$

where C_0 is the nanocluster initial concentration, K_0 is the non-catalytic process rate constant, K_c is the catalytic process rate constant, C is the nanocluster current concentration, and t is the time. The values of K_0 were estimated from the slope of the dependence during the induction period, and it was assumed that the catalytic process rate is negligible during this period (of the non-catalytic reaction), which is a standard assumption in such cases. The experimental data for the interval, corresponding to the rapid course of the catalytic process with further deceleration

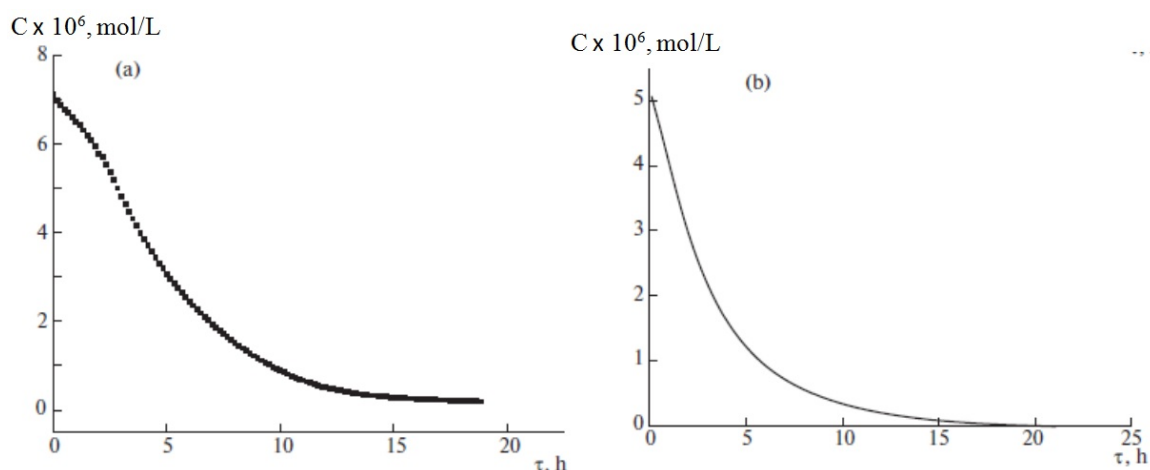


FIG. 11. Typical kinetic dependencies (concentration - time) of the Mo_{132} destruction process [198] at an initial concentration of $7 \cdot 10^{-6}$ mol/L (a) with an induction period; shape of dependence with no induction period (b) at the introduction of sodium molybdate (the initial Mo_{132} concentration: $5 \cdot 10^{-6}$ mol/L). ©Pleiades Publishing, Ltd. 2016

due to the consumption of autocatalytic particles, were used for determining K_c values for each experimental point, and then plotting the time dependence of this parameter.

It is impossible to deduce the K_c value from the above equation by using the analytical method, therefore a special algorithm was developed for determining this value. It consists in the following:

1. Since the equation is transcendental, it was rewritten as:

$$C(K_c C_0 + K_0 \exp((K_0 + K_c C_0)t) - C_0(K_0 + K_c C_0)) = 0 \text{ or } F(C, t, K_c) = 0.$$

2. The available data array $C=C(t)$ was used to construct the function $F=F(C, t, K_c)$, according to which, the time-dependent K_c values were reconstructed.

The performed calculations showed that the value of the catalytic process rate constant practically did not change in the corresponding interval in time and averaged about $4.8 \cdot 10^2$ L/mol/min at the initial POM concentration of 10^{-5} mol/L, and $6 \cdot 10^2$ L/mol/min at $5 \cdot 10^{-6}$ mol/L, respectively. The half-transformation time estimated on the basis of such rate constant values, correlates well with the experimental data (about 4-5 hours). Thus, it can be considered that the destruction process proceeds as an autocatalytic reaction, and the used assumptions are correct, since the shape of kinetic dependence could be approximated successfully by a corresponding equation. The possible reasons for the differences in the obtained K_c values at different initial concentrations will be discussed below. The value of K_0 in this case was about $1.8 \cdot 10^{-3} \text{ min}^{-1}$, regardless of the initial POM concentration in the range of 1-10 μM .

The features of Mo_{132} destruction in the presence of calcium ions, associated with the POM polyanion, are also considered. The hydrated calcium ions are capable of forming differently configured associates with POMs [119]. Calcium can stabilize POM in solutions, thus increasing the effective value of its lifetime in solutions. In this case, as in that of POM association with polymers, the non-additive properties are observed, for instance, the nonlinear concentration-dependent ability of calcium to stabilize POM. In the processes of calcium cations and POM interaction, apparently, 20 pores in the Keplerate structure are involved as active centers, i.e., the places where the association of the hydrated ions of divalent metals occurs [296]. It cannot be excluded that the filling of these positions leads to the associate's stabilization. In addition, the next level of interactions is realized along with the increase in the associated ions concentration. Naturally, ion associates are found in dynamic equilibrium with free ions in a solution, and a certain excess of associated ions is required to ensure the filling of active positions. The change in time of the solutions optical density at the POM characteristic wavelength indicated that the almost completely destroyed pure Mo_{132} persisted for several days in the presence of calcium, especially at the Ca-POM ratios of 8:1, 24:1, and 60:1. The presence of POM with the original structure was confirmed by Raman spectroscopy.

This is another case when the POM destruction process is described as an autocatalytic reaction. Such parameters as the induction period duration, and the rate constants in this interval and during the catalytic process were determined for the destruction reaction. When the Ca content increases, the induction period lengthens, and the rate constant of the noncatalytic stage decreases (Fig. 12), but nonmonotonically depends on the Ca content in solutions, and has minima for some compositions. The autocatalytic process rate constant increased along with an increase in the Ca content. It

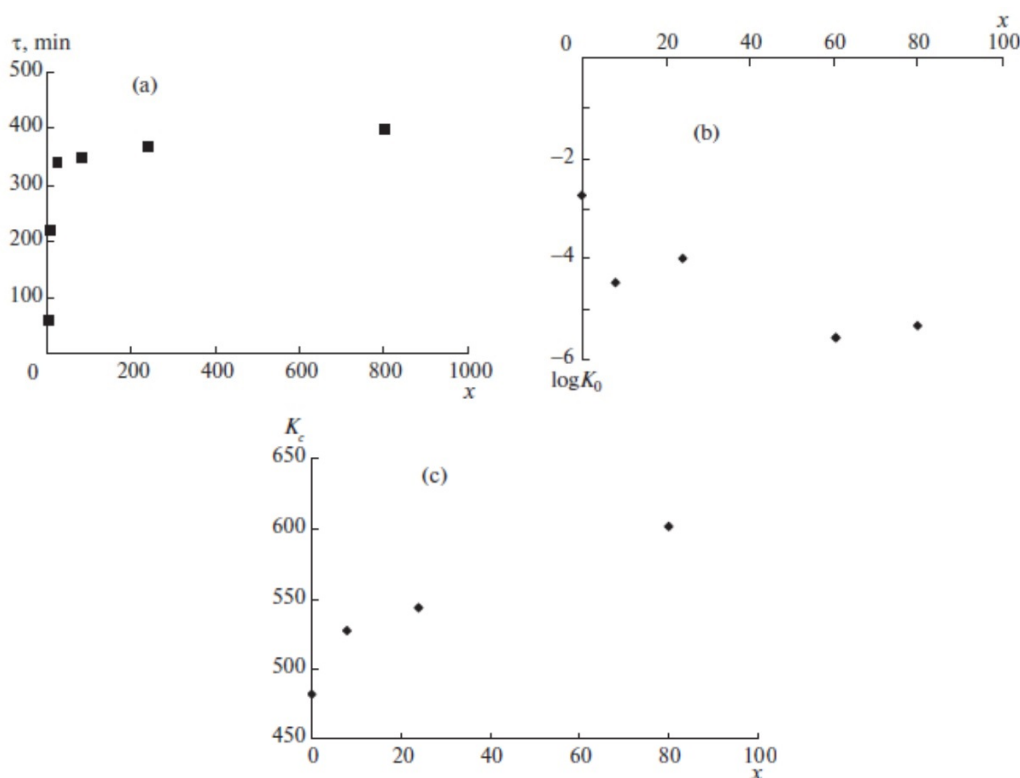
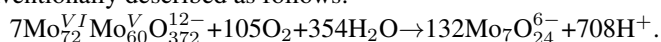


FIG. 12. Dependencies of the induction period duration (a), K_0 (b), and K_c (c) on the Ca^{2+} -POM ratio for solutions with the initial Mo_{132} concentration of 10^{-5} mol/L [198]. ©Pleiades Publishing, Ltd. 2016

should be noted that since the formation of variously structured POM-Ca associates is possible, the rate constants can really differ, as the mechanism of POM destruction is determined by its structure.

It was noted during the research that the pH of freshly prepared POM solutions decreased depending on the amount of Ca (Fig. 13) at POM concentrations of 1 and 10 μM , and the nature of the kinetic parameters dependence (in absolute value) on the Ca concentration was generally similar to the pH concentration curve, although the pure Mo_{132} solution did not fit this series. On the one hand, this shows that the destruction mechanism and rate are determined not only by the solution pH. Along with that, it can be stated that the maximum stability of some compositions is determined by a combination of a sufficiently long induction period and a relatively low non-catalytic stage rate constant.

When considering the pure Mo_{132} destruction process again, a monotonic decrease in the pH of solutions was observed at a concentration of 10 μM . Notable is that this decrease was more rapid during the induction period. From the point of view of the direction of change in acidity, this regularity is quite logical taking into account the possible simultaneous process of the available pentavalent molybdenum oxidation with atmospheric oxygen, which can be conventionally described as follows:



Due to the presence of the above-described change in acidity, the hydroxonium ions H_3O^+ were considered as autocatalytic particles, which is often the case. However, it was taken into account that along with the decreasing pH of calcium-containing solutions and increasing amount of Ca^{2+} in them, the rate constant of the non-catalytic stage of the process decreases, and its duration increases. Therefore, non-condensed molybdate (or dimolybdate) ions that appear during the destruction of Mo_{132} , can act as the autocatalytic particles. Further on, in addition, the diagram from [184] (Fig. 9) was taken into account, as it showed the regions of stability of various molybdate forms (including Mo_{132} ions) depending on the total molybdenum in solutions, and on the pH of the medium. The point corresponding to a POM solution with initial concentration of 10 μM in a more detailed fragment of the diagram (Fig. 14), is found in the region of heptamolybdate ions stable existence. It should be noted that the earlier studies of POM decomposition by photon correlation spectroscopy [184] discovered the appearance of POM particles with an effective size of about 1.3 nm, which is close to the estimated size of the heptamolybdate ion. If, in addition, fragments containing less than 7 molybdenum atoms also appear during the POM destruction, then they must be completed up to a heptamolybdate

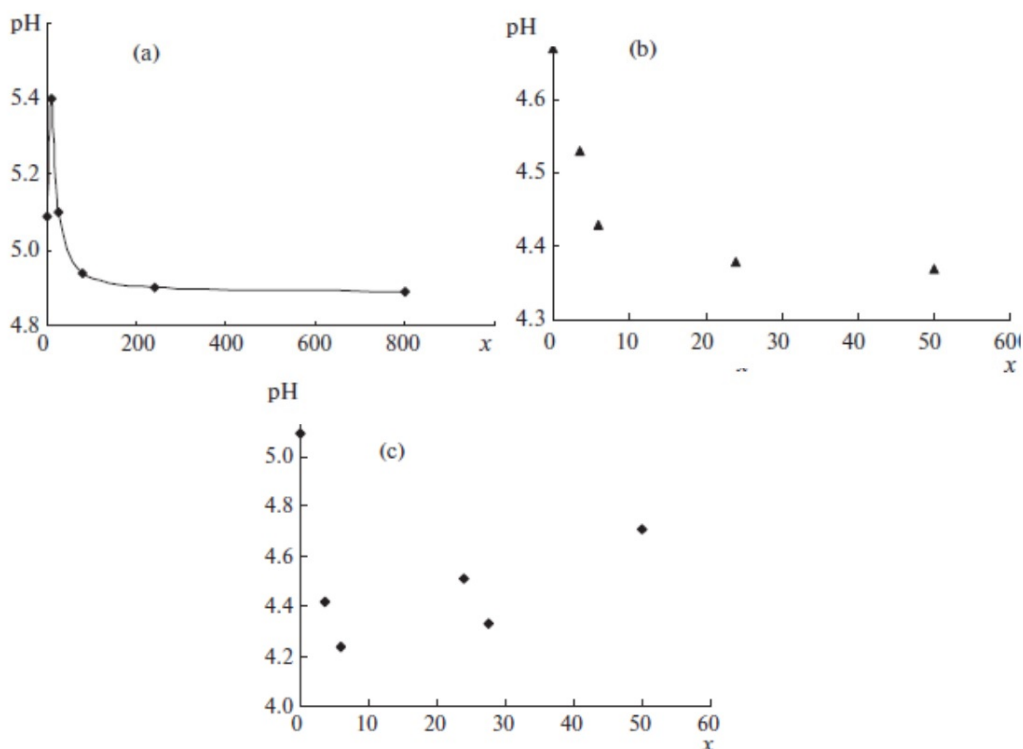


FIG. 13. Dependencies of the Mo_{132} solutions pH on the calcium-POM ratio (a) at the concentration of 10^{-6} mol/L, as well as on the experimental time at concentrations of 10^{-5} (b) and 10^{-6} mol/L (c) [198]. ©Pleiades Publishing, Ltd. 2016

form that is stable in this region. Then, it cannot be ruled out that these particles “attack” a POM to obtain the required material. An accelerated destruction in this case is achieved when weakly condensed compounds or monomolybdate forms get accumulated in the solution. The slowing down of the destruction process corresponds to the consumption of the mentioned autocatalytic particles. At the initial Mo_{132} concentration of $1 \mu\text{M}$, the resulting monomolybdate particles do not need to build up to heptamolybdate.

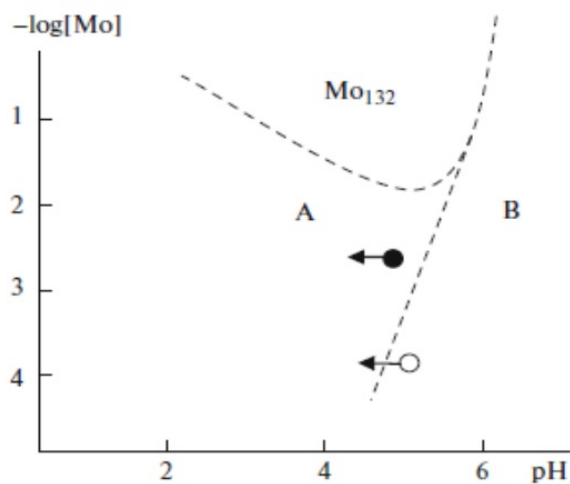


FIG. 14. Fragment of the phase diagram of forms of ions in a solution: A - heptamolybdate ions stability region; B - monomolybdate existence region. The arrows indicate the direction of change in the acidity of the solution during the Mo_{132} destruction [198]. ©Pleiades Publishing, Ltd. 2016

The conclusions made above about the nature of autocatalytic particles are consistent with the data on increase in POMs stability in acidic buffer solutions [279]. These data indirectly indicate that hydronium ions do not catalyze destruction. The catalytic action of monomolybdate ions can be confirmed by a direct experiment. The addition of sodium molybdate into the Mo_{132} solution (with the initial concentration of $5 \mu\text{M}$) practically did not affect the pH of the solution, and led to the exclusion of the induction stage from the destruction process (Fig. 11b). In this case, the molar content of molybdenum in the form of monomolybdate was set equal to the molar content of molybdenum contained in the form of Mo_{132} . Changes in the solutions acidity during the destruction of more diluted (e.g., μM) Mo_{132} solutions without additives did not have a monotonic character (Fig. 11). It is also related to the thermodynamic factor (diagram in Fig. 14). The point corresponding to the indicated concentration is found in another region of the diagram, where simpler ions are stable. However, the pH decreases in the course of destruction, and the composition transits across the boundary between two regions (Fig. 14). At the initial Mo_{132} concentration of μM , the appearing monomolybdate particles do not need to build up to heptamolybdate before crossing the boundary of the indicated regions. Such a flow of processes is even more complicated than in the first case, so it becomes difficult to unambiguously interpret the kinetics and describe it by the used autocatalytic equation. The course of reaction can be additionally complicated by the fact that products of destruction, including pentavalent molybdenum, have different degree of stability in different regions of phase diagram. They have a higher stability [200] in the condensed forms in region A (Fig. 14). As for the Keplerate structures destruction, it was noted that the Keplerate decomposition stage (with the solution turning blue) [104] can be followed by the Mo(V) compounds oxidation, accompanied by discoloration. The change in the medium acidity during POM destruction in the presence of Ca^{2+} is also not monotonic in all cases. However, the above-noted general trend of an increase in the induction period duration along with an increase in the amount of Ca^{2+} in the solution, may be associated with the fact that calcium ions are able to form sufficiently stable associates with molybdate, which leads to at least partial binding of autocatalytic particles. However, calcium molybdate (CaMoO_4) solubility product was not obtained at the studied concentrations of solutions, and no precipitation in noticeable amounts was observed. To summarize, let us note once again that POM destruction is a process, the rate of which is determined by both POM concentration and medium acidity. The destruction mechanism can vary depending on these conditions. There are possibilities for temporal stabilization of POMs and a decrease in the value of the process rate constant – by regulating either the acidity of the medium and POM self-aggregation, or POM interaction with stabilizing agents, including those of natural origin.

The effect of light on POM solutions increases the rate of their destruction [297, 298] and can change the mechanism of this process (to be discussed in more detail in the next section). Mutual stabilization of POMs and water-soluble nonionic polymers (including biocompatible ones) during the formation of their associates, which manifested itself under sufficiently severe photothermal effect on systems, was studied in [198, 297–299]. This aspect is important not only in itself, but also when using POM as, e.g., part of ointment compositions, or sterilized materials. The stabilization effect was studied by means of the EPR spectroscopy for determining the number of paramagnetic centers (spins) as an indicator of the composition components destruction processes. Quite interesting are the results of studies, which indicate the above-noted significant stabilization of $\text{Mo}_{72}\text{Fe}_{30}$ POM due to the interaction with proteins of the blood serum [161, 300], which has an alkaline pH. In buffer solutions with a similar pH, POM destruction proceeded at a very high rate, while in the serum they persisted for up to dozens of hours. The destruction rate constant of POM in the resulting conjugates with serum proteins was at least an order of magnitude lower than in aqueous solutions of the POM itself. Thus, there exists a possibility to regulate POMs stability, their lifetime, and the period of the conjugated drugs release. Preliminary stabilization of POM in solutions can be carried out outside the body.

5. Prospects for the creation of POM-based releasing systems with feedback

An integrated approach to the study of the physicochemical properties of the Mo_{132} and $\text{Mo}_{72}\text{Fe}_{30}$ Keplerate POMs [138, 161, 301], as well as the possibility of their association with bioactive molecules and fluorescent dyes, made it possible to formulate the concepts [302–304] of creating long-time-drug-releasing systems (LDRS) with a function LDRS will be based on the release of molecules of bioactive (medicinal) substances, initially bound with POM, and the intensification of fluorescent labels luminescence. The release occurs at the normal pH (7.2–7.4) of the body environment, due to the POM destruction. The main principle LDRS are based on is the discovered effect [302–304] of a fluorescent label (xanthene dye rhodamine-B, RhB) inactivation on the POM surface due to charge transfer processes. This makes it possible to monitor the drugs release due to the intensification of the signal from the fluorescent labels [305, 306] incorporated in the applied LDRS. In [307], it was found that RhB, chosen from a number of xanthene dyes, is characterized by the concentration quenching of luminescence due to a static mechanism, i.e., formation of non-luminescent H-aggregates. It was shown in [304] that the reason for the RhB fluorescence quenching in an associate with POM is the photoinduced charge transfer from the level of the lowest unoccupied molecular orbital (LUMO) of the donor (RhB) to the LUMO level of the acceptor (POM). According to the cyclic

voltammetry data [308, 309], the LUMO level of RhB is 0.65 eV higher than the LUMO level of POM, which leads to the spontaneous electron transfer from RhB to POM in an excited state and formation of the $\text{RhB}^+/\text{Mo}_{132}^{n-2}$ ionic pair.

It should be noted that the transfer of electrons between the HOMO/LUMO levels of dye molecules and POM (Fig. 15) also underlies the promising use of such photosensitized systems in catalysis [310]. The experiments performed to date have yielded such components of the above systems (Fig. 16) as the NHS ester of rhodamine-B - a potential fluorescent label [302, 303], which can be covalently fixed on the macromolecular backbone of biocompatible polymers (chitosan, polyallylamine) by an amide bond. It was shown that the Mo_{132} nanocluster, which had been chosen as a model POM, can be connected with matrix macromolecules of biocompatible polymers, such as polyallylamines, aminopropyltrimethoxysilane, and chitosan, resulting in microgels based on similar matrices. In principle, the proposed LDRS can be used as a subcutaneous implant with the function of on-line pharmacokinetic monitoring. Such nanoscale systems can, in principle, be created on the basis of hybrid supramolecular assemblies that act autonomously, like liposomes with highly specific ligands on their surface [311]. Such systems can also be components of a microscopic implant [312] or of a biocompatible polymer matrix capable of carrying a large number of bioactive molecules (BAM) for the long-time release [313, 314]. As regards the future, the further steps under consideration relate to both realization of the target properties of the proposed LDRS systems [302], and to optimization of their chemical design, and *in vitro* and *in vivo* study of their biological properties. Such a task can be solved, for instance, by studying a possibility of pairwise assembly of components of a composition that includes a polymer, a POM, a xanthene dye (rhodamine) covalently bound in the form of NHS-ester, and a drug.

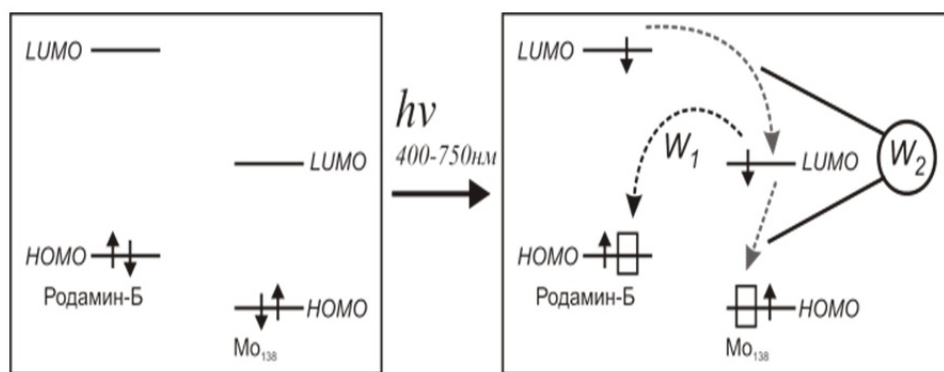


FIG. 15. Photochemical processes in a POM-dye system on the example of a toroidal compound Mo_{138}

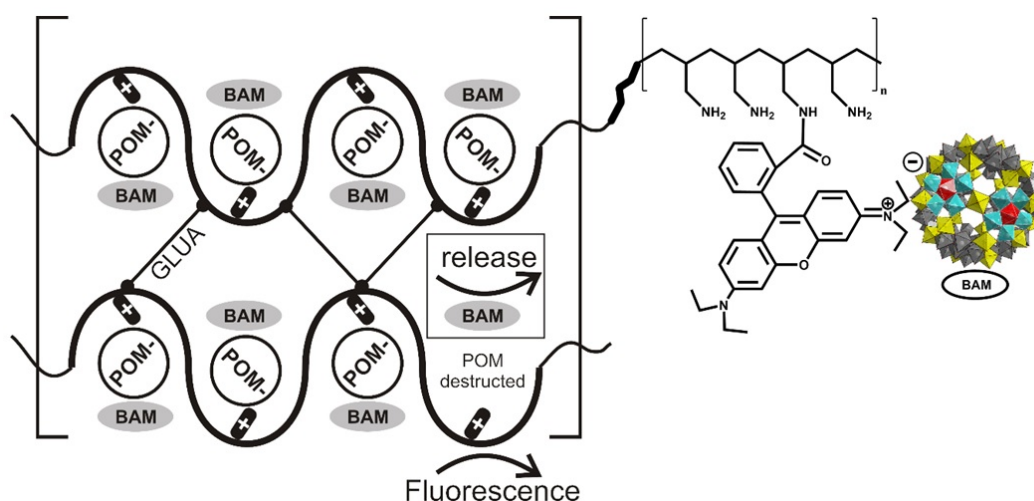


FIG. 16. Diagram of a promising POM-based releasing system. BAM - bioactive molecules; GLUA - glutaric dialdehyde

The oscillatory nature of the dependence of the physicochemical characteristics of POM-based associates (Section 3) and the possibility of influencing the compositions by ultraviolet radiation have been pointed out above. It

is important to understand the light-influenced behavior of nanostructured objects when developing photoinduced controlled-release systems (Section 1.1) and feedback systems (Section 5). It is impossible to miss the fact that in some cases, oscillatory phenomena are observed during the impact on the systems that contain gradually destructing POMs, [297,303]. In this case, fluctuations depend not only on the composition; temporal oscillations of fundamental physical and chemical properties, such as optical density, photovoltaic potential, etc. also occur. Oscillations of physical properties are most often characteristic of the systems containing macromolecular components, e.g., polymers or POMs [175,201,315]. For POMs, the oscillatory phenomena prerequisites include the large size of polyanions, as well as the nonlinearity of characteristics, including the optical properties [316] of molybdenum-containing complexes (associates) with organic substances, e.g., with citric acid [317]. Due to the reversibility of redox reactions of d-metal ions (electron transfer in associates [297]), POMs are able to participate in oscillatory processes. The oscillatory phenomena mechanism can have significant differences in the differently composed systems and in varying conditions in which these phenomena are observed. Each case requires a detailed consideration, which we did below for the above-described systems containing Mo_{132} , rhodamine-B, and also showing signs of properties oscillation.

The experiments aimed at studying Mo_{132} destruction in aqueous solutions with a concentration of $5.4 \mu\text{M}$ and in contact with argon showed that this process is stimulated by the influence of light [303]. For irradiation, two LEDs were used together, the first of which emitted light mainly at 630 and 570 nm wavelengths, and the second at 466 nm. This combination made it possible to reproduce the main spectral components of daylight. Before irradiation of the solutions, they were preliminarily purged with argon. In the course of the experiments (Fig. 17), there was a general decrease in the optical density (A) at 455 nm wavelength, associated with POM destruction, and the measured value A was found to fluctuate exceeding the measurement error. The previously performed experiments [318] demonstrated similar oscillations related to the potential difference U between the frontally UV-irradiated Mo_{132} solution, which also contained polyvinyl alcohol (PVA), and a likewise solution, though light-protected (Fig. 18). The potential difference had a negative value and increased with time. It occurred due to a decrease in the Mo(V) concentration in the irradiated solution during the photochemical destruction of POM, and the oxidation to Mo(VI) during Mo_{132} destruction despite the presence of PVA. On the contrary, when other POMs were present in solutions instead of Mo_{132} , partial reduction of molybdenum ions occurred during the interaction with PVA and was accompanied by an increase in positive values of the potential difference. The presence of a photoinduced potential difference accompanying the photochromic effect manifestation in molybdenum-containing systems, as well as signs of nonlinear and oscillatory processes, are also described in [317,319]. Oscillatory processes could occur in this case due to the partial reversibility of photochemical processes.

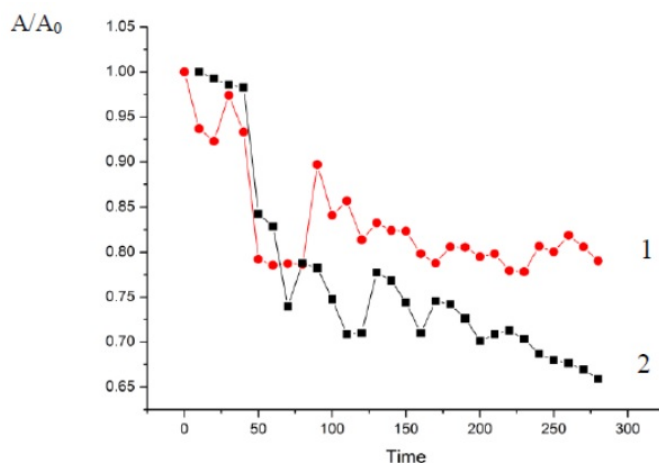


FIG. 17. Relative optical density of Mo_{132} solutions as a function of the irradiation time (min) in contact with argon (1) and air (2). The initial optical density is designated as 1

It should be noted that, in contrast to the systems containing, e.g., ammonium heptamolybdate, where redox reactions are reversible [297] and the occurrence of fluctuations in the potential difference is generally understandable, Mo_{132} destruction proceeds irreversibly [198]. The products of destruction do not absorb light intensely at the 455 nm wavelength characteristic of Mo_{132} . In this relation, there arises a question about the causes of the fluctuating optical density of Mo_{132} solutions and of the concentration-induced potential difference. If the value of U could fluctuate due to a reversible change in the content of Mo(V) , including its non-Keplerate forms, upon their interaction with PVA, then why did the optical density fluctuate? Note that the LEDs irradiated the studied solutions from above [303], i.e.,

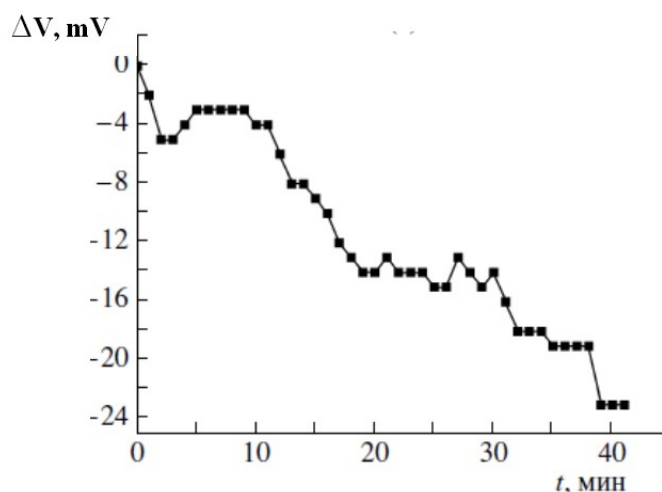
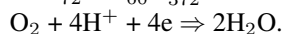
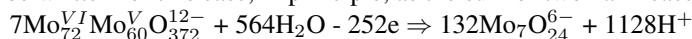


FIG. 18. Potential difference (ΔV) between the illuminated and light-protected Mo_{132} solution (0.015 wt. %) - PVA (10 wt. %) [318]. ©Pleiades Publishing, Ltd. 2009

from where the gaseous medium was in contact with the solutions. In this case, the harder part of the LEDs radiation at 466 nm was absorbed by the solution itself, the characteristic wavelength of which is in the near region. Therefore, it can be assumed that the photoinitiated reaction of Mo_{132} destruction, accompanied by the oxidation of molybdenum to Mo(VI), was localized precisely at the solution surface in a relatively thin layer, the thickness of which did not exceed 0.5 mm [320]. In this case, the described above potential difference appeared between the liquid-gas interface and bulk solution. So, the solution surface can be considered formally as a positive electrode (cathode). The reaction of POM oxidative destruction, which occurs due to the interaction with residual oxygen in argon (no more than 1 vol.%), can be written for this case, in principle, as the sum of two half-reactions, e.g., the following ones:



The oxidation-reduction potentials of the components of the considered system make the above reaction feasible. At least for the second half-reaction, the standard potential is +1.229 V.

During Mo_{132} decomposition in accordance with the proposed reaction scheme, the acidity of the medium is supposed to increase, which was confirmed experimentally [198]. The potential difference between the solution surface layer and its lower part should accelerate the migration of protons (hydronium ions H_3O^+) deeper into the solution and the supply of anions to the cathode. Taking into account the circumstance that the spectrophotometer beam aperture did not cover the entire measuring cell and the beam was passing through its middle part, it can be assumed that the relative increase in optical density in the observed oscillations was associated with an increase in the Mo_{132} concentration in the aperture due to the accelerated diffusion from the lower part of the cell. The diffusion coefficients of hydronium ions and polyanions are sufficiently different; therefore, an oppositely directed diffusion potential could occur in the system under study, which, on the contrary, slowed down the flow of ions, thus leading to a stepwise decrease in the value of A (Fig. 17), since POM destruction continued. The interaction of these factors could lead to the observed fluctuations.

Another factor that could potentially lead to a temporary partial blocking of the reaction of POM destruction is the oxygen deficiency in the solution, because the rate of oxygen dissolution in a liquid medium is limited. The value of D, the coefficient of oxygen diffusion in an aqueous medium given in [320], is around $2 \cdot 10^{-5} \text{ cm}^2/\text{s}$. A comparison of this value with the effective D value of Mo_{132} polyanions under electrodiffusion conditions ($1.8 \cdot 10^{-7} \text{ cm}^2/\text{s}$) [107] (POM concentration of $4 \cdot 10^{-4} \text{ mol/L}$), shows that the latter are much less mobile. For this reason, the supply of polyanions to the solution surface is more likely the limiting stage of the oxidative photodecomposition process. In this case, the diffusion restrictions, as well as fluctuations of A values, can at least be partially removed due to intensive vertical mixing of the solution. However, this is difficult to implement with the used measurement scheme. On the other hand, in order to obtain additional information, it is possible to increase the oxygen content in the medium contacting the solution, as it was done in the next experiment (Fig. 17) by replacing argon with air. With an increase in the oxygen content in the gaseous medium, the process of POM destruction accelerated in general, but the optical density fluctuations did not disappear, which indirectly confirms the hypothesized mechanism of the occurrence of oscillations

of A. In addition, attention should be paid to the amount of oxygen required in accordance with the reaction scheme for the oxidation of Mo_{132} in the solution: it takes about $1.5 \cdot 10^{-6}$ g of oxygen per 1 ml of a solution in the used concentration. The solubility of oxygen at room temperature in water and diluted solutions is about $6.6 \cdot 10^{-3}$ g/L. If 1 ml of the initial solution could contain about $6.6 \cdot 10^{-6}$ g of dissolved oxygen, then its amount was about 4.4 times higher than that required for POM oxidation.

The photochemical nature of POM oxidative destruction can be confirmed by the stabilization of Mo_{132} upon formation of its associates with rhodamine-B, a dye of the xanthene series [303] (the main absorption maximum at a wavelength of 558 nm, near one of the maxima of the used LED). Stabilization manifests itself, for instance, during irradiation of such solutions (Mo_{132} - RhB molar ratio of 1:8) in contact with air (Fig. 19). In another case, when a substance that is more easily oxidized than POM is in contact with the above associates, the Mo_{132} -rhodamine-B system is capable of playing the role of a photoactivated catalyst. The oxidation of compounds such as toluene and isopropyl alcohol proceeds under quite mild conditions. Toluene is selectively oxidized to benzyl alcohol and benzaldehyde [321], and isopropyl alcohol is oxidized to acetone. Photoactivated compounds of the nanocluster type, including d-metals in different oxidation states, can be practically useful as catalysts for the oxidation of organic compounds [322,323], for instance in processes of organic synthesis, and of alternative energetics (hydrogen production) for reducing the potential of electrochemical decomposition of aqueous solutions [324]. Examples of the use of molybdenum and tungsten compounds in the photolysis of water [316,325] are known from the literature.

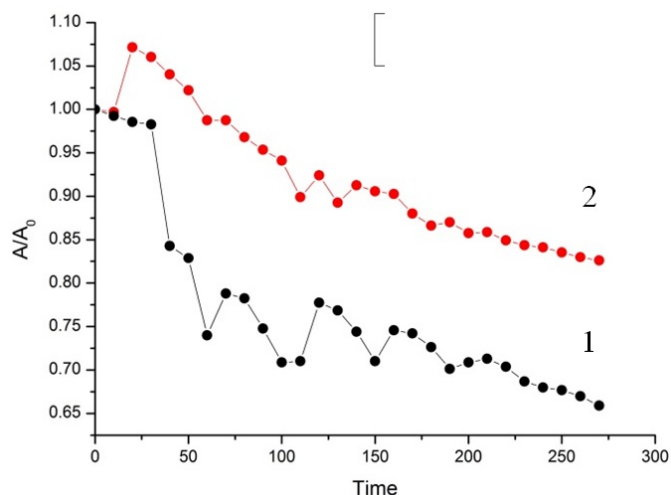


FIG. 19. Relative optical density of the irradiated solutions of Mo_{132} (1) and Mo_{132} - rhodamine-B (2) in contact with air (as a function of time, in min)

So, it has been shown that diffusion processes can be the cause of the oscillatory phenomena occurrence, in particular, of oscillations of the measured optical density of Mo_{132} POM aqueous solutions under local exposure to light. In the studied system, the processes of POM oxidative photodestruction occurring in the surface part of the solution, are limited by the mobility of Mo_{132} polyanions, the speed of which periodically changes depending on the ratio of the values of the concentration and diffusion potentials arising between the surface of the solution and its deep part. Further studies of oscillatory phenomena involving POM are of interest, especially taking into account the possibility of using these compounds in catalysis. It should be assumed that similar phenomena can occur in the body's environment, and it should be taken into account, in particular, when monitoring drug release.

6. Conclusion

Thus, there are a number of factors that make it possible to consider molybdenum-based nanocluster POMs as compounds for use in biomedicine which show promise. These physical and biochemical properties include: the ability of POMs to undergo decomposition *in vivo*; the absence of accumulation of POM and their components in organs and tissues due to elimination in the course of natural metabolism; the possibility of obtaining conjugates of drugs and bioactive substances (including protein), biocompatible polymers, indicator dyes; targeted transport (for instance, ionophoresis) of POM and their conjugates into the body. $\text{Mo}_{72}\text{Fe}_{30}$ is able to penetrate into immuno-privileged organs (e.g., brain, eyes, thymus, spleen, etc.) and overcome blood-tissue barriers. At the same time, $\text{Mo}_{72}\text{Fe}_{30}$ has low toxicity for warm-blooded organisms; its administration by various methods does not lead to disruption of organs

and systems, being reflected only in small reversible changes at the metabolic level, e.g., in the aminotransferase activity. In addition, it was noted that the organism of animals (rats) is capable of adapting to the influence of POM, which, among other things, provides the normalization of the above-mentioned parameter. The effect of $\text{Mo}_{72}\text{Fe}_{30}$ at the molecular level revealed itself only in a change in the content of heat shock proteins, which are involved in the adaptation of the organism and maintenance of homeostasis. The single and multiple action of POM did not cause a decrease in the amount of histone proteins in blood lymphocytes, which makes a suggestion about the absence of autoimmune aggression of these cells against liver tissue. The effect of rapid recovery of the hemoglobin level and the number of erythrocytes was established upon administration of $\text{Mo}_{72}\text{Fe}_{30}$ preparations to animals in a state of post-hemorrhagic anemia. It indicates the possibility of therapeutic use for POMs, which have a positive effect on the processes of erythropoiesis.

Mo_{132} , which contains Mo(V), is more toxic than $\text{Mo}_{72}\text{Fe}_{30}$, in general. A study of the effect of these two POMs on cell cultures of normal and transformed fibroblasts showed that $\text{Mo}_{72}\text{Fe}_{30}$ is practically non-toxic for normal fibroblasts, while Mo_{132} is toxic for both normal and transformed fibroblasts, and its damaging effect on transformed fibroblasts is stronger: a decrease in cell proliferative activity and an accelerated differentiation of transformed rat fibroblasts were recorded. The experimental results indicate the potential use of Mo_{132} in chemotherapy.

It is important to study the aspects related to the processes of POM destruction under various conditions in their free and conjugated states, as it allows predicting the lifetime of POM-based functional transport units and regulating their stability. The studies have shown possible mechanisms of POM destruction, including photoinitiated ones, and established that stabilizing factors can include self-aggregation of POM into hollow globular associates, the interaction of POM with such biogenic ions as calcium, and association with water-soluble nonionic biocompatible polymers. One of the most important stabilizing factors influencing POM upon entering normal alkaline environments of the body (e.g., blood) is the interaction with proteins, in particular, with albumins (protein corona appearance), while in the environment of a corresponding alkaline buffer solution, POMs decompose much more quickly.

Fundamental approaches for the creation of new POM-based controlled releasing systems with feedback have been proposed. In these systems, POM conjugates with a drug and an indicator luminescent dye are initially bound with a matrix of a biocompatible polymeric organic or inorganic carrier in the microgel composition. This should ensure prolonged release of drugs and simultaneous monitoring of their residual concentration indicated by the fluorescent signal of the dye molecules.

Acknowledgements

The paper was prepared in the framework of implementation of the State Assignment from the Ministry of Education and Science of the Russian Federation (Projects Nos. AAAA-A20-120061990010-7 (FEUZ-2020-0052) and AAAA-A18-118020590107-0), as well as of the Program for Increasing Competitiveness of UrFU (financially supported according to the Decree No. 211 of the Government of the Russian Federation, Contract No. 02.A03.21.0006). The research aimed at creating the long-time drug release systems with feedback was carried out within the framework of the project of the Russian Science Foundation No. 19-73-00177.

References

- [1] Gregoriadis G., Swain C.P., Wills E.J., Tavill A.S. Drug-carrier potential of liposomes in cancer chemotherapy. *Lancet*, 1974, **1**, P. 1313–1316.
- [2] Torchilin V.P. Recent advances with liposomes as pharmaceutical carriers. *Nat. Rev. Drug Discov.*, 2005, **4**, P. 145–160.
- [3] Johnston M.J., Semple S.C., Klimuk S.K., Ansell S., Maurer N., Cullis P.R. Characterization of the drug retention and pharmacokinetic properties of liposomal nanoparticles containing dihydrosphingomyelin. *Biochim. Biophys. Acta*, 2007, **1768**, P. 1121–1127.
- [4] Fenske D.B., Cullis C.A. Liposomal Nanomedicines: An Emerging Field. *Toxicologic Pathology*, 2008, **36**, P. 21–29.
- [5] Raney S.G., Wilson K.D., Sekirov L., Chikh G., de Jong S.D., Cullis P.R., Tam Y.K. The effect of circulation lifetime and drug-to-lipid ratio of intravenously administered lipid nanoparticles on the biodistribution and immunostimulatory activity of encapsulated CpG-ODN. *J. Drug Target*, 2008, **16**(7), P. 564–77.
- [6] Fenske D.B., Cullis P.R. Liposomal Nanomedicines. *Expert Opin. Drug. Deliv.*, 2008, **5**(1), P. 25–44.
- [7] Farokhzad O.C., Langer R. Impact of Nanotechnology on Drug Delivery. *ACS Nano*, 2009, **3**(1), P. 16–20.
- [8] Takahama H., Minamino T., Asanuma H., Fujita M., Asai T., Wakeno M., Sasaki H., Kikuchi H., Hashimoto K., Oku N., Asakura M., Kim J., Takashima S., Komamura K., Sugimachi M., Mochizuki N., Kitakaze M. Prolonged targeting of ischemic/reperfused myocardium by liposomal adenosine augments cardioprotection in rats. *J. Amer. College of Cardiology*, 2009, **53**(8), P. 709–717.
- [9] Chen Y., Bose A., Bothun G.D. Controlled Release from Bilayer-Decorated Magnetoliposomes via Electromagnetic Heating. *ACS Nano*, 2010, **4**(6), P. 3215–3221.
- [10] Parashar A.K., Kakde D., Chadhar V., Devaliya R., Shrivastav V., Jai U.K. A review on Solid Lipid Nanoparticles (SLN) for controlled and targeted delivery of medicinal agents. *Curr. Res. Pharm. Sci.*, 2011, **1**(2), P. 367–47.
- [11] Anwekar H., Patel S., Singhai A.K. Liposomes as drug carriers. *Int. J. Pharm. Life Sci. (IJPLS)*, 2011, **2**(7), P. 945–951.
- [12] Tam Y.C., Chen S., Cullis P.R. Advances in Lipid Nanoparticles for siRNA Delivery. *Pharmaceutic*, 2013, **5**, P. 498–507.
- [13] Akbarzadeh A., Rezaei-Sadabady R., Nejati K. Liposome: classification, preparation, and Applications. *Nanoscale Research Letters*, 2013, **8**(1), P. 102–111.

- [14] Smyslov R.Yu., Ezdakova K.V., Kopitsa G.P., Khripunov A.K., Bugrov A.N., Tkachenko A.A., Angelov B., Pipich V., Szekely N.K., Baranchikov A.E., Latysheva E., Chetverikov Yu.O., Haramus V. Morphological structure of Gluconacetobacter xylinus cellulose and cellulose-based organic-inorganic composite materials. *J. Phys.: Conf. Ser.*, 2017, **848**(1), P. 012017.
- [15] Almjasheva O.V., Garabadzhiu A.V., Kozina Yu.V., Litvinchuk L.F., Dobritsa V.P. Biological effect of zirconium dioxide-based nanoparticles. *Nanosystems: Physics, Chemistry, Mathematics*, 2017, **8**(3), P. 391–396.
- [16] Popov A.L., Shcherbakov A.B., Zholobak N.M., Baranchikov A.Ye., Ivanov V.K. Cerium dioxide nanoparticles as third-generation enzymes (nanozymes). *Nanosystems: Physics, Chemistry, Mathematics*, 2017, **8**(6), P. 760–781.
- [17] Shydlovska O., Kharchenko E., Zholobak N., Shcherbakov A., Marynin A., Ivanova O., Baranchikov A., Ivanov V. Cerium oxide nanoparticles increase the cytotoxicity of TNF alpha in vitro. *Nanosystems: Physics, Chemistry, Mathematics*, 2018, **9**(4), P. 537–543.
- [18] Almjasheva O.V., Smirnov A.V., Fedorov B.A., Tomkovich M.V., Gusarov V.V. Structural features of ZrO_2 - Y_2O_3 and ZrO_2 - Gd_2O_3 nanoparticles formed under hydrothermal conditions. *Russ. J. Gen. Chem.*, 2014, **84**(5), P. 804–809.
- [19] Popov A.L., Savintseva I.V., Mysina E.A., Shcherbakov A.B., Popova N.R., Ivanova O.S., Kolmanovich D.D., Ivanov V.K. Cytotoxicity analysis of gadolinium doped cerium oxide nanoparticles on human mesenchymal stem cells. *Nanosystems: Physics, Chemistry, Mathematics*, 2018, **9**(3), P. 430–438.
- [20] Vardanyan Z., Gevorkyan V., Ananyan M., Vardapetyan H., Trchounian A. Effects of various heavy metal nanoparticles on *Enterococcus hirae* and *Escherichia coli* growth and proton coupled membrane transport. *J. Nanobiotechnol.*, 2015, **13**(69), P. 2–9.
- [21] Popov A.L., Ermakov A.M., Shekunova T.O., Shcherbakov A.B., Ermakova O.N., Ivanova O.S., Popova N.R., Baranchikov A.Ye., Ivanov V.K. PVP-stabilized tungsten oxide nanoparticles inhibit proliferation of NCTC L929 mouse fibroblasts via induction of intracellular oxidative stress. *Nanosystems: Physics, Chemistry, Mathematics*, 2019, **10**(1), P. 92–101.
- [22] Sharker S.Md., Kim S.M., Lee J.E., Choi K.H., Shin G., Lee S., Lee D.K., Jeong J., Park S.Y. Functionalized biocompatible WO_3 nanoparticles for triggered and targeted in vitro and in vivo photothermal therapy. *J. Control. Release*, 2015, **217**, P. 211–220.
- [23] Zhou Z., Kong B., Yu C., Shi X., Wang M., Liu W., Sun Y., Zhang Y., Yang H., Yang S. Tungsten Oxide Nanorods: An Efficient Nanoplatforam for Tumor CT Imaging and Photothermal Therapy. *Sci. Rep.*, 2014, **4**, P. 3653–3663.
- [24] Xing Y., Li L., Ai X., Fu L. Polyaniline-coated upconversion nanoparticles with upconverting luminescent and photothermal conversion properties for photothermal cancer therapy. *Intern. J. Nanomed.*, 2016, **11**, P. 4327–4338.
- [25] Slowing I.I. Mesoporous silica nanoparticles as controlled release drug delivery and gene transfection carriers. *Adv. Drug Deliv. Rev.*, 2008, **60**(11), P. 1278–1288.
- [26] Kroto H.W., Heath J.R., O'Brien S.C., Curl, R.F. C_{60} : Buckminsterfullerene. *Nature*, 1985, **318**, P. 162–163.
- [27] Mendes R.G., Bachmatiuk A., Buchner B., Cuniberti G., Rummeli M.H. Carbon nanostructures as multi-functional drug delivery platforms. *J. Mater. Chem. B*, 2013, **1**(4), P. 401–428.
- [28] Mo K., Jiang T., Sun W., Gu Z. ATP-responsive DNA-graphene hybrid nanoaggregates for anticancer drug delivery. *Biomater.*, 2015, **50**, P. 67–74.
- [29] Thabitha P., Shareena D., McShan D., Dasmahapatra A.K., Tchounwou P.B. A Review on Graphene-Based Nanomaterials in Biomedical Applications and Risks in Environment and Health. *Nano-Micro Lett.*, 2018, **10**(53), P. 1–34.
- [30] Ren L., Zhang Y., Cui C., Bi Y., Ge X. Functionalized graphene oxide for anti-VEGF siRNA delivery: preparation, characterization and evaluation in vitro and in vivo. *RSC Adv.*, 2017, **7**, P. 20553–20566.
- [31] Jakubek L.M., Marangoudakis S., Raingo J., Liu X., Lipscombe D., Hurt R.H. The inhibition of neuronal calcium ion channels by trace levels of yttrium released from carbon nanotubes. *Biomater.*, 2009, **30**, P. 6351–6357.
- [32] Bianco A., Kostarelos K., Partidos C.D., Prato M. Biomedical applications of functionalized carbon nanotubes. *Chem. Commun. (Cambridge, UK)*, 2005, **5**, P. 571–577.
- [33] Singh R., Pantarotto D., McCarthy D. Binding and condensation of plasmid DNA onto functionalized carbon nano-tubes: toward the construction of nanotube-based gene delivery vectors. *J. Am. Chem. Soc.*, 2005, **127**, P. 4388–4396.
- [34] Mahmood M., Karmakar A., Fejleh A., Mocan T., Iancu C., Mocan L., Iancu D.T., Xu Y., Dervishi E., Li Z., Biris A.R., Agarwal R., Ali N., Galanzha E.I., Biris A.S., Zharov V.P. Synergistic enhancement of cancer therapy using a combination of carbon nanotubes and antitumor drug. *Nanomed.*, (London), 2009, **4**, P. 883–893.
- [35] Liu Z., Fan A.C., Rakhra K., Sherlock S., Goodwin A., Chen X., Yang Q., Felsner D.W., Dai H. Supramolecular stacking of doxorubicin on carbon nanotubes for in vivo cancer therapy. *Angew. Chem. Int. Ed. Engl.*, 2009, **41**(48), P. 7668–7672.
- [36] Pastorin G., Wu W., Wiecekwski S., Briand J.P., Kostarelos K., Prato M. Bianco A. Double functionalization of carbon nanotubes for multimodal drug delivery. *Chem. Commun.*, 2006, **11**, P. 1182–1184.
- [37] Kateb B., Yamamoto V., Alizadeh D., Zhang L., Manohara H.M., Bronikowski M.J., Badie B. Multi-walled carbon nanotube (MWCNT) synthesis, preparation, labeling, and functionalization. *Immunotherapy of Cancer, Methods in Molecular Biology*, 2010, **651**, P. 307–317.
- [38] Garcia B.O., Kharissova O.V., et al. Nanocomposites with antibacterial properties using CNTs with magnetic nanoparticles. *Nanosystems: Physics, Chemistry, Mathematics*, 2016, **7**(1), P. 161–168.
- [39] Foldvari M., Bagonluri M. Carbon nanotubes as functional excipients for nanomedicines: II. Drug delivery and biocompatibility issues. *Nanomed.*, 2008, **4**(3), P. 183–200.
- [40] Cai D., Mataraza J.M., Qin Z.H., Huang Z., Huang J., Chiles T.C., Carnahan D., Kempa K., Ren Z. Highly efficient molecular delivery into mammalian cells using carbon nanotube spearing. *Nat. Methods*, 2005, **2**, P. 449–454.
- [41] Turcheniuk K., Mochalin V.N. Biomedical Applications of Nanodiamond (Review). *Nanotechnology*, 2017, **28**, P. 252001–252027.
- [42] Rosenholm J.M., Vlasov I.I., Burikov S.A., Dolenko T.A., Shenderova O.A. Nanodiamond Based Composite Structures for Biomedical Imaging and Drug Delivery (Review). *J. Nanosci. Nanotechnol.*, 2015, **15**, P. 959–971.
- [43] Kulvelis Y.V., Shvidchenko A.V., Aleksenskii A.E., Yudina E.B., Lebedev V.T., Shestakov M.S., Dideikin A.T., Khozyaeva L.O., Kuklin A.I., Gy T., Rulev M.I., Vul A.Y. Stabilization of detonation nanodiamonds hydrosol in physiological media with poly (vinylpyrrolidone). *Diamond and Related Mater.*, 2018, **87**, P. 78–89.
- [44] Girard H., Pager V., Simic V., Arnault J.C. Peptide nucleic acid nanodiamonds: Covalent and stable conjugates for DNA targeting. *RSC Adv.*, 2014, **4**, P. 3566–3572.
- [45] Bokarev A.N., Plastun I.L. Possibility of drug delivery due to hydrogen bonds formation in nanodiamonds and doxorubicin: molecular modeling. *Nanosystems: Physics, Chemistry, Mathematics*, 2018, **9**(3), P. 370–377.

- [46] Giammarco J., Mochalin V.N., Haeckel J., Gogotsi Y. The adsorption of tetracycline and vancomycin onto nanodiamond with controlled release. *J. Colloid Interface Sci.*, 2016, **468**, P. 253–261.
- [47] Schimke M., Steinmüller-Nethl D., Kern J., Krüger A., Lepperdinger G. Biofunctionalization of nano-scaled diamond particles for use in bone healing and tissue engineering. *Experimental Gerontology*, 2015, **68**, P. 100.
- [48] Chen M., Pierstorff E.D., Li Sh-Y., Robert Lam R., Huang H., Eiji Osawa E., Dean Ho D. Nanodiamond-mediated delivery of water-insoluble therapeutics. *ASC Nano*, 2009, **7**(3), P. 2012–2022.
- [49] Solomatin A.S., Yakovlev R.Yu., Efremenkova O.V., Sumarukova I.G., Kulakova I.I., Lisichkin G.V. Antibacterial activity of Amikacin immobilized detonation nanodiamond. *Nanosystems: Physics, Chemistry, Mathematics*, 2017, **8**(4), P. 531–534.
- [50] Vul A.Y., Dideikin A.T., Alexenskii A.E., Baidakova M.V. Detonation nanodiamonds: Synthesis, Properties and Applications. Chapter 2. In: Nanodiamond. Ed. Williams O.A. Published by the Royal Society of Chemistry, Cambridge, 2014, P. 27–48.
- [51] Bondar' V.S., Puzyr' A.P. Nanodiamonds for Biological Investigations. *Physics of the Solid State*, 2004, **46**(4), P. 716–719.
- [52] Krysanov E.Yu., Demidova T.B., Ivanova O.S., Ordzhonikidze K.G., Shcherbakov A.B., Ivanov V.K. Synergetic action of ceria nanoparticles and doxorubicin on the early development of two fish species, Danio rerio and Puntius tetrazona. *Nanosystems: Physics, Chemistry, Mathematics*, 2019, **10**(3), P. 289–302.
- [53] Semenov K.N., Andrusenko E.V., Charykov N.A., Litasova E.V., Panova G.G., Penkova A.V., Murin I.V., Piotrovskiy L.B. Carboxylated Fullerenes: Physico-Chemical Properties and Potential Applications. *Prog. Solid State Chem.*, 2017, **47–48**, P. 19–36.
- [54] Tyurin D.P., Kolmogorov F.S., Cherepkova I.A., Charykov N.A., Semenov K.N., Keskinov V.A., Safyannikov N.M., Pukhareno Y.V., Letenko D.G., Segeda T.A., Shaimardanov Z. Antioxidant properties of fullereneol-d. *Nanosystems: Physics, Chemistry, Mathematics*, 2018, **9**(6), P. 798–810.
- [55] Safyannikov N.M., Charykov N.A., Garamova P.V., Semenov K.N., Keskinov V.A., Kurilenko A.V., Cherepkova I.A., Tyurin D.P., Klepikov V.V., Matuzenko M.Y., Kulenova N.A., Zolotarev A.A. Cryometry data in the binary systems bisadduct of C₆₀ and indispensable aminoacids – lysine, threonine, oxyproline. *Nanosystems: Physics, Chemistry, Mathematics*, 2018, **9**(1), P. 46–48.
- [56] Dubinina I.A., Kuzmina E.M., Dudnik A.I., Vnukova N.G., Churilov G.N., Samoylova N.A. Study of antioxidant activity of fullereneols by inhibition of adrenaline autoxidation. *Nanosystems: Physics, Chemistry, Mathematics*, 2016, **7**(1), P. 153–157.
- [57] Shultz M.D., Duchamp J.C., Wilson J.D., Shu C.Y., Ge J., Zhang J., Gibson H.W., Fillmore H.L. Encapsulation of a radiolabeled cluster inside a fullerene cage, ¹⁷⁷Lu_xLu_(3-x)N@C₈₀: an interleukin-13-conjugated radiolabeled metallofullerene platform. *J. Amer. Chem. Soc.*, 2010, **132**(14), P. 4980–4981.
- [58] Bolskar R.D. Gadofullerene MRI contrast agents. *Nanomedicine (Lond.)*, 2008, **3**(2), P. 201–213.
- [59] Lebedev V.T., Kulvelis Yu.V., Runov V.V., Szhogina A.A., Suyasova M.V. Biocompatible water-soluble endometallofullerenes: peculiarities of self-assembly in aqueous solutions and ordering under an applied magnetic field. *Nanosystems: Physics, Chemistry, Mathematics*, 2016, **7**(1), P. 22–29.
- [60] Kuchma E., Zolotukhin P., Belanova A., Soldatov M., Lastovina T., Kubrin S., Nikolsky A., Mirmikova L., Soldatov A. Low Toxic Maghemite Nanoparticles for Theranostic Applications. *International Journal of Nanomedicine*, 2017, **12**, P. 6365–6371.
- [61] Lojk J., Bregar V.B., Strojkan K., Hudoklin S., Veranič P., Pavlin M., Kreft M.E. Increased Endocytosis of Magnetic Nanoparticles into Cancerous Urothelial Cells versus Normal Urothelial Cells. *Histochemistry and Cell Biology*, 2018, **149**(1), P. 45–59.
- [62] Firouzi M., Poursalehi R., Delavari H., Saba F., Oghabian M.A. Chitosan coated tungsten trioxide nanoparticles as a contrast agent for X-ray computed tomography. *Int. J. Biol. Macromol.*, 2017, **98**, P. 479–485.
- [63] Gelperina S., Maksimenko O., Khalansky A., Vanchugova L., Shipulo E., Abbasova K., Berdiev R., Wohlfart S., Chepurnova N., Kreuter J. Drug delivery to the brain using surfactant-coated poly (lactide-co-glycolide) nanoparticles: influence of the formulation parameters. *Eur. J. Pharm. Biopharm.*, 2010, **74**, P. 157–163.
- [64] Popova N.R., Popov A.L., Shcherbakov A.B., Ivanov V.K. Layer-by-layer capsules as smart delivery systems of CeO₂ nanoparticle-based theranostic agents. *Nanosyst. Phys. Chem. Math.*, 2017, **8**(2), P. 282–289.
- [65] Venkatesan H., Radhakrishnan S., Parthibavarmam M., Kumar R.D., Sekar C. Synthesis of polyethylene glycol (PEG) assisted tungsten oxide (WO₃) nanoparticles for L-dopa bio-sensing applications. *Talanta*, 2011, **85**(4), P. 2166–2174.
- [66] Mornet S., Vasseur S., Grasset F., Duguet E. Magnetic Nanoparticle Design for Medical Diagnosis and Therapy. *Journal of Materials Chemistry*, 2004, **14**(14), P. 2161–2175.
- [67] Garanina A.S., Kireev I.I., Alieva I.B., Majouga A.G., Davydov V.A., Murugesan S., Khabashesku V.N., Agafonov V.N., Uzbekov R.E. New superparamagnetic fluorescent Fe@C-C₅ON₂H₁₀-Alexa Fluor 647 nanoparticles for biological applications. *Nanosystems: Physics, Chemistry, Mathematics*, 2018, **9**(1), P. 120–122.
- [68] Alieva I., Kireev I., Rakhmanina A., Garanina A., Strelkova O., Zhironkina O., Cherepaninets V., Davydov V., Khabashesku V., Agafonov V., Uzbekov R. Magnetinduced behavior of iron carbide (Fe₇C₃@C) nanoparticles in the cytoplasm of living cells. *Nanosystems: Physics, Chemistry, Mathematics*, 2016, **7**(1), P. 158–160.
- [69] Koulikova M., Kochubey V.I. Synthesis and Optical Properties of Iron Oxide Nanoparticles for Photodynamic Therapy. *Reports of Samara Scientific Center of Russian Academy of Sciences (RAS)*, 2012, **14**(4), P. 206–209.
- [70] Dykman L.A., Khlebtsov N.G. Gold Nanoparticles in Biology and Medicine: Recent Advances and Prospects. *Acta Naturae*, 2011, **3**(2), P. 34–55.
- [71] Preethika R.K., Ramya R., Ganesan M., Nagaraj S., Pandian K. Synthesis and characterization of neomycin functionalized chitosan stabilized silver nanoparticles and study its antimicrobial activity. *Nanosystems: Physics, Chemistry, Mathematics*, 2016, **7**(4), P. 759–764.
- [72] Akbarzadeh A., Mohammad Samiei M., Soodabeh Davaran S. Magnetic nanoparticles: preparation, physical properties, and applications in biomedicine. *Nanoscale Res. Lett.*, 2012, **7**, P. 144–157.
- [73] Tartaj P., Morales M.D.D., Veintemillas-Verdaguer S., Gonzalez-Carreno T., Serna C.J. The preparation of magnetic nanoparticles for applications in biomedicine. *J. Phys. D: Appl. Phys.*, 2003, **36**, P. R182–R197.
- [74] Ghadiri M., Vasheghani-Farahani E., Atyabi F., Kobarfard F., Mohamadyar-Toupkanlou F., Hosseinkhani H. Transferrin-conjugated magnetic dextran-spermine nanoparticles for targeted drug transport across blood-brain barrier. *J. Biomed. Mater. Res. A*, 2017, **105A**(10), P. 2851–2864.
- [75] MacBain S.C., Yiu H.H., Dobson J. Magnetic nanoparticles for gene and drug delivery. *Int. J. Nanomed.*, 2008, **3**(2), P. 169–180.

- [76] Akbarzadeh A., Zarghami N., Mikaeili H., Asgari D., Goganian A.M., Khiabani H.K., Samiei M., Davaran S. Synthesis, characterization, and in vitro evaluation of novel polymer-coated magnetic nanoparticles for controlled delivery of doxorubicin. *Nanotechnol. Sci. Appl.*, 2012, **5**, P. 13–25.
- [77] Reddy L.H., Arias J.L., Nicolas J., Couvreur P. Magnetic nanoparticles: design and characterization, toxicity and biocompatibility, pharmaceutical and biomedical applications. *Chem. Rev.*, 2012, **112**, P. 5818–5878.
- [78] Kayal S., Ramanujan R.V. Anti-cancer drug loaded iron – gold core – shell nanoparticles (Fe@Au) for magnetic drug targeting. *J. Nanosci. Nanotechnol.*, 2010, **10**, P. 5527–5539.
- [79] Popov A.L., Popova N.R., Selezneva I.I., Akkizov A.Y., Ivanov V.K. Cerium oxide nanoparticles stimulate proliferation of primary mouse embryonic fibroblasts in vitro. *Materials Science and Engineering C*, 2016, **68**, P. 406–413.
- [80] Goldt A.E., Polyakov A.Yu., Sorkina T.A., Dubov A.L., Davidova G.A., Selezneva I.I., Maximov Y.V., Presnyakov I.A., Polyakova N.Yu., Goodilin E.A., Perminova I.V. Humic acid-stabilized superparamagnetic maghemite nanoparticles: surface charge and embryotoxicity evaluation. *Nanosystems: Physics, Chemistry, Mathematics*, 2019, **11**(3), P. 184–189.
- [81] Popov A.L., Popova N., Gould D.J., Shcherbakov A.B., Sukhorukov G.B., Ivanov V.K. Ceria Nanoparticles-Decorated Microcapsules as a Smart Drug Delivery/Protective System: Protection of Encapsulated *P. pyralis* Luciferase. *ACS Appl. Mater. Interfaces*, 2018, **10**, P. 14367–14377.
- [82] Popov A.L., Popova N.R., Tarakina N.V., Ivanova O.S., Ermakov A.M., Ivanov V.K., Sukhorukov G.B. Intracellular Delivery of Antioxidant CeO₂ Nanoparticles via Polyelectrolyte Microcapsules. *ACS Biomater. Sci. Eng.*, 2018, **4**, P. 2453–2462.
- [83] Popov A.L., Popova N., Gould D.J., Shcherbakov A.B., Sukhorukov G.B., Ivanov V.K. Ceria Nanoparticles-Decorated Microcapsules as a Smart Drug Delivery/Protective System: Protection of Encapsulated *P. pyralis* Luciferase. *ACS Appl. Mater. Interfaces*, 2018, **10**, P. 14367–14377.
- [84] Pope M.T., Müller A. Polyoxometalate Chemistry: An Old Field with New Dimensions in Several Disciplines. *Angew. Chem., Int. Ed. Engl.*, 1991, **30**, P. 34–48.
- [85] Pope M.T. *Heteropoly and Isopoly Oxometalates*. New York: Springer Verlag, 1983, 180 pp.
- [86] Proust A. Functionalized Polyoxometalates. *Polyoxometalate Molecular Science*, 2003, **98**, P. 233–252.
- [87] Gouzerh P., Che M. From Scheele and Berzelius to Müller Polyoxometalates (POMs) revisited and the “missing link” between the bottom up and top down approaches. *L'actualité chimique. Recherche et développement*, 2006, **298**, P. 1–14.
- [88] Müller A., Krickemeyer E., Meyer J., Bögge H., Peters F., Plass W., Diemann E., Dillinger S., Nonnenbruch F., Randerath M., Menke C. [Mo₁₅₄(NO)₁₄O₄₂₀(OH)₂₈(H₂O)₇₀]^{(25±5)-}: A Water Soluble Big Wheel with More than 700 Atoms and a Relative Molecular Mass of About 24000. *Angew. Chem. Int. Ed.*, 1995, **34**(19), P. 2122–2124.
- [89] Liu T., Diemann E., Müller A. Hydrophilic Inorganic Macro-Ions in Solution: Unprecedented Self-Assembly Emerging from Historical “Blue Waters”. *J. Chemical Education*, 2007, **84**(3), P. 526–532.
- [90] Müller A., Maiti R., Schmidtman M., Bögge H., Samar K.D., Zhang W. Mimicking oxide surfaces: different types of defects and ligand coordination at well defined positions of a molybdenum oxide based nanocluster. *Chem. Commun.*, 2001, P. 2126–2127.
- [91] Zhu Y., Cammers-Goodwin A., Zhao B., Dozier A., Dickey E.C. Kinetic precipitation of solution-phase polyoxomolybdate followed by transmission electron microscopy: A window to solution-phase nanostructure. *Chem. Eur. J.*, 2004, **10**, P. 2421–2427.
- [92] Müller A., Krickemeyer E., Bögge H., Schmidtman M., Peters F. Organizational Forms of Matter: An Inorganic Super Fullerene and Keplerate Based on Molybdenum Oxide. *Angewandte Chemie International Edition*, 1998, **37**(24), P. 3359–3363.
- [93] Müller A., Gouzerh P. From Linking of Metal-Oxide Building Blocks in a Dynamic Library to Giant Clusters with Unique Properties and towards Adaptive Chemistry. *Chemical Society Reviews*, 2012, **41**(22), P. 7431–7463.
- [94] Ostroushko A.A., Korotaev V.Yu., Tonkushina M.O., Vazhenin V.A., Artemov M.Yu., Men'shikov S.Yu., Kutyashev I.B. Spectroscopic studies of molybdenum polyoxometallates with the buckyball structure and polymer-containing compositions based thereon. *Russ. J. Inorg. Chem.*, 2011, **56**(2), P. 276–281.
- [95] Müller A., Diemann E., Shah S. Q. N., Kuhlmann C., Letzel M.C. Soccer-Playing Metal Oxide Giant Spheres: A First Step Towards Patterning Structurally Well Defined Nano-Object Collectives. *Chem. Commun.*, 2002, P. 440–441.
- [96] Müller A., Polarz S., Das S.K., Krickemeyer E., Bögge H., Schmidtman M., Hauptfleisch B. “Open and shut” for guests in molybdenum oxide-based giant spheres, baskets, and rings containing the pentagon as a common structural element. *Angew. Chem. Int. Ed.*, 1999, **38**(21), P. 3241–3245.
- [97] Müller A., Botar B., Das S.K., Bögge H., Schmidtman M., Merca A. On the complex hedgehog-shaped cluster species containing 368 Mo atoms: simple preparation method, new spectral details and information about the unique formation. *Polyhedron*, 2004, **23**(15), P. 2381–2385.
- [98] Hall N. Bringing Inorganic Chemistry to Life. *Chem. Commun. (The Royal Society of Chemistry)*, 2003, **7**, P. 803–806.
- [99] Müller A., Sarkar S., Shah S.Q.N., Bögge H., Schmidtman M., Sarkar S., Kögerler P., Hauptfleisch B., Trautwein V.X., Schünemann V. Archimedean Synthesis and Magic Numbers: “Sizing” Giant Molybdenum-Oxide-Based Molecular Spheres of the Keplerate Type. *Angew. Chem. Int. Ed. Engl.*, 1999, **38**(21), P. 3238–3241.
- [100] Liu T., Imber B., Diemann E., Liu G., Cokleski K., Li H., Chen Z., Müller A. Deprotonations and Charges of Well-Defined Mo₇₂Fe₃₀ Nanoacids Simply Stepwise Tuned by pH Allow Control/Variation of Related Self-Assembly Processes. *Journal of the American Chemical Society*, 2006, **128**(49), P. 15914–15920.
- [101] Besson C., Schmitz S., Capella K.M., Kopilevich S., Weinstock I.A., Kögerler P. A regioselective Huisgen reaction inside a Keplerate polyoxomolybdate nanoreactor. *Dalton Trans.*, 2012, **41**(33), P. 9852–9854.
- [102] Henry M., Bögge H., Diemann E., Müller A. Chameleon water: assemblies confined in nanocapsules. *J. Mol. Liq.*, 2005, **118**(1-3), P. 155–162.
- [103] Müller A., Gouzerh P. From linking of metal-oxide building blocks in a dynamic library to giant clusters with unique properties and towards adaptive chemistry. *Chem. Soc. Rev.*, 2012, **41**(22), P. 7431–7463.
- [104] Popa A.M., Hu L., Crespy D., Henry M., Rene M., Rossi R.M. Polyoxomolybdate-based selective membranes for chemical protection. *J. Membrane Science*, 2011, **373**(1-2), P. 196–201.
- [105] Ostroushko A.A., Sennikov M.Yu., Tonkushina M.O. Interaction of Polyoxometalate Mo₁₃₂ with Poly(vinyl alcohol). *Russ. J. Inorg. Chem.*, 2009, **54**(4), P. 617–623.

- [106] Ostroushko A.A., Tonkushina M.O., Korotaev V.Yu., Prokof'eva A.V., Kutyashev I.B., Vazhenin V.A., Danilova I.G., Men'shikov S.Yu. Stability of the Mo₇₂Fe₃₀ Polyoxometalate Buckyball in Solution. *Russ. J. Inorg. Chem.*, 2012, **57**(9), P. 1210–1213.
- [107] Ostroushko A.A., Tonkushina M.O., Martynova N.A. Mass and charge transfer in systems containing nanocluster molybdenum polyoxometallates with a fullerene structure. *Russ. J. Phys. Chem. A*, 2010, **84**(6), P. 1022–1027.
- [108] Ostroushko A.A., Gagarin I.D., Tonkushina M.O., Grzhegorzhevskii K.V., Gette I.F., Medvedeva S.Yu., Mukhlynina E.A., Ulitko M.V., Danilova I.G. Promising Means of Targeted Delivery of Medical Product on the Basis of Nanocluster Polyoxometalates // XX Mendeleev Congress on general and applied chemistry. Five volumes book. Vol. 4: abstracts. – Ekaterinburg: Ural Branch of the Russian Academy of Sciences, 2016. P. 511.
- [109] Grzhegorzhevskii K., Ostroushko A., Koriakova O., Ovchinnikova I., Kim G. Photoinduced charge transfer in the supramolecular structure based on toroid polyoxomolibdate Mo₁₃₈ and xanthene dye - Rhodamine-B. *Inorganica Chim. Acta*, 2015, **436**, P. 205–213.
- [110] Grzhegorzhevskii K.V., Adamova L.V., Eremina E.V., Ostroushko A.A. On the Possibility of Controlling the Hydrophilic/Hydrophobic Characteristics of Toroid Mo₁₃₈ Nanocluster Polyoxometalates. *Russ. J. Phys. Chem. A*, 2017, **91**(3), P. 561–568.
- [111] Grzhegorzhevskii K.V., Ostroushko A.A. Supramolecular Structural Design in a System Based on Nanocluster Mo₁₃₈ and a Cationic Surfactant: Influence of Components Ratio and pH of the Solutions. *Colloids and Surfaces A. Physicochemical and Engineering Aspects*, 2015, **480**, P. 130–137.
- [112] Ostroushko A.A., Fedorova O.V., Titova Yu.A., Vigorov K.V., Grzhegorzhevskii K.V. Enantioselective Catalytic Effect of Soft Thermal Decomposition Products of Iron-Molybdenum Polyoxometalate. *Proceedings of the 3rd All-Russian Conference with International Participation on Advances of Synthesis and Complex Formation, Moscow, Russia, April 21-25, 2014*, (RUDN, Moscow, 2014), **2**, P. 207.
- [113] Ostroushko A.A., Fedorova O.V., Titova Yu.A., Grzhegorzhevskii K.V. Iron-Molybdenum Polyoxometalate: Enantioselective Catalytic Activity of Soft Thermal Decomposition Products. *Proceedings of the 2nd Russian Congress on Catalysis ROSKATALIZ, Samara, October 2-5, 2014*, Ed. by V.N. Parmon and A.S. Noskov, Inst. Kataliza Boreskova, Sib. Otdel. RAN, Novosibirsk, 2014, **2**, P. 75.
- [114] Michelis F.V., Delitheos A., Tiligada E. Molybdate modulates mitogen and cyclosporin responses of human peripheral blood lymphocytes. *Journal of Trace Elements in Medicine and Biology*, 2011, **25**, P. 138–142.
- [115] Yamase T. Polyoxometalates for Molecular Devices: Antitumor Activity and Luminescence. *Molecular Engineering*, 1993, **3**(1-3), P. 241–262.
- [116] Yamase T., Fujita H., Fukushima K. Medical Chemistry of Polyoxometalates. Part 1. Potent Antitumor Activity of Polyoxomolybdates on Animal Transplantable Tumors and Human Cancer Xenograft. *Inorganica Chimica Acta*, 1988, **151**(1), P. 15–18.
- [117] Merca A., Haupt E.T.K., Mitra T., Bögge H., Rehder D., Müller A. Mimicking biological cation-transport based on sphere-surface supramolecular chemistry: Simultaneous interaction of porous capsules with molecular plugs and passing cations. *Chemistry – a European Journal*, 2007, **13**(27), P. 7650–7658.
- [118] Ziv A., Grego A., Kopilevich S., Zeiri L., Miro P., Bo C., Müller A., Weinstock I.A. Flexible Pores of a Metal Oxide-Based Capsule Permit Entry of Comparatively Larger Organic Guests. *J. Am. Chem. Soc.*, 2009, **131**(18), P. 6380–6382.
- [119] Rubcic M., Korenev V.S., Toma L., Bögge H., Fedin V.P., Müller A. Molecular recognition of Ca²⁺ cations by internal and external receptors/interfaces in a spherical porous molybdenum-oxide capsule: unusual coordination scenarios *Inorganic Chemistry Frontiers*, 2014, **1**(10), P. 740–744.
- [120] Watfa N., Melgar D., Haouas M., Taulelle F., Hijazi A., Naoufal D., Avalos J.B., Floquet S., Bo C., Cadot E. Hydrophobic Effect as a Driving Force for Host-Guest Chemistry of a Multi-Receptor Keplerate-Type Capsule. *J. Am. Chem. Soc.*, 2015, **137**(17), P. 5845–5851.
- [121] Elistratova J., Akhmadeev B., Korenev V., Sokolov M., Nizameev I., Gubaidullin A., Voloshina A., Mustafina A. Self-assembly of Gd³⁺-bound keplerate polyanions into nanoparticles as a route for the synthesis of positive MRI contrast agents. Impact of the structure on the magnetic relaxivity. *Soft Matter*, 2018, **14**(38), P. 7916–7925.
- [122] Elistratova J., Akhmadeev B., Korenev V., Sokolov M., Nizameev I., Ismaev I., Kadirov M., Sapunova A., Voloshina A., Amirov R., Mustafina A. Aqueous solutions of triblock copolymers used as the media affecting the magnetic relaxation properties of gadolinium ions trapped by metal-oxide nanostructures. *Journal of Molecular Liquids*, 2019, **296**, P. 111821.
- [123] Pizzanelli S., Zairov R., Sokolov M., Mascherpa M.C., Akhmadeev B., Mustafina A., Calucci L. Trapping of Gd(III) Ions by Keplerate Polyanionic Nanocapsules in Water: A 1H Fast Field Cycling NMR Relaxometry Study. *J. Phys. Chem. C*, 2019, **123**(29), P. 18095–18102.
- [124] Yin P., Li D., Liu T. Counterion Interaction and Association in Metal-Oxide. Cluster Macranionic Solutions and the Consequent Self-Assembly. *Isr. J. Chem.*, 2011, **51**, P. 191–204.
- [125] Yang H.-K., Cheng Y.-X., Su M.-M., Xiao Y., Hu M.-B., Wang W., Wang Q. Polyoxometalate-biomolecule Conjugates: A New Approach to Create Hybrid Drugs for Cancer Therapeutics. *Bioorganic & Medicinal Chemistry Letters*, 2013, **23**(5), P. 1462–1466.
- [126] Awada M., Floquet S., Marrot J., Haouas M., Morcillo S.P., Bour Ch., Gandon V., Coeffard V., Greck Ch., Cadot E. Synthesis and Characterizations of Keplerate Nanocapsules Incorporating L- and D-Tartrate Ligands. *J. Clust. Sci.*, 2017, **28**(2), P. 799–812.
- [127] Ostroushko A.A., Adamova L.V., Eremina E.V., Grzhegorzhevskii K.V. Interaction between nanocluster polyoxometallates and low-molecular-weight organic compounds. *Russ. J. Phys. Chem. A*, 2015, **89**(8), P. 1439–1444.
- [128] Tonkushina M.O., Gagarin I.D., Grzhegorzhevskii K.V., Ostroushko A.A. Electrophoretic Transfer of Nanocluster Polyoxometalate Mo₇₂Fe₃₀ Associates through the Skin Membrane. *Bulletin of Ural Medical Academic Science*, 2014, **3**(49), P. 59–61.
- [129] Ostroushko A.A., Grzhegorzhevskii K.V. Electric Conductivity of Nanocluster Polyoxomolybdates in the Solid State and Solutions. *Russ. J. Phys. Chem. A*, 2014, **88**(6), P. 1008–1011.
- [130] Ostroushko A.A., Gette I.F., Danilova I.G., Mukhlynina E.A., Tonkushina M.O., Grzhegorzhevskii K.V. Studies on the Possibility of Introducing Iron-Molybdenum Buckyballs into an Organism by Electrophoresis. *Nanotechnologies in Russia*, 2014, **9**(9-10), P. 586–591.
- [131] Ostroushko A.A., Danilova I.G., Gette I.F., Tonkushina M.O., Behavior of Associates of Keplerate-Type Porous Spherical Mo₇₂Fe₃₀ Clusters with Metal Cations in Electric Field-Driven Ion Transport. *Russ. J. Inorg. Chem.*, 2015, **60**(4), P. 500–504.
- [132] Ostroushko A.A., Danilova I.G., Gette I.F., Medvedeva S.Yu., Tonkushina M.O., Prokofieva A.V., Morozova M.V. Study of Safety of Molybdenum and Iron-Molybdenum Nanocluster Polyoxometalates Intended for Targeted Delivery of Drugs. *Journal of Biomaterials and Nanobiotechnology*, 2011, **2**(5), P. 557–560.
- [133] Ostroushko A.A., Gette I.F., Medvedeva S.Y., Danilova I.G., Mukhlynina E.A., Tonkushina M.O., Morozova M.V. Study of Acute and Subacute Action of Iron-Molybdenum Nanocluster Polyoxometalates. *Nanotechnologies in Russia*, 2013, **8**(9-10), P. 672–677.

- [134] Gette I.F., Medvedeva S.Yu., Ostroushko A.A. Condition of the Immune System Organs and Blood Leucocytes in Rats after the Exposition of Iron-Molybdenum Polyoxometalates. *Russian J. of Immunology*, 2017, **11**(2), P. 280–282.
- [135] Ostroushko A.A., Tonkushina M.O. Destruction of Molybdenum Nanocluster Polyoxometallates in Aqueous Solutions. *Russ. J. Phys. Chem. A*, 2015, **89**(3), P. 443–446.
- [136] Ostroushko A.A., Danilova I.G., Medvedeva S.J., Gette I.F., Tonkushina M.O. Studying of safety of molybden nanocluster polyoxometalates indented for address delivery of medicinal substances. *Ural Medical Journal*, 2010, **9**(74), P. 114–117.
- [137] Ostroushko A.A., Gette I.F., Medvedeva S.J., Tonkushina M.O., Danilova I.G., Prokofyeva A.V., Morozova M.V. Estimation of safety of ferrum-molybdenum nanocluster polyoxometallates indented for address delivery of medicines. *Bulletin of Ural Medical Academic Science*, 2011, **2**(34), P. 107–110.
- [138] Sodemann W.A., Sodemann Th.M. Pathologic physiology. Philadelphia: W.B.Saunders Co., 1985, 1154 pp.
- [139] Ostroushko A.A., Adamova L.V., Grzhegorzhevskii K.V., Gagarin I.D., Koveza E.V., Danilova I.G., Gette I.F., Ulitko M.V., Vlasov D.A., Belozerovala K.A., Men'shikov S. Yu. Studies of the Functional Properties of Nanocluster Polyoxomolybdates and Materials on Their Basis. XXI Mendeleev Congress on General and Applied Chemistry. Saint Petersburg, 2019. Book 2a: Abstracts. - Saint Petersburg, 2019, P. 86.
- [140] Zurabyan S.E. Fundamentals of Bioorganic Chemistry. GEOTAR-Media, 2012. 304 pp.
- [141] Ostroushko A.A., Gette I.F., Brilliant S.A., Danilova I.G. Application of Nanocluster Iron-Molybdene Polyoxometalates for Correction of Experimental Posthemorrhagic Anemia. *Nanotechnol. Russia*, 2019, **14**(3-4), P. 159–164.
- [142] Ostroushko A.A., Tonkushina M.O., Gagarin I.D., Grzhegorzhevskii K.V., Danilova I.G., Gette I.F. Method of post-hemorrhagic anemia correction. *Patent RU 2671077 (C1) RU*, 2018.
- [143] Danilova I.G., Gette I.F., Medvedeva S.Y., Mukhlynina E.A., Tonkushina M.O., Ostroushko A.A. Changing the Content of Histone Proteins and Heat-Shock Proteins in the Blood and Liver of Rats after the Single and Repeated Administration of Nanocluster Iron-Molybdenum Polyoxometalates. *Nanotechnologies in Russia*, 2015, **10**(9-10), P. 820–826.
- [144] Mecke A., Uppuluri S., Sassanella T.M., Lee D.K., Ramamoorthy A., Baker J.R. Jr., Orr B.G., Banaszak Holl M.M. Direct observation of lipid bilayer disruption by poly (amidoamine) dendrimers. *Chem. Phys. Lipids*, 2004, **132**(1), P. 3–14.
- [145] Sayes C.M., Wahi R., Kurian P.A., Liu Y., West J.L., Ausman K.D., Warheit D.B., Colvin V.L. Correlating nanoscale titania structure with toxicity: A cytotoxicity and inflammatory response study with human dermal fibroblasts and human lung epithelial cells. *Toxicol Sci.*, 2006, **92**(1), P. 174–185.
- [146] Zager R.A., Johnson A.C. Progressive histone alterations and proinflammatory gene activation: consequences of heme protein/iron-mediated proximal tubule injury. *Am. J. Physiol. Renal Physiol.*, 2010, **298**(3), P. 827–837.
- [147] Gette I.F. Content of histone proteins in lymphocytes of rats with alloxanic diabetes in the conditions of modulation activity of macrophages. *Bulletin of Ural Medical Academic Science*, 2014, **3**(49), P. 19–20.
- [148] Villeneuve L.M., Reddy M.A., Lanting L.L., Wang M., Meng L., Natarajan R. Epigenetic histone H3 lysine 9 methylation in metabolic memory and inflammatory phenotype of vascular smooth muscle cells in diabetes. *Proc. Natl. Acad. Sci. USA*, 2008, **105**(26), P. 9047–9052.
- [149] Kampinga H.H., Hageman J., Vos M.J., Kubota H., Tanguay R.M., Bruford E.A., Cheetham M.E., Chen B., Hightower L.E. Guidelines for the nomenclature of the human heat shock proteins. *Cell Stress Chaperones*, 2009, **14**(1), P. 105–111.
- [150] Stacchiotti A., Rodella L.F., Ricci F., Rezzani R., Lavazza A., Bianchi R. Stress proteins expression in rat kidney and liver chronically exposed to aluminium sulphate. *Histol Histopathol.*, 2006, **21**(2), P. 131–140.
- [151] Walter S., Buchner J. Molecular chaperones-cellular machines for protein folding. *Angew. Chem. Int. Ed. Engl.*, 2002, **41**(7), P. 1098–1113.
- [152] Bonardi M.A., Giovanetti E., Legname G., Fossati G., Porro G., Gromo G., Modena D., Marcucci F. Cochaperonins are histone-binding proteins. *Biochem. Biophys. Res. Commun.*, 1995, **206**(1), P. 260–265.
- [153] Wuillemin N., Terracciano L., Beltraminelli H., Schlapbach C., Fontana S., Krähenbühl S., Pichler W.J., Yerly D. T cells infiltrate the liver and kill hepatocytes in HLA-B(*):57:01-associated floxacillin-induced liver injury. *Am. J. Pathol.*, 2014, **184**(6), P. 1677–1682.
- [154] Ghedira I., Landolsi H., Mankai A., Fabien N., Jeddi M. Antihistones antibodies in systemic lupus erythematosus, comparison of three assays: Elisa, dot blot and immunoblot. *Pathol. Biol. (Paris)*, 2006, **54**(3), P. 148–154.
- [155] Westerheide S.D., Kawahara T.L., Orton K., Morimoto R.I. Triptolide, an inhibitor of the human heat shock response that enhances stress-induced cell death. *J. Biol. Chem.*, 2006, **281**(14), P. 9616–9622.
- [156] Wickner S., Maurizi M.R., Gottesman S. Posttranslational quality control: folding, refolding, and degrading proteins. *Science*, 1999, **286**(5446), P. 1888–1893.
- [157] Reference book on laboratory methods of a research (Sprawochnik po laboratornym metodam issledovaniya). Ed. Danilova L.A. SPb: Piter, 2003, 736 pp. (In Russian).
- [158] Chshieva F.T., Tsirihov O.T., Chshieva M.O., Muzaeva R.V., Timoshenko V.Yu. Studying the Influence of Nanocrystal Silicon on Maintenance of Aminotransferases, Alkaline Phosphatase, Bilirubin and Cholesterol in Rats Blood. Reports of Samara Scientific Center of Russian Academy of Sciences (RAS), 2011, **13**, 1(7), P. 1764–1766.
- [159] Danilova I.G., Gette I.F., Medvedeva S.Yu., Belousova A.V., Tonkushina M.O., Ostroushko A.A. Influence of Iron-Molybdenum Nanocluster Polyoxometalates on the Apoptosis of Blood Leukocytes and the Level of Heat-Shock Proteins in the Cells of Thymus and Spleen in Rats. *Nanotechnologies in Russia*, 2016, **11**(9-10), P. 653–662.
- [160] Gette I., Ostroushko A., Danilova I., Medvedeva S., Pozdina V. Impact of iron-molybdenum polyoxometalates on the thymus and blood leukocytes in rats. *Virchows Archiv. European Journal of Pathology*, 2018, **473**(Suppl. 1), P. 325–326.
- [161] Ostroushko A.A., Gagarin I.D., Grzhegorzhevskii K.V., Gette I.F., Vlasov D.A., Ermoshin A.A., Antosyuk O.N., Shikhova S.V., Danilova I.G. The Physicochemical Properties and Influence on Living Organisms of Nanocluster Polyoxomolybdates as Prospective Bioinspired Substances (Based on Materials from the Plenary Lecture). *J. Molec. Liq.*, 2019, **301**, P. 110910.
- [162] Popov A.L., Ermakov A.M., Shekunova T.O., Shcherbakov A.B., Ermakova O.N., Ivanova O.S., Popova N.R., Baranchikov A.Ye., Ivanov V.K. PVP stabilized tungsten oxide nanoparticles inhibit proliferation of NCTC L929 mouse fibroblasts via induction of intracellular oxidative stress. *Nanosystems: Physics, Chemistry, Mathematics*, 2019, **10**(1), P. 92–101.
- [163] Ostroushko A.A., Ulitko M.V., Tonkushina M.O., Zubarev I.V., Medvedeva S.Yu., Danilova I.G., Gubaeva O.V., Gagarin I.D., Gette I.F. Influence of nanocluster molybdenum-containing polyoxometalates on the morpho-functional condition of fibroblastes in culture. *Nanotechnologies in Russia*, 2018, **13**(1-2), P. 3–11.

- [164] Volkmer, D., Du Chesne A., Kurth D.G., Schnablegger H., Lehmann P., Koop M.J., Müller A. Toward nanodevices: Synthesis and characterization of the nanoporous surfactant-encapsulated Keplerate (DODA)₍₄₀₎(NH₄)₍₂₎[(H₂O)_(n)] subset of Mo₁₃₂O₃₇₂(CH₃COO)₍₃₀₎(H₂O)₍₇₂₎. *J. Am. Chem. Soc.*, 2000, **122**(9), P. 1995–1998.
- [165] Clemente-Leon M., Ito T., Yashiro H., Yamase T. Two-Dimensional Array of Polyoxomolybdate Nanoball Constructed by Langmuir-Blodgett Semiamphiphilic Method. *Chem. Mater.*, 2007, **19**, P. 2589–2594.
- [166] Fan D., Hao J. Phase stability of Keplerate-type polyoxomolybdates controlled by added cationic surfactant. *J. Colloid Interface Sci.*, 2009, **333**, P. 757–763.
- [167] Car P.-E., Patzke G.R. The Fascination of Polyoxometalate Chemistry. *Inorganics*, 2015, **3**(2), P. 511–515.
- [168] Watfa N., Floquet S., Terazzi E., Salomon W., Guénee L., Buchwalder K.L., Hijazi A., Naoufal D., Piguet C., Cadot E. Synthesis, Characterization and Study of Liquid Crystals Based on the Ionic Association of the Keplerate Anion [Mo₁₃₂O₃₇₂(CH₃COO)₃₀(H₂O)₇₂]⁴²⁻ and Imidazolium Cations. *Inorganics*, 2015, **3**(2), P. 246–266.
- [169] Floquet, S., Terazzi V.S., Korenev V.S., Hijazi A., Guénee L., Cadot E. Layered ionic liquid-crystalline organisations built from nano - capsules [Mo₁₃₂O₃₁₂S₆₀(SO₄)_x(H₂O)_{132-2x}]^{(12+2x)-} and DODA+ cations. *Liq. Cryst.*, 2014, **41**(6), P. 1000–1007.
- [170] Kurth D.G., Lehmann P., Volkmer D., Müller A., Schwahn D. Biologically inspired polyoxometalate-surfactant composite materials. Investigations on the structures of discrete, surfactant-encapsulated clusters, monolayers, and Langmuir-Blodgett films of (DODA)₄₀(NH₄)₂[(H₂O)_n] C Mo₁₃₂O₃₇₂(CH₃CO₂)₃₀ × (H₂O)₇₂. *J. Chem. Soc. Dalton Trans.*, 2000, **21**, P. 3989–3998.
- [171] Floquet S., Terazzi E., Hijazi A., Guénee L., Piguet, C., Cadot E. Evidence of Ionic Liquid Crystal Properties for a DODA+ Salt of the Keplerate [Mo₁₃₂O₃₇₂(CH₃COO)₃₀(H₂O)₇₂]⁴²⁻. *New J. Chem.*, 2012, **36**, P. 865–868.
- [172] Panagiotopoulos A., Douvas A.M., Argitis P., Coutsolelos A.G. Porphyrin-Sensitized Evolution of Hydrogen using Dawson and Keplerate Polyoxometalate Photocatalysts. *ChemSusChem*, 2016, **9**, P. 3213–3219.
- [173] Liu S., Tang Z. Polyoxometalate-based functional nanostructured films: Current progress and future prospects. *Nano Today*, 2010, **5**, P. 267–281.
- [174] Fan D., Hao J. Fabrication and Electrochemical Properties of Chitosan and Keplerate-Type Polyoxometalate {Mo₇₂Fe₃₀} Hybrid Films. *J. Phys. Chem. B*, 2009, **113**, P. 7513–7516.
- [175] Tonkushina M.O., Alekseeva O.V., Agafonov A.V., Ostroushko A.A. Viscosity and Electrophysical Characteristics of Solutions Containing Nanocluster Polyoxometalates and Polyvinylpyrrolidone. *Russ. J. Phys. Chem. A*, 2016, **90**(4), P. 838–842.
- [176] Tonkushina M.O., Kraev A.S., Alekseeva O.V., Ostroushko A.A., Agafonov A.V. Effect of Polyoxomolybdate Nanocluster Doping on the Dielectric Characteristics of Polyvinyl Alcohol Nanocomposite Films. *Russ. J. Inorg. Chem.*, 2016, **61**(4), P. 477–481.
- [177] Ostroushko A.A., Safronov A.P., Tonkushina M.O. Thermochemical Study of Interaction between Nanocluster Polyoxomolybdates and Polymers in Film Compositions. *Russ. J. Phys. Chem. A*, 2014, **88**(2), P. 295–300.
- [178] Ostroushko A.A., Sennikov M.Yu., Tonkushina M.O. Interaction of Polyoxometalate Mo₁₃₂ with Poly(vinyl alcohol). *Russ. J. Inorg. Chem.*, 2009, **54**(4), P. 617–623.
- [179] Ostroushko A.A., Gagarin I.D., Danilova I.G., Gette I.F. The use of nanocluster polyoxometalates in the bioactive substance delivery systems. *Nanosystems: Physics, Chemistry, Mathematics*, 2019, **10**(3), P. 318–349.
- [180] Cui J., Fan D., Hao J. Magnetic Mo₇₂Fe₃₀-embedded hybrid nanocapsules. *J. Coll. Interface Sci.*, 2009, **330**(2), P. 488–492.
- [181] Zhao W., Cui J., Hao J., Van Horn J.D. Co-assemblies of polyoxometalate {Mo₇₂Fe₃₀}/double-tailed magnetic surfactant for magnetic-driven anchorage and enrichment of protein. *J. Coll. Interface Sci.*, 2019, **536**, P. 88–97.
- [182] Ostroushko A.A., Adamova L.V., Eremina E.V., Grzhegorzhevskii K.V., Velichko E.V., Bogdanov S.G., Pirogov A.N. Thermodynamics of Acetone Sorption from Vapor Phase by Keplerate and Toroid Polyoxomolybdate Nanoclusters. *Russ. J. Phys. Chem. A*, 2017, **91**(7), P. 1313–1318.
- [183] Tonkushina M.O., Ostroushko A.A. Enthalpy of Mixing of Porous Nanocluster Polyoxometalates of Keplerate-Type Mo₇₂Fe₃₀ with Polyvinyl Alcohol and Polyethylene Glycol. *Russ. J. Phys. Chem. A*, 2017, **91**(6), P. 1076–1079.
- [184] Ostroushko A.A., Tonkushina M.O., Safronov A.P. New Data for Molybdenum Polyoxometallate with the Buckyball Structure Containing Acetate Groups and Compositions Based Thereon. *Russ. J. Inorg. Chem.*, 2010, **55**(5), P. 808–813.
- [185] Ostroushko A.A., Gagarin I.D., Tonkushina M.O., Grzhegorzhevskii K.V., Adamova L.V., Eremina E.V., Russkikh O.V., Gette I.F., Danilova I.G., Kim G.A. The Functionalization of Nanocluster Polyoxomolybdates by Various Molecules. VIIIth Intern. Symp. “Design and Synthesis of Supramolecular Architectures”, IInd Yoyuth School on Supramolecular and Coordination Chemistry. Apr. 25–29, 2016. Kazan, Russia. P. 136.
- [186] Barsukov L.I. Liposomes. *Soros Education J.*, 1998, **10**, P. 2–9.
- [187] Taboada P., Velasquez G., Barbosa S., Castelletto V., Nixon S.K., Yang Z., Heatley F., Hamley I.W., Mosquera V., Ashford M., Attwoodand D., Booth C. Block copolymers of ethylene oxide and phenyl glycidyl ether: Micellization, gelation and drug solubilization. *Langmuir*, 2005, **21**, P. 5263–5271.
- [188] Hamley I.W., Castelletto V., Fundin J., Crothers M., Attwoodand D., Talmon Y. Close-packing of Diblock Copolymer Micelles. *Colloid Polym. Sci.*, 2004, **282**, P. 514–517.
- [189] Hamley I.W. Nanoshells and Nanotubes from Block Copolymers. *Soft Matter*, 2005, **1**, P. 36–43.
- [190] De Geest B.G., De Koker S., Sukhorukov G.B., Kreft O., Parak W.J., Skirtach A.G., Demeester J., De Smedt S.C., Hennink W.E. Polyelectrolyte microcapsules for biomedical applications. *Soft Matter*, 2009, **5**, P. 282–291.
- [191] Hernández R.M., Orive G., Murua A., Pedraz J.L. Microcapsules and microcarriers for in situ cell delivery. *Adv. Drug Delivery Rev.*, 2010, **62**, P. 711–730.
- [192] Jämsä S., Mahlberg R., Holopainen U., Ropponen J., Savolainen A., Ritschkoff A.-C. Slow release of a biocidal agent from polymeric microcapsules for preventing biodeterioration. *Progress in Organic Coatings*, 2013, **76**, P. 269–276.
- [193] Zhang Y., Chan H.F., Leong K.W. Advanced materials and processing for drug delivery: the past and the future. *Adv. Drug Delivery Rev.*, 2013, **65**, P. 104–120.
- [194] Kaur I.P., Singh H. Nanostructured drug delivery for better management of tuberculosis. *J. Controlled Release*, 2014, **184**, P. 36–50.
- [195] Elisstratova J., Akhmadeev B., Gubaidullin A., Korenev V., Sokolov M., Nizameev I., Stepanov A., Ismaev I., Kadirov M., Voloshina A., Mustafina A. Nanoscale hydrophilic colloids with high relaxivity and low cytotoxicity based on Gd(III) complexes with Keplerate polyanions. *New J. Chem.*, 2017, **41**(13), P. 5271–5275.

- [196] Ostroushko A.A., Danilova I.G., Gette I.F., Tonkushina M.O. Behavior of Associates of Keplerate Type Porous Spherical Mo₇₂Fe–30 Clusters with Metal Cations in Electric Field Driven Ion Transport. *Russ. J. Inorg. Chem.*, 2015, **60**(4), P. 500–504.
- [197] Ostroushko A., Gagarin I., Tonkushina M., Grzhegorzhevskii K., Russkikh O. Association of spherical porous nanocluster Keplerate-type polyoxometalate Mo₇₂Fe₃₀ with biologically active substances. *Journal of Cluster Science*, 2018, **29**(1), P. 111–120.
- [198] Ostroushko A.A., Tonkushina M.O. Destruction of Porous Spherical Mo₁₃₂ Nanocluster Polyoxometallate of Keplerate Type in Aqueous Solutions. *Russ. J. Phys. Chem. A*, 2016, **90**(2), P. 436–442.
- [199] Verhoeff A.A., Kistler M.L., Bhatt A., Pigga J., Groenewold J., Klokkenburg M., Veen S., Roy S., Liu T., Kegel W.K. Charge Regulation as a Stabilization Mechanism for Shell-Like Assemblies of Polyoxometalates. *Physical Review Letters*, 2007, **99**(6), P. 066104.
- [200] Ostroushko A.A., Zubarev A.Yu., Bublik I.V., Sennikov M.Yu., Iskakova L.Yu., Safronov A.P. Modeling and calculation of the association processes between oxygen-containing polyanions and nonionic polymers. *Russ. J. Inorg. Chem.*, 2004, **49**(7), P. 1028–1033.
- [201] Ostroushko A.A. Interaction of Keplerate-Type Molybdenum-Based Porous Spherical Nanoclusters with Polymer Macromolecules. *Russ. J. Inorg. Chem.*, 2015, **60**(3), P. 387–391.
- [202] Ostroushko A.A., Danilova I.G., Tonkushina M.O., Medvedeva S.Yu., Gette I.F., Mukhlynina E.A., Prokofieva A.V., Morozova M.V., Russkikh O.V. Toxicity Studying of Polyoxometalate Mo₇₂Fe₃₀, Possibilities of Its Transport in Organism and Interactions with other Substances. Congress and Exhibition on Advanced Materials and Processes. 25.–27. Sept. 2012, Darmstadt, Germany. F2-1098.
- [203] Cedervall T., Lynch I., Lindman S., Berggard T., Thulin E., Nilsson H., Dawson K.A., Linse S. Understanding the nanoparticle–protein corona using methods to quantify exchange rates and affinities of proteins for nanoparticles. *Proc. Natl Acad. Sci. USA*, 2007, **104**, P. 2050–2055.
- [204] Lundqvist M., Stigler J., Elia G., Lynch I., Cedervall T., Dawson K.A. Nanoparticle size and surface properties determine the protein corona with possible implications for biological impacts. *Proc. Natl Acad. Sci. USA*, 2008, **105**, P. 14265–14270.
- [205] Casals E., Pfaller T., Duschl A., Oostingh G.J., Puntès V. Quantitative study of protein coronas on gold nanoparticles with different surface modifications. *ACS Nano*, 2010, **4**, P. 3623–3632.
- [206] Docter D., Westmeier D., Markiewicz M., Stolte S., Knauer S.K., Stauber R.H. The nanoparticle biomolecule corona: lessons learned – challenge accepted? *Chem. Soc. Rev.*, 2015, **44**, P. 6094–6121.
- [207] Walkey C.D., Olsen J.B., Song F., Liu R., Guo H., Olsen D.W., Cohen Y., Emili A., Chan W.C. Protein corona fingerprinting predicts the cellular interaction of gold and silver nanoparticles. *ACS Nano*, 2014, **8**, P. 2439–2455.
- [208] Arcamone F., Cassinelli G., Franceschi G., Penco S., Pol C., Redaelli S., Selva A. Structure and Physicochemical Properties of Adriamycin (Doxorubicin). *Int. Symp. Adriamycin*, 1972, P. 9–22.
- [209] Arcamone F. Discovery and Development of Doxorubicin. *Med. Chem. (Los Angeles)*, Academic Press, New York, 1981, P. 1–47.
- [210] Arcamone F. Antitumor anthracyclines: Recent developments. *Med. Res. Rev.*, 1984, **4**, P. 153–188.
- [211] Cagel M., Grotz E., Bernabeu E., Moretton M.A., Chiappetta D.A. Doxorubicin: nanotechnological overviews from bench to bedside. *Drug Discov. Today*, 2017, **22**, P. 270–281.
- [212] Borišev I., Mrdanovic J., Petrovic D., Seke M., Jović D., Srdenović B., Latinovic N., Djordjevic A. Nanoformulations of doxorubicin: How far have we come and where do we go from here? *Nanotechnology*, 2018, **29**, P. 33202(1–21).
- [213] Gewirtz D. A critical evaluation of the mechanisms of action proposed for the antitumor effects of the anthracycline antibiotics adriamycin and daunorubicin. *Biochemical pharmacology*, 1999, **57**(7), P. 727–741.
- [214] Tacar O., Sriamornsak P., Dass C.R. Doxorubicin: An update on anticancer molecular action, toxicity and novel drug delivery systems. *J. Pharm. Pharmacol.*, 2013, **65**, P. 157–170.
- [215] Fojtu M., Gumulec J., Stracina T., Raudenska M., Skotakova A., Vaculovicova M., Masarik M. Reduction of doxorubicin-induced cardiotoxicity using nanocarriers: a review. *Current drug metabolism*, 2017, **18**(3), P. 237–263.
- [216] Hatakeyama H., Akita H., Ishida E., Hashimoto K., Kobayashi H., Aoki T., Yasuda J., Obata K., Kikuchi H., Ishida T., Kiwada H., Harashima H. Tumor targeting of doxorubicin by anti-MT1-MMP antibody-modified PEG liposomes. *Int. J. Pharm.*, 2007, **342**, P. 194–200.
- [217] Peller M., Willerding L., Limmer S., Hossann M., Dietrich O., Ingrisch M., Sroka R., Lindner L.H. Surrogate MRI markers for hyperthermia-induced release of doxorubicin from thermosensitive liposomes in tumors. *J. Control. Release*, 2016, **237**, P. 138–146.
- [218] Haeri A., Zalba S., ten Hagen T.L.M., Dadashzadeh S., Koning G.A. EGFR targeted thermosensitive liposomes: A novel multifunctional platform for simultaneous tumor targeted and stimulus responsive drug delivery. *Colloids Surfaces B Biointerfaces*, 2016, **146**, P. 657–669.
- [219] Sesarman A., Tefas L., Sylvester B., Licarete E., Rauca V., Luput L., Patras L., Banciu M., Porfire A. Anti-angiogenic and anti-inflammatory effects of long-circulating liposomes co-encapsulating curcumin and doxorubicin on C₂₆ murine colon cancer cells, *Pharmacol. Reports*, 2017, **70**, P. 331–339.
- [220] Li Q., Tang Q., Zhang P., Wang Z., Zhao T., Zhou J., Li H., Ding Q., Li W., Hu F., Du Y., Yuan H., Chen S., Gao J., Zhan J., You J. Human epidermal growth factor receptor-2 antibodies enhance the specificity and anticancer activity of light-sensitive doxorubicin-labeled liposomes. *Biomaterials*, 2015, **57**, P. 1–11.
- [221] Xie Q., Deng W., Yuan X., Wang H., Ma Z., Wu B., Zhang X. Selenium-functionalized liposomes for systemic delivery of doxorubicin with enhanced pharmacokinetics and anticancer effect. *Eur. J. Pharm. Biopharm.*, 2018, **122**, P. 87–95.
- [222] Plourde K., Derbali R.M., Desrosiers A., Dubath C., Vallée-Bélisle A., Leblond J., Aptamer-based liposomes improve specific drug loading and release. *J. Control. Release*, 2017, **251**, P. 82–91.
- [223] Park J.W. Liposome-based drug delivery in breast cancer treatment. *Breast Cancer Res.*, 2002, **4**, P. 93–97.
- [224] Immordino M.L., Dosio F., Cattel L. Stealth liposomes: Review of the basic science, rationale, and clinical applications, existing and potential. *Int. J. Nanomedicine*, 2006, **1**, P. 297–315.
- [225] Gonçalves M., Mignani S., Rodrigues J., Tomás H. A glance over doxorubicin based-nanotherapeutics: From proof-of-concept studies to solutions in the market. *J. Control. Release*, 2020, **317**, P. 347–374.
- [226] Benesch M., Urban C. Liposomal cytarabine for leukemic and lymphomatous meningitis: recent developments. *Expert Opin. Pharmacother.*, 2008, **9**, P. 301–309.
- [227] Yu M.K., Park J., Jon S. Targeting Strategies for Multifunctional Nanoparticles in Cancer Imaging and Therapy. *Theranostics*, 2012, **2**(1), P. 3–44.
- [228] Qu X., Yang C., Zhang J., Ding N., Lu Y., Huang L., Xiang G. In vitro evaluation of a Folate-bovine serum albumin-doxorubicin conjugate. *J. Drug Targeting*, 2010, **18**(5), P. 351–361.

- [229] Sun J., Zhang L., Zhang Y., Yue C. W., Lin J., Wang H., Fang Z.-J., Wu J. Smart albumin-loaded Rose Bengal and doxorubicin nanoparticles for breast cancer therapy. *J. microencapsulation*, 2019, **36**(8), P. 728–737.
- [230] Park C., Meghani N., Amin H., Tran P. H. L., Tran T. T. D., Nguyen V. H., Lee B. J. The roles of short and long chain fatty acids on physicochemical properties and improved cancer targeting of albumin-based fattigation-platform nanoparticles containing doxorubicin. *Int. J. Pharmaceutics*, 2019, **564**, P. 124–135.
- [231] Kimura K., Yamasaki K., Nishi K., Taguchi K., Otagiri M. Investigation of anti-tumor effect of doxorubicin-loaded human serum albumin nanoparticles prepared by a desolvation technique. *Cancer chemotherapy and pharmacology*, 2019, **83**(6), P. 1113–1120.
- [232] Lee J.H., Moon H., Han H., Lee I.J., Kim D., Lee H.J., Ha Sh.-W., Kim H., Chung J.W. Antitumor Effects of Intra-Arterial Delivery of Albumin-Doxorubicin Nanoparticle Conjugated Microbubbles Combined with Ultrasound-Targeted Microbubble Activation on VX2 Rabbit Liver Tumors. *Cancers*, 2019, **11**(4), P. 581.
- [233] Muniswamy V.J., Raval N., Gondaliya P., Tambe V., Kalia K., Tekade R.K. 'Dendrimer-Cationized-Albumin' encrusted polymeric nanoparticle improves BBB penetration and anticancer activity of doxorubicin. *Int. J. Pharmaceutics*, 2019, **555**, P. 77–99.
- [234] Delorme V., Lichon L., Mahindad H., Hunger S., Laroui N., Daurat M., Godefroy A., Gary-Bobo M., Van Den Berghe H. Reverse Poly (ϵ -caprolactone)-g-Dextran Graft Copolymers. Nano-carriers for Intracellular Uptake of Anticancer Drugs. *Carbohydrate Polymers*, 2019, P. 115764.
- [235] Wang H., Li Z., Lu S., Li C., Zhao W., Zhao Y., Yu Sh., Wang T., Sun T. Nano micelles of cellulose-graft-poly (l-lactic acid) anchored with epithelial cell adhesion antibody for enhanced drug loading and anti-tumor effect. *Materials Today Communications*, 2020, **22**, P. 100764.
- [236] Wang M., Yan J., Li C., Wang X., Xiong J., Pan D., Wang L., Xu Yu., Xiaotian Li Yang M. Cationic Poly (amide-imide)-Conjugated Camptothecin Prodrug with Variable Nanomorphology for Efficient Reductive-Responsive Drug Delivery. *European Polymer Journal*, 2019, P. 109462.
- [237] Li Y., Gao F., Guo J., Ren P., Tian Z., Bai J., Hua J. Polymeric micelles with aggregation-induced emission based on microbial ϵ -polylysine for doxorubicin delivery. *European Polymer Journal*, 2020, **122**, P. 109355.
- [238] Fang J.Y., Lin Y.K., Wang S.W., Lee R.S. Synthesis, and characterization folate-conjugated photocleavable poly (4-substituted- ϵ -caprolactone) polymers for drug delivery. *Int. J. Polymeric Materials and Polymeric Biomaterials*, 2020, **69**(1), P. 53–63.
- [239] Ni G., Yang G., He Y., Li X., Du T., Xu L., Zhou S. Uniformly sized hollow microspheres loaded with polydopamine nanoparticles and doxorubicin for local chemo-photothermal combination therapy. *Chemical Engineering Journal*, 2020, **379**, P. 122317.
- [240] Liu P., Zhang R. Polymer microspheres with high drug-loading capacity via dual-modal drug-loading for modulating controlled release property in pH/reduction dual-responsive tumor-specific intracellular triggered doxorubicin release. *Colloids and Surfaces A: Physicochemical and Engineering Aspects*, 2019, **577**, P. 291–295.
- [241] Jiang J., Li J., Zhou B., Niu C., Wang W., Wu W., Liang J. Fabrication of Polymer Micelles with Zwitterionic Shell and Biodegradable Core for Reductively Responsive Release of Doxorubicin. *Polymers*, 2019, **11**(6), P. 1019.
- [242] Banerjee D., Bose S. Effects of polymer chemistry, concentration, and pH on doxorubicin release kinetics from hydroxyapatite-PCL-PLGA composite. *Journal of Materials Research*, 2019, **34**(10), P. 1692–1703.
- [243] Tan Y., Yang X., Dai S., Lian K., Wen L., Zhu Y., Meng T., Liu X., Yuan H., Hu F. In vivo programming of tumor mitochondria-specific doxorubicin delivery by a cationic glycolipid polymer for enhanced antitumor activity. *Polymer Chemistry*, 2019, **10**(4), P. 512–525.
- [244] Butowska K., Kozak W., Zdrorowicz M., Makurat S., Rychłowski M., Hać A., Anna Herman-Antosiewicz A., Piosik J., Rak J. Cytotoxicity of doxorubicin conjugated with C₆₀ fullerene. Structural and in vitro studies. *Structural Chemistry*, 2019, **30**(6), P. 2327–2338.
- [245] Grebinyk A., Prylutska S., Grebinyk S., Prylutsyy Y., Ritter U., Matyshevska O., Dandekar T., Frohme M. Complexation with C₆₀ Fullerene Increases Doxorubicin Efficiency against Leukemic Cells In Vitro. *Nanoscale research letters*, 2019, **14**(1), P. 61.
- [246] Kepinska M., Kizek R., Milnerowicz H. Fullerene as a doxorubicin nanotransporter for targeted breast cancer therapy: Capillary electrophoresis analysis. *Electrophoresis*, 2018, **39**(18), P. 2370–2379.
- [247] Petrovic D., Seke M., Borovic M. L., Jovic D., Borisev I., Srdjenovic B., Rakocevic Z., Pavlovic V., Djordjevic A. Hepatoprotective effect of fullereneol/doxorubicin nanocomposite in acute treatment of healthy rats. *Experimental and molecular pathology*, 2018, **104**(3), P. 199–211.
- [248] Zhou Y., Li J., Ma H., Zhen M., Guo J., Wang L., Jiang L., Shu C., Wang C. Biocompatible [60]/[70] Fullereneols: Potent Defense against Oxidative Injury Induced by Reduplicative Chemotherapy. *ACS applied materials & interfaces*, 2018, **9**(41), P. 35539–35547.
- [249] Grebinyk A., Prylutska S., Chepurna O., Grebinyk S., Prylutsyy Y., Ritter U., Ohulchanskyy T. Y., Matyshevska O., Dandekar T., Frohme M. Synergy of chemo-and photodynamic therapies with C₆₀ fullerene-doxorubicin nanocomplex. *Nanomaterials*, 2019, **9**(11), P. 1540.
- [250] Ramalingam V., Varunkumar K., Ravikumar V., Rajaram R. Target delivery of doxorubicin tethered with PVP stabilized gold nanoparticles for effective treatment of lung cancer. *Sci. Rep.*, 2018, **8**, P. 1–12.
- [251] Chen W.-H., Xu X.-D., Jia H.-Z., Lei Q., Luo G.-F., Cheng S.-X., Zhuo R.-X., Zhang X.-Z. Therapeutic nanomedicine based on dual-intelligent functionalized gold nanoparticles for cancer imaging and therapy in vivo. *Biomaterials*, 2013, **34**, P. 8798–8807.
- [252] Prabakaran M., Graier J.J., Pilla S., Steeber D.A., Gong S. Gold nanoparticles with a monolayer of doxorubicin-conjugated amphiphilic block copolymer for tumor-targeted drug delivery. *Biomaterials*, 2009, **30**, P. 6065–6075.
- [253] Elbially N.S., Fathy M.M., Khalil W.M. Doxorubicin loaded magnetic gold nanoparticles for in vivo targeted drug delivery. *Int. J. Pharm.*, 2015, **490**, P. 190–199.
- [254] Jeon S., Ko H., Vijayakameswara Rao N., Yoon H.Y., You D.G., Han H.S., Um W., Saravanakumar G., Park J.H. A versatile gold cross-linked nanoparticle based on triblock copolymer as the carrier of doxorubicin. *R. Soc. Chem. Adv.*, 2015, **5**, P. 70352–70360.
- [255] Benyettou F., Rezgui R., Ravaux F., Jaber T., Blumer K., Jouiad M., Motte L., Olsen J.-C., Platas-Iglesias C., Magzoub M., Trabolsi A. Synthesis of silver nanoparticles for the dual delivery of doxorubicin and alendronate to cancer cells. *J. Mater. Chem.*, 2015, **B. 3**, P. 7237–7245.
- [256] Liu Y., Yang K., Cheng L., Zhu J., Ma X., Xu H., Li Y., Guo L., Gu H., Liu Z. PEGylated FePt@Fe₂O₃ core-shell magnetic nanoparticles: Potential theranostic applications and in vivo toxicity studies. *Nanomedicine Nanotechnology, Biol. Med.*, 2013, **9**, P. 1077–1088.
- [257] Gaihre B., Khil M.S., Lee D.R., Kim H.Y. Gelatin-coated magnetic iron oxide nanoparticles as carrier system: Drug loading and in vitro drug release study. *Int. J. Pharm.*, 2009, **365**, P. 180–189.
- [258] Halupka-Bryl M., Asai K., Thangavel S., Bednarowicz M., Krzymiński R., Nagasaki Y. Synthesis and in vitro and in vivo evaluations of poly(ethylene glycol)-block-poly(4-vinylbenzylphosphonate) magnetic nanoparticles containing doxorubicin as a potential targeted drug delivery system. *Colloids Surfaces B Biointerfaces*, 2014, **118**, P. 140–147.

- [259] Nadeem M., Ahmad M., Akhtar M.S., Shaari A., Riaz S., Naseem S., Masood M., Saeed M.A. Magnetic properties of polyvinyl alcohol and doxorubicin loaded iron oxide nanoparticles for anticancer drug delivery applications. *PLoS One*, 2016, **11**, P. 1–12.
- [260] Kayal S., Ramanujan R.V. Doxorubicin loaded PVA coated iron oxide nanoparticles for targeted drug delivery. *Mater. Sci. Eng.*, 2010, **30**, P. 484–490.
- [261] Grzhegorzhevskii K.V., Tonkushina M.O., Fokin A.V., Belova K.G., Ostroushko A.A. Coordinative interaction between nitrogen oxides and ironmolybdenum POM Mo₇₂Fe₃₀. *Dalton Transactions*, 2019, **48**(20), P. 6984–6996.
- [262] McCleverty J.A., Chemistry of nitric oxide relevant to biology. *Chem. Rev.*, 2004, **104**(2), P. 403–418.
- [263] Akaike T., Maeda H. Nitric oxide and virus infection. *Immunology*, 2000, **101**(3), P. 300–308.
- [264] Ignarro L.J. Preface to this special journal issue on nitric oxide chemistry and biology. *Arch. Pharm. Res.*, 2009, **32**(8), P. 1099–1101.
- [265] Cattaneo D., Warrender S.J., Duncan M.J., Castledine R., Parkinson N., Haley I., Morris R.E. Water based scale-up of CPO-27 synthesis for nitric oxide delivery. *Dalt. Trans.*, 2016, **45**(2), P. 618–629.
- [266] Lakomkin V.L., Abramov A.A., Ruuge E.K., Kapel'ko V.I., Chazov E.I., Vanin A.F. The hypotensive effect of the nitric monoxide donor Oxacom at different routes of its administration to experimental animals. *Eur. J. Pharm.*, 2015, **765**, P. 525–532.
- [267] McCleverty J.A. Chemistry of Nitric Oxide Relevant to Biology. *Chem. Rev.*, 2004, **104**, P. 403–418.
- [268] Aldoshin S.M., Lysenko K.A., Antipin M.Yu., Sanina N.A., Gritsenko V.V. Precision X-ray study of mononuclear dinitrosyl iron complex [Fe(SC₂H₃N₃)(SC₂H₂N₃)(NO)₂]-0.5H₂O at low temperatures. *J. Molec. Struct.*, 2008, **875**, P. 309–315.
- [269] Roudneva T.N., Syrsova L.A., Sanina N.A., Shkondina N.I., Kotel'nikov A.I., Aldoshin S.M. Formation of iron nitrosyl complexes of ferri- and ferrocytochrome C at its interaction with nitrosyl iron complex cysaconite. *Nitric Oxide: Biology and Chemistry*, 2010, **22**, P. 546.
- [270] Timoshin A.A., Lakomkin V.L., Abramov A.A., Ruuge E.K., Vanin A.F. Effect of dinitrosyl iron complexes on NO level in rat organs during endotoxin shock. *Doklady Biochemistry and Biophysics*, 2015, **462**(1), P. 166–168.
- [271] Andreyev-Andriyevskiy A.A., Mikoyan V.D., Serezhenkov V.A., Vanin A.F. Penile erectile activity of dinitrosyl iron complexes with thiol-containing ligands. *Nitric Oxide - Biology and Chemistry*, 2011, **24**(4), P. 217–223.
- [272] Shumaev K.B., Kosmachevskaya O.V., Timoshin A.A., Vanin A.F., Topunov A.F. Globins and other nitric oxide-reactive proteins. Dinitrosyl iron complexes bound with haemoglobin as markers of oxidative stress. *Methods in Enzymology*, 2008, **436**, P. 441–457.
- [273] Vanin A.F., Sanina N.A., Serezhenkov V.A., Burbaev D.Sh., Lozinsky V.I., Aldoshin S.M. Dinitrosyl-iron complexes with thiol-containing ligands: Spatial and electronic structures. *Nitric Oxide – Biology and Chemistry*, 2007, **16**(1), P. 82–93.
- [274] Kurtikyan T.S., Martirosyan G.G., Lorkovic I.M., Ford P.C. Comparative IR Study of Nitric Oxide Reactions with Sublimed Layers of Iron(II)- and Ruthenium(II)-meso-Tetraphenylporphyrinates. *J. Am. Chem. Soc.*, 2002, **124**, P. 10124–10129.
- [275] Atsutoshi Y., Han J.E., Karlin K.D., Nam W. An isolectronic NO dioxygenase reaction using a nonheme iron(III)-peroxo complex and nitrosonium ion. *Chem. Commun.*, 2014, **50**, P. 1742–1744.
- [276] Müller A., Plass W., Krickemeyer E., Dillinger S., Bögge H., Armatage A., Proust A., Beugholt Ch., Bergmann U. [Mo₅₇Fe₆(NO)₆O₁₇₄(OH)₃(H₂O)₄₁]¹⁵⁻: A Highly Symmetrical Giant Cluster with an Unusual Cavity and the Possibility of Positioning Paramagnetic Centers on Extremely Large Cluster Surfaces. *Angew. Chem. Int. Ed. Engl.*, 1994, **33**(8), P. 849–851.
- [277] Müller A., Krickemeyer E., Dillinger S., Bögge H., Plass W., Proust A., Dloczik L., Menke C., Meyer J., Rohlfing R. New Perspectives in Polyoxometalate Chemistry by Isolation of Compound Containing Very Large Moieties as Transferable Building Blocks: (NMe₄)₅[As₂Mo₈V₄AsO₄₀]-3H₂O, (NH₄)₂₁[H₃Mo₅₇V₆(NO)₆O₁₈₃(H₂O)₁₈]-65H₂O, (NH₂Me₂)₁₈(NH₄)₆[Mo₅₇V₆(NO)₆O₁₈₃(H₂O)₁₈]-14H₂O and (NH₄)₁₂[Mo₃₆(NO)₄O₁₀₈(H₂O)₁₆]-33H₂O. *Z. anorg. allg. Chem.*, 1994, **620**, P. 599–619.
- [278] Müller A., Krickemeyer E., et al. [Mo–154(NO)₁₄O₄₂₀(OH)₂₈(H₂O)₇₀]^{(25±5)-}: A Water-Soluble Big Wheel with More than 700 Atoms and a Relative Molecular Mass of About 24 000. *Angew. Chem. Int. Ed. Engl.*, 1995, **34**(19), P. 2122–2124.
- [279] Matsumoto T., Nakamura I., Ishiguro K., Tsunashima R. Concentration Dependent Stability of Fullerene-Shaped Metal-Oxide Nanocluster {Mo₁₃₂} in Aqueous Solution. *Sci. Adv. Mat.*, 2014, **6**, P. 1–5.
- [280] Grzhegorzhevskii K.V., Zelenovskiy P.S., Koryakova O.V., Ostroushko A.A. Thermal destruction of giant polyoxometalate nanoclusters: a vibrational spectroscopy study. *Inorg. Chim. Acta*, 2019, **489**, P. 287–300.
- [281] Ostroushko A.A., Tonkushina M.O., et al. Study of the stability of solid polyoxometalate Mo₇₂Fe₃₀ with a buckyball structure. *Russ. J. Inorg. Chem.*, 2012, **57**(6), P. 858–863.
- [282] Ostroushko A.A., Tonkushina M.O., Safronov A.P., Men'shikov S.Yu., Korotaev V.Yu. Thermal Behavior of Polyoxometalate Mo₁₃₂. *Russ. J. Inorg. Chem.*, 2009, **54**(2), P. 172–179.
- [283] Ostroushko A.A., Sennikov M.Yu. Polythermal Study of Electrophysical Characteristics of Poly(vinyl alcohol) Polymer-Salt Films. *Russ. J. Inorg. Chem.*, 2009, **54**(1), P. 115–120.
- [284] Bielan'ski A., Małacka-Luban'ska A., Micek-Ilnicka A., Müller A., Diemann E. Thermal properties of (NH₄)₃₂[Mo₁₃₈O₄₁₆H₆(H₂O)₅₈(CH₃COO)₆]-approximately 250H₂O: on the route to prove the complexity of a nanostructured landscape-especially with different type of H₂O ligands-embedded in an 'ocean' of water molecules. *Inorg. Chim. Acta*, 2002, **338**, P. 7–12.
- [285] Bielan'ski A., Małacka-Luban'ska A., Micek-Ilnicka A., Diemann E. Thermal stability of giant wheel type polyoxomolybdates and their derivatives. *J. Molec. Struct.*, 2006, **365**, P. 55–65.
- [286] Ostroushko A.A., Korotayev V.Yu., Tonkushina M.O., Grzhegorzhevskii K., Vazhenin V.A., Kutyashev I.B., Martynova N.A., Men'shikov S.Yu., Selezneva N.V. Electrotransport, Sorption, and Photochemical Properties of Nanocluster Polyoxomolibdates with a Toroidal Structure. *Russ. J. Phys. Chem. A*, 2012, **86**(8), P. 1268–1273.
- [287] Müller A., Diemann E., Kuhlmann Ch., Eimer W., Serain C., Tak T., Knochel A., Pranzas P.K. Hierarchic patterning: architectures beyond 'giant molecular wheels'. *Chem. Commun.*, 2001, **19**, P. 1928–1929.
- [288] Kistler M.L., Liu T., Gouzerh P., Todea A.-M., Müller A. Molybdenum-oxide based unique polyprotic nanoacids showing different deprotonations and related assembly processes in solution. *Dalton Trans.*, 2009, **26**, P. 5094–5100.
- [289] Liu T. An Unusually Slow Self-Assembly of Giant Inorganic Ions in Aqueous Solution. *J. Am. Chem. Soc.*, 2003, **125**, P. 312–313.
- [290] Liu T. Surfactant-Induced Trans-Interface Transportation and Complex Formation of Giant Polyoxomolybdate Clusters, *J. Clust. Sci.* (Achim Müller Issue), 2003, **14**, P. 215–226.
- [291] Liu, G., Liu T. Thermodynamic properties of the unique self-assembly of Mo₇₂Fe₃₀ inorganic macro-ions in salt-free and salt-containing aqueous solutions. *Langmuir*, 2005, **21**(7), P. 2713–2720.

- [292] Zhang J., Li D., Liu G., Glover K.J., Liu T. Lag Periods during the Self-Assembly of $\text{Mo}_{(72)}\text{Fe}_{(30)}$ Macroions: Connection to the Virus Capsid Formation Process. *J. Am. Chem. Soc.*, 2009, **131**, P. 15152–15159.
- [293] Steinfeld J.I., Francisco J.S., Hase W.L. *Chemical Kinetics and Dynamics*, 2nd Edition., Prentice Hall. 1998, 409 pp.
- [294] Stanciu I. *Mechanism of autocatalytic reactions*. Publisher Lap Lambert Academic Publishing. 2014, 64 pp.
- [295] Ramirez W.F. *Computational Methods in Process Simulation*. 2nd edit. Butterworth-Heinemann. Oxford. 1997, 512 pp.
- [296] Müller A., Das S.K., Talismanov S., Roy S., Beckmann E., Bögge H., Schmidtman M., Merca A., Berkle A., Allouche L., Zhou Y., Zhang L. Trapping Cations in Specific Positions in Tuneable “Artificial Cell” Channels: New Nanochemistry Perspectives. *Angew. Chem. Int. Ed. Engl.*, 2003, **42**, P. 5039–5044.
- [297] Ostroushko A.A., Sennikov M.Yu., Sycheva N.S. Features of Photochemical Reactions in Polymer-Salt Compositions Containing Ammonium Heptamolybdate and Polyvinyl Alcohol. *Russ. J. Inorg. Chem.*, 2005, **50**(7), P. 1050–1054.
- [298] Ostroushko A.A., Vazhenin V.A., Tonkushina M.O. Features of Thermophotoinitiated Degradation of Nanocluster Polyoxomolybdate Mo_{132} and Its Polymer-Containing Composites. *Russ. J. Inorg. Chem.*, 2017, **62**(4), P. 483–488.
- [299] Ostroushko A.A., Tonkushina M.O., Safronov A.P., Vazhenin V.A., Artemov M.Yu. Mutual Stabilization of Components in Composites of Polyoxomolybdates of Buckyball Structure and Water-Soluble Nonionic Polymers. *Russ. J. Appl. Chem.*, 2010, **83**(2), P. 332–336.
- [300] Gagarin I., Tonkushina M., Ostroushko A. Stabilization of Keplerate-type Spheric Porous Nanocluster Polyoxometalate $\text{Mo}_{72}\text{Fe}_{30}$. 2018 Ural Symposium on Biomedical Engineering, Radioelectronics and Information Technology (USBREIT). IEEE sponsors: Russia (Siberia) Section. 7-8 May 2018 Yekaterinburg, Russia. P. 41–44.
- [301] Ostroushko A., Grzhegorzhevskii K., Gagarin I., Danilova I., Gette I., Ulitko M., Antosyuk O., Shikhova S., Vlasov D., Belozerova K. On some opportunities of using Keplerate-type polyoxomolybdates in biomedicine // 4th Russ. Conf. on Medicinal Chemistry with intern. Participants. MedChem 2019. Abstract book. Ekaterinburg: Ural Branch of the Russian Academy of Sciences, 2019, 448 p. P. 96.
- [302] Grzhegorzhevskii K., Ostroushko A. The concept of novel drug relising system with feedback function based on inorganic-organic hybrid material. 4th Russ. Conf. on Medicinal Chemistry with intern. participants. MedChem 2019. Abstract book. Ekaterinburg: Ural Branch of the Russian Academy of Sciences, 2019, 448 p. P. 200.
- [303] Grzhegorzhevskii K.V., Shevtsev N.S., et al. Prerequisites and prospects for the development of novel systems based on the Keplerate type polyoxomolybdates for the controlled release. *Russian Chemical Bulletin, International Edition*, 2020, **69**(4), P. 804–814.
- [304] Fazylova V., Shevtsev N., Mikhailov S., Kim G., Ostroushko A., Grzhegorzhevskii K. Fundamental aspects of xanthen dye aggregation on the surfaces of nanocluster polyoxometalates: H to J aggregate switching. *Chemistry Eur. J.*, 2020, P. 05781.
- [305] Sasaki S., Drummen G.P.C., Konishi G.C. Recent advances in twisted intramolecular charge transfer (TICT) fluorescence and related phenomena in materials chemistry. *J. Mater. Chem. C*, 2016, **4**, P. 2731–2743.
- [306] Merkushev D.A., Usoltsev S.D., Marfin Y.S., Pushkarev A.P., Volyniuk D., Grazulevicius J.V., Rummyantsev E.V. BODYPY associates in organic matrices: spectral properties, photostability and evaluation as OLED emitters. *Mater. Chem. Phys.*, 2017, **187**, P. 104–111.
- [307] Arbeloa F.L., Ojeda P.R., Arbeloa I.L. Fluorescence self-quenching of the molecular forms of rhodamine B in aqueous and ethanolic solutions. *J. Lumin.*, 1989, **44**, P. 105–112.
- [308] Austin J.M., Harrison I.R., Quickenden T.I. Electrochemical and photoelectrochemical properties of rhodamine B. *J. Phys. Chem.*, 1986, **90**, P. 1839–1843.
- [309] Xu S., Wang Y., Zhao Y., Chen W., Wang J., He L., Su Z., Wang E., Kang Z.J. Keplerate-type polyoxometalate/semiconductor composite electrodes with light-enhanced conductivity towards highly efficient photoelectronic devices. *Mater. Chem. A*, 2016, **4**, P. 14025–14032.
- [310] Grzhegorzhevskii K., Ostroushko A., Koriakova O., Ovchinnikova I., Kim G. Photoinduced charge transfer in the supramolecular structure based on toroid polyoxomolibdate Mo_{138} and xanthen dye - Rhodamine-B. *Inorganica Chim. Acta*, 2015, **436**, P. 205–213.
- [311] Noble G.T., Stefanick J.F., et al. Ligand-targeted liposome design: challenges and fundamental considerations. *Trends Biotechnol.*, 2014, **32**, P. 32–45.
- [312] Gao W., Wang J. Synthetic micro/nanomotors in drug delivery. *Nanoscale*, 2014, **6**, P. 10486–10494.
- [313] Bordat A., Boissenot T., Nicolas J., Tsapis N. Thermoresponsive polymer nanocarriers for biomedical applications. *Adv. Drug Deliv. Rev.*, 2019, **138**, P. 167–192.
- [314] Patel S.G., Patel M.D., Patel A.J., Chougule M.B., Choudhury H. Solid lipid nanoparticles for targeted brain drug delivery. *Nanotechnology-Based Targeted Drug Delivery Systems for Brain Tumors*, Elsevier, 2018, P. 191–244.
- [315] Gao Y., Chen J., Zhang T., Szymanowski J.E.S., Burns P.C., Liu T. Inhomogeneous Distribution of Cationic Surfactants around Anionic Molecular Clusters. *Chem. Eur. J.*, 2019, **25**, P. 15741–15745.
- [316] Niu J.-Y., You X.-Z., Chun-ying Duan C.-Y., Fun H.-K., Zhong-yuan Zhou Z.-Y. A Novel Optical Complex between an Organic Substrate and a Polyoxometalate. Crystal and Molecular Structure of $\alpha\text{-H}_4\text{SiW}_{12}\text{O}_{40}\cdot 4\text{HMPA}\cdot 2\text{H}_2\text{O}$ (HMPA = Hexamethylphosphoramide). *Inorg. Chem.*, 1996, **35**(14), P. 4211–4217.
- [317] Andreev V.N., Chudnovskii F.A., Nikitin S.E., Kozyrev S.V. Photochromic effect in MoO Clusters - Citronic acid - H_2O system. *Mol. Mat.*, 1998, **11**, P. 139–142.
- [318] Ostroushko A.A., Sennikov M.Yu. The Kinetics of Photochemical Processes in Polymer-Salt Systems. *Russian Journal of Physical Chemistry A*, 2009, **83**(1), P. 111–115.
- [319] Yamase T. Photo- and Electrochromism of Polyoxometalates and Related Materials. *Chem. Rev.*, 1998, **98**, P. 307–325.
- [320] Bogomolova T.G. Diffusion of atmospheric oxygen into resting and moving mass of liquid (Diffuzia atmosfernogo kisloroda w pokoyashu-usa i dwigushuusa massu gidkosti). *Wesnyk MGSU*, 2009, **3**, P. 205–210, (in Russian).
- [321] Ostroushko A.A., Adamova L.V., et al. Studies of the Functional Properties of Nanocluster Polyoxomolybdates and Materials on Their Basis. XXI Mendeleev Congress on General and Applied Chemistry. Saint Petersburg, 2019. Abstracts. Book 2a. P. 86.
- [322] Yamase T., Kurozumi T. Photoreduction of Polymolybdates in Aqueous Solutions containing Acetic Acid. *J. Chem. Soc. Dalton Trans.*, 1983, P. 2205–2209.
- [323] Boggs B.K., King R.L., Botte G.G. Urea electrolysis: direct hydrogen production from urine. *Chem. Commun.*, 2009, P. 4859–4861.
- [324] Yamase T., Ikawa T. Photogalvanic effect in alkylammonium molybdate solutions and production of hydrogen. *Inorganica Chimica Acta*, 1979, **37**, P. 529–531.
- [325] Yamase T. Hydrogen production by ultraviolet irradiation of alkylammonium polytungstate in neutral aqueous solutions. *Inorganica Chimica Acta*, 1982, **64**, P. 155–156.

Analysis of the energy spectrum of indium antimonide quantum dots with temperature changes

V. F. Kabanov, A. I. Mikhailov, M. V. Gavrikov

Saratov State University, Department of Nanoand Biomedical Technologies,
Astrakhanskaya, 83, Saratov, 410012, Russia

maks.gavrikov.96@gmail.com

DOI 10.17586/2220-8054-2021-12-1-113-117

In this paper we have analyzed the broadening of the levels of the energy spectrum of indium antimonide quantum dots with a change of sample temperature. The position of the levels was determined by processing normalized differential tunneling current-voltage characteristics using the “cubic” model of a quantum dot. Comparison of the calculated values of spectrum broadening with experimental results showed qualitative and quantitative agreement between the results. It is concluded that with a decrease in the quantum dot size and, accordingly, an increase in the energy gap $\varepsilon_{c1} - \varepsilon_{v1}$, the broadening in percentage will decrease, which should lead to an increase in the temperature stability of the electrophysical parameters.

Keywords: quantum dots, indium antimonide, differential tunnel current-voltage characteristics, energy spectrum.

Received: 9 November 2020

Revised: 22 January 2020

1. Introduction

Semiconductor quantum dots (QDs) are very interesting and promising objects from both scientific and practical points of view. Currently, a fairly large number of various effective electronic and optoelectronic devices have already been created on their basis, primarily lasers and photodetectors [1]. This became possible due to their unique optical characteristics [2, 3], and especially because of the narrow symmetrical fluorescence peak, which position is adjusted by changing the characteristic size, composition and form of the QDs.

Another important feature of QDs – temperature stability over the emission spectrum, in many cases observed up to room temperatures, which is associated with the three-dimensional localization of charge carriers.

One of the most popular areas of application of semiconductor QDs is creating efficient heterostructure lasers with QDs as an active medium [4, 5]. This possibility is largely determined by the carrier relaxation rate. Carrier relaxation in quantum dots differs significantly from relaxation in quantum wires and quantum wells or in bulk materials. The discrete structure of the energy levels of electrons and holes in quantum dots imposes a number of restrictions on relaxation processes. Among the main factors affecting relaxation are the spectrum of electronic energy states of quantum dots, electron-hole interaction (exciton effect), the phonon states spectrum, electron-phonon interaction, the presence of excess carriers in quantum dots, as well as experimental conditions, in particular the temperature of the samples [6].

Quantum dots based on InSb are of particular interest due to the unique properties of indium antimonide: low effective masses of electrons ($0.013 m_0$, m_0 – mass of a free electron) and, accordingly, a de Broglie wavelength – up to 55 nm, which is bigger than in other materials. This makes it possible to use this material in a variety of optoelectronic devices, sensors, IR detectors, etc. [7, 8].

The use of indium antimonide quantum dots relieves, to some extent, one of the main problems of this material – the significant temperature instability of the electrophysical properties associated with the small band gap of this material (~ 0.17 eV). With a characteristic size of InSb QDs about 10 nm, the value of the energy gap $\varepsilon_{c1} - \varepsilon_{v1}$ is about 0.8 eV, which should lead to a significantly higher temperature stability of the electrophysical properties.

The purpose of this work was to study the influence of the temperature of macroscopic samples with InSb quantum dots on their electronic energy spectrum.

2. Sample preparation technologies and research methods

Colloid synthesis of InSb QDs was carried out in anhydrous oleylamine using indium chloride InCl_3 and antimony tris[bis(trimethylsilyl)amide] of $\text{Sb}[\text{N}(\text{Si}(\text{Me})_3)_2]_3$ as precursors according to the technique [9, 10]. An additional modification of the technique was that a mixture of acetate and indium chloride in the ratio 4:1 was used as the indium precursor. The halide in this system is necessary for the reaction, and the addition of acetate allows to minimize the aggregation processes. QD were transferred from a colloidal solution to the glass substrates with indium-tin oxide (ITO) layer by self-organization of ensembles on the surface with subsequent controlled evaporation of the solvent and control of the layer parameters. The synthesis of InSb quantum dots was carried out in the environment of oleylamine. Oleylamine ligands stabilize and passivate their surface and preventing their conglomeration by forming a shell. This shell is non-conductive and it acts as a “tunnel gap” or part of it in the system “probe – tunnel gap – quantum dot” in STM measurements.

The obtained samples were studied by scanning tunneling microscopy (STM) using a SOLVER Nano scanning probe microscope, as well as using a Zetasizer Nano ZS laser particle size analyzer. The research technique using the analysis of normalized differential tunneling CVCs is described in [11]. Additionally, in this work, measurements were carried out at sample temperatures of 23 °C and 95 °C.

In quantum dots the energy spectrum is discrete, and the distribution of the density of states depending on the energy of the charge carrier (electron) $g(\varepsilon)$ is described using the Dirac δ -function and theoretically represents a set of infinitely narrow and high peaks:

$$g(\varepsilon) = \sum_i \delta(\varepsilon - \varepsilon_i), \quad (1)$$

where ε_i – is the energy of the i -level of the discrete QD spectrum.

The discreteness of the energy spectrum leads to the appearance of practically atomically narrow lines in the luminescence (or absorption) spectrum of a QDs. Direct observation of narrow lines for an ensemble of QDs is impossible due to a sufficiently large scatter of the QDs parameters, which leads to a noticeable inhomogeneous line broadening.

When using the model of a cubic QD with edge a , the value of the energy of the discrete level can be determined as [12]:

$$\varepsilon_i = \frac{(\pi\hbar)^2}{2m^*} \cdot \frac{1}{a^2} \cdot (l^2 + m^2 + n^2), \quad (2)$$

where $l, m, n = 1, 2, 3, \dots$; m^* is effective mass of electron in a bulk material; a is the characteristic size of QD.

The carrier scattering leads to broadening of energy levels and limiting the height of the peaks: $\Delta\varepsilon_i \sim \hbar\tau$, where τ is the lifetime of electron in quasistationary states of QDs [13].

Such broadening in a real QDs occurs because of the limited lifetime of charge carriers due to spontaneous emission, interaction with phonons, temperature fluctuations, and some other processes.

The magnitude of broadening $\Delta\varepsilon_i$ is related to the value ε_i . Both of these parameters affect the form and character of the $g(\varepsilon)$ dependence.

The nature and magnitude of the broadening $\Delta\varepsilon_i$, in accordance with the concepts presented by the authors of [13], in the case of simple energy bands with a quadratic dispersion law, taking into account the corresponding simplifications, can be represented by the equation:

$$\Delta\varepsilon_i \approx 16 \frac{\varepsilon_i^{1/2}}{\varepsilon_i} (\varepsilon_i - \varepsilon)^{3/2} \cdot e^{-2\Delta r (2m^* (\varepsilon_i - \varepsilon)^{1/2} / \hbar)}, \quad (3)$$

where Δr is QD shell thickness.

The value of ε_i is largely determined by the characteristic size of the QDs, the composition and form of the QDs and, thus, is largely determined by the QDs producing technology.

3. Results and discussion

We studied samples of indium antimonide quantum dots with a characteristic size 8 – 10 nm (Fig. 1). Magnitude estimate of the first energy spectrum level ε_1 in accordance with (2) was in the range from 0.8 to 1.5 eV.

Localized energy levels ε_i associated with the properties of a quantum-size object appear in normalized differential tunneling CVCs as individual peaks. To analyze the experimental tunneling I – V characteristics, similarly to the approaches described in [14, 15], we used the dependence of $(dI/dV)/(I/V)$ on the voltage V , since the method of normalized differential CVCs is more informative in experimental data processing. Typical result for investigated samples are shown in Fig. 2.

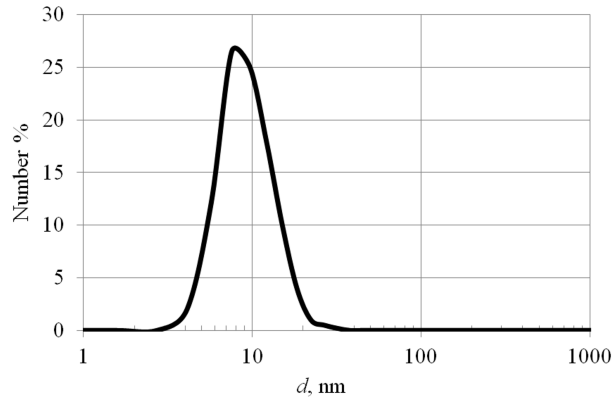


FIG. 1. Determination of the characteristic size of InSb QDs using a laser particle size analyzer

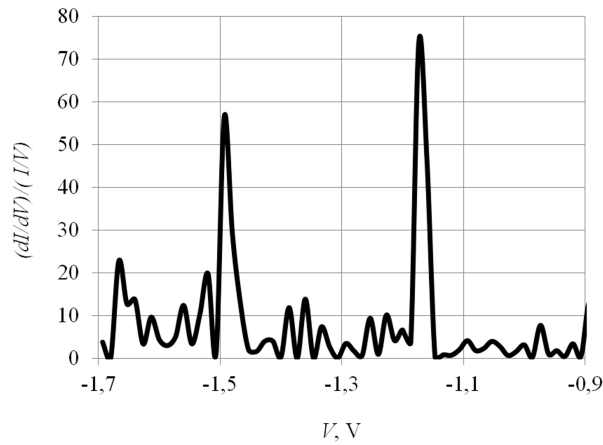


FIG. 2. Typical normalized differential tunneling CVC of InSb QDs

A change in the energy of the system, for example, upon heating the samples, should affect the broadening $\Delta\varepsilon_i$ in accordance with (3) and lead to changes in the energy spectrum of QDs. Typical experimental results of normalized differential CVCs are shown in Fig. 3.

An analysis of the experimental results showed that the position of the peak corresponding to the local energy levels of QDs shifts by 3 – 5 % (0.03 – 0.04 V). This is within the measurement accuracy (about $2kT$), but nevertheless the statistically reproducible data allow us to conclude that the results are not a measurement error.

In accordance with (3), Fig. 4 shows the calculated values of the broadening of the first energy level of InSb QDs upon heating to 95 °C. In the calculations, we chose the energy intervals $2kT$ relative to ε_1 . Estimation shows that in the considered energy range corresponding to the characteristic QDs sizes, the broadening of the first level is in the range from 2.5 to 4.0 %, depending on the level energy (the QDs shell thickness was chosen as 2 nm).

Comparison with the experimental results (Fig. 3) showed a fairly good agreement between the calculated and experimentally determined broadening of the first energy level of InSb QDs.

It should be noted that in the analysis of the broadening of the QDs energy levels, other factors were not taken into account, for example, the spectrum of phonon states, electron-phonon interaction and ect.

Obviously, a change in the value of $\Delta\varepsilon_1$ will affect the width and energy position of the fluorescence (or absorption) peak and, accordingly, the characteristics of devices with quantum dots in their structure. In this regard, the analysis of this issue is absolutely necessary. However, as can be seen from the calculation and experiment, the broadening of the first energy level of the QDs for the considered characteristic sizes and the selected temperature range does not exceed $2kT$ (which is within the measurement accuracy). Therefore, an increase in temperature in considered range has practically no effect on the energy characteristics of the QD. With a decrease in the QD size and, accordingly, an increase in the energy gap $\varepsilon_{c1} - \varepsilon_{v1}$, the broadening in percentage will decrease (Fig. 4), which should further increase the temperature stability of the parameters.

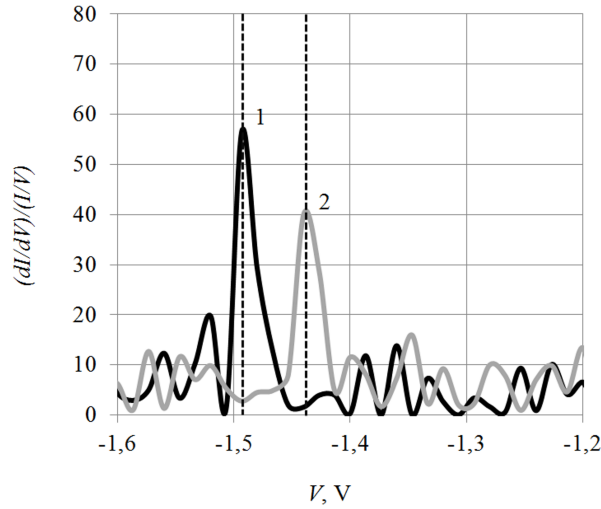


FIG. 3. Typical normalized differential tunneling CVCs of InSb QDs at two samples temperatures: 1 – 23 °C, 2 – 95 °C

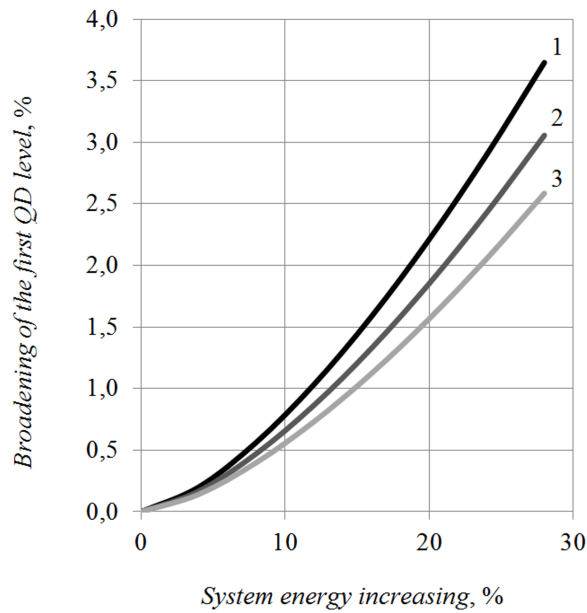


FIG. 4. The calculated values of the broadening of the first level of InSb QDs at various specified values of ε_1 : 1 – 0.7 eV, 2 – 1.0 eV, 3 – 1.4 eV

4. Conclusion

Thus, we analyzed the effect of temperature change on the energy spectrum of InSb quantum dots regarding broadening of the energy spectrum levels. The position of the levels was determined by processing normalized differential tunneling CVCs using the “cubic” QD model. Comparison of the calculated values of spectrum broadening with experimental results showed qualitative and quantitative agreement.

It was concluded that the broadening of the first QDs energy level, which is the most important in practice applications, for the considered characteristic sizes does not exceed $2kT$ (which is within the measurement accuracy), i.e. a change in temperature does not significantly affect the change in the energy characteristics of QDs in the considered temperature range. With a decrease of the QDs size and, accordingly, an increase in the energy gap $\varepsilon_{c1} - \varepsilon_{v1}$, the broadening of the first energy level of the QDs in percentage will decrease, which should lead to an increase in the temperature stability of the parameters of electronic and optoelectronic devices using InSb QDs.

The obtained results can be used to study the effect of temperature operations regimes on the optical and electronic characteristics of devices with semiconductor quantum dots.

Acknowledgements

This work was supported by grants from the Russian Foundation for Basic Research Projects No. 19-07-00087 and No. 19-07-00086.

References

- [1] IFedorov A.V. *Optics of nanostructures*. Nedra, St.-Petersburg, 2005, 326 p.
- [2] Oleinikov V.A., Sukhanova A.V., Nabiev I.R. Fluorescent semiconductor nanocrystals in biology and medicine. *Russian nanotechnology*, 2007, **2**, P. 160–173.
- [3] Sukhanova A.V., Venteo L., et al. Highly Stable Fluorescent Nanocrystals as a Novel Class of Labels for Immunohistochemical Analysis of Paraffin-Embedded Tissue Sections. *Lab Invest*, 2002, **82**, P. 1259–1261.
- [4] Ledentsov N.N., Grundmann M., et al. Quantum-dot heterostructure lasers. *Journal of Selected Topics in Quantum Electronics*, 2000, **6** (3), P. 439–451.
- [5] Bimberg D. Quantum dots for lasers, amplifiers and computing. *Journal of Physics D Applied Physics*, 2005, **38** (13), P. 2055–2058.
- [6] Ignatiev I.V., Kozin I.E. *Carrier dynamics in semiconductor quantum dots*. St.-Petersburg State university, St.-Petersburg, 2005, 126 p.
- [7] Reiss P., Carriere M., et al. Synthesis of Semiconductor Nanocrystals, Focusing on Nontoxic and Earth-Abundant Materials. *Chem. Rev.*, 2016, **116** (18), P. 10731–10819.
- [8] Yoffe A.D. Semiconductor quantum dots and related systems: Electronic, optical, luminescence and related properties of low dimensional systems. *Advances in Physics*, 2010, **50** (1), P. 1–208.
- [9] Brichkin S.B., Razumov V.F. Colloidal quantum dots: synthesis, properties and applications. *Russ. Chem. Rev.*, 2016, **85** (12), P. 1297–1312.
- [10] Liu W., Chang A.Y., Schaller R.D., Talapin D.V. Colloidal InSb Nanocrystals. *J. Am. Chem. Soc.*, 2012, **134**, P. 20258–20261.
- [11] Mikhailov A.I., Kabanov V.F., Zhukov N.D., Glukhovskoy E.G. Features of the energy spectrum of quantum dots indium antimonide. *Nanosystems: Physics, Chemistry, Mathematics*, 2017, **8** (5), P. 596–599.
- [12] Dragunov V.P., Neizvestny I.G., Gridchin V.A. *Fundamentals of nanoelectronics*. Fizmatkniga, Moscow, 2006, 496 p.
- [13] Zegrya G.G., Samosvat D.M. Energy spectrum and lifetime of charge carriers in open quantum dots in an electric field. *Journal of Experimental and Theoretical Physics*, 2009, **135** (6), P. 1043–1055.
- [14] Mikhailov A.I., Kabanov V.F., Gorbachev I.A., Glukhovskoy E.G. Study of the properties of $A^{II}B^{VI}$ and $A^{III}B^V$ semiconductor quantum dots. *Semiconductors*, 2018, **52** (6), P. 603–607.
- [15] Mikhailov A.I., Kabanov V.F., et al. Methodology of analyzing the CdSe semiconductor quantum dots parameters. *Nanosystems: Physics, Chemistry, Mathematics*, 2018, **9**, P. 464–467.

Young's modulus of phyllosilicate nanoscrolls measured by the AFM and by the in-situ TEM indentation

M. M. Khalisov^{1,2}, V. A. Lebedev³, A. S. Poluboyarinov⁴, A. V. Garshev⁴,
E. K. Khrapova¹, A. A. Krasilin¹, A. V. Ankudinov¹

¹Ioffe Institute Politekhnikeskaya, 26, Saint-Petersburg 194021, Russian Federation

²Pavlov Institute of Physiology, Russian Academy of Sciences
Makarova emb., 6, Saint-Petersburg, 199034, Russian Federation

³University of Limerick Limerick, V94 T9PX, Ireland

⁴Lomonosov Moscow State University GSP-1, Leninskie Gory, Moscow, 119991, Russian Federation

Alexander.ankudinov@mail.ioffe.ru

PACS 07.79.Lh, 87.64.Ee

DOI 10.17586/2220-8054-2021-12-1-118-127

$\text{Ni}_3\text{Si}_2\text{O}_5(\text{OH})_4$ phyllosilicate nanoscrolls were investigated by two techniques: the bending-based test method of AFM and the indentation method with visual control in STEM. In the first case, the average measured Young's modulus, about 200 GPa, turned out to be significantly higher than in the second one, 40 GPa. The reasons for this discrepancy are analyzed.

Keywords: AFM, in-situ TEM, nanomechanics, indentation, Young's modulus.

Received: 10 December 2020

Revised: 1 February 2021

1. Introduction

Phyllosilicates with chrysotile, pecoraite, halloysite structure, as well as some others [1] roll up into long nanotubes and nanoscrolls with outer and inner diameters being in the range of 20 – 200 nm and 4 – 30 nm, respectively. The driving forces of the phyllosilicate layers scrolling are the surface structure differences and the crystal lattice mismatches between the metal-oxygen (octahedral) and silicon-oxygen (tetrahedral) sheets [2]. A similar mechanism underlies the method of 3D micro- and nanostructures production [3], in which a strained semiconductor film is separated from the substrate using a sacrificial layer, and then scrolled to compensate the strains. Scrolled structures may also be formed from a thin, unstressed film to compensate the surface energy difference of the top and bottom sides of the film, [4]. Owing to their composition, structure and morphology, phyllosilicate nanoscrolls are considered as promising adsorbents and capsules [5–7], catalysts [8–12] and reinforcing components of composite materials [13–16]. In the view of their latter application, it seems interesting and important to determine the mechanical properties of the individual phyllosilicate nanoscrolls.

The morphology, composition, structure, and mechanical properties of individual nanoobjects can be studied using the methods of scanning and transmission electron microscopy (SEM, TEM), as well as atomic force microscopy (AFM) [17–19]. The bending-based test method of AFM [20–22] provides an opportunity to measure the Young's modulus of tubes, rods, and scrolls. For such a quasi-one-dimensional object, a nanobridge, bending stiffness is determined, and the result is analyzed using the theory of elasticity [23,24]. The nanobridges are formed, for example, over the pores of the track membrane after a droplet of colloid of one-dimensional nanoobjects has dried [25], or by using other sample preparation methods [26]. For nanoobjects located on a solid substrate, the Young's modulus can also be measured using the novel indentation technique with in-situ detection of the actual object's deformation by TEM or SEM [27].

In this study, aimed at determining the Young's modulus of synthetic nanoscrolls $\text{Ni}_3\text{Si}_2\text{O}_5(\text{OH})_4$ with a pecoraite structure, the capabilities of the AFM and the in-situ TEM indentation techniques are compared.

2. Sample preparation and investigation methods

The $\text{Ni}_3\text{Si}_2\text{O}_5(\text{OH})_4$ phyllosilicate nanoscrolls were synthesized by hydrothermal treatment at 350°C of the product of the reverse precipitation reaction from NiCl_2 and Na_2SiO_3 solutions, the procedure details are given in [28].

TEM data were collected at 200 kV in HAADF-STEM mode using Libra 200 microscope (Zeiss, Germany). To minimize undesired charging effects, beam monochromatization was employed. For the in-situ TEM indentation, Hysitron PI-95 picoindenter (Bruker, USA) was implemented. This setup permits to control tip displacements and the

force applied with a high precision using the embedded actuator. Moreover, series of (S)TEM images acquired during the measurements allows one to observe the entire indentation process.

Sample preparation was performed as follows: a droplet of a suspension of particles in isopropyl alcohol was applied to silicon substrates with a trapezoidal microprotrusion with a top base width of $1 \mu\text{m}$ (Flat-top silicon wedges; Bruker, USA) and then dried in air. The substrates were attached with conductive paste to a copper prism which than mounted into the Hysitron PI-95. The force applied by the indenter was pre-calibrated on a microcantilever with a known stiffness, 45 N/m . Loading and unloading forces as functions of sample deformation were corrected for drift in accordance with TEM data. This made it possible to determine the position of the picoindenter tip with an accuracy sufficient to investigate samples $20 - 50 \text{ nm}$ thick.

The indentation data processing was carried using the Hertz contact theory. The selected section of the corrected force curve was approximated by the dependence of this theory for the paraboloid-cylinder contact:

$$F = \frac{4}{3} E^* \sqrt{\frac{R^*}{\gamma}} \delta^{\frac{3}{2}}. \quad (1)$$

The following designations are used. Effective Young's modulus $E^* = ((1 - \nu_P^2)/E_T + (1 - \nu_S^2)/E_S)^{-1}$; reduced radius $R^* = R_T R_S / (R_T + 2R_S)$ and the ellipticity parameter $\varepsilon = (R_S + R_T)/R_S$ characterize the bodies in contact; $\gamma \approx 2(1 + 0.4 \ln \varepsilon)^3 \varepsilon^{-0.27} / (3\varepsilon + 1.8)$; load force F , δ is the total deformation of the nanoscroll and the diamond indenter (we neglected the latter); R_S and $R_T \approx 100 \text{ nm}$ are the radii of cylindrical nanoscroll, sample (S), and parabolic indenter (T); E_S and $E_T = 1140 \text{ GPa}$ are the sample and indenter Young's moduli; Poisson's ratios $\nu_S = \nu_T \approx 0.3$. Eq. (1) were obtained for an axially symmetric indenter and when the length of the cylindrical sample is significantly greater than its radius. The latter makes it possible to neglect the sample-substrate contact's deformation, see Appendix.

Several samples for TEM experiments were studied by AFM on an NTEGRA Aura setup with Nova Px control program and HybriD Mode of the operation (NT-MDT SI, Russia).

To prepare the samples with nanobridges for AFM testing, a suspension of $\text{Ni}_3\text{Si}_2\text{O}_5(\text{OH})_4$ nanoscrolls in isopropanol with a concentration of about 0.3 g/l was used. A droplet of the suspension was applied and dried on a TGZ3 silicon calibration grating (NT-MDT SI) with a period of $3 \mu\text{m}$ and a rectangular groove depth of 558 nm . The advanced version of the bending-based test method of AFM was used with special algorithm to establish the nanobridge span length and to identify the boundary conditions of the nanobridge fixation [29]. If one end of the nanobridge rested on a protrusion and the other was in a depression, we used the results of [30] to correct the contribution to the deformation signal from an AFM probe sliding over an inclined object. The nanobridges, formed from nanoscrolls deposited on the gratings, were preliminarily studied in a Quanta 200 scanning electron microscope (FEI, USA). Subsequently, SEM data were used to facilitate the detection of the nanobridges in a BioScope Catalyst atomic force microscope (Bruker, Germany) integrated into a Z16 APO optical microscope (Leica, Germany).

The bending-based tests were conducted in the PeakForce QNM AFM mode, simultaneously registering the signals of the sample relief height, the deformation D , and the peak force error F_E . The signals were determined by an automatic force curve analysis algorithm in the scanning program. To visualize and analyze the AFM data, the NanoScope Analysis 1.80 (Bruker) program and free software Gwyddion version 2.55 were used [31].

In the signal D , the instrumental contributions were corrected. Automatically, the deformation is determined by 85% of the contact part of the force curve and does not correspond to the setpoint force F_{SP} , but to the actual force, which is the sum of F_{SP} and F_E . To eliminate the contribution from the AFM probe sliding on inclined sample areas into the signal D , we used a simplified version of the filter [30], which is reduced to multiplying the measured signal value by the square of the cosine of the angle θ between the vertical direction and the surface normal at the point of measurements. Such a correction does not affect the bending profile of horizontally located nanobridges, since it is equal to unity on them. The corrected deformation was calculated, thus, by the expression:

$$D_C = \frac{DF_{SP} \cos^2 \theta}{0.85F_{SP} + 0.85F_E}. \quad (2)$$

Two nanobridge bending profiles were extracted from the AFM image of D_C values: (1) with the nanobridge span length (the distance between the attachment points at the boundaries of the calibration grating groove) l_T , determined from the AFM topography data; (2) with a span length l_S , the start and end points of which were set at the locations where the D_C signal began to exceed the horizontal baseline of zero signal.

Then the profiles (1) and (2) were normalized vertically, $\zeta = D_C/D_C^{MAX}$, and horizontally, $\chi = x/l_i$ (x is the coordinate value along the profile, $i = T, S$), and approximated by the expression:

$$\zeta_n(\chi) = 4^n (\chi - \chi^2)^n, \quad \chi \in [0, 1]. \quad (3)$$

The fitting parameter n describes the model of deformation and fixation of the nanobridge at the edges of the depression. For $n = 1$, the object under study exhibits the properties of a stretched string, for $n = 2$ – a supported beam, for $n = 3$ – a clamped beam [29].

From the two profiles with $2 \leq n \leq 3$, the one with a minimum residual with the fit, Eq. (3), was selected, i.e. more consistent with the theory [29], which was then approximated by the expression:

$$\zeta^\lambda(\chi) = 4^3(\chi - \chi^2)^3 \frac{(2 + \lambda)}{(1 + 2\lambda)(2 + 3\lambda)} + 4^2(\chi - \chi^2)^2 \frac{6\lambda(\lambda + 1)}{(2\lambda + 1)(3\lambda + 2)}. \quad (4)$$

Young's modulus, E , was calculated using the λ value, which characterizes the nanobridge fixing conditions and is the result of fitting [29]:

$$E = \Phi(\lambda)E_{CB}; \quad E_{CB} = \frac{k_S^{MIN} \cdot l^3}{192 \cdot I}, \quad \Phi(\lambda) = \frac{4\lambda + 2}{\lambda + 2}. \quad (5)$$

Equation 5 uses: a correction factor $\Phi(\lambda)$; a Young's modulus E_{CB} in the case of a clamped beam, conditional for the nanobridge; a minimum stiffness $k_S^{MIN} = F_{SP}/D_C^{MAX}$ at the point of maximum deflection D_C^{MAX} ; a span length l , selected earlier from the l_T and l_S ; a moment of inertia $I = \pi d^4/64$ for a model shape of the nanobridge, a cylindrical beam with a section diameter d .

3. Results and discussion

3.1. In-situ TEM indentation

Figure 1 shows the load-unload indentation curves for two test cycles of a 60 nm diameter nanoscroll with TEM visualization of the process. In the first cycle, the indentation force is close to $10 \mu\text{N}$ at the maximum deformation, about 20 nm (about a third of the diameter). In the second cycle, the force increases to $40 \mu\text{N}$, while the deformation remains at about the same level. The apparent strengthening of the nanoscroll by almost four times in the second cycle seems to refer to an increasing stiffness of the contact of the nanoscroll with the non-smooth substrate, see Fig. 1(a) and inset, in other words, to the formation of a closer contact between them. In addition, the observable particles can be associated with phyllosilicate foreign granulas in the path of the electron beam. They can be located both in the plane in front of or behind the analyzed nanoscroll, as well as directly below it. In the last case, the measured stiffness will be significantly decreased.

Since the radii of the studied nanoscrolls are much smaller than their length, the load-unload curves can be processed using Eq. (1), see also Appendix. Accounting for data noisiness and the comparability of the nanoscroll

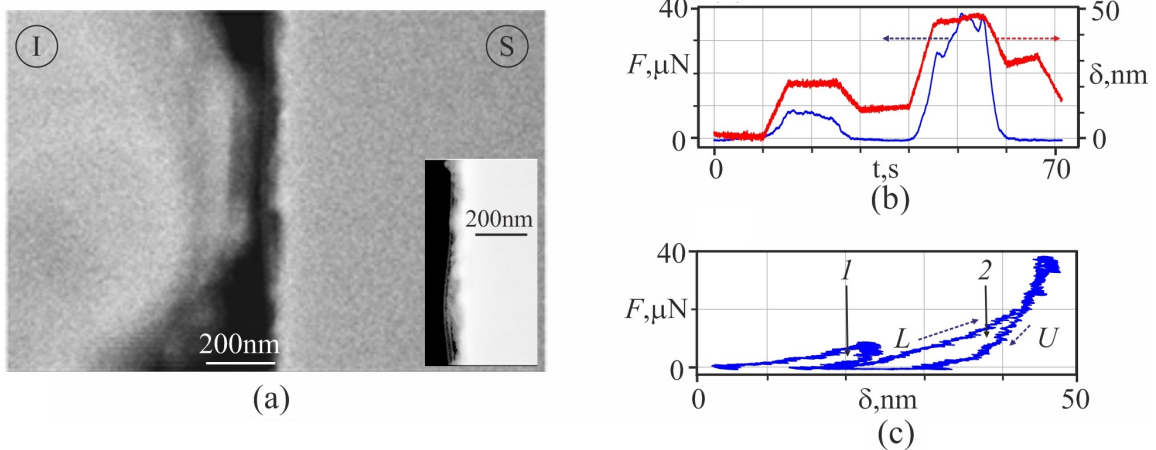


FIG. 1. (a) A STEM image of a phyllosilicate nanoscroll between the picoindenter (I) and the substrate (S) (experiment No. 7, Table 1). Inset: the STEM image of the nanoscroll-substrate interface (experiment No. 5, Table 1). (b) Measured dependences of the indentation force $F(t)$ and of the indenter displacement $\delta(t)$ on time in the experiment; (c) load (L) and unload (U) dependences $F(\delta)$. The steepest section without hysteresis (cycle 2 marked by a corresponding number and an arrow) apparently reveals the picoindenter-substrate contact

TABLE 1. Young's moduli of the nanoscrolls, E , results of the in-situ TEM indentation

No	d , nm	E , according to load dependence, GPa	E , according to unload dependence, GPa
1	60	Cycle 1:15; Cycle 2:50	Cycle 1:60
2	60	Cycle 1:2; Cycle 2:20	Cycle 1:10; Cycle 2:40
3	50	40	–
4	65	50	163
5	25	Cycle 1:12; Cycle 2:35; Cycle 3:45	Cycle 1:55; Cycle 2:42; Cycle 3:50
6	60	15	–
7	60	Cycle 1:10; Cycle 2:20	Cycle 1:20; Cycle 2:35

deformation with its radius, such processing gives an estimated result. Because the indentation experiment can be accompanied by inelastic processes of formation, compaction and/or elastic processes of deformation in the nanoscroll-substrate contact, this is an underestimation.

The data of seven indentation experiments are summarized in Table 1. If each experiment is averaged over all cycles, without distinguishing between the cases of loading and unloading, and then the results of all experiments are averaged, then the final value of Young's modulus will be 40 ± 30 GPa. Distinguishing these two cases, we get: 30 ± 10 GPa (load) and 60 ± 50 GPa (unload). A systematic increase in the value of Young's modulus calculated from the unloading section of the $F(\delta)$ dependence can also indicate in favor of creating a tighter nanoscroll-substrate contact.

3.2. Results of bending-based tests and their comparison with in-situ TEM indentation data

AFM data of bending-based tests of $\text{Ni}_3\text{Si}_2\text{O}_5(\text{OH})_4$ nanoscrolls obtained in PeakForce QNM mode are shown in Fig. 2. The nanoscroll formed a bridge across the grating groove, as seen in the image in Fig. 2(a). On the simultaneously measured and then corrected image of the deformation signal, Fig. 2(b), the signal is maximal in the nanobridge middle, light contrast. The large signal at the nanobridge top and bottom edges is apparent and has an instrumental origin associated with the AFM probe slippage [30]. The signal profile along the dashed line on the nanobridge is shown in Fig. 2(c), the right axis shows the deformation values.

According to the presented data, the nanobridge minimal stiffness is about 0.6 N/m, Table 2. In Fig. 2(c), the left axis, the normalized experimental profile is in optimal agreement with the model one, Eq. (4), at $\lambda = 1.01$. Thus, the boundary conditions for the nanobridge are intermediate between the supported and clamped ends. The span length of the nanobridge is approximately $2.2 \mu\text{m}$, and the nanoscroll height on the flat protrusions of the grating is 46 nm. Accounting for the fixing (boundary) conditions, the calculated Young's modulus is 299 GPa.

Table 2 summarizes the bending-based test data for twenty nanobridges. Disregarding the fixing conditions, the Young's modulus averaged over the all experimental values are 120 GPa and 110 GPa, excluding the minimum and maximum values; taking these conditions into account – 200 GPa and 170 GPa, respectively.

In most cases, the AFM experiment shows a significantly higher value of Young's modulus than the TEM experiment does. In the both experiments, the nanoscrolls diameters do not differ on average (54 ± 14 nm, Table 1; 56 ± 14 nm, Table 2). However, depending on the way of averaging, mean values of the Young's modulus in the AFM experiments are 3–6 times higher than those in the TEM experiments. Since the projected TEM image of the nanoscroll on the $1 \mu\text{m}$ -thick-substrate is analyzed, it is difficult to inspect the nanoscroll-substrate contact directly at the vicinity of the indentation region. If, for example, the nanoscroll covers a cavity on the substrate, then processing of the indentation curves will give an incorrect and underestimated value of Young's modulus. Let us estimate the cavity width corresponding to the stiffness values ~ 1 kN/m in the TEM experiment, see Fig. 1. According to the data in Table 2, on average, a $2 \mu\text{m}$ -nanobridge has a bending stiffness of 1 N/m. The beam stiffness is inversely proportional to the cube of its length, and the nanobridge over the 200 nm-wide-cavity will have the stiffness ~ 1 kN/m.

As shown in [7], phyllosilicate nanoscrolls with a pecoraite structure have a small positive zeta potential < 30 mV, hence, they are prone to aggregation. During the sample preparation, the substrate can become contaminated with particle aggregates, so that small particles, or even layers of such particles, which are softer than the substrate, appear under the nanoscroll. This may violate an indentation experiment condition, which requires the nanoscroll adheres

TABLE 2. Young's modulus of the nanoscrolls, E , according to the AFM data of the bending-based tests processed by the algorithm of [29]

No	k_S^{MIN} N/m	d nm	l_T nm	l_S nm	R_T	R_S	n	λ	$\Phi(\lambda)$	E_{CB} GPa	E GPa
1	0.63	52	1890	1980	0.005	0.003	2.7 S	0.12	1.17	71	83
2	1.04	53	1860	1820	0.008	0.006	2.3 S	0.49	1.59	84	134
3	0.53	35	–	1270	–	0.004	2.4 S	0.40	1.50	76	115
4	0.73	58	–	1390	–	0.004	2.9 S	0.05	1.07	18	20
5	0.89	62	2010	1830	0.010	0.005	2.0 S	8.88	3.45	39	136
6	2.67	44	1870	1890	0.030	0.006	2.7 S	0.13	1.18	510	603
7	0.61	46	2170	2060	0.003	0.004	2.2 T	1.01	2.01	149	299
8	0.63	81	1970	2370	0.067	0.004	2.5 S	0.24	1.32	21	27
9	1.05	37	1870	2010	0.013	0.008	2.2 S	0.69	1.77	480	849
10	0.84	53	2130	2030	0.004	0.005	2.1 T	1.06	2.04	109	222
11	0.54	52	–	2280	–	0.002	2.1 S	1.19	2.12	93	196
12	0.71	81	2120	1970	0.025	0.003	2.8 S	0.09	1.13	13	15
13	2.68	51	2090	1960	0.023	0.009	2.5 S	0.26	1.35	318	427
14	0.33	68	1940	1810	0.023	0.004	2.7 S	0.14	1.20	10	12
15	0.50	50	1970	1870	0.003	0.003	2.0 S	2.65	2.71	56	151
16	0.88	50	1910	1740	0.005	0.010	2.6 T	0.17	1.24	104	128
17	0.33	44	1900	1830	0.013	0.004	2.6 S	0.17	1.24	57	70
18	0.96	54	2060	1790	0.005	0.007	2.0 T	4.02	3.00	105	314
19	0.48	81	1900	2000	0.024	0.008	2.4 S	0.36	1.46	9	14
20	1.55	64	1920	2210	0.024	0.008	2.4 S	0.30	1.39	106	148
Average Young's modulus:										120±150	200± 220
Average Young's modulus across the entire sample without two extreme values:										110±120	170± 160

Designations used: minimum stiffness k_S^{MIN} and diameter d of the nanobridge; residual, R_T or R_S , of the model and experimental profile and the span length, l_T or l_S , according to the stiffness, S , topography, T ; fitting parameters n and λ of model dependences (3) and (4); correction factor $\Phi(\lambda)$ for E_{CB} conditional case of clamped beam, Eq.(5).

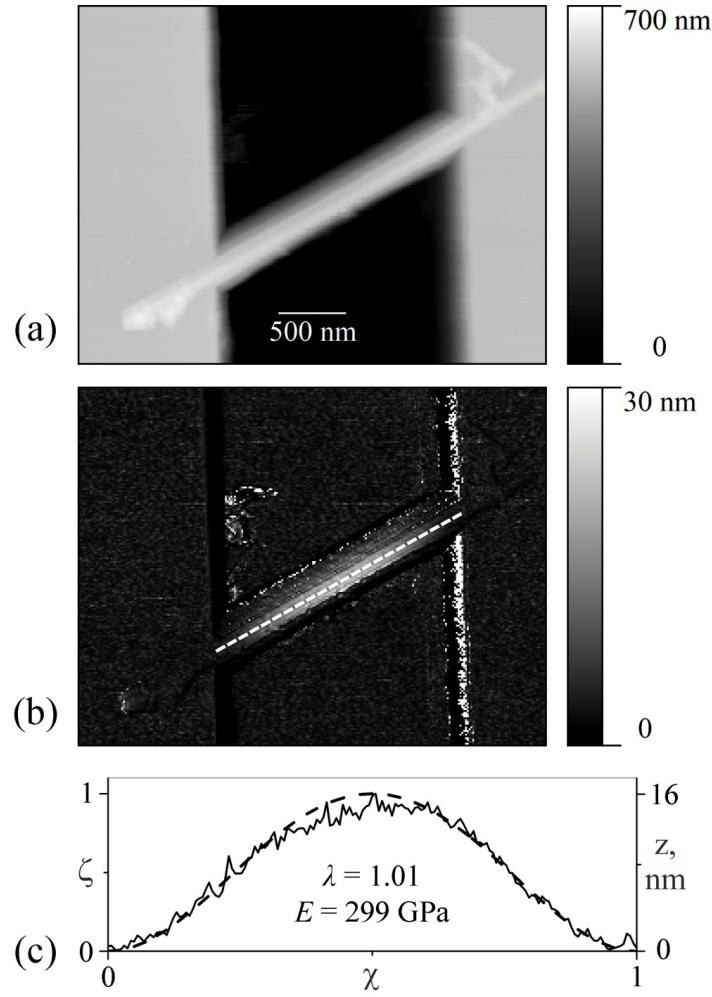


FIG. 2. AFM experiment No. 7. (a) The AFM topography image of a region of the TGZ3 grating with the $\text{Ni}_3\text{Si}_2\text{O}_5(\text{OH})_4$ nanobridge. (b) The AFM image of the D_C signal, corrected deformation. The nanobridge bending profile data were taken along the dashed line (c). The normalized nanobridge bending profile D_C/D_C^{MAX} and the model profile (dashed line), Eq. (4) with a fitting parameter $\lambda = 1.01$. PeakForce QNM parameters: $F_{SP} = 10$ nN, Peak Force Amplitude – 150 nm, Peak Force Frequency – 1 kHz, Scan Rate – 0.3 Hz, Frame Size – 256×196 , cantilever FMG01 (NT-MDT SI)

tightly to the substrate. It is difficult to identify inappropriate nanoscrolls in TEM, as noted above. Such an opportunity is provided by combined SEM and AFM studies.

Two samples prepared for TEM experiments were investigated by SEM and AFM, see Fig. 3. To test the suitability of nanoscrolls for the TEM experiments, the AFM stiffness signal was analyzed. This signal measured in Hybrid Mode (NT-MDT SI) corresponds to the force curve slope. On a solid and flat sample, it is maximum and is considered equal to the cantilever stiffness. The amount of the signal reduction determines the stiffness of the probe-sample contact; see more details in [30]. In Fig. 3(b), the AFM signal is maximal on the upper portion of the substrate and on a nanoscroll. Since this nanoscroll is indistinguishable from a solid substrate in terms of stiffness, it can be assumed that it adheres tightly to it. On another nanoscroll in Fig. 3(d), the signal differs (darker contrast) from the maximum by about 10%. Neglecting the probe-nanoscroll contact contribution, one can estimate the nanoscroll-substrate contact stiffness as $500 \text{ N/m} (\cong 54 \cdot 0.9/0.1)$. That is close to characteristic stiffness values $\sim 1 \text{ kN/m}$ in the in-situ TEM indentation experiments, Fig. 1.

The AFM data in Fig. 3 reproduced well in repeated scans. Consequently, they reflect elastic responses and, in particular, the elastic behavior of the probe-nanoscroll-substrate contacts. The presented results reveal very likely the elastic deformation of the nanoscroll-substrate contact that might lead to underestimated values of Young's modulus

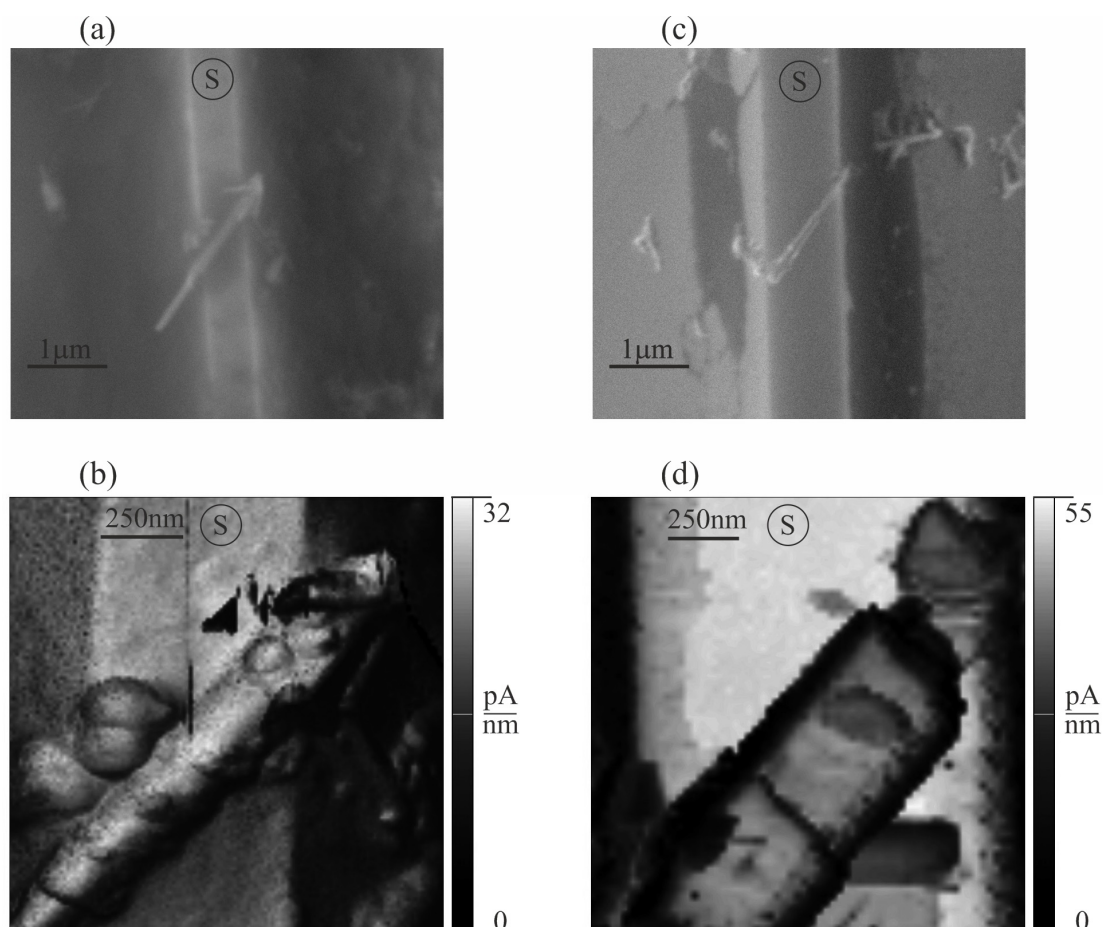


FIG. 3. (a), (c) SEM images of $\text{Ni}_3\text{Si}_2\text{O}_5(\text{OH})_4$ nanoscrolls on the substrates, S; these substrates are also used in the TEM experiments. (b), (d) The AFM stiffness signal images of the same nanoscrolls as in (a) and (c), correspondingly. Hybrid Mode parameters: (a) $F_{SP} = 300$ nN, cantilever stiffness calibrated by the Sader method [32] 56 N/m, Amplitude – 50 nm, Frequency – 1 kHz, Scan Rate – 0.25 Hz, Frame Size – 128×128 ; (b) 150 nN, 54 N/m, 50 nm, 1 kHz, 0.2 Hz, 64×64 ; cantilevers RTESPA-300 (Bruker)

in the TEM experiments, Fig. 1 and Table 1. The AFM study of inelastic deformations in the nanoscroll-substrate contact may be difficult to implement, since it will require two orders of magnitude larger indentation forces, as in the TEM experiments. In conclusion it should be emphasized that the presented SEM and AFM results show the way to select the nanoscrolls for further in-situ TEM indentation measurements.

4. Conclusions

In this research, the Young's modulus of synthetic phyllosilicate $\text{Ni}_3\text{Si}_2\text{O}_5(\text{OH})_4$ nanoscrolls with a pecoraite structure was measured by AFM and in-situ TEM indentation techniques. For the first time, the quantitative results obtained by both the techniques were cross-compared.

In AFM experiments, advanced bending-based tests with an algorithm that identifies and takes into account the boundary conditions of nanobridges formed by the nanoscrolls were applied to measure their Young's moduli. The average Young's modulus was 200 GPa.

Additionally, the nanoscrolls were tested by modern in-situ TEM indentation technique using the Hysitron PI-95 setup. The mean measured Young's modulus value obtained was 40 GPa.

Also to analyze the indentation experiments, a convenient form of Hertz theory dependence for the contact of an elliptic paraboloid with a cylinder was proposed and used.

The nanoscrolls prepared for TEM measurements were also studied by SEM and AFM methods. Evidences of deformation of the nanoscroll-substrate contact were found. For the nanoscroll indentation experiments, this unaccounted deformation could be the main reason for the obtained low values of Young's modulus. This result seems to

be very useful for systematizing in-situ TEM indentation measurements, as it shows that preliminary combined SEM and AFM studies allow selection of the nanoscrolls presumably weakly or strongly attached to the substrate.

Acknowledgements

This work was supported by the Russian Science Foundation grant 19-13-00151. An access to the Libra 200 TEM and Hysitron PI-95 in-situ picoindenter was provided by the M. V. Lomonosov Moscow State University Program of Development.

Appendix

A probe (an indenter) with an elliptic paraboloid surface is described in the XYZ coordinate system by the function

$$z_P = \frac{x^2}{2r_x} + \frac{y^2}{2r_y}. \quad (6)$$

The surface of the cylinder corresponding to a sample (a nanoscroll) is specified in the $X_S Y_S Z$ coordinate system by the function

$$z_S^* \cong -\frac{x_S^2}{2R}, \quad |x_S| \ll R, \quad (7)$$

see Fig. 4. The principal radii of curvature of the elliptic paraboloid, r_x and r_y , and the radius of the cylinder, R , are introduced. If the angle $\widehat{X, X_S} = \alpha$, then $x_S = x \cos \alpha + y \sin \alpha$, and in the XYZ coordinate system the cylinder surface is described by the function

$$z_S = -\frac{\cos^2 \alpha x^2 + \sin^2 \alpha y^2}{2R}. \quad (8)$$

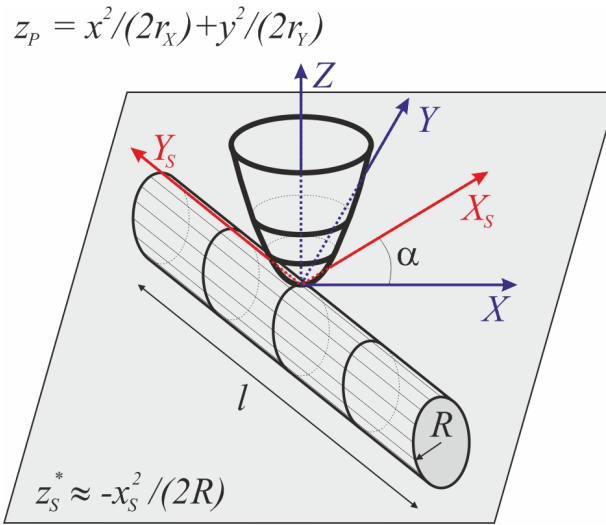


FIG. 4. The model indenter with the elliptic paraboloid surface, z_P dependence, and the nanoscroll sample with the cylinder surface, z_S^* dependence. The origin of the coordinates of both systems is at the point of contact

In the XYZ coordinate system, the distance between some point on the cylinder (sample surface of the nanoscroll, nanotube) and the point located vertically above it on the elliptic paraboloid (the indenter surface) is determined by the function z (also the elliptic paraboloid):

$$z = z_P - z_S = \frac{x^2}{2R_x} + \frac{y^2}{2R_y}, \quad (9)$$

with curvature radii at the point $x, y, z = 0$:

$$R_x = \frac{Rr_x}{R + r_x \cos^2 \alpha}, \quad R_y = \frac{Rr_y}{R + r_y \sin^2 \alpha}. \quad (10)$$

We also introduce the reduced radius R^* at this point and the ellipticity parameter ϵ of the horizontal section of the surface (9) by any plane $z = \text{const} > 0$:

$$R^* = \frac{R_x R_y}{R_x + R_y} = \frac{R r_x r_y}{R(r_x + r_y) + r_x r_y}, \quad \epsilon = \frac{R_y}{R_x} = \frac{r_y(R + r_x \cos^2 \alpha)}{r_x(R + r_y \sin^2 \alpha)}. \quad (11)$$

If the distance between the points located on the same vertical on the probe and on the sample is described by the elliptic paraboloid, then there is the following solution to the Hertz problem, see Eqs. (9) and (10) in [33]:

$$\delta_1 = \left[\gamma \frac{9F^2}{16E^* R^*} \right]^{1/3}, \quad \gamma = \frac{2\mathcal{F}^3}{\pi^2 k^2 \mathcal{E}}. \quad (12)$$

The exact solution of the Hertz problem for a spherical indenter probe of radius r on a flat sample is obtained from (12) by substituting $\gamma = 0.5$ and $R^* = r/2$. The reduced Young's modulus E^* is expressed in terms of Young's moduli E_P , E_S and Poisson's ratios ν_P , ν_S of the probe, P , and of the sample, S : $E^* = ((1 - \nu_P^2)/E_P + (1 - \nu_S^2)/E_S)^{-1}$; δ_1 deformation of the contact area, F force of indentation; \mathcal{E} and \mathcal{F} values of complete elliptic integrals of the first and second kind, k ellipticity of the contact area (approximately equal to $\epsilon^{2/3}$), [33]. In [33], see equations (6)–(8), analytical dependences were obtained that approximately relate k , \mathcal{E} and \mathcal{F} with the ellipticity parameter ϵ :

$$k \cong 1.0339\epsilon^{0.636}, \quad (13)$$

$$\mathcal{E} \cong 1.0003 + 0.5968\epsilon^{-1}, \quad (14)$$

$$\mathcal{F} \cong 1.5277 + 0.6023 \ln \epsilon, \quad (15)$$

$$k^2 \mathcal{E} \cong 1.0693\epsilon^{1.272} + 0.6379\epsilon^{0.272}. \quad (16)$$

Using (15) and (16), we obtain an approximate dependence for γ from (12):

$$\gamma = \frac{2(1.5277 + 0.6023 \ln \epsilon)^3}{\pi^2(1.0693\epsilon^{1.272} + 0.6379\epsilon^{0.272})}. \quad (17)$$

For a spherical indenter on a flat sample $\epsilon = 1$, and from (13–15) and (17) we obtain: $\mathcal{E}(1) \cong 1.5971$, $\mathcal{F}(1) \cong 1.5277$, $k(1) \cong 1.0339$, and $\gamma = 2 \times 1.5277^3 / (\pi^2 1.0339^2 1.5971) \cong 0.4232 < 0.5$. Substitution of (15) in (12) in the case $\epsilon = 1$ underestimates the indentation value ($\delta_1/\delta_H = \sqrt[3]{0.4232/0.5} \cong 0.95$) in comparison with the exact Hertz solution by 5%. As shown in [33], in the other cases the error is smaller.

To calculate the values of E^* in the in-situ TEM indentation experiment, the indentation curves can be analyzed using the simplified expression (17) for γ in (12):

$$\gamma \approx \frac{2(1 + 0.4 \ln \epsilon)^3}{\epsilon^{0.27}(3\epsilon + 1.8)}. \quad (18)$$

Considering the picoindenter (probe tip) as a paraboloid of revolution with a radius of curvature r , and a nanoscroll as a cylinder with a radius of curvature R , we have:

$$R^* = \frac{Rr}{2R + r} \quad \text{and} \quad \epsilon = \frac{R + r}{R}. \quad (19)$$

R^* differs from the reduced contact radius of two balls with radii r and $R(= R/(R + r))$.

The experimental force curves can be characterized, for example, by the stiffness of the picoindenter-nanoscroll-substrate composite system. Eq. (12), taking into account (18) and (11), makes it possible to determine the stiffness of the picoindenter-nanoscroll contact k_1 :

$$k_1 = \frac{\partial F}{\partial \delta_1} = 2E^* \sqrt{R^* \delta_1 / \gamma}. \quad (20)$$

In the TEM experiment, the total deformation is measured: $\delta = \delta_1 + \delta_2$. Where δ_1 and δ_2 are the deformations of the picoindenter-nanoscroll contact and of the nanoscroll-substrate contact, see also Fig. 4. It is possible to determine k_2 as the stiffness of a cylinder of length l with a substrate with Young's modulus E_{Sb} and Poisson's ratio ν_{Sb} . It does not depend on the cylinder radius R , [24, 34]:

$$F = \frac{\pi}{4} E^{**} l \delta_2, \quad E^{**} = \left(\frac{1 - \nu_S^2}{E_S} + \frac{1 - \nu_{Sb}^2}{E_{Sb}} \right)^{-1}, \quad k_2 = \frac{\partial F}{\partial \delta_2} = \frac{\pi}{4} E^{**} l. \quad (21)$$

Assuming $E^* \sim E^{**}$, the deformation δ_2 can be ignored in the experiment when $\pi l \gg 8\sqrt{R^* \delta_1 / \gamma}$. Since $\delta_1 \leq \delta \leq R$, and $\gamma \sim 1$, the condition is simplified to $l \gg R^*$.

References

- [1] Krasilin A.A., Khrapova E.K., Maslennikova T.P. Cation Doping Approach for Nanotubular Hydrosilicates Curvature Control and Related Applications. *Crystals*, 2020, **10**(8), P. 654(1–41).
- [2] Krasilin A.A. Energy modeling of competition between tubular and platy morphologies of chrysotile and halloysite layers. *Clays Clay Miner.*, 2020, **68**, P. 436–445.
- [3] Prinz V.Ya., Seleznev V.A., Gutakovskiy A.K., Chehovskiy A.V., Preobrazhenskii V.V., Putyato M.A., Gavrilova T.A. Free-standing and overgrown InGaAs/GaAs nanotubes, nanohelices and their arrays. *Physica E: Low-dimensional Systems and Nanostructures*, 2000, **6**, P. 828–831.
- [4] Gulina L.B., Tolstoy V.B., Lobinsky A.A., Petrov Yu.V. Formation of Fe and Fe₂O Microspirals via Interfacial Synthesis. *Part. Part. Syst. Charact.*, 2018, **35**, P. 1800186
- [5] Scarfato P., Avallone E., Incarnato L., Di Maio L. Development and evaluation of halloysite nanotube-based carrier for biocide activity in construction materials protection. *Appl. Clay Sci.*, 2016, **132**, P. 336–342.
- [6] Cavallaro G., Danilushkina A., Evtugyn V., Lazzara G., Milioto S., Parisi F., Rozhina E., Fakhruddin R. Halloysite Nanotubes: Controlled Access and Release by Smart Gates. *Nanomaterials*, 2017, **7**(8), 199, P. 1–12.
- [7] Krasilin A.A., Danilovich D.P., Yudina E.B., Bruyere S., Ghanbaja J., Ivanov V.K. Crystal violet adsorption by oppositely twisted heat-treated halloysite and pecoraite nanoscrolls. *Appl. Clay Sci.*, 2019, **173**, P. 1–11.
- [8] Zhang C., Zhu W., Li S., Wu G., Ma X., Wang X., Gong J. Sintering-resistant Ni-based reforming catalysts obtained via the nanoconfinement effect. *Chem. Commun.*, 2013, **49**, P. 9383(1–3).
- [9] Ashok J., Bian Z., Wang Z., Kawi S. Ni-phyllsilicate structure derived Ni–SiO₂–MgO catalysts for bi-reforming applications: acidity, basicity and thermal stability. *Catal. Sci. Technol.*, 2018, **8**(6), P. 1730–1742.
- [10] Bian Z., Kawi S. Highly carbon-resistant Ni–Co/SiO₂ catalysts derived from phyllosilicates for dry reforming of methane. *J. CO₂ Util.*, 2017, **18**, P. 345–352.
- [11] Krasilin A.A., Straumal E.A., Yurkova L.L., Khrapova E.K., Tomkovich M.V., Shunina I.G., Vasil'eva L.P., Lermontov S.A., Ivanov V.K. Sulfated Halloysite Nanoscrolls as Superacid Catalysts for Oligomerization of Hexene-1. *Russ. J. Appl. Chem.*, 2019, **92**(9), P. 1251–1257.
- [12] Park J.C., Kang S.W., Kim J.-C., Kwon J.I., Jang S., Rhim G.B., Kim M., Chun D.H., Lee H.-T., Jung H., et al. Synthesis of Co/SiO₂ hybrid nanocatalyst via twisted Co₃Si₂O₅(OH)₄ nanosheets for high-temperature Fischer–Tropsch reaction. *Nano Res.*, 2017, **10**(3), P. 1044–1055.
- [13] Liu Y., Liu M. Conductive carboxylated styrene butadiene rubber composites by incorporation of polypyrrole-wrapped halloysite nanotubes. *Compos. Sci. Technol.*, 2017, **143**, P. 56–66.
- [14] Afanas'eva N.V., Gubanova G.N., Romashkova K.A., Sapegin D.A., Kononova S.V. Relaxation processes in an aromatic polyamide-imide and composites on its basis with hydrosilicate nanoparticles. *Polym. Sci. Ser. A*, 2016, **58**(6), P. 956–967.
- [15] Mo H., Yang K., Li S., Jiang P. High thermal conductivity and high impact strength of epoxy nanodielectrics with functionalized halloysite nanotubes. *RSC Adv.*, 2016, **6**(73), P. 69569–69579.
- [16] Roy K., Debnath S.C., Pongwisuthiruchte A., Potiyaraj P. Up-to-date review on the development of high performance rubber composites based on halloysite nanotube. *Appl. Clay Sci.*, 2019, **183**, P. 105300(1–15).
- [17] Binnig G., Quate C.F., Gerber Ch. Atomic Force Microscope. *Phys. Rev. Lett.*, 1986, **56**(9), P. 930–933.
- [18] Wong E.W., Sheehan P.E., Lieber C.M. Nanobeam Mechanics: Elasticity, Strength, and Toughness of Nanorods and Nanotubes. *Science*, 1997, **277**(5334), P. 1971–1975.
- [19] Bhushan B. edd. *Nanotribology and Nanomechanics - An Introduction*. Springer-Verlag Berlin Heidelberg, 2005, 1148 p.
- [20] Salvétat J.-P., Kulik A.J., Bonard J.-M., Briggs G.A.D., Stockli T., Méténier K., Bonnamy S., Béguin F., Burnham N.A., Forró L. Elastic Modulus of Ordered and Disordered Multiwalled Carbon Nanotubes. *Adv. Mater.*, 1999, **11**(2), P. 161–165.
- [21] Salvétat J.-P., Bonard J.-M., Thomson N.H., Kulik A.J., Forró L., Benoit W., Zuppiroli L. Mechanical properties of carbon nanotubes. *Appl. Phys. A*, 1999, **69**(3), P. 255–260.
- [22] Zheng X.-P., Cao Y.-P., Li B., Feng X.-Q., Wang G.-F. Surface effects in various bending-based test methods for measuring the elastic property of nanowires. *Nanotechnology*, 2010, **21**(20), P. 205702(1–6).
- [23] Timoshenko S., Goodier J.N. *Theory of elasticity*. McGraw-Hill, New York, 1970, 567 p.
- [24] Landau L.D., Lifshitz E.M. *Theory of Elasticity*. Pergamon Press Ltd., Oxford, 1970, 165 p.
- [25] Cuenot S., Demoustier-Champagne S., Nysten B. Elastic modulus of polypyrrole nanotubes. *Phys. Rev. Lett.*, 2000, **85**(8), P. 1690–1693.
- [26] Kis S. *Mechanical properties of mesoscopic objects*. Thesis. Ecole Polytechnique Federale de Lausanne, 2003, 166 p.
- [27] Bruker Hysitron nanomechanical test instruments. URL: <https://www.bruker.com/products/surface-and-dimensional-analysis/nanomechanical-test-instruments.html>
- [28] Khrapova E.K., Ugolkov V.L., et al. Thermal behavior of Mg-Ni-phyllsilicate nanoscrolls and performance of the resulting composites in hexane-1 and acetone hydrogenation. *Chem. Nano. Mat.*, 2020, P. 1–14.
- [29] Ankudinov A.V. A New Algorithm for Measuring the Young's Modulus of Suspended Nanoobjects by the Bending-Based Test Method of Atomic Force Microscopy. *Semiconductors*, 2019, **53**(14), P. 1891–1899.
- [30] Ankudinov A.V., Khalisov M.M. Contact Stiffness Measurements with an Atomic Force Microscope. *Technical Physics*, 2020, **65**(11), P. 1866–1872.
- [31] Nečas D., Klapeček P. Gwyddion: an open-source software for SPM data analysis. *Cent. Eur. J. Phys.*, 2012, **10**(1), P. 181–188.
- [32] Sader J.E., Chon J.W.M., Mulvaney P. Calibration of rectangular atomic force microscope cantilever. *Rev. Sci. Instrum.*, 1999, **70**, P. 3967–3969
- [33] Brewe D.E., Hamrock B.J. Simplified solution for elliptical contact deformation between two elastic solids. *J. Lubrication Technology*, 1977, **99** (4), P. 485–487.
- [34] Popov V.L., Heß M., Willert E. *Handbook of Contact Mechanics. Exact Solutions of Axisymmetric Contact Problems*. Translation from the German Language edition: Popov et al: *Handbuch der Kontaktmechanik*. Springer-Verlag GmbH Deutschland, 2018, 347 p.



NANOSYSTEMS:

PHYSICS, CHEMISTRY, MATHEMATICS

INFORMATION FOR AUTHORS

The journal publishes research articles and reviews, and also short scientific papers (letters) which are unpublished and have not been accepted for publication in other magazines. Articles should be submitted in English. All articles are reviewed, then if necessary come back to the author to completion.

The journal is indexed in Web of Science Core Collection (Emerging Sources Citation Index), Chemical Abstract Service of the American Chemical Society, Zentralblatt MATH and in Russian Scientific Citation Index.

Author should submit the following materials:

1. Article file in English, containing article title, the initials and the surname of the authors, Institute (University), postal address, the electronic address, the summary, keywords, MSC or PACS index, article text, the list of references.
2. Files with illustrations, files with tables.
3. The covering letter in English containing the article information (article name, MSC or PACS index, keywords, the summary, the literature) and about all authors (the surname, names, the full name of places of work, the mailing address with the postal code, contact phone number with a city code, the electronic address).
4. The expert judgement on possibility of publication of the article in open press (for authors from Russia).

Authors can submit a paper and the corresponding files to the following addresses: nanojournal.ifmo@gmail.com, popov1955@gmail.com.

Text requirements

Articles should be prepared with using of text editors MS Word or LaTeX (preferable). It is necessary to submit source file (LaTeX) and a pdf copy. In the name of files the English alphabet is used. The recommended size of short communications (letters) is 4-6 pages, research articles– 6-15 pages, reviews – 30 pages.

Recommendations for text in MS Word:

Formulas should be written using Math Type. Figures and tables with captions should be inserted in the text. Additionally, authors present separate files for all figures and Word files of tables.

Recommendations for text in LaTeX:

Please, use standard LaTeX without macros and additional style files. The list of references should be included in the main LaTeX file. Source LaTeX file of the paper with the corresponding pdf file and files of figures should be submitted.

References in the article text are given in square brackets. The list of references should be prepared in accordance with the following samples:

- [1] Surname N. *Book Title*. Nauka Publishing House, Saint Petersburg, 2000, 281 pp.
- [2] Surname N., Surname N. Paper title. *Journal Name*, 2010, **1** (5), P. 17-23.
- [3] Surname N., Surname N. Lecture title. In: Abstracts/Proceedings of the Conference, Place and Date, 2000, P. 17-23.
- [4] Surname N., Surname N. Paper title, 2000, URL: <http://books.ifmo.ru/ntv>.
- [5] Surname N., Surname N. Patent Name. Patent No. 11111, 2010, Bul. No. 33, 5 pp.
- [6] Surname N., Surname N. Thesis Title. Thesis for full doctor degree in math. and physics, Saint Petersburg, 2000, 105 pp.

Requirements to illustrations

Illustrations should be submitted as separate black-and-white files. Formats of files – jpeg, eps, tiff.



NANOSYSTEMS:

PHYSICS, CHEMISTRY, MATHEMATICS

Журнал зарегистрирован

Федеральной службой по надзору в сфере связи, информационных технологий и массовых коммуникаций
(свидетельство ПИ № ФС 77 - 49048 от 22.03.2012 г.)
ISSN 2220-8054

Учредитель: федеральное государственное автономное образовательное учреждение высшего образования

«Санкт-Петербургский национальный исследовательский университет информационных технологий, механики и оптики»

Издатель: федеральное государственное автономное образовательное учреждение высшего образования

«Санкт-Петербургский национальный исследовательский университет информационных технологий, механики и оптики»

Отпечатано в Учреждении «Университетские телекоммуникации»

Адрес: 197101, Санкт-Петербург, Кронверкский пр., 49

Подписка на журнал НФХМ

На второе полугодие 2021 года подписка осуществляется через
ОАО Агентство «Роспечать»

Подписной индекс 57385 в каталоге «Издания органов научно-технической информации»